

COILED SHAPE MEMORY ALLOY (CSMA) ACTUATORS AND CONDUCTIVE
FILAMENT FOR THE REALIZATION OF 3D PRINTED ROBOTS

by

Akshay Potnuru



APPROVED BY SUPERVISORY COMMITTEE:

Yonas Tadesse, Chair

Dong Qian

Majid Minary

Taylor Ware

Wooram Park

Oziel Rios

Copyright © 2018

Akshay Potnuru

All rights reserved

*Dedicated to my wife, Amulya,
my son, Ayan Samuel, and family..*

COILED SHAPE MEMORY ALLOY (CSMA) ACTUATORS AND CONDUCTIVE
FILAMENT FOR THE REALIZATION OF 3D PRINTED ROBOTS

by

AKSHAY POTNURU, BTech, MS

DISSERTATION

Presented to the Faculty of
The University of Texas at Dallas
in Partial Fulfillment
of the Requirements
for the Degree of

DOCTOR OF PHILOSOPHY IN
MECHANICAL ENGINEERING

THE UNIVERSITY OF TEXAS AT DALLAS

August 2018

ACKNOWLEDGMENTS

This PhD dissertation would not have been possible without the guidance and the help of several individuals who in one way or the other contributed and extended their valuable assistance in the preparation and completion of this study.

I would like to extend my deepest gratitude to my advisor, Dr. Yonas Tadesse for his impeccable support, trust and guidance during the course of my research work. I am very thankful to Dr. Oziel Rios for his guidance and support during my service as a teaching assistant. I am very thankful to my committee members Dr. Dong Qian, Dr. Majid Minary, Dr. Ware Taylor, Dr. Wooram Park, and Dr. Oziel Rios for their insightful comments, suggestions and motivation. The Department of Mechanical Engineering at The University of Texas at Dallas played a very crucial role during the course of my PhD. Some part of this work was supported financially by the Office of Naval Research (ONR) under the grant number N00014-15-1-2503. Many of my friends kept supporting and motivating me, especially my fellow lab mates which include, Lokesh Saharan, Lianjun Wu, Armita Hamidi, Yara Almubarak, Mohsen Jafarzadeh, Farzad Karami, Alec Burns, Abhishek Girish Saxena and Poojan Khanpara. Last but not the least, I am extremely grateful to my wife, Amulya, my son, Ayan Samuel, and family, and the one above all of us, the omnipresent God, for answering my prayers and giving me the strength and for always being there with me. Praise the Lord!!

August 2018

COILED SHAPE MEMORY ALLOY (CSMA) ACTUATORS AND CONDUCTIVE FILAMENT FOR THE REALIZATION OF 3D PRINTED ROBOTS

Akshay Potnuru, PhD
The University of Texas at Dallas, 2018

Supervising Professor: Yonas Tadesse, Chair

Soft robots and humanoids need actuators with low profile, lightweight, high strain and relatively high frequency. Coiled shape memory alloy (CSMA) actuators satisfy these requirements, as SMAs are high-energy density actuators. There are a number of variables that affect the performance of the CSMA actuators. We present the manufacturing, characterization and simulation of the NiTi based CSMA actuators mainly focusing on the geometry and performance relationships. The manufacturing technique resulted in 80% strain with respect to loaded length and greater than 1000% with respect to original length, when actuated with an input voltage of 3.4 V, 0.66 A, and 6 MPa load. The strain response at different frequency was determined experimentally and these actuators can be used in many soft robots. To improve actuation speed, a novel 2-step hot-cold water-cooling was implemented.

One of the requirements of fully functional 3D printed robots is electrical connections in some part of the printed structure. To this effort, we present composite materials consisting of conductive carbon nanoparticles, thermoplastics, and solvents to create filaments for 3D printing. The mechanical and electrical properties of filaments were investigated using a concentration of 0 – 15% weight of carbon nanoparticles (NC) in polylactide (PLA) using dichloromethane (DCM) solvent and subsequently, the DCM is evaporated by drying. The

electrical conductivity of the composite filament is compared with commercial and academia counterparts.

To demonstrate the application of CSMA, three devices /systems are presented in this study. The first one is the actuation of an artificial musculoskeletal (MS) system that can be used as a building block for bioinspired soft robots. The second one is a soft robotic pump inspired by the pumping action of a biological heart. The soft artificial heart can be used in a humanoid robot with facial expressions and can simulate someone blushing or angry by circulating a blood-like fluid. Different designs and their characterization are presented both experimentally and via simulations. The third application is a coronary artery stent. In this work, we performed a case study on the double helix coiled SMA for use as a stent to overcome the mechanical failure due to stress concentration in existing stents. Simulation and experiments were conducted using hyperelastic silicone rubber that mimics the human coronary arteries.

TABLE OF CONTENTS

ACKNOWLEDGMENTS	v
ABSTRACT	vi
LIST OF FIGURES	xii
LIST OF TABLES	xxiii
CHAPTER 1 INTRODUCTION	1
1.1 Motivation of the Study	1
1.2 Objectives of the Study	2
1.3 Dissertation Outline	3
CHAPTER 2 3D PRINTED HUMANOIDS FOR SOCIAL INTERACTION , . . .	4
2.1 Introduction to Humanoids	4
2.1.1 Humanoids with Legged Motion	4
2.1.2 Humanlike Robots	6
2.2 Initial Design of Humanoid HBS-1	7
2.3 Humanoid Buddy	9
2.3.1 Introduction of Social Robots and Human Interaction	11
2.3.2 Humanoid “Buddy” Hardware	12
2.3.3 Ballet Dance Sequence of the Servo Motors	16
2.3.4 Audio Interfacing of Arduino for Dance	18
2.3.5 Color Recognition using the Camera	19
2.3.6 Stress Analysis of the Arm	20
2.3.7 Experimental Analysis of Load Carrying Capacity	23
2.3.8 Conclusion and Future Work	24
CHAPTER 3 INVESTIGATION OF POLYLACTIDE AND CARBON NANOCOM- POSITE FILAMENT FOR 3D PRINTING	27
3.1 Introduction	27
3.2 Experiments	35
3.2.1 Materials	35
3.2.2 Solution Preparation for Filament	35

3.2.3	Filament Preparation	36
3.2.4	Long Filament Fabrication	40
3.3	Experimental Results	42
3.3.1	Viscosity of PLA, NC and DCM solution	42
3.3.2	Electrical property of the PLA and carbon nanoparticles composite filaments	42
3.3.3	Mechanical property of the PLA and carbon nanoparticles composite filaments	46
3.3.4	Micro-structure of Filaments	48
3.4	Observations and Discussions	53
3.5	Application in Humanoids	55
3.6	Conclusion	57
CHAPTER 4 FABRICATION AND CHARACTERIZATION OF COILED SHAPE MEMORY ALLOY (CSMA) ACTUATORS FOR SOFT ROBOTS		60
4.1	Introduction	60
4.2	Shape Memory Effect	70
4.3	Influence of Annealing Temperature on CSMAs	71
4.4	Experimental Setup for Actuation	73
4.4.1	Fabrication	73
4.5	Results and Discussion of Characterization of CSMAs	77
4.5.1	Experimental Setup for the Testing Actuator	77
4.6	Cyclic Testing of Coiled SMA Actuators	89
4.7	Artificial Musculoskeletal System Actuated by Coiled SMA with 2-Step Hot-Cold Water Cooling	89
4.8	Conclusion on Actuation of CSMA	93
4.9	Modeling of CSMA based on only Temperature at Low Load Conditions	98
4.9.1	Heat Transfer Model	98
4.9.2	Small Diameter Coiled SMA Preparation	101
4.9.3	Modeling Temperature of CSMA at Low Load	106
4.9.4	Simulation	111

4.9.5	Discussion	113
CHAPTER 5	APPLICATION OF COILED SMAS FOR HUMANOIDS AND HEALTH-CARE	117
5.1	Artificial heart for humanoid robot (SMAs Vs CSMA) ,	117
5.1.1	Biological Heart	118
5.1.2	History and Existing Artificial Hearts	120
5.1.3	Shape Memory Alloy Artificial Muscles	121
5.1.4	Related Robotic Heart Works	122
5.1.5	Humanoid Robots with Facial Expressions (HRwFE)	124
5.1.6	Design and Manufacturing	125
5.1.7	Coiled Shape Memory Alloy (SMA) Actuators for the Robotic Heart	129
5.1.8	Characterization of Coiled SMAs	130
5.1.9	Design and Manufacturing of the Robotic Heart (Design 2)	133
5.1.10	Fabrication of Design 2	135
5.1.11	Modeling and Simulation of SMA Heart	137
5.1.12	Modeling and Simulation of CSMA Heart (Design 2 and Design 3)	144
5.1.13	Experimental Setup	151
5.1.14	Applications	156
5.1.15	Conclusion on robotic heart	165
5.2	Case Study: Simulation and Experimental Study of NITI Double Helix Stents for Human Coronary Arteries	166
5.2.1	Introduction	166
5.2.2	Simulation	168
5.2.3	Experiment	171
5.2.4	Simulation and Experimental Validation	174
5.2.5	Stent Implantation Techniques	177
5.2.6	Discussion	178
5.2.7	Conclusion	181
CHAPTER 6	SUMMARY AND CONCLUSION	183
6.1	Summary	183

6.2	Contributions	184
6.2.1	Humanoids Buddy and HBS-1	184
6.2.2	Investigation of Polylactide and Carbon Nanocomposite Filament for 3D printing	186
6.2.3	Fabrication and characterization of coiled shape memory alloy (CSMA) actuators for soft robots	189
6.2.4	Design and characterization of artificial heart for humanoid robot (SMAs Vs CSMA)	190
6.2.5	Simulation and experimental study of NiTi double helix stents for hu- man coronary arteries	192
	BIBLIOGRAPHY	194
	BIOGRAPHICAL SKETCH	215
	CURRICULUM VITAE	

LIST OF FIGURES

2.1	The cost of humanoids divided according to their price range in US dollars. . .	8
2.2	HBS-1 compared to humans [232]	9
2.3	HBS-1 initial design, robot to robot interaction, rendered image showing work environment of HBS-1.	10
2.4	Humanoid Buddy (a) with an 8-year old normal child and (b) the humanoid parts and raising hands gesture. (Parental consent form was obtained for the photograph of underage child next to the robot).	13
2.5	Humanoid buddy hardware full view and base.	14
2.6	Hardware Neck and Head	14
2.7	Schematic diagram of the robot and the head mechanisms along with the minimum and maximum servo position of the joints.	15
2.8	Simplified diagram of Buddy gestures (max and min).The corresponding angles are shown in figure 2.7.	16
2.9	Servo motor actuation sequence during ballet dance. Different graphs show the on and off time of each servo represented in figure 2.7.	17
2.10	Photograph of the ballet dance of the robot in 1 cycle that was obtained from video recording.	17
2.11	Demonstrated Humanoid robot “Buddy” before 1200 people before the screening of the movie “Terminator Genisys” to encourage young students to pursue STEM majors at AMC NorthPark 15, 8687 North Central Expressway, Dallas, TX 75225. Published in Dallas Morning News.	18
2.12	Flowchart of color recognition	19
2.13	Finding colored objects, (a) green object, (b) blue objects and (c) experimental setup for color recognition.	21
2.14	Stress analysis of the robot arm part, (a) wrist von-Mises stress, (b) wrist - displacement, (c) lower arm von-Mises Stress, (d) lower Arm - displacement, (e) upper arm von-Mises Stress, and (f) upper arm - displacement.	22
2.15	Photograph of load carrying capacity of the robot during experiment, (a) 0 g, (b) 100 g, (c) 200 g and 300 g load.	24
2.16	Experimental results of actuation angles of the shoulder joint of the robot at different loads at the tip	25
3.1	The molecular structures of the materials used for filament preparation. The major process includes dissolving biodegradable thermoplastic Polylactide (PLA) with dichloromethane (DCM) and adding mesoporous carbon nanoparticles (NC).	33

3.2	Preparation of filaments and 3D printing. (a) Magnetic stirring with closed container (b) picture of the drying technique and schematic view and (c) MakerBot Replicator 2 3D printer used for printing the made filaments.	37
3.3	(a) 3D printed load carrier structures (b) Full horizontal drying setup with weights.	39
3.4	(a) SolidWorks 2014 CAD model of the cutting apparatus for splicing the rubber mold that has initial per-cut. (b) Assembled cutting apparatus when the rubber tube is pulled by hand.	40
3.5	(a) The spring mechanism implemented in the holders for more load (b) 1.5m long filament preparation using spring mechanism and (c) prepared long filament.	41
3.6	Viscosity (mPa-s) of carbon nanoparticles percentage for 1 g PLA and respective volumes of DCM from table 3.2 at 25 rpm and at room temperature for 1:5 wt. ratio.	43
3.7	Resistivity and conductivity of the filaments made of various wt.% of carbon nanoparticles in PLA. The samples were 1.75mm in diameter and 100 mm long, where the resistances of each sample were taken at 10 mm distance along the filament, both the average and standard deviation of the measurement are shown.	44
3.8	Comparison of the conductivity of nano-additives in host thermoplastic polymer. [242, 138, 227, 3, 6, 2, 135] . The commercially available filaments are shown in grey, the academically published filaments are shown in salmon color and the presented work is shown in mustard color.	45
3.9	Tensile testing of (a) Clear PLA (right) and 15wt.% NC and PLA (left), (b) clear PLA (left) and 15wt.% NC and PLA (right).	47
3.10	Mechanical property of filaments made of various compositions of wt.% NC in PLA (a) Tensile stress-strain curve (diamond marker shows breakpoint) and (b) magnitude of tensile stress (MPa) & tensile strain (%) at the break for all samples with along with a 3D printed structure.	49
3.11	Microscopy and image analysis of various wt.% of NC in PLA along the surface: (Top) SEM images of the filaments of NC 0.5, NC 1.5, NC 9 and NC 15 at 10 μ m resolution; and (Bottom) Bar graph of particle distribution of nanoparticles in the respective SEM images.	50
3.12	SEM Images of samples at the surface: (a) clear PLA, (b) PLA+ DCM through tube drying and (c) SEM image of NC15 lower resolution showing the effects of horizontal drying.	51
3.13	Microscopy and image analysis of various wt.% of NC in PLA: SEM images of the filaments of NC0.5, NC1.5, NC9 and NC15 at 100 μ m resolution in cross-sectional view.	52

3.14	(a) MakerBot 3D printer test system and (b) 30 mm x 5 mm x 1 mm dog bone structure printed from a composition of 15 wt.% carbon nanoparticles and Polylactide fiber (PLA) using MakerBot 3D printer.	54
3.15	Complex wring examples of 3D printed humanoid (a) Front side of Buddy-3D printed humanoid having mobile base [30], (b) a child-size humanoid, HBS-1 similar in size to a 7-year old, 3D printed in the laboratory [232].	57
3.16	(a) Humanoid application dimensions , (b) the 3D printed assembly with the syringe and needle used and (c) 3D printed assembly with the ink jet (hand) printed cast	58
4.1	Coiled SMA actuator based applications: (a) Coiled SMA proposed for humanoid faces. [199]; (b) artificial heart for humanoid robot using coiled SMA actuators with sequential actuation of the robotic heart [161, 158]; SMA torsional actuators with Ni-Cr heating coil (c) Y-type and (d) Z-type bolted down front view [146]; (e) Spherical prototype for crawling and jumping [195]; (f) the bending of the Type B actuator [211]; (g) a gripper prototype holding an object [238] and (h) Side View of SMA springs in antagonistic configuration for actuating single robot joint [33], (i) The end segment of MINIR-II robot moves back and forth under active cooling of SMA actuators. [33]	62
4.2	3D stress-strain-temperature diagram of SMA phase transformation (Super elastic and Shape memory effect [11])	71
4.3	Fabrication (coiling and annealing) and testing of the SMA spring actuator. After motor coiling, all the 9 samples are kept inside a furnace for 350 °C for 45 mins and air cooled to room temperature.(Strain with respect to loaded length $\varepsilon_L = \delta/L_L$; Strain with respect to original length $\varepsilon_O = \delta/L_O$, where $\delta = L_L - L_a$)	74
4.4	Experimental Setup used to characterize the coiled SMAs (a) Schematic and (b) Actual. The CSMA is connected to a load cell which is attached to a stand and a load weight is hanged. A thermocouple is attached on the top of the actuator to measure the temperature changes during actuation. A laser sensor is used to measure the displacement. All sensors are connected to the NI DAQ which is connected to computer with LabVIEW to measure the readings in real-time. A camera is used to record the actuation which is used for displacement measurement as a backup using Tracker software.	75
4.5	Actuation results for square input of 4.4 V with a frequency of 0.25 and duty of 50%. (a) at time = 0 sec, (b) at time = 2 sec and (c) at time = 4 sec showing 80% actuation. (Number of Coils, N = 12; length of actuator wire, Lw = 120 * 10 ⁻³ m; length of the spring, Ls = 10.06 * 10 ⁻³ m; Wire diameter, ds or dw = 0.2 * 10 ⁻³ m [49]; spring diameter, Ds = 3.175 * 10 ⁻³ m)	76
4.6	Parameters and values of the SMA springs used.	77
4.7	All 9 samples before actuation and after actuation.	78

4.8	A comparison graph of static deflection at different loads for SMA springs of 3 different diameters of 3.18 mm (D1),3.96 mm (D2) and 4.75 mm (D3) at a different number of coils per unit length of 1.26 per mm (32 TPI) (P1), 1.406 per mm (36 TPI) (P2), and 1.575 per mm (40 TPI) mm (P3) respectively. All SMA springs are made with 120 mm long cylindrical SMA wire of radius 0.1 mm, which has a weight of 24 mg. The lines represent polynomial fits of the data points.	82
4.9	A comparison graph of actuation strain % with respect to loaded length ε_L for SMA springs of 3 different diameters of 3.18 mm (D1),3.96 mm (D2) and 4.75mm (D3) at a different number of coils per unit length of 1.26 per mm (32 TPI) (P1), 1.406 per mm (36 TPI) (P2), and 1.575 per mm (40 TPI) mm (P3) respectively. The lines represent polynomial fits of the data points.	83
4.10	A comparison graph of actuation strain % with respect to original length ε_o for SMA springs of 3 different diameters of 3.18 mm (D1),3.96 mm (D2) and 4.75mm (D3) at a different number of coils per unit length of 1.26 per mm (32 TPI) (P1), 1.406 per mm (36 TPI) (P2), and 1.575 per mm (40 TPI) (P3) mm respectively. The lines represent polynomial fits of the data points.	84
4.11	Effect of diameter for one pitch of 1.406 per mm (36 TPI) (P2), (a) strain % with respect to loaded length ε_L , (b) strain % with respect to original length and (c) static deflection at different loads for SMA springs of 3 different diameters of 3.18 mm (D1), 3.96 mm (D2) and 4.75mm (D3) with spring original lengths of 8.54 mm L_{o21} , 6.86 mm L_{o22} and 5.72 mm L_{o23} respectively. The lines represent polynomial fits of the data points.	85
4.12	Influence of pitch for one diameter of 3.96 mm (D2), (a) strain % with respect to loaded length ε_L , (b) strain % with respect to original length ε_o and (c) static deflection at different loads for SMA springs of 3 different number of coils per unit length 1.26 per mm (32 TPI) (P1), 1.406 per mm (36 TPI) (P2), and 1.575 per mm (40 TPI) (P3) mm respectively with spring original lengths of 7.65 mm L_{o12} , 6.86 mm L_{o22} and 6.12 mm L_{o13} respectively. The lines represent polynomial fits of the data points.	86
4.13	Representative sample D1P3, (a) strain % with respect to loaded length ε_L , (b) strain % with respect to the original length ε_o and (c) static deflection at different loads D1P3 CSMA spring (number of coils per unit length 1.575 per mm (40 TPI) mm (P3) with spring original lengths of 7.63 mm L_{o31} and spring diameter of 3.175 mm (D1).)	87
4.14	Time domain result of sample D1P3, (a) displacement at different loads, (b) voltage, (c) current,(d) temperature and (e) force for D1P3 CSMA spring (number of coils per unit length 1.575 per mm (40 TPI) mm (P3) with spring original lengths of 7.63 mm, L_{o31} and spring diameter of 3.175 mm (D1) respectively. All SMA springs are made with 120 mm long cylindrical SMA wire of radius 0.1 mm which has a weight of 24 mg. All the SMA springs are actuated at a constant current of 0.666 A (recommended by the manufacturer Dynalloy Inc. for cylindrical SMA) with a voltage of 4.2V approximately.)	88

4.15	A comparison graph of different frequencies $f = 1$ Hz, $f = 0.5$ Hz, $f = 0.25$ Hz, $f = 0.167$ Hz and $f = 0.125$ Hz for D2P2 CSMA spring (number of coils per unit length 1.406 per mm (40 TPI) mm (P2) with spring original lengths of 12 mm and spring diameter of 3.96 mm (D2) respectively. SMA spring is made with 90 mm long cylindrical SMA wire of radius 0.1 mm which has a weight of 18 mg. SMA spring is actuated at a constant current of 0.666 A (recommended by the manufacturer Dynalloy Inc. for cylindrical SMA) with a voltage of 3.3V approximately at a load of 18 g (1000 times its weight).)	90
4.16	A comparison graph of different duty cycle and frequencies keeping ON time of 2 seconds constant, $D = 80$ %, $D = 66.67$ %, $D = 57.4$ %, $D = 50$ % and $D = 44.44$ % for D2P2 CSMA spring (number of coils per unit length 1.406 per mm (40 TPI) mm (P2) with spring original lengths of 12 mm and spring diameter of 3.96 mm (D2) respectively.)	91
4.17	(a) and (b) we see the schematic diagram of the CSMA actuators in the MS joint. In (b) we see the angular measurement method used. MS joint actuation with 2 coiled SMAs in opposite sides for 1 cycle of 1.332 A constant current for both sides with a pulse actuation of 4 seconds on and off as shown in (c) and (d) for left and right SMA actuators respectively. In (e) we see the movement of the MS joint. The SMA coils used here are 2 on each side of wire diameter 0.2 mm, spring diameter of 1.524 mm with 40 rings and a pitch of 3.15 turns per mm. (f) MS joint actuation with 2 coiled SMAs in opposite sides for 1 cycle of 1.332 A constant current for both sides with a pulse actuation of 4 seconds ON and OFF (No active cooling). The video is supplied in supplementary material (Video: S2).	94
4.18	Schematic diagram of 2-step hot - cold cooling setup. We have used 4 pumps, 2 for hot (~ 50 °C) water and 2 for cold (~ 23 °C) water.	95
4.19	Experimental setup for 2-step hot - cold cooling. We have used 4 pumps, 2 for hot water and 2 for cold water. The pipes and wires used for connecting the pumps to the MS joint are ultra soft which do not keep any external stress on the joint against the actuation motion.	95
4.20	Experimental results of the 2-step hot - cold water actuation of coiled SMAs in the MS joint for 5 cycles. In figure 4.21 we see the graphical representation of the movement of the MS joint for 5 cycles.	96
4.21	Sequential actuation of CSMA in MS joint and the 2-step hot - cold cooling system actuation of coiled SMAs in the MS joint for 5 cycles. The 2-step hot - cold cooling is used as only cold water quenches the coiled SMAs from high temperature to room temperature which may lead to previous shape memory loss. (a) and (b) represent the pulse actuation of left and right actuators respectively. The pulse actuation of the left hot and cold and right hot and cold is shown in (c), (d), (e) and (f).	97

4.22	3D stress-strain-temperature diagram of SMA phase transformation (Super elastic and Shape memory effect [11])	99
4.23	(a) Schematic Diagram of the bobbin winder made in Sketchup® (b) The final prepared coiled SMA after annealing.	101
4.24	Experimental setup of the coiled SMA preparation (a) the completer setup (b) the detailed view of SMA wire on the mandrel.	103
4.25	Fabrication (coiling and annealing) and Testing of the SMA Spring actuator .	103
4.26	(a)SMA Experimental setup for characterization of small diameter CSMA (d = 0.1 mm) (b) Best actuation at 10.7V and 0.2A at load at 4.375 g (200 times its weight) with 82.75 % strain at a square pulse voltage actuation with duty of (300)/7 % and a period of 7 seconds	104
4.27	SMA Experimental results of characterization: Load Vs Strain	105
4.28	SMA Experimental results of characterization: Load Vs Deformation & Initial Length (Spring Constant)	105
4.29	Simulink® Matlab™ simulation flowchart	107
4.30	Simulink Matlab™ simulation results and experimental results for square input of 3.48 V, 0.66A at 4 g load. (a) Temperature in °C for all 9 samples experimental and (b) Temperature in °C for all 9 samples of different diameter and pitch individual comparison of experimental and simulation.	108
4.31	Martensite volume fraction Vs Temperature, Simulink® Matlab™ simulation results for square input of 3.5 V with a frequency of 0.02 for D1P3 sample. (Parameters are seen in table 4.8)	113
4.32	Simulink® Matlab™ simulation results for square input of 3.5 V with a frequency of 0.02 for D1P3 sample at different diameter reduction parameters. (a) Input Voltage in V, (b) Temperature in °C (c) Displacement in mm, (d) Martensite volume fraction, e. (Parameters are seen in table 4.8)	114
4.33	Simulink® Matlab™ simulation results for square input of 3.5 V, 2.75 V, 2.05 V and 2 V with a frequency of 0.02 for D1P3 sample. (a) Input Voltage in V, (b) Temperature in °C (c) Displacement in mm, (d) Martensite volume fraction, e. (Parameters are seen in table 4.8).	115
4.34	Simulink® Matlab™ simulation results for different pitches for square input of 3.5 V (a) Input Voltage in V, (b) Temperature in °C (c) Displacement in mm, (d) Martensite volume fraction, e. (Parameters are seen in table 4.8).	116
5.1	Peristalsis motion by sequential actuating (a-d) of the robotic heart	118
5.2	Artificial heart (a) CardioWest™ : Total artificial heart and human heart illustrations with detailed callouts (Courtesy of SynCardia Systems Inc.) [15] and (b) AbioCor® : World's First Artificial Heart (Courtesy of Abiomed Inc.)	119

5.3	Facially expressive humanoids robots : (a) Albert-piezo: ultrasonic motors based humanoid head, (b) Lilly humanoid: servo motors and embedded piezoelectric sensors in the face, (c) Shape memory alloy based baby head, (d) Albert-HUBO, servo motors based humanoid (Courtesy of Hanson Robotics Inc.).	123
5.4	Humanoids developed in our laboratory (a) Buddy [153, 30], facially expressive but without skin in the face, (b) Buddy with embedded sensors in the skin and mounted in the arm and (c) HBS-1 a 7-year-old child size humanoid as compared to an eight-year-old child.	123
5.5	Artificial Heart (Design-1) (a) Schematic diagram of the front view of the artificial heart wrapped with SMA,(b) the section view of the artificial heart and (c) prototype, (d) CAD model and (e) SMA wrapped around the heart.	126
5.6	Manufacturing diagram for creation of artificial heart wrapping with SMA fibers.	128
5.7	Fabrication of coiled SMA wires: SMA wires wrapped around bolts and secured by nuts	129
5.8	Deformation Vs. Voltage of the coiled SMA actuator at no load. (Length = 20 mm, d = 200 μ m, D = 2 mm)	131
5.9	Timeline sequence of the actuation at no load condition at 4V at T = 0 sec and 2 sec and an overlapped merged image of actuation.	132
5.10	Timeline sequence of the actuation at 0.1 g load condition at 4V at T = 0 sec and 2 sec and an overlapped merged image of actuation.	132
5.11	Timeline sequence of the actuation at 0.66 g load condition at 4V at T = 0 sec and 2 sec with an overlapped merged image of actuation.	133
5.12	Artificial Heart (Design 2): (a) Schematic diagram of the top view of the artificial heart attached with hard structure pressure distributors,(b) the section view of the artificial heart and (c) prototype, (d) CAD model and (e) Coiled SMA attached to the side of the hard structures the cover the robotic heart.	134
5.13	Manufacturing process diagram for creation of artificial heart.	136
5.14	General hyperelastic material stress-strain curves (a) single curvature, (b) one inflection point and (c) two inflection points.	138
5.15	Hyperelastic stress analysis in ABAQUS 6.13 (a-f) at pressure of 0.01 MPa . . .	140
5.16	FEM simulation results plotted in MATLAB 2013b (a) Stress vs strain at center top (Node 37) and (b) Pressure Vs (Deformation, % deformation and volume of liquid being pumped in mL (calculated)) on one side of the model	141
5.17	(a) Volume of the fluid inside the heart model during flow simulation = 116 mm^3 or 116 mL (b). Shows the inlet and outlet valves of the flow simulation	143
5.18	Plot of maximum velocity Vs pressure drop	144

5.19	Flow analysis of computer aided design of the artificial heart in SolidWorks (1-3) in pipes in 1,1.5 and 2 seconds of simulation run respectively and (4) in balls for the maximum pressure drop of 32 psi (220.63 kPa) (where inlet pressure is 43 psi (296.48 kPa) and outlet pressure is 11 psi (75.84 kPa))	145
5.20	Hyperelastic Stress Analysis in ABAQUS 6.14 (a-d) at Pressure of 0.025 MPa for a two-section peristalsis motion by sequential actuating.	146
5.21	(a) Stress Vs Strain at a load of 0.25 MPa applied load and (b) Deformation, % deformation and volume of liquid being pumped in mL (calculated)) on one side of the model for 2 section peristalsis motion by sequential actuating (c) Stress vs strain vs load applied in 3D of two section actuation	147
5.22	Comparison of three and two-section peristalsis motion by sequential actuation.	148
5.23	Plot of Maximum Velocity Vs Pressure Drop	149
5.24	Flow analysis of computer aided design of the artificial heart in SolidWorks (a) in pipes and (b) in balls for the maximum pressure drop of 32 psi (where inlet pressure is 43 psi and outlet pressure is 11 psi)	150
5.25	(a) Schematic diagram of the experimental setup, and (b) picture of the laboratory experimental setup	152
5.26	(a) Voltage applied to the SMA fibers(130 μm in diameter) and (b) the displacement of the drop of the black ink.	153
5.27	(a)Deformation of the artificial heart, and (b) &(c) magnified views of the deformation (No.1 No.7).	154
5.28	(a) Test 1:SMA fibers contact with artificial heart directly and (b) Test 2: Artificial heart covered with tape.	155
5.29	Displacement of the drop of blank ink using a tape on the silicone and without.	156
5.30	The transparent silicone layer embedded with tube for demonstrating the facial color change	157
5.31	Sequential actuation of the robotic heart, results of trail 3 at time = 0 , 60 and 120 sec	158
5.32	A few examples of insulin pumps [126]	159
5.33	Experimental setup of the artificial heart soft pump actuation testing with cheek structure on a mannequin.	161
5.34	Schematic (Design 3) (a) Top View and (b) Side view of the soft pump with the rectangular plates showing the SMAs in the front and back section (c) Top and Side view of the soft pump with the rectangular plates and CSMA.	162

5.35	Time domain plot of voltage and current supply to back 10 SMAs and front 8 SMAs corresponding to the output volume flow rate of the soft pump (Design 3). (a) and (c) show the voltage and current for back 10 SMAs and similarly (b) and (d) show the voltage and current for front 8 SMAs. (e) shows the volume change (cm^3) with respect to time (sec) for four different voltage and current inputs. . .	163
5.36	Comparison of the robotic heart (a) CSMA heart presented in this work with (b) pneumatic [169] ,(c) internal combustion heart [180] and (d) SMA artificial heartbeat [224]	164
5.37	Superelastic effect of NiTi material	168
5.38	Double helix stent model : (a) side view of the coronary artery showing the different sections adventitia, media, intima, plague and the double helix stent, (b) the section view with the double helix stent profile, (c) the boundary conditions of the simulation in a transparent view; Stress distribution in the vessel during artery moving process (d) is at time = 0.1 sec with maximum von-Mises stress of 0.45 MPa, (e) half of a cardiac cycle with maximum von-Mises stress of 1.5 MPa, (f) is 4/5 of a cardiac cycle, t = 0.6 sec with maximum von-Mises stress of 0.54 MPa.	169
5.39	Simplified testing of double helix stent model (a) The EcoFlex™ 10 silicone coronary artery model, (b) the coiled and clamped Nitinol wire of diameter 0.1 mm around a metal screw in its thread, (c) the fabricated NiTi single helix stent after annealing at 390°C and removed from the screw (d) the double helix stent fabricated and clamped before the experiment, (e) slightly deformed double helix stent after the experiment where maximum deformation of about 6 times the simulation at a static load of 100 g, (f) the stent-coronary model, with the stent embedded carefully. The stent can be seen partially with the flexible non-rigid fishing line wire super-glued on both ends, not in center, (g) the experimental setup with stand with firmly fixed horizontal rods, calibrated weights and camera.	172
5.40	Experimental Results: (a-f) shows the snapshots of deformation when different loads are applied and with an initial curvature of 30 mm. The different loads are 0 or no load, 10 g, 20 g, 50 g, 100 g and merged picture of the all pictures. . . .	173
5.41	Tensile testing silicone (a) shows the ASTM D412 Type C 3D printed casings for Ecoflex-10 silicone casting, (b) the casted dog bone structures, (c) and (d) show the Instron tensile tester (maximum load 50 kN) machine with the silicone dog bone structure.	175
5.42	Uniaxial data (Stress vs Strain) of 6 samples Ecoflex-10 silicone ASTM D412 Type C casted dog bone structures using the Instron tensile tester (maximum load 50 kN) machine. Sample 3 result is used for simulation.	176
5.43	FEM Analysis: (a) and (b) show the boundary conditions (fixed and load points) used in ANSYS simulation to validate the experimental model ; (c) and (d) show the physics and model controlled meshing in ANSYS; Simulation results for uniformly distributed load of 20 g (e) deformation and (f) stress in the material.	177

5.44	Matlab plot of experimental and simulated deformation with respect to 10 to 100g load with all the hyperelastic models. It shows the central deformation about 3.5 mm, which is almost 5 times more than the coronary artery deformation.	178
5.45	Stent implantation method 1: (a) The NiTi SMA stent is completely deformed to any desired shape for easy insertion ,(b) annealing done in a furnace (exposing to body heat is possible for other composition) above transition temperature and (c) shows the schematic diagram of the insertion technique using the SMA effect.	179
5.46	Stent implantation method 2: (a) shows a regular SMA spring stent, (b) slightly twisted SMA spring by hands showing reduction in diameter, (c) relaxed or torque released SMA spring stent and (d) shows the schematic diagram of insertion on the SMA spring stent inside the coronary artery using a compressive balloon for pre stress to reduce the diameter of the spring stent while insertion.	179
5.47	Comparison of the (a) NiTi double helix stent with (b)cross cage 54/46 NiTi stent [76] and (c) single helix NiTi stent [162]	181
6.1	Overview of chapter 2: (1) Humanoid Buddy - 3D printed robot , (2) Simulation of load carrying capacity of humanoid Buddy arm,(3) “Ballet” dance performance by humanoid Buddy, (4) Experimental verification of load carrying capacity, (5) Complex wiring of Buddy and HBS-1 and (6) Humanoid HBS-1 initial design. [153, 155, 232]	185
6.2	Overview of chapter 3: (a) molecular structure of PLA, DCM and graphitic carbon, (b) comparison of conductivity of the filament from the present work with other published or commercially available conductive filaments, (c) Tensile testing of the filaments with different weight percentage carbon nanoparticle filler and the 3D printed part, (d) 3D printing the NC15 filament, (e) 3D printed dog bone structure and (f) SEM images of cross-section of the NC15 filament. [160]	187
6.3	Overview of chapter 4: (a) Time domain characterization of D1P3 CSMA sample, (b) MS joint actuation using CSMA, (c) CSMA actuation time sequence, (d) 9 samples strain with respect to loaded length at different loads (strain > 80%) , (e) Simulation and experimental comparison of thermal profile of the CSMA actuation, (f) Initial deflection of the SMA spring with respect to load and (g) fabrication method and parameters used. [159]	188
6.4	Overview of chapter 5 (a): (a) Time sequence of CSMA (Design 2) artificial heart pumping fluid into cheek structure, (b) characterization of CSMA (Design 3) artificial heart pumping (time domain), (c) ABAQUS simulation of 2 section peristalsis motion (Design 2), (d) SolidWorks flow simulation of the CSMA (Design 2 & 3) artificial heart pumping fluid ,(e) Experimental Setup of CSMA (Design 3) artificial heart pumping, (f) and (g) show the design 1. [161, 157] . .	191

6.5 Overview of chapter 5 (b): (1) ANSYS multiphysics (hyperealstic and superelastic) simulation of the stent modal in the coronary artery, (2) Experimental setup and the custom made NiTi double helix stent in soft EcoFlex-10 silicone material, (3) Experiential results of the deformation with respect to load and (4) ANSYS simulation and experimental verification of the custom made NiTi double helix stent in soft EcoFlex-10 silicone material. [154] 193

LIST OF TABLES

2.1	General profile of Humanoid “Buddy”	26
3.1	Literature review on additive materials in thermoplastics and the properties improved.	34
3.2	The composition of materials studied, which include various carbon nanoparticles (NC) proportions in 1 gram of PLA. (*The DCM volume was increased to keep the viscosity in the optimum value for solid filaments. @The 6% wt. filaments were not 3D printable for testing.)	36
3.3	Tensile test results of all the PLA/DCM/NC specimens of 1.75mm diameter.	48
4.1	Fabrication of CSMA and characterization by various authors.	64
4.2	Observed parameters which influence the performance of CSMA	70
4.3	Comparison to commercially available Coiled SMA	73
4.4	Original spring length, $L_{o_{i,j}}$ for different diameters, D_i and different no. of coils per unit length, P_j	77
4.5	Load that provided maximum strain for different diameters, D_i , and different no. of coils per unit length, P_j	77
4.6	Maximum strain wrt. loaded length, $\varepsilon_L = \frac{\delta}{L_L}$ for different diameters, D_i & different no. of coils per unit length, P_j	79
4.7	Maximum strain wrt. the original length, $\varepsilon_o = \frac{\delta}{L_{o_{ij}}}$ for different diameters, D_i & different no. of coils per unit length, P_j	79
4.8	Simulation parameters used in Simulink model	111
5.1	Actuator parameters of SMA wires	153
5.2	Material properties of NiTi nitinol [234] as seen in figure 5.37	168
5.3	Material properties of the coronary artery layers - coefficients of the strain energy density function [235]	168
5.4	Coefficients of the strain energy density function for each hyperelastic model [81], where W is strain energy potential; C'_{ij} is material constants characterizing the deviatoric deformation of the material; I_i is deviatoric strain invariant	176
6.1	Typical profile of CSMA	189

CHAPTER 1

INTRODUCTION

This dissertation provides a detailed description of the research activities, developments, results on NiTi based shape memory alloy and composite filament for 3D printing. The dissertation explores coiled shape memory alloys (CSMAs) as actuators for use in robotics and humanoids, and as stents for humans. This work introduces a novel idea on fabrication and characterization of low cost conductive nano-carbon (NC) polylactic acid (PLA) composite 3D printable filaments that can be used for robots. The dissertation consists of six chapters. In this chapter, we will present the motivation for the work, the objectives, and the structure of the dissertation.

1.1 Motivation of the Study

This research is deeply motivated to advance humanoids making them more human-like and solve some limitations and issues. Two major aspects of humanoids are considered in this study: manufacturing and actuators. Recently, several humanoids have been manufactured using 3D printing technologies and they are servo actuated like humanoid Buddy [153, 155] and HBS [232] to mention a few. 3D printing is expected to be the leading manufacturing method of the future of robotics. All robots are electrically wired and these wires have a potential to detach or tangle during actuation. This was the motivation to study other alternatives to traditional wiring in robots. In this work, a novel 3D printable conductive nano-carbon PLA circuitry is proposed as one solution for the problem.

With respect to actuation, several actuators are used in humanoids which include servos, pneumatics, etc. Servo motors are the most commonly used since they have good control and frequency but are bulky, heavy components and have noisy operation. They also do

not mimic human muscles. Artificial muscles like SMAs [156], twisted coiled polymers [66], electroactive polymers [198], etc., are of great interest for replacing servo motors. Out of all the artificial muscles, SMAs have the highest energy density, making them a potential for a low profile, silent and lightweight actuator. The major limitation of SMAs is their strain of 4-7%. This work is aimed at increasing the strain of SMAs by coiling them in a helical structure and study how CSMAs are influenced by different parameters of fabrication and spring geometry. A fabrication technique to get huge strains with high load capacity to its weight ratio is proposed. Several applications of using CSMAs are presented including an artificial heart soft pump for humanoids, a musculoskeletal joint, and a novel double helix stent model.

1.2 Objectives of the Study

The study aims at establishing the relationship between geometrical properties and performance of coiled SMAs. This study also aims at understanding and characterizing of nano-carbon PLA composite for use in 3D printing for electrical circuitry.

The main objectives are presented below:

(a) NC-PLA composite 3D printing for humanoid electrical circuitry

- Understanding carbon-nano particles in PLA with dichloromethane (DCM) in solution blending. Fabrication of a uniform 3D printable filaments with different compositions of NC and PLA. Characterization of the filaments with different compositions of NC and PLA by conducting tensile test, electrical conductivity studies and microscopy. 3D printing the filament and characterizing the 3D printed part.

(b) Fabrication, characterization and applications of CSMAs

- Understanding the relationship between geometry and performance of CSMAs. Manufacturing and characterization of the CSMAs with different spring geometry, stress-strain, frequency test, active cooling and microscopy.

- Application of CSMA in soft pump artificial heart for humanoids for human like expressions like blushing.
- Application of CSMA in stents and musculoskeletal joint. Design and development of devices based on CSMA.

1.3 Dissertation Outline

A comprehensive study is conducted in the areas of manufacturing and actuators in this work for potential applications in humanoids and other robots. Several case studies have been conducted to show how CSMA perform in humanoid and other robotic applications. This study is divided into six chapters as follows:

In chapter 1 (the present chapter), a detailed introduction to the study, motivation and objectives are presented. In chapter 2 , a brief introduction to humanoids and a detailed section on the capabilities of humanoid “Buddy” are explained.

In chapter 3, we present an exhaustive study of nano-carbon PLA composite filament for 3D printing in commonly used FDM printers.

In chapter 4, we study CSMA as actuators from fabrication, characterization, basic modeling at low loads, cyclic tests and frequency study with active cooling in novel musculoskeletal joint.

In chapter 5, we study several applications or case studies of CSMA in humanoids and robotics. The chapter covers applications like artificial heart soft pump for humanoids actuated by CSMA and a novel doubled helix stent model for humans.

In chapter 6, we conclude with the summary in both manufacturing and actuation and the contributions to science and technology. In the end, we will present the future course of work.

CHAPTER 2

3D PRINTED HUMANOIDS FOR SOCIAL INTERACTION ^{1, 2}

2.1 Introduction to Humanoids

Humanoid robots have great potential for use in our daily life by accompanying or working together with people. Growing interest in humanoid robots has spurred a substantial increase in their development over the past decade. Researchers have shown several prototypes in the literature focusing on various aspects. This section primarily focuses on the design of a humanoid robots named “Buddy”. The overall form factor is an important parameter in the design of humanoids. A small humanoid robot that matches children 2 years old could be used for several application areas. These include teaching, training and therapeutic treatment for children with autism spectral disorder (ASD). The majority of children in this age range enjoy interacting with humanoids. It is extremely important to review the existing humanoid robots in various categories and to describe their DOF, characteristics and cost to give a wider perspective to readers or researchers in the area. The existing humanoids can be categorized into three: humanoids with wheeled locomotion, humanoids with legged locomotion and human-like robots [19].

2.1.1 Humanoids with Legged Motion

Humanoids with legged motion are simply humanoid robots that have legs and can walk. Extensive research to improve the performance of bipedal robots has been conducted, from which many advanced and highly successful humanoids have emerged. In 1997, the design of a

¹Some parts are reprinted by permission from **Robotics, HBS-1: A Modular Child-Size 3D Printed Humanoid**, Lianjun Wu, Miles Larkin, Akshay Potnuru and Yonas Tadesse, ©2016

²Some parts are reprinted by permission from **IEEE International Conference on Automation Science and Engineering (CASE), 3D printed dancing humanoid robot “Buddy” for homecare**, Akshay Potnuru, Mohsen Jafarzadeh Yonas Tadesse, ©2016 IEEE

35 DOF humanoid was presented for a fundamental research tool, model-based programming, vision research, for sensor integration and a testbed for adaptive behavior [82]. ASIMO (the most advanced humanoid) [173] is designed for useful roles in offices or households by interacting with humans through recognition of moving objects, postures and gestures. ASIMO is 130 cm tall, the size of an average nine-year-old boy, with 34 DOF, and costs around \$1 million to buy and more than \$100,000 to rent [48]. Robonaut 2 humanoid, designed by NASA and General Motors for use in space applications, can handle many tools, repair aircraft and communicate with astronauts in space [48]. It is 190 cm (6'3") tall, costs about \$2.5 million [48] and has 42 DOF. HRP-4C [91] is designed to work in human environments, uses tools like a human to manipulate objects and is able to speak and sing as an entertainment robot. It has 42 DOF, is the size of a 14-year-old adolescent, with 158 cm in height, and costs about \$200,000 [26]. Mahru and Ahra [104] were developed to operate as network-based machines that can walk at a speed of 0.9 km/h (0.56 mph), talk and recognize gestures. They can both understand speech and learn from their own experience. They are 150 cm tall, the average 13-year-old boy, with a 35 DOF, and cost around \$236,000 [7]. Pino [237] is developed by ZMP Inc. to accelerate the research and development of humanoids by providing technical information to the general public. It has a height of 70 cm, the average nine-month-old baby, 26 DOF, and costs around \$30,000 [12].

Sony's QRIO [51] is designed to perform voice and face recognition; it can remember people's faces, as well as express its likes and dislikes. The costs of QRIO have been compared to the price of a luxury car [164]. It has 38 DOF and is 58 cm tall, about the size of a four-month-old baby. Toyota's Partner Robots [101] are being developed with human characteristics, which include being agile, friendly and intelligent enough to operate devices for personal assistance and care for the elderly. They are 83 cm tall, resembling a 1-6 year-old child. Kotaro [129] has a human-like skeletal structure and a flexible spine that acts very similar to human muscles. Kotaro is 133 cm tall, approximately the size of a nine-year-old child, with

91 DOF. Poppy is a humanoid, which is mostly 3D printed, like the humanoid presented in this work. It is 84 cm tall, weighs 3 kg, has 25 motors and an LCD screen, and it costs around \$11,000 [43, 107].

2.1.2 Humanlike Robots

Humanlike robots are designed to mimic the appearance and behavior of humans realistically [19], such as facial movements (facial expressions). The robots may be legged, as in Albert HUBO [141] and HRP-4C [91], or stationary, as in SAYA [19] and Repliee Q2 [85]. Several examples are given in this section. EveR-4 [10] is an adult-sized entertainment robot that has a modular design for facial expressions and an artificial tongue. It is 180 cm tall and has 64 DOF. EveR-1, the first EveR model, costs \$321,000 [47]. Zeno (RoboKind) [163] is designed by Hanson Robotics Inc. to behave and resemble a little boy. Zeno is 27-inches (67 cm) tall and has 37 DOF at a price of \$ 16,750 [44]. Geminoid's HI-1 [85] is a life-sized human-like robot that looks like its maker Hiroshi Ishiguro from Osaka University. While HI-1 lacks the ability to walk, it has a lifelike appearance and uses its 50 DOF to perform human-like movements, including facial expressions. Repliee Q2 or Actroid [186] is a female humanlike robot that can do lifelike expressions, such as blinking, speaking and breathing. It has 42 DOF, 13 of which are in the head, and the rental cost is \$3500 for five days [42]. A child size robot, iCUB (90 cm and < 23 kg mass), was developed for cognitive study and is an open platform based on a 2.5-year-old child [216]. KASPAR is a minimally-expressive robot suitable for human-robot interaction studies, such as the treatment of autistic children. It is a low cost (around \$2118 [217]) and effective product, as discussed in Dautenhahn *et al.* [41]. Roboy is another unique bio- inspired humanoid robot. It is designed based on musculoskeletal structures, which use tendon-driven actuation that provides soft and flexible motions. Its cost is around \$270,000 [103, 151]. There are many other humanoids presented in the literature and web resources, such as DARwln [136], CHARLI [109], Hanson Robokind

[62], NAO [32], Nimbro-OP [181] and Kenshiro [99].

There are differences between “humanoids with legged motion” and “human-like robots”. For the former, the focus is on the mobility of the robot, whereas, in the latter, the focus is on the skin technology that makes the robot similar in appearance and behavior to humans. Some researchers combined legged motion with a human-like appearance for the robot. One example is the Albert HUBO [141]. Albert HUBO robot is a legged robot and has 31 facial expressions. In figure 2.1, we see the summary of the cost of humanoids that are divided in their price range in USD. Sophia [4], a highly facially expressive robot by Hanson Robotics, is the latest addition to the world of humanoids. It is built with artificial general intelligence (AGI) which can have an intelligent conversation with a human. Sophia is highly popular and widely known in service robots.

2.2 Initial Design of Humanoid HBS-1

The basic structure of the humanoid is an important design parameter. Based on literature review and for closing the gap in USD we designed and developed a 3D printed robot called “HBS”. As shown in figure 2.2, the HBS-1 is designed to be a small humanoid robot that matches the general physique of 5 to 10-year-old child [118] with 51 DOF (degrees of freedom). This size domain is usable for several application areas like teaching, training and therapeutic treatment for children with autism spectral disorder (ASD). Most children in this age range enjoy interacting with humanoids. In figure 2.3, we see the initial design of HBS-1 created using SolidWorks. The size and dimensions of every part were considered close to human anatomy ratios [122]. Several dimensions were considered while designing every part in detail to mimic the human body. The goal of the HBS-1 is to mimic the human anatomy as closely as possible and to enhance the abilities of humanoid to perform superhuman tasks effectively and efficiently. The initial design of HBS-1 has no face detailing, which was added later and used a combination of several pin and ball socket joints mimicking the

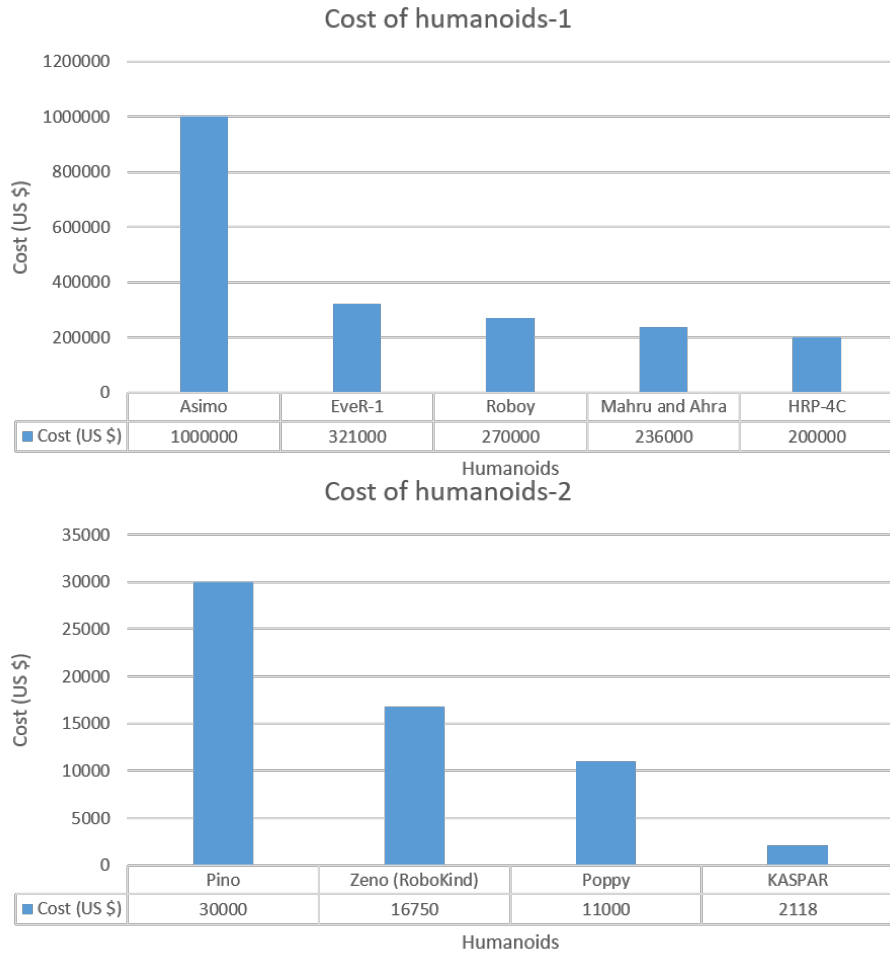


Figure 2.1. The cost of humanoid robots divided according to their price range in US dollars.

human anatomy. Several more researchers worked on the initial design to perfect the model and manufacture the HBS-1 as, seen in current form in figure 2.2. We have also explored the robot to robot interaction virtually in CAD models, how the robots operate in work environment utilizing CAD tools. Figure 2.3 shows some of the initial HBS design in rendered images.

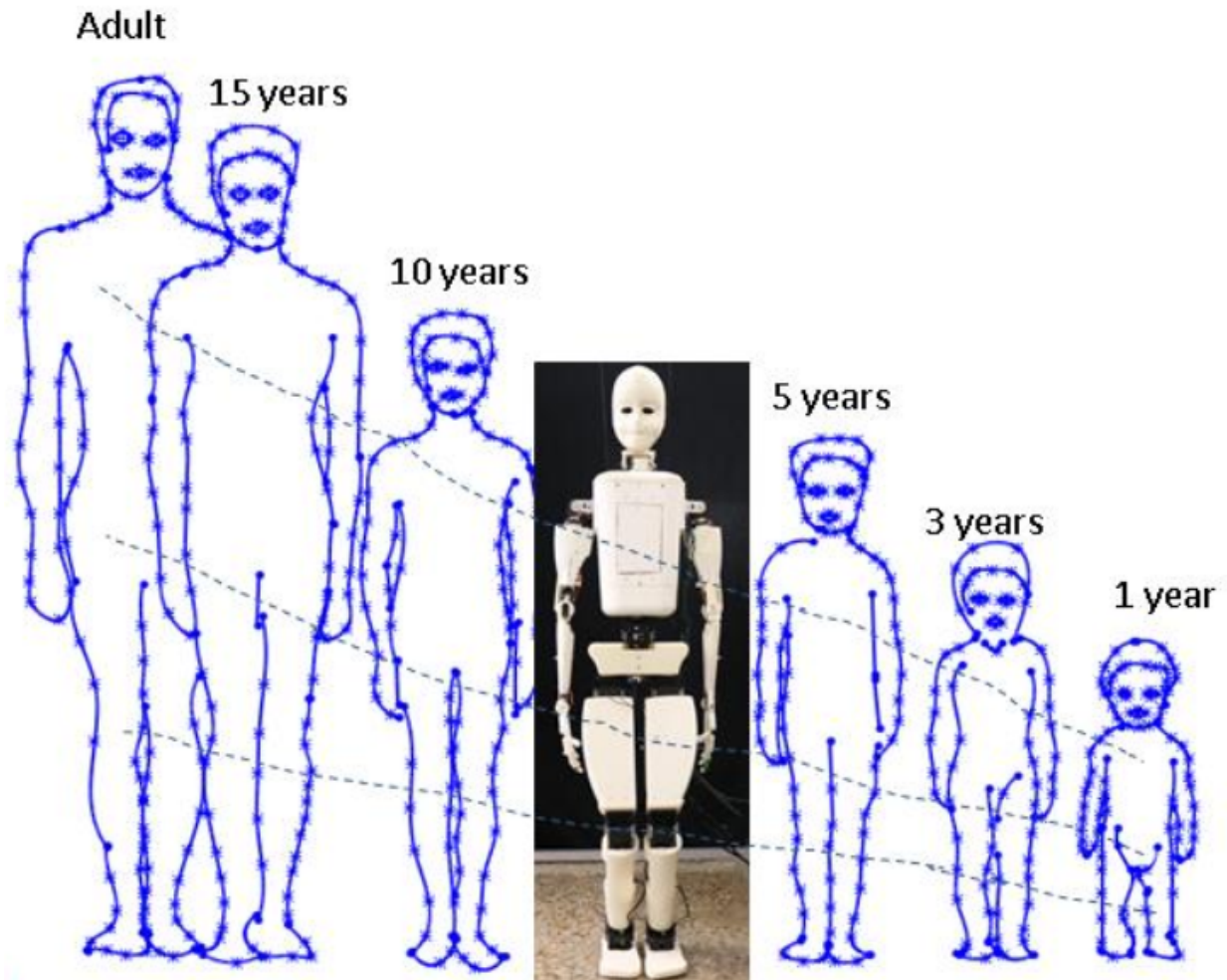


Figure 2.2. HBS-1 compared to humans [232]

2.3 Humanoid Buddy

This section describes a 3D printed humanoid robot “Buddy” as seen in figure 2.4 that can perform dancing and demonstrate human-like facial expressions to expand humanoid robotics in entertainment and at the same time to have an assistive role for children and elderly people. The humanoid is small and has an expressive face that is in a comfort zone for a child or an older person. It can maneuver in a day care or home care environment using its wheeled base. This section discusses on the capabilities of the robot to carry and handle small loads like pills, common measurement tools such as pressure and temperature

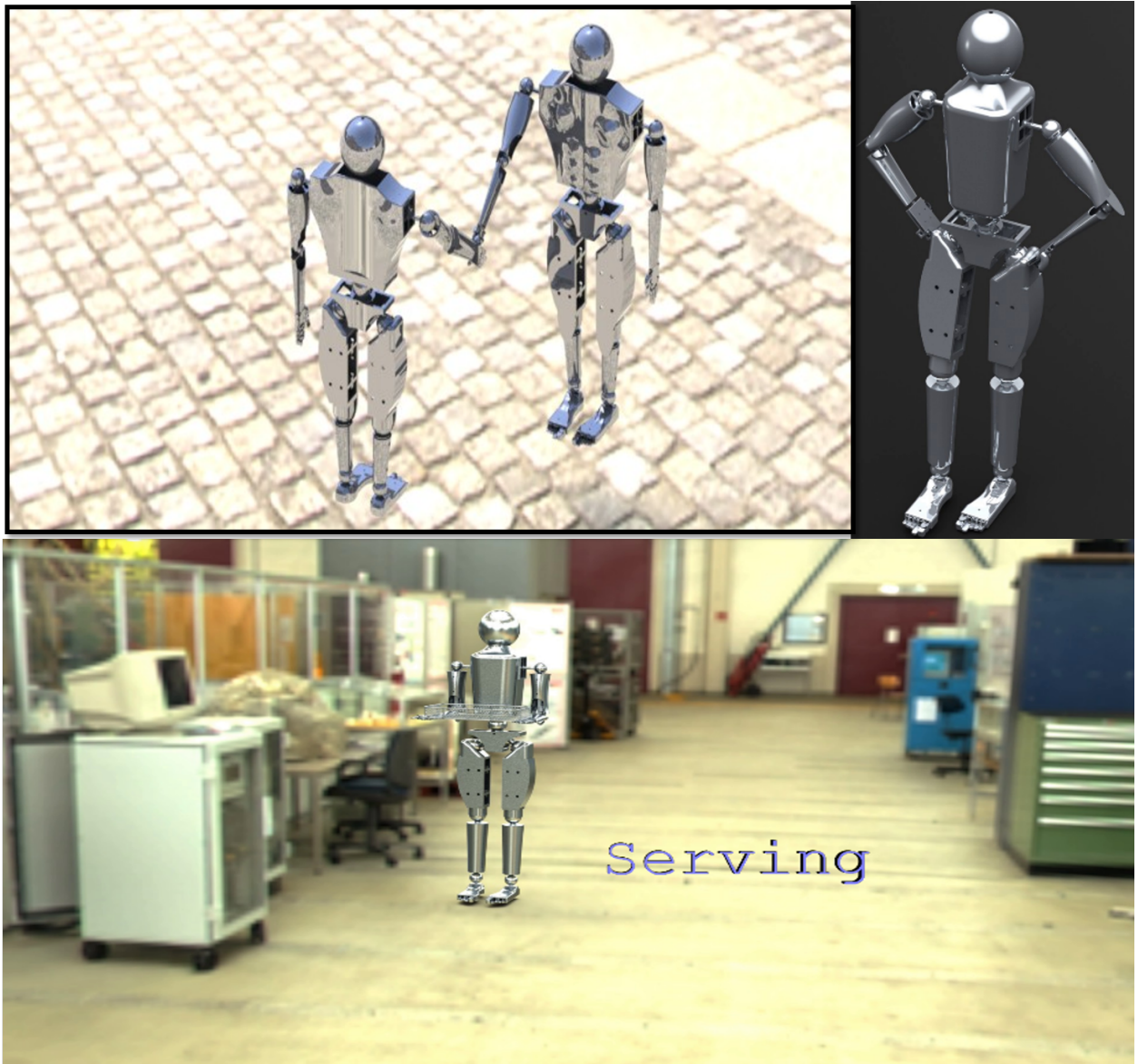


Figure 2.3. HBS-1 initial design, robot to robot interaction, rendered image showing work environment of HBS-1.

measurement units. The section discusses the use of IP camera for color identification and an Arduino based audio system to synchronize music with dance movements of the robot.

2.3.1 Introduction of Social Robots and Human Interaction

Research on humanoids or human-like robots for use in assistive device or rehabilitation for children and elderly has increased recently. The effectiveness of humanoids for the therapy of some disabilities is promising than human interaction in rehabilitation, particularly in autism research for children [166]. The other application of humanoids is to assist elderly people to live comfortably and independently adapting like pets in homes. The robots will be able to do simple assistive household works such as bringing small utensils to users, or performing some chores, or monitor their health and as a socially interactive companion. Hence, it is important to research and study more the acceptance and use of social robots for elderly and children. A social robot interacts with human via human social cues such as facial expressions [117, 40, 202]. Several human-like and animal-like robots have been shown to be effective in the rehabilitation field of children and elderly. One of the few is Keepon [127], which dances to musical tunes and has shown effective therapeutic tools for children with autism and elderly. Keepon uses actuators for synchronized movement to rhythmic sound beats attracting the attention of a subject in the therapy. Tanaka *et al.* [209, 208] created dance sequences for QRIO humanoid robot in the presence of children, in a playroom and observed a considerable change in attention of the children.

Children and the elderly showed interest towards the dog-like robot of Sony, the AIBO [21, 90] when it socially interacts or dances. Shamsuddin *et al.* [183], observed that the implementation of NAO robot has significantly changed the autistic behavior of children during a direct child and robot interaction, and in a classroom environment. Dautenhahn *et al.* built a humanoid robot Kaspar [41, 26], a minimally expressive robot and proved the effectiveness of the humanoid to enhance the attention of autistic children. Several more

[29, 179] have shown similar work and have proven the effectiveness of social robots in the rehabilitation of children and elderly, building the case for the necessity of studying these robots. Some other robots which are used in day care or home care are car-o-bot [67], Robo MD [220], TeCaRob [73] and sectiono [144]. The aim of this section is to expand our prior efforts in the area, [30] towards a complete independent mobile humanoid robotic system for home care. This section shows more capabilities of the robot such as dancing, color detection and lifting loads that might encounter in daily activities. This section is divided into eight sections starting with hardware used in the humanoid system, their description and advantages for the advancement of assistive device or system. Next, the ability of the robot to mimic human-like movements similar to a ballet dance is described. Later, the section describes the methodology used to play audio and how to track color using the camera. Finally, we discuss the stress analysis and experimental data of load carrying capacity of the robot arm.

2.3.2 Humanoid “Buddy” Hardware

The humanoid robot has an on-board wireless camera and microphone, with a mobile base, ultrasonic distance sensor, touch sensors and on-board battery. It has 15 DOF, 580 mm tall and 925 mm arm span. The detailed hardware and characteristics of the robot will be briefly discussed in this section that allows us to demonstrate various dancing movements. Figure 2.4 shows the size of the robot in comparison with an 8-year old child sitting next to the robot. The most important aspect of this robot is that all the structural parts are 3D printed enabling one to recreate again for use in home care.

(a) Servo Actuators

Figures 2.5 and 2.6 show all the different types of servo actuators used at different locations of the humanoid Buddy, which are selected based on size limitations and load capacities.



Figure 2.4. Humanoid Buddy (a) with an 8-year old normal child and (b) the humanoid parts and raising hands gesture. (Parental consent form was obtained for the photograph of underage child next to the robot).

The servo motors actuate the arms, the head and the eyebrow, and the lips. DC motors with encoders are used for maneuvering the base for locomotion. Most of the selected servo actuators have metal gear, which have a longer lifetime than the plastic geared servo actuators. Some servo motors have plastic gear but are sufficient to manipulate small loads.

(b) DCS 942L Camera

Buddy is equipped with DCS 942L camera (inset of figure2.5). The camera has an aperture of F2.8 with fixed focal length of 3.15 mm, 1/5 VGA progressive CMOS sensor and exposure time of 1/3.75 to 1/14640 sec. It has 4X digital zoom, built-in microphone, PIR motion sensor, 5 meter Infrared (IR) illumination distance, minimum illumination of 0 lux with IR LEDs on, built in infrared cut removable (ICR) filter module and angle of views of (H) 45.3,

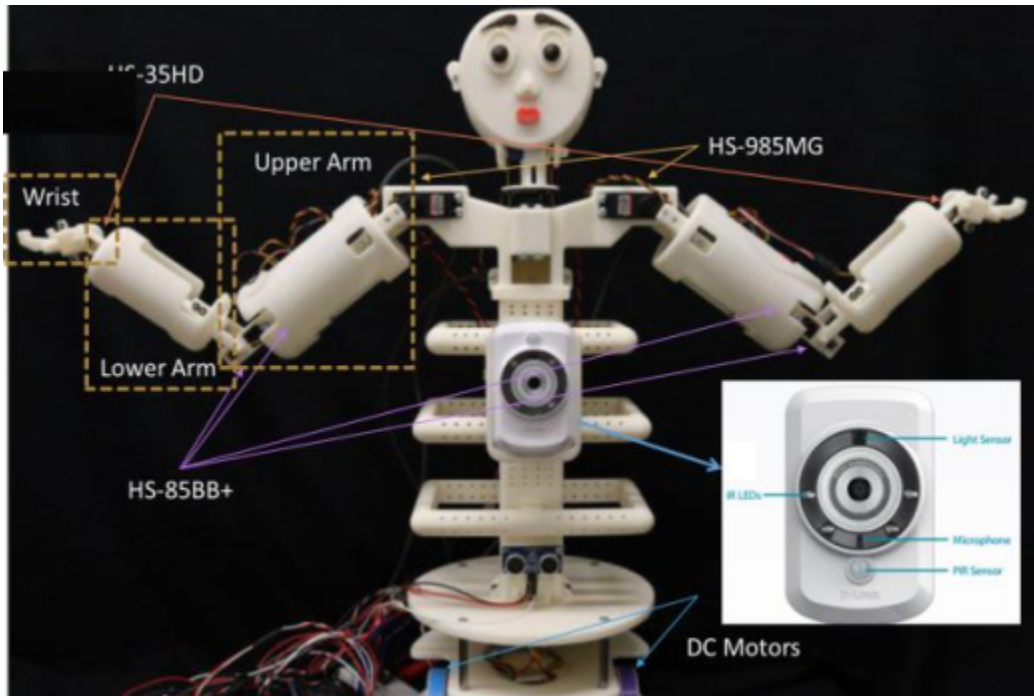


Figure 2.5. Humanoid buddy hardware full view and base.

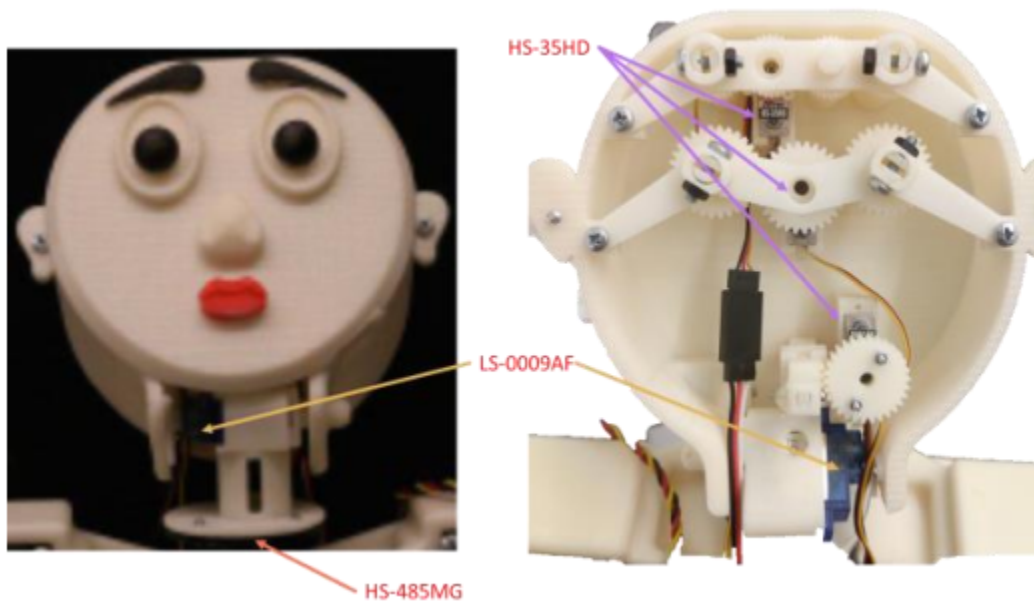


Figure 2.6. Hardware Neck and Head

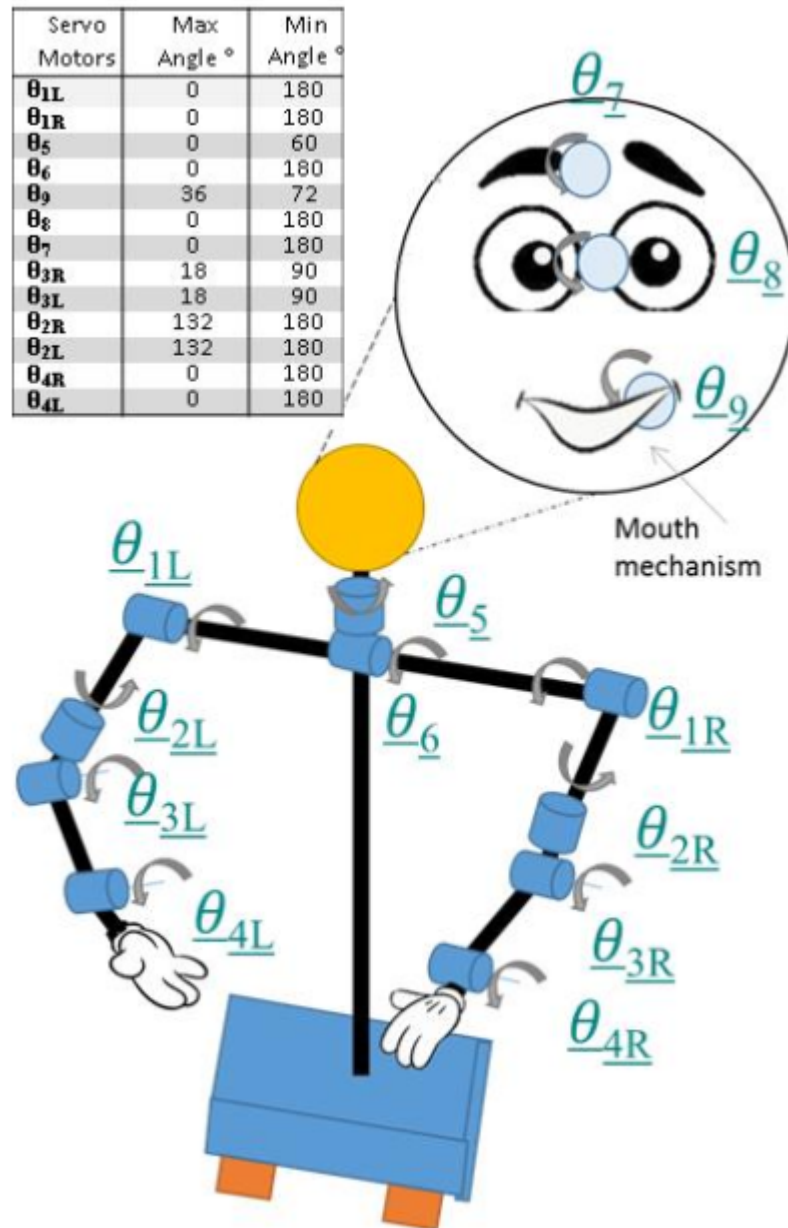


Figure 2.7. Schematic diagram of the robot and the head mechanisms along with the minimum and maximum servo position of the joints.

(V) 34.5 and (D) 54.9. These features just show how the DSC 942L is properly suited for continuous monitoring of both audio and visuals information remotely through WIFI [212] and can be observed and interact using the built interface and two-way audio interactions.

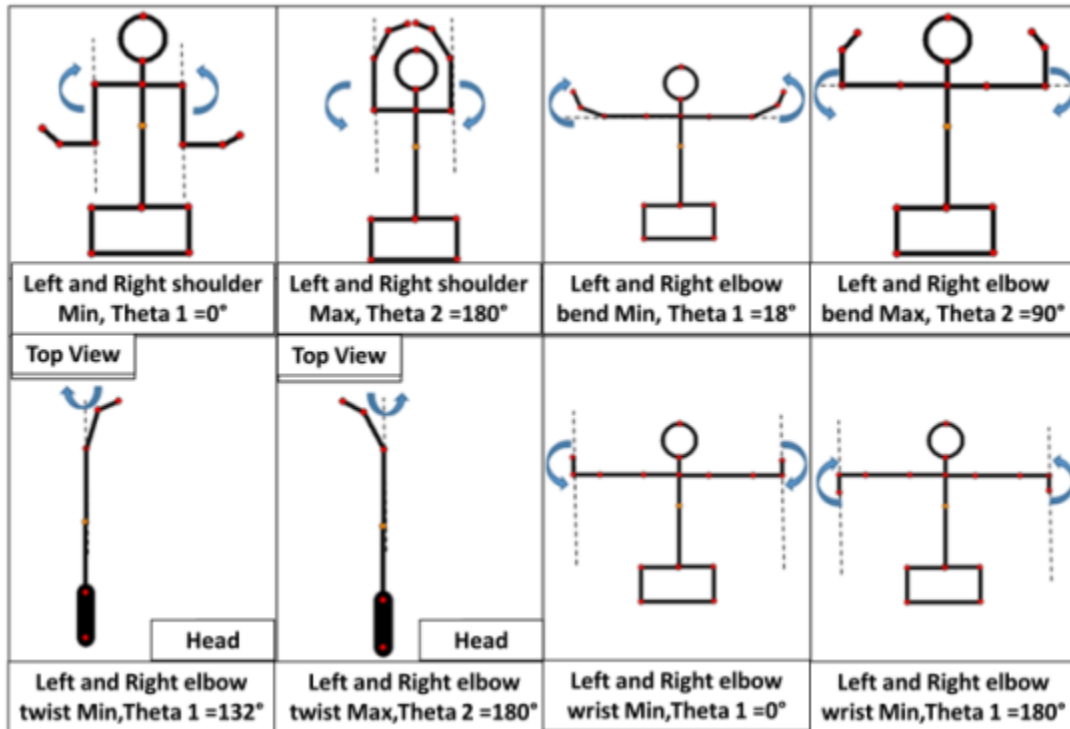


Figure 2.8. Simplified diagram of Buddy gestures (max and min).The corresponding angles are shown in figure 2.7.

Figure 2.7 shows a schematic layout of the humanoid Buddy, which is a small baby-sized robot mimicking a 2 year toddler in height. The schematic layout in figure 2.7 shows where the servo actuators are located and the relative angular movements.

(c) Maximum and Minimum Values of Servo Motors (Without Obstruction)

The simplistic representation in figure 2.8, show the different possible angles of the humanoid, which we considered while coordinating the dance moves for the robot. This is just one of the feasible dances and other can be made in similar way.

2.3.3 Ballet Dance Sequence of the Servo Motors

In figure 2.9, we see a different servo actuation of Buddy during the ballet dance move with corresponding actuated servos in time domain. The corresponding snapshots of the robot are

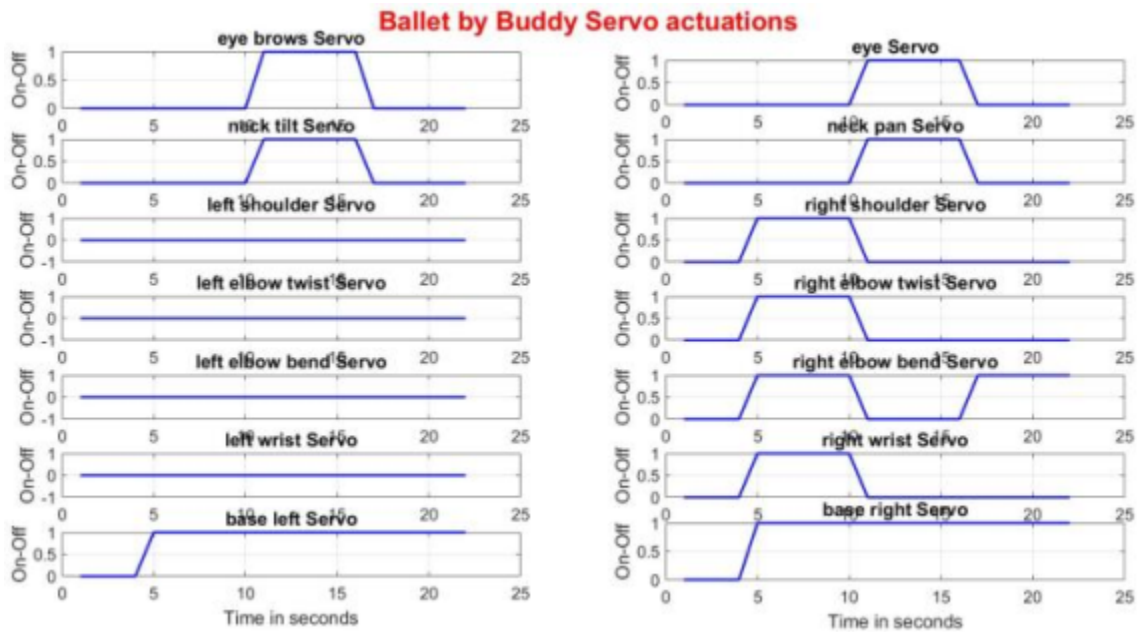


Figure 2.9. Servo motor actuation sequence during ballet dance. Different graphs show the on and off time of each servo represented in figure 2.7.

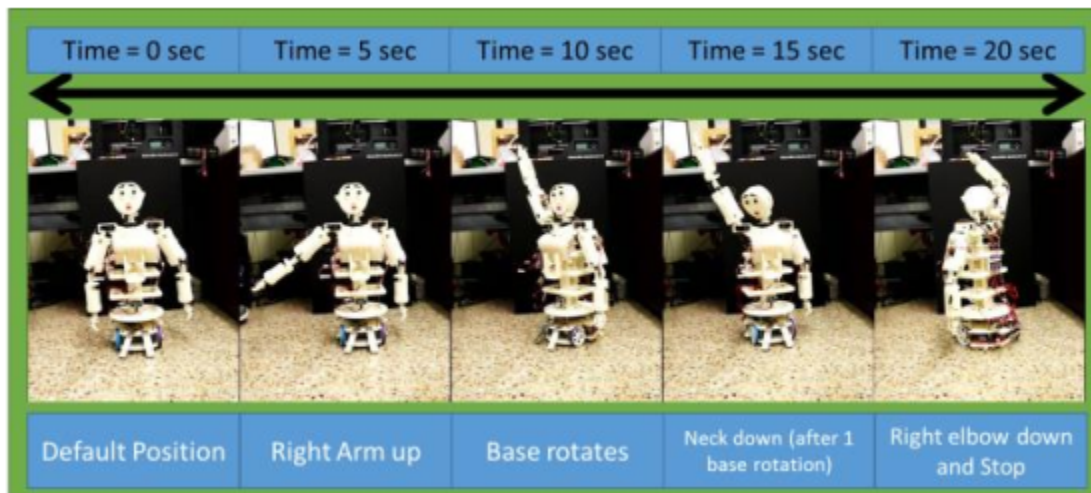


Figure 2.10. Photograph of the ballet dance of the robot in 1 cycle that was obtained from video recording.



Figure 2.11. Demonstrated Humanoid robot “Buddy” before 1200 people before the screening of the movie “Terminator Genisys” to encourage young students to pursue STEM majors at AMC NorthPark 15, 8687 North Central Expressway, Dallas, TX 75225. Published in Dallas Morning News.

shown in figure 2.10 when the ballet dance sequence is implemented. It was observed that the ballet dance move is very well accepted by all types of audience from young to old people for entertainment. The humanoid performed the ballet dance for over 1200 audiences in an invited event at the AMC NorthPark, Dallas, TX during the movie screening of Terminator 3 (Terminator Genisys) as seen in figure 2.11, and received wide acceptance of audience and made them more interested in the coupled engineering and entertainment aspect of the robot.

2.3.4 Audio Interfacing of Arduino for Dance

In order to synchronize the music with dance movement, we designed a subsystem in the robot to play music. Nowadays, Secure Digital (SD) card is one of the popular portable

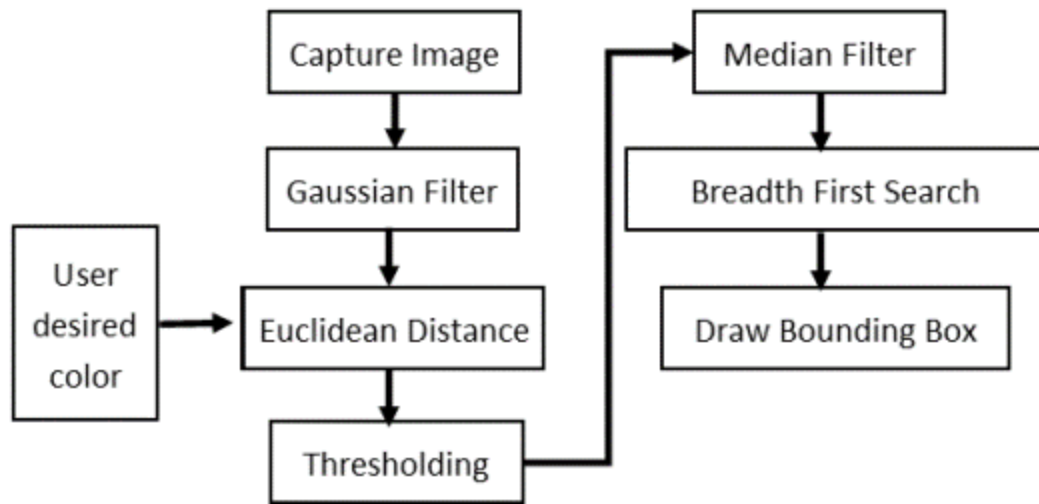


Figure 2.12. Flowchart of color recognition

memory. We used SD card to save music files. Advantages of SD card are availability and cost effectiveness. We used a MicroSD shield board to connect the SD card to our controller, Arduino Uno. The Serial Peripheral Interface (SI) is used as communication protocol to read data from the SD card. FAT32 was used for file system because it is recognized by many devices and operation systems. Thus, users can easily0 copy their music into the memory. Currently, the robot uses an open source library, which can play the .wav format with 44100 Hz and 16-bit stereo quality. Although, the input file is stereo channel, the library plays music in mono channel as well. The library reads music file in the root directory of the SD card. This library takes control of PWM pin. Therefore, a speaker was connected to this pin through an amplifier.

2.3.5 Color Recognition using the Camera

One of the subsystems of the Buddy robot is recognition of objects with a solid color. This subsystem captures images of a scene and identifies different colored objects assigned by a user. As mentioned in sub-subsection 2.3.2, the camera sends image through a WI-Fi to a computer to provide monitoring of the environment. We used this image as an input of our

subsystem to find the objects. In this way, we used Computer Vision Toolbox of MATLAB software and the algorithm shown in figure 2.12.

Colors in digital image are determined with vectors, which belong to a color space. There are many color spaces such as RGB, HSV, HSL, YCbCr, and so on. Buddy's camera captures RGB images. In this section, we used Euclidean distance to determine how much pixel's color is similar to user-defined color. In the following paragraph, we describe the details.

The camera images always have noise. This noise makes change to the color of the pixels. If we use a noisy image and directly find the Euclidean distance, the result will have several false objects. In order to decrease noise, we used a digital low pass filter. It is assumed that Buddy needs to find objects in the environment with Gaussian noise. Although it is not always true, our experiment shows acceptable results. After filtering an image, the Euclidean distance of color of each pixel with desired color is calculated and saved in a matrix, which is same size with one channel of input image. Then, if the Euclidean distance of each array is greater than a threshold, we write zero on that array, and if it is less than or equal to this threshold, we write one. Comparing a matrix with a threshold and writing zero or one is called thresholding. Sometimes, thresholding produces a lot of noise. To remove these noise, we used a median filter. The result of the above steps is a matrix with one where the color is similar to desired color and zero otherwise.

After determining which pixels belong to desired color, we combined the neighbor pixels to find objects. We used breadth first search (BFS) algorithm for traversing the matrix and numbering each objects. Then, we draw a bounding box around each object to show to user. Figure 2.13 (a) and (b) show how the algorithm shown before is used to find green and blue objects. Figure 2.13(c) shows the implementation of color recognition using our robot.

2.3.6 Stress Analysis of the Arm

One of the most important aspects of 3D printed robot is the load carrying capacity of the robot for carrying tools for measuring like temperature, pressure, etc. To evaluate the

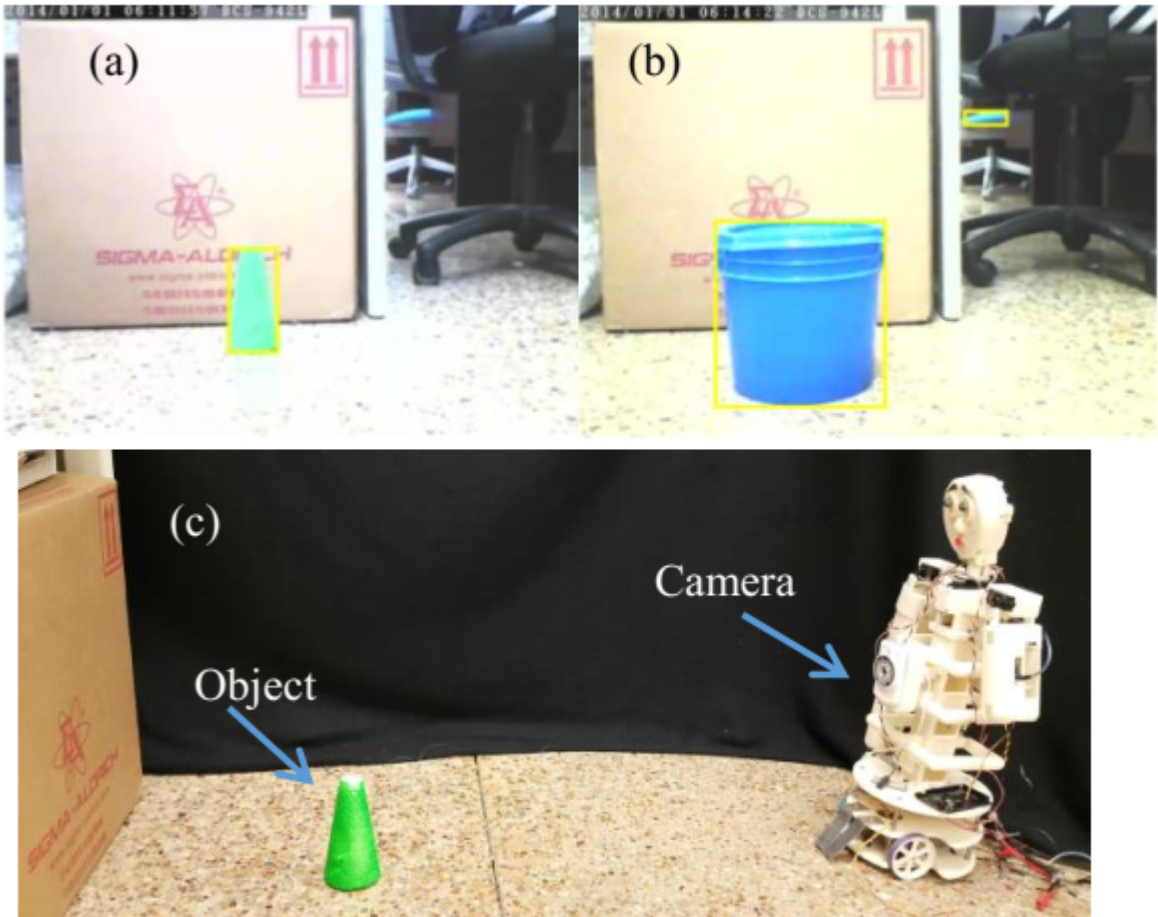


Figure 2.13. Finding colored objects, (a) green object, (b) blue objects and (c) experimental setup for color recognition.

load bearing capabilities, finite element analyses were performed. The wrist servo motor is HS-35HD ultra nano servo motor, which has a stall torque of 0.8 kg/cm at 4.8V and the elbow servo motor is HS-85BB premium micro servo motor which has the torque of 3 kg/cm. The stress analysis for static load was conducted at 300 g load, which was the maximum observable weight the arm can carry. The weights of the parts were obtained from SolidWorks material library using ABS material and cross-checked by measuring the printed parts and found to be very similar with negligible difference. SolidWorks 2014 was used to simulate the stress distributed in each part when the maximum possible weight or load is lifted. The meshing for all parts was done using the default mesher of SolidWorks. Figure

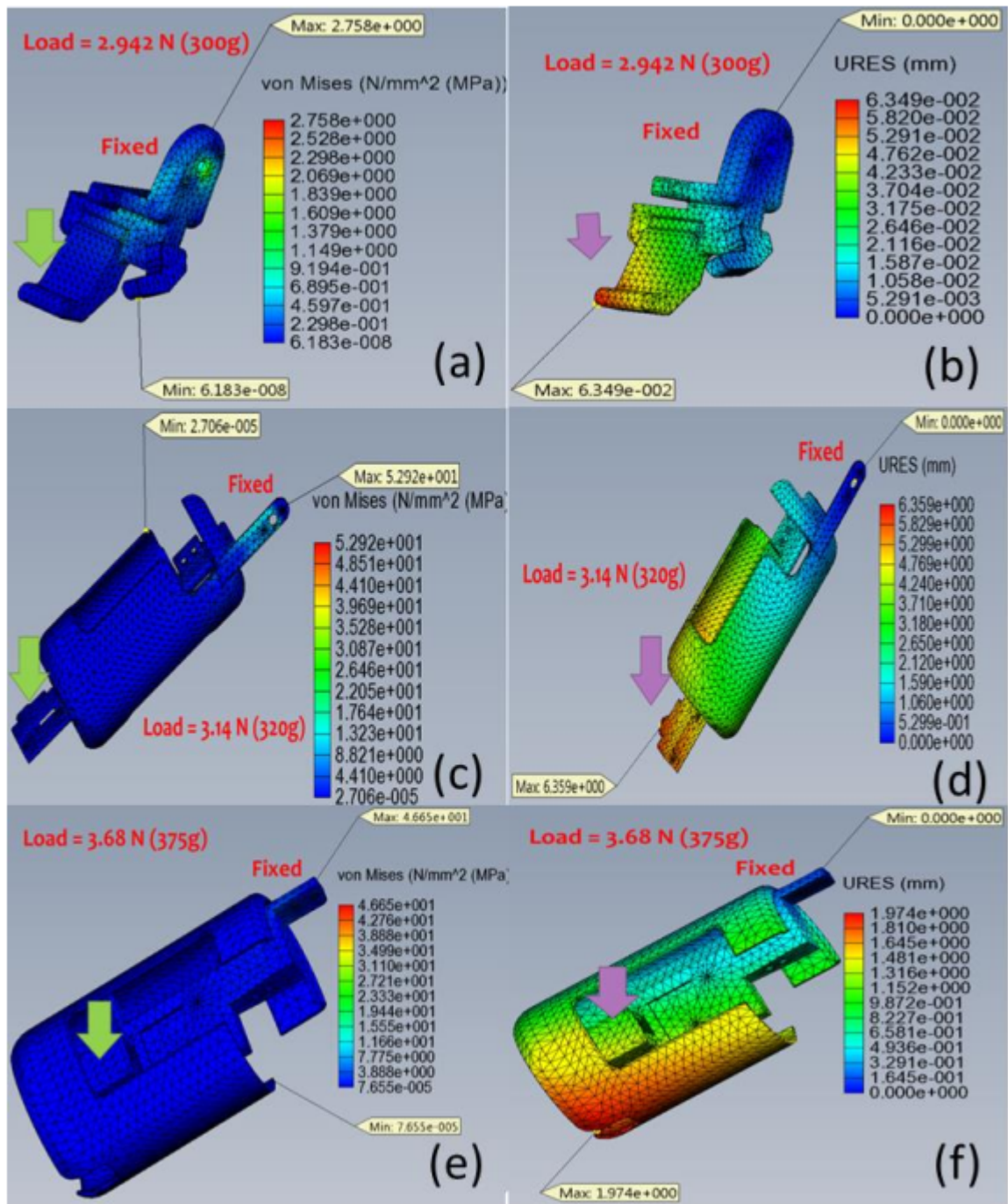


Figure 2.14. Stress analysis of the robot arm part, (a) wrist von-Mises stress, (b) wrist - displacement, (c) lower arm von-Mises Stress, (d) lower Arm - displacement, (e) upper arm von-Mises Stress, and (f) upper arm - displacement.

2.14 (a) and (b) show the von-Mises stress (max 2.758 MPa) and displacement (max 0.0635 mm) of the wrist for 2.942 N load. Figure 2.14 (c) and (d) show the von-Mises stress (max 52.92 MPa) and displacement (max 6.359 mm) of the lower arm at 3.14N applied load and figure 2.14 (e) and (f) show the von-Mises stress (max 46.65 MPa) and displacement (max 1.974 mm) of the upper arm at 3.68N.

Figure 2.14 shows the stress analysis results based on respective loads applied on consecutive parts including the weights of the former parts, the fixed location and the load locations are shown in the figure. The load locations are the starting point of the parts (arrows in the figure). The stress analysis has shown that there is some high stress in the lower arm and upper arm due to complicated geometry (thin and slender structures in the arm) and other stress concentration points, which needs modification to carry higher load. The strength of common ABS material is 31 MPa [232] and therefore the applied load 300 g is higher. To carry higher load, the thin structures and the geometry should be modified. However, the robot will not be subjected to higher loads, which will be discussed in the next section.

2.3.7 Experimental Analysis of Load Carrying Capacity

Experiments were performed on the humanoid by mounting a known weight and recording the movement of the mass using a video camera. The angular position of the shoulder joint was measured by varying the mass. Calibrated weights were hung on the palm of the arm using thread with negligible weight and then the servo arm was actuated while keeping the servo arm at 0 position, to perform an arm lift from default angle of 33° to angle 115° as shown in no load condition in figure 2.15a. Other loads are shown in the pictures in figure 2.15. The angular positions (lifting capacities) of the robot for various loads were recorded and the results are presented in figure 2.16. In figure 2.16, we can see that the angle reduces to zero gradually as we increase the weights. As the weights were added, the angle to which the arm can lift reduced, and at 500 g, it could not lift the weight anymore. Considering

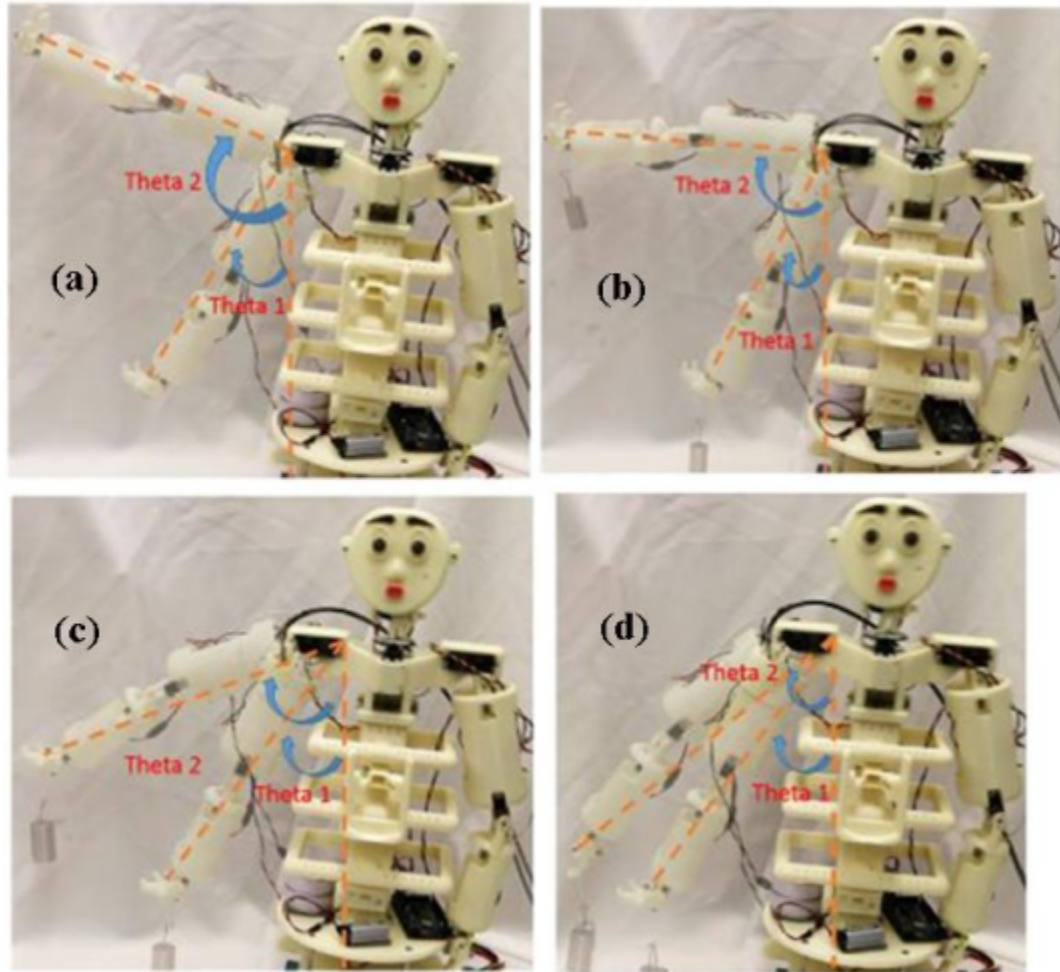


Figure 2.15. Photograph of load carrying capacity of the robot during experiment, (a) 0 g, (b) 100 g, (c) 200 g and 300 g load.

the dynamic motion and the load, we can see that the arm could not lift beyond 300 g significantly. From the experiential results, 200 g is a good weight after considering the angle the arm can lift and the static load discussed in the finite element analysis.

2.3.8 Conclusion and Future Work

This section presents a 3D printed small and affordable human-like robot that can serve as an assistive device or co-robot and at the same time entertain users. We briefly described the hardware, feasible movements, ballet dance synchronization, implementation of audio

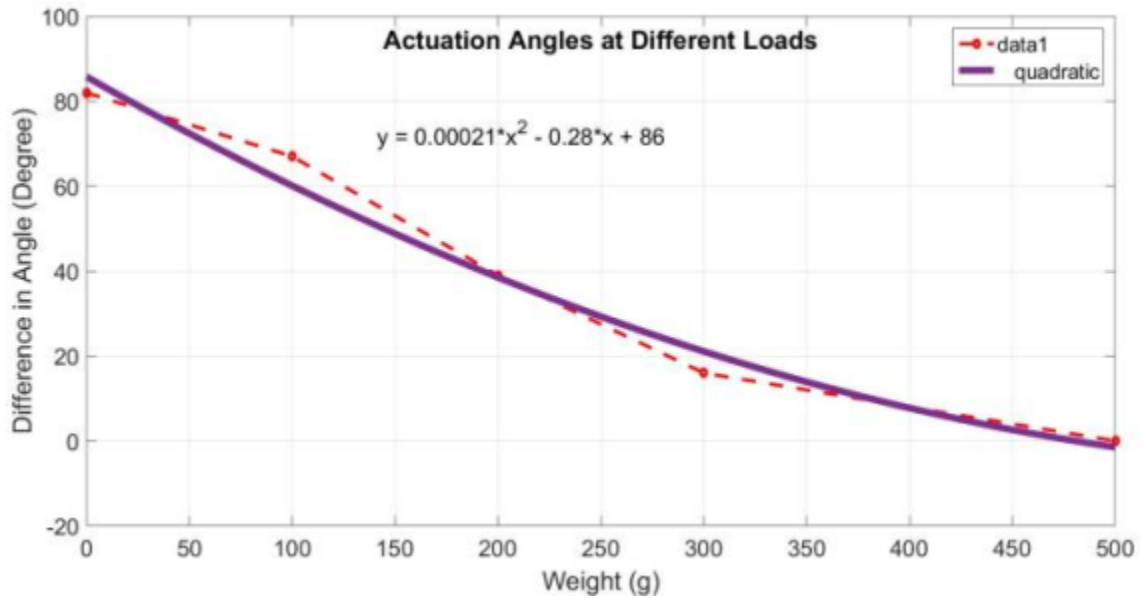


Figure 2.16. Experimental results of actuation angles of the shoulder joint of the robot at different loads at the tip

through open source Arduino board, color recognition of using the camera and finally the load carrying capacity of the arm. The 3D printing enables the flexibility and customizability according to the need of the subject. The audio synchronization with the dance makes it more lovely, whereas the color detection can help in checking the health condition of the subject by doing more work in color recognition. The important factor for the 3D printed robot, which is the load carry capacities of the arm were, determined both experimentally and theoretically. It was shown that the robot can easily handle commonly used objects and help users in fetching and providing tools like thermometer, heart monitors, etc.

The future works include further characterization and implementation in laboratory settings and home care environment with human interaction. In table 2.1 we see the general profile of humanoid “Buddy”.

Table 2.1. General profile of Humanoid “Buddy”

Size	DOF	Load Carrying Capacity	Battery	Camera
2-3 year old	21	200 g	up-to 4 hrs usage (5000 mAh Li-Po Battery)	DCS 942L (2 way audio)

CHAPTER 3

INVESTIGATION OF POLYLACTIDE AND CARBON NANOCOMPOSITE FILAMENT FOR 3D PRINTING ¹

Fused deposition modeling (FDM) has been used to manufacture complicated structures and robots in the past few years. However, most FDM machines do not fabricate fully functional robots that are ready for use. One of the requirements of fully functional 3D printed robots is electrical connection in some part of the printed structure. Recently, electrically conductive commercial filaments are emerging to the market but the actual chemical compositions of the filler and host materials as well as mechanical properties are not available. This chapter presents composite materials consisting of conductive carbon nanoparticles, thermoplastics, and solvents to create a filament material for 3D printing. The mechanical and electrical properties of filaments fabricated were investigated using a concentration of 0-15% weight of carbon nanoparticles (NC) in polylactide (PLA) using dichloromethane (DCM) solvent and subsequently, the DCM is evaporated by drying. The electrical conductivity of the composite filament is compared with commercial and academia counterparts. Possible applications of the composite materials for fabrication of electrical circuitry for 3D printed robots are discussed.

3.1 Introduction

3D printing is becoming a widely used technology, to develop numerous devices or systems [18]. 3D printing was used to fabricate many devices and robots such as child-size robot

¹Reprinted by permission from **Progress in Additive Manufacturing: Springer Nature, Investigation of polylactide and carbon nanocomposite filament for 3D printing** , Akshay Potnuru, Yonas Tadesse, ©2018

[232], dancing robot [155], prosthetics[16, 172], orthosis[171] and skeletal systems [206] using thermoplastic materials mainly. These robots are fabricated by using 3D printing and electrical connections are provided by wire systems that result in shabby and complex appearance. Wiring problem has been prevalent in humanoids and a conductive material that can be printed together with the structural thermoplastic material improves the way one manufactures such systems. Hence, there is a need to improve the 3D printing techniques to produce complete models with electronic circuitry for applications such as humanoids. Researchers so far haven't found a solution to replace wire with a cheap and effective way. In this work, we present a low-cost alternative for the problem of robot wiring. Different types of metal 3D printing techniques, which are inherently conductive, exist such as liquid metal printing [105] and direct metal laser sintering [95] for manufacturing strong devices and components. Rosochowski and Matuszak [170] explained many types of rapid prototyping methods among which fused deposition modeling is the most widely used and commercially successful method employed for fabrication of different materials. Inkjet printing technique is another technique used for printing conductive metal patterns for electronic circuitry such as using the direct writing of copper. Conductive patterns [148], narrow conductive tracks on untreated polymeric substrates [221] and a complete review of this method are shown in the past [92, 7]. The major problem in the most commercialized 3D printing techniques for metals (metal 3D printing in particular) is the cost and the high working temperatures which reduce its portability and affordability.

3D printing is an additive manufacturing method where a 3D printer adds mass to form a model. The different materials that can be 3D printed today are thermoplastics, thermopolymers, metals, and composite materials. Thermosetting polymers are those that set irreversibly to solid or semi-solid state in the presence of heat or chemicals such as curing agents generally at ambient temperature [84]. 3D printing is now used for prototyping in many engineering firms, artist design studios [223], medical tools [165] and for orthopedic implant [100]

because of its easy and fast production [18]. Its customizability using direct CAD modeling makes it a major advantage for today's manufacturing process as even a small change in the product leads to major changes in the production cycle and high financial investments. 3D manufacturing gives the designers flexibility for custom build structures including complex shapes and multiple material usages which is a major market demand of today and future. Even though significant efforts are made in the 3D printing since its introduction [78], there are several challenges and researches that need to be done to make multi-functional materials.

FDM process uses thermoplastic materials such as acrylonitrile butadiene styrene (ABS), polylactide (PLA), polycaprolactone (PCL) and nylon [140]. The process starts by heating up the thermoplastic to a semi-liquid state (1° C higher than the solidification temperature). Then, the 3D printer software uses complex digital modeling data from the CAD file to generate the 3D product layer by layer. Most FDM 3D printers just print the CAD models. Some advanced 3D printers print soluble supporting material in the cavities and supports for complex hanging features of the model to help the model retain its complex shape. The thermoplastic material has a filamentous shape which helps the heat transfer to maintain the semi-liquid state. Filamentous shape assists in the movement of the print head in the x, y and z directions. After printing each layer, a stepper motor connected to screw thread moves the platform down or the head up in z-axis where the distance moved is the thickness of the printed layer. This process repeats until the entire model is printed. The major benefits of FDM technology are its ease of control, use, maintenance, low cost of the machine and material.

ABS-Cu and ABS-Fe composite filaments were produced by Hwang *et al.* [80], which were printed by the FDM process to improve thermo-mechanical properties. They showed an improved thermal conductivity and a decrease in mechanical properties of the filament

and the printed structure. Carbon fiber infused ABS filaments were used for 3D printing by Love *et al.* [119] and showed the increase in strength, stiffness and thermal conductivity. Mechanical properties of highly filled Iron-ABS composites filament were produced by Sa'ude *et al.* [177] using a mixture of iron powder filled in an ABS and surfactant powder material. A comparison of the effect of incorporating nanoparticles in materials being used in 3D printing applications was presented by Tsiakatouras *et al.* [218] consisting of ABS, carbon fiber and carbon nanotubes, and improved mechanical properties were reported. Zhang *et al.* [242] showed a PLA graphene composite produced by melt extrusion to print complex 3D structures with electrical conductivity. Conductive filaments using 15-20 wt% graphene with polymethyl methacrylate (PMMA) were fabricated by Nicholson [138]. The resistances were found to be $1.5 \pm 0.4 \text{ M}\Omega$ and $60 \pm 7 \text{ k}\Omega$ for the 15 and 20 wt.% filaments (filament length of 25.4 mm and 1.75 mm in diameter). Graphene and ABS filaments were prepared by Wei *et al.* [227] similar to the work presented in this work but by using N-Methyl-2-pyrrolidone rather than DCM. Graphene is 5 times more expensive than carbon nano particles which was used in this work. All high-end products these days come with electrical circuitry during manufacturing. FDM uses thermoplastics (insulators), which cannot be used to print the whole functional model with electrical circuitry. The need for making conductive thermoplastic in FDM 3D printing material is the next step to push the 3D manufacturing of complex structures.

Similar work was proposed by the company Graphene 3D Lab [3], where a commercial plastic/graphene composite filament used for 3D printing of graphene-enhanced plastic structures. The filament has a volume resistivity of $6 \times 10^{-3} \Omega \text{m}$ and a standard filament diameter of 1.75mm. Some of the properties of the filament are not available such as tensile strength. Proto- pasta Conductive PLA is a commercially available conductive filament which is a compound of NatureWorks 4043D PLA and conductive carbon black with a volume resistivity of molded resin (not 3D Printed) of $0.15 \Omega \text{m}$ and with a maximum volume resistivity of

3D printed parts through layers (along Z axis) of $1.15 \Omega \text{ m}$ [34]. Functionalize Electric PLA [2], a commercially available conductive filament has a $7.5 \times 10^{-3} \Omega \text{ m}$ volume resistivity made from carbon nanotube-based PLA filament. Electrifi filament [135] is another commercially available conductive filament with a resistivity of $6 \times 10^{-5} \Omega \text{ m}$ from Multi3d. They have not disclosed their composition of copper and polyester. Sigma-Aldrich has a commercially available carbon nanotube reinforced polyethylene terephthalate glycol copolymer 3D printing filament trademarked as 3DXNANO ESD CNT-PETG, which has a surface resistivity of 10^7 to $10^9 \Omega$ on 3DP sample using concentric ring test method [31].

Several attempts have been made to produce 3D printable or inkjet printable electrical circuitry. Espalin *et al.* studied stereo lithography used for 3D printing electronics with the FDM based system and demonstrated an automated FDM process with the possibility of using direct write for electronic circuitry. In this process, thermoplastics and copper wires were used to increase performance and durability of 3D-printed electronics [53]. Similar work presented in this work is shown by Leigh *et al.* [111]. They demonstrated a concept in 3D printing technology with the formulation of a simple, low-cost conductive composite material (termed 'carbomorph'). They used 15wt% carbon black in the polycaprolactone (PCL) composite, which falls above the literature percolation threshold of carbon black in polymer composites [45]. According to [111], higher percentages of carbon black gave a composite that was unable to pass through the standard heated nozzle of a 3D printer and required the nozzle to be drilled out to 1.5 mm diameter and prints to be carried out at 260°C and above, which significantly compromised print resolution. They presented a 5mm 3D printed cube that showed an in-plane resistance of $0.09 \pm 0.01 \Omega \text{ m}^{-1}$ and perpendicular to the layers, the resistivity was $0.12 \pm 0.01 \Omega \text{ m}^{-1}$.

This work presents the study of carbon nanoparticles in polylactide (PLA) fiber in this work rather than polycaprolactone (PCL) 3D printable material at various concentrations

of carbon nanoparticles. PLA is more widely used material for 3D printing and has a tensile strength of up to 60 MPa, whereas, PCL has a tensile strength of 14 MPa [17]. Furthermore, PLA has shown very good results for the synthesis of polypyrrole (PPy) based composite actuators/artificial muscles [156, 200, 201]. The percolation threshold of carbon black in polyethylene is shown by Foulger [55] related to the electrical conductivity of the composites. The percolation threshold is the maximum allowable amount of a filler material inside a host material before the host material starts showing more affinity towards itself and results in a significant drop in resistance depending on the host polymer material.

Morgan *et al.* presented 3D printed micro-fluidic devices that operated using an inexpensive and readily accessible printer [133]. Similar work was presented by Belter *et al.* where a technique for increasing the strength of thermoplastic printed parts, by carefully placing voids in the printed parts and filling them with high strength resins. They improved the overall part strength and stiffness by up to 45% and 25%, respectively [22]. Gao *et al.* showed high-performance GaIn₁₀-based electrical ink, as both electrical conductors and interconnects. Electrical ink is used for directly writing flexible electronics via a rather simple and cost-effective way, with electrical resistivity measured as $34.5 \times 10^{-8} \Omega m$ at 297°K by four-point probe method [60]. Yeo *et al.* [240] presented a flexible electronics fabrication using direct metal patterning based on the laser-induced local melting of metal nanoparticle ink. Their method was a promising low-temperature alternative to vacuum deposition and photo-lithography based conventional metal patterning processes. They demonstrated high-quality Ag patterning ($2.1 \times 10^{-8} \Omega m$) and high-performance flexible organic field effect transistor arrays. Carbon forms in PLA were used in several applications previously. The examples include relative humidity sensor using carbon nanotubes in PLA by Devaux *et al.* [45]; vapor sensors using PLA multi-wall carbon nanotubes (MWCNT) by Kumar *et al.* [102]; glucose biosensors using PLA/Carbon nanotubes by Oliveira *et al.* [30] and

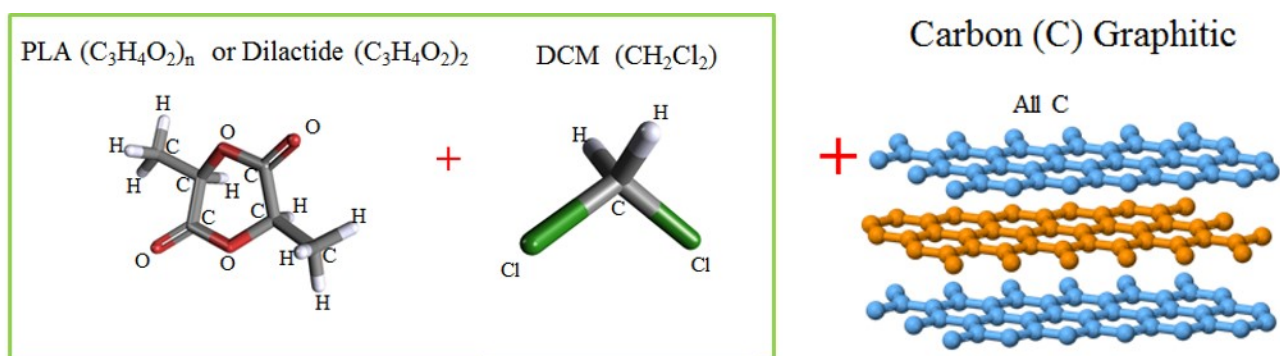


Figure 3.1. The molecular structures of the materials used for filament preparation. The major process includes dissolving biodegradable thermoplastic Polylactide (PLA) with dichloromethane (DCM) and adding mesoporous carbon nanoparticles (NC).

more applications are presented by Mukhopadhyay [134]. Hughes *et al.* [222] fabricated nanocomposite materials using solvent-cast 3D printing technique of PLA and 5, 10, and 20 wt.% MWCNT concentrations. They observed the electrical conductivity at a maximum of 1,206 S/m at 20 wt.% MWCNT. The tensile strength increased to 58 MPa for the 5 wt.% fiber while it decreased for the 20 wt.% MWCNT. The cost of MWCNT is 5 times more than carbon nanoparticles used in the presented work and, the filaments can be printed in most commercially available FDM 3D printers. Guo *et al.* [64] made a multi-functional 3D liquid sensor using PLA/MWCNT nanocomposites and shaped as a free-form helical structure by solvent cast 3D printing which featured a relatively high electrical conductivity. A comparison literature review is presented in table 3.1.

The molecular structure of the presented work substrate materials for filament preparation are shown in figure 3.1, where polylactide (C₃H₄O₂)_n is dissolved in dichloromethane CH₂Cl₂ and mixed with mesoporous carbon nanoparticles. The mesoporous carbon nanoparticles can be described by graphitic structure [112] as shown in figure 3.1. The detailed fabrication will be discussed in the experimental section.

The chapter is divided into 6 sections. Section 2 covers the experimental setup, method and materials. Experimental results like viscosity, electrical, mechanical and microstructures

Table 3.1. Literature review on additive materials in thermoplastics and the properties improved.

Reference	Substrate materials	Additive	Altered Property
Hwang <i>et al.</i> [80]	ABS	Cu, Fe	Improved thermal conductivity; decreased in mechanical properties
Love <i>et al.</i> [119]	ABS	Carbon fiber	Increase in strength, stiffness, thermal conductivity
Sa'ude <i>et al.</i> [177]	ABS	Fe powder + surfactant powder	Improved in mechanical properties
Tsiakatouras <i>et al.</i> [218]	ABS	Carbon fiber + carbon nanotubes	Carbon fiber + carbon nanotubes
Zhang <i>et al.</i> [242]	PLA	Graphene	Improved in electrical properties
Nicholson [138]	Polymethyl methacrylate (PMMA)	15-20 w.t.% graphene	Improved in electrical properties
Wei <i>et al.</i> [227]	ABS	Graphene + N-Methyl-2-pyrrolidone	Improved in electrical properties
Graphene 3D Lab [3]	PLA	Graphene	Improved in electrical properties
Leigh <i>et al.</i> [111]	Polycaprolactone (PCL)	15 w.t.% carbon black	Improved in electrical properties
Devaux <i>et al.</i> [45]	PLA	Carbon nanotubes	For relative humidity sensor
Oliveira <i>et al.</i> [142]	PLA	Carbon nanotubes	For glucose biosensors
Hughes <i>et al.</i> [222]	PLA	MWCNT	Improved in electrical properties; Improved in mechanical properties
Guo <i>et al.</i> [64]	PLA	MWCNT	Improved in electrical properties; multi-functional 3D liquid sensor

at different compositions is covered in section 3. Section 4 has the results and discussion and section 5 shows the potential application of this study in humanoids and robots to replace wires and finally in section 6 the work concludes on its high points.

3.2 Experiments

3.2.1 Materials

Clear PLA filament of 1.75 mm diameter was purchased from MakerBot Inc.; magnetic stirrer with the hot plate was purchased from VWR International; rubber tubing of 1.75 mm inner diameter was obtained from McMaster-Carr; dichloromethane (DCM), syringe with the needles and carbon nanoparticles (Carbon, mesoporous nanopowder, graphitized, μ 500 nm particle size, > 99.95% trace metals basis) were purchased from Sigma Aldrich and MakerBot Replicator 2 printer was used for 3D printing.

3.2.2 Solution Preparation for Filament

The method is called “Encapsulated Dissolving”, which provides the right viscosity of the PLA/DCM solution for adding mesoporous carbon nanoparticles (NC) later. PLA filaments were cut into small pieces (\sim 50 mm on average) and DCM was added in a closed glass container, and then heated. The optimum mixture composition was determined to be 1:5 weight ratio of PLA and DCM for the experiments till 6% wt. of NC and PLA. The heating of the solution with closed lid adds DCM vapors in the chamber, which was used to dissolve the long un-submerged PLA inside the glass. The nanoparticles were added after the PLA was fully dissolved, which took about half the time of the synthesis. The solution is left alone for 5 mins for the DCM vapors to settle down. The synthesis time is proportional to the amount of PLA used, which means smaller samples take less time. Table 3.2 shows the PLA and carbon nanoparticles proportions, and the relative time of preparation. The time of

preparation is relative to the ratio of PLA and DCM. There are several major advantages of this method: no wastage of DCM due to evaporation in the process of solution preparation; no need to pre-cut small pieces of PLA to submerge and dissolve; and the controlled amount of the contents in the solution. The PLA pieces can be cut as big as the base of the glass. The un-submerged PLA is dissolved by the DCM vapors trapped inside. Large amounts of PLA and NC solutions can be prepared for large filament samples. Other advantages include simpler procedure, repeatable with no need of constant observation to estimate the right viscosity range. The prepared solution can be stored with closed lid for next usage before drying (2 days to 2 weeks depending upon the sealing of the container).

Table 3.2. The composition of materials studied, which include various carbon nanoparticles (NC) proportions in 1 gram of PLA. (*The DCM volume was increased to keep the viscosity in the optimum value for solid filaments. @The 6% wt. filaments were not 3D printable for testing.)

Percentage by weight, (NC:PLA)%	Carbon nanoparticles (g)	Dichloromethane, (mL)	Relative time of preparation (mins)
0	0	5	20
0.5	0.005	5	20
1.5	0.015	5	20
6 @	0.06	5	20
9	0.09	7.5*	17
15	0.15	10*	15

3.2.3 Filament Preparation

Figure 3.2 shows the experimental procedure of solution preparation, injection of the solution into a rubber tube, and 3D printing. First, the PLA/NC/DCM solution was mixed with a magnetic stirrer as described in the previous section. Next, the solution was taken from the glass using syringes and injected into a 1.75mm rubber tube from both sides for

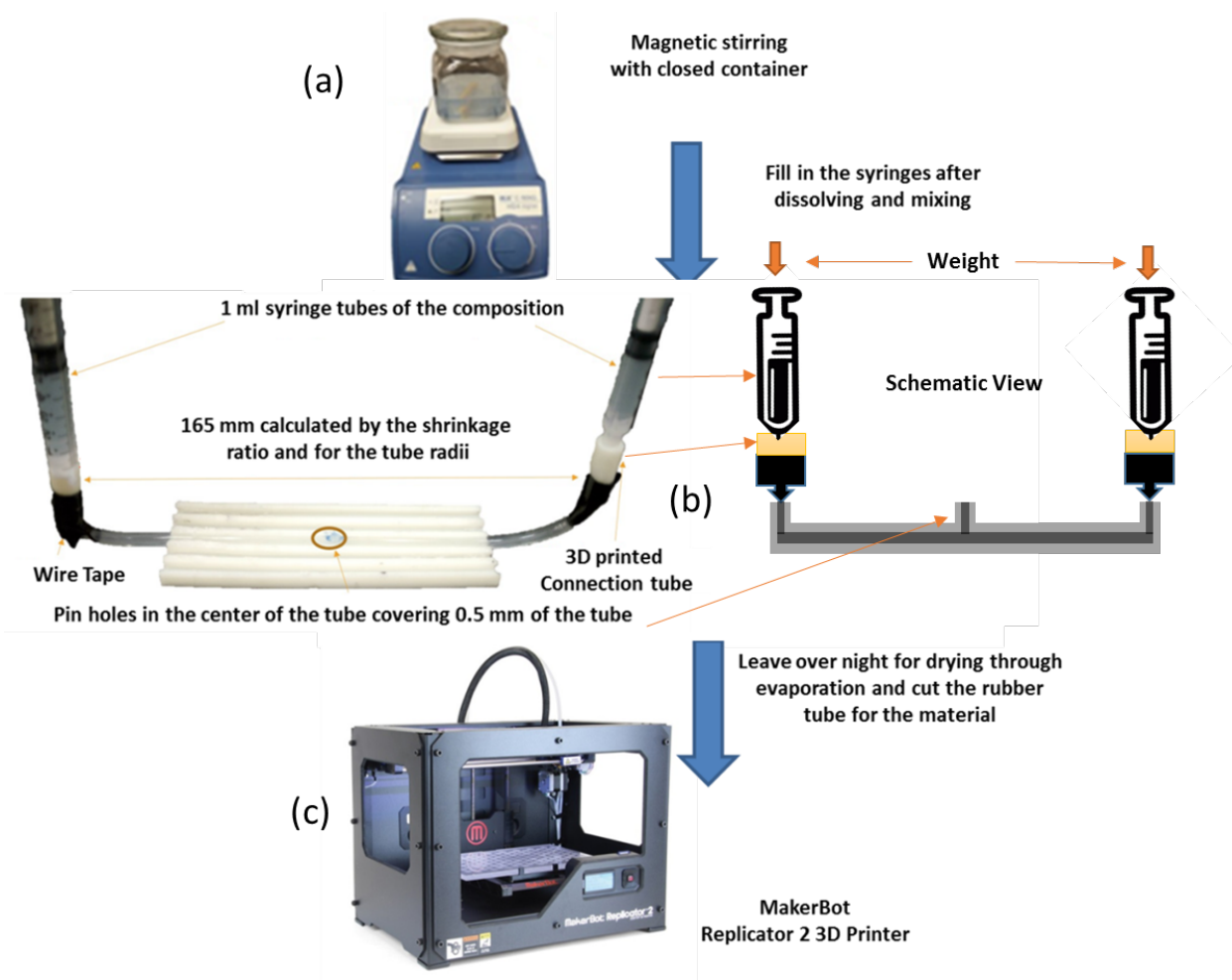


Figure 3.2. Preparation of filaments and 3D printing. (a) Magnetic stirring with closed container (b) picture of the drying technique and schematic view and (c) MakerBot Replicator 2 3D printer used for printing the made filaments.

uniform distribution of pressure. Holes were punched in the middle of the tube for the DCM to evaporate. Finally, the setup was left for 24 hrs. for drying in a fume hood. The filament was taken out of the mold (This will be discussed later). Similar solution blending technique was used when grafting a PLA to carbon nanoparticle surfaces for bionanocomposites preparation [189]. PLA is a biodegradable and bio-compatible material that can be used for diverse applications.

Several experiments were conducted to observe the volume shrinkage of the solution prepared during the evaporation (horizontal drying) process of the DCM. The volume shrinkage was observed to be 1:5 PLA and DCM volume ratio. This ratio helps in understanding how many-dried filament sample can be made from a given solution mixture. The syringe is connected to the 1.75 mm rubber tube using a 3D printed connector of varying holes on both ends for uniform distribution and tightly sealed using wire tape. To get 165 mm long solid filament, two syringes were used with 1 mL solution in each syringe and then injected into the rubber tube from both sides as shown in figure 3.2. The major advantages of horizontal drying are that the nanoparticles will be properly distributed throughout the tube rather than vertical drying, where the nanoparticles coagulate at the bottom due to gravity. This effect is prominent as the drying time is around 24 hours. Pressure on both ends eliminated the air bubbles while open-ended tubes without pinholes showed tunneling effect. Tunneling effect is the process of evaporation of the solution inside the tube creating a tunnel in the filament. This results in hollow filaments that are unsuitable for printing. The tube is kept inside a 3D printed frame structure for proper holding of the tube in shape. The pin holes (0.5 mm diameter) are kept only at the center of the tube on the open side rather than all over the tube, which gave sufficient outlet for the DCM to evaporate.

Figure 3.3 shows the designed 3D printed load carrier structures for proper compression of the rubber tube throughout the drying process. The calibrated weights are used as a load and are applied from the top at both ends. A hole is inbuilt in the design for vertical assembly of the structure on the stand to the required calibrated weight dimensions. A hole is provided to hold the syringes in position while drying. These stands are custom designed for different weights and syringes. The loads were varied from 0.75 kg to 1.25 kg as required for different compositions. The drying time with NC was around 24 hours and without NC it was around 12 hours. A frame structure was made inside a chemical hood which can hold up to 4 full setups simultaneously.

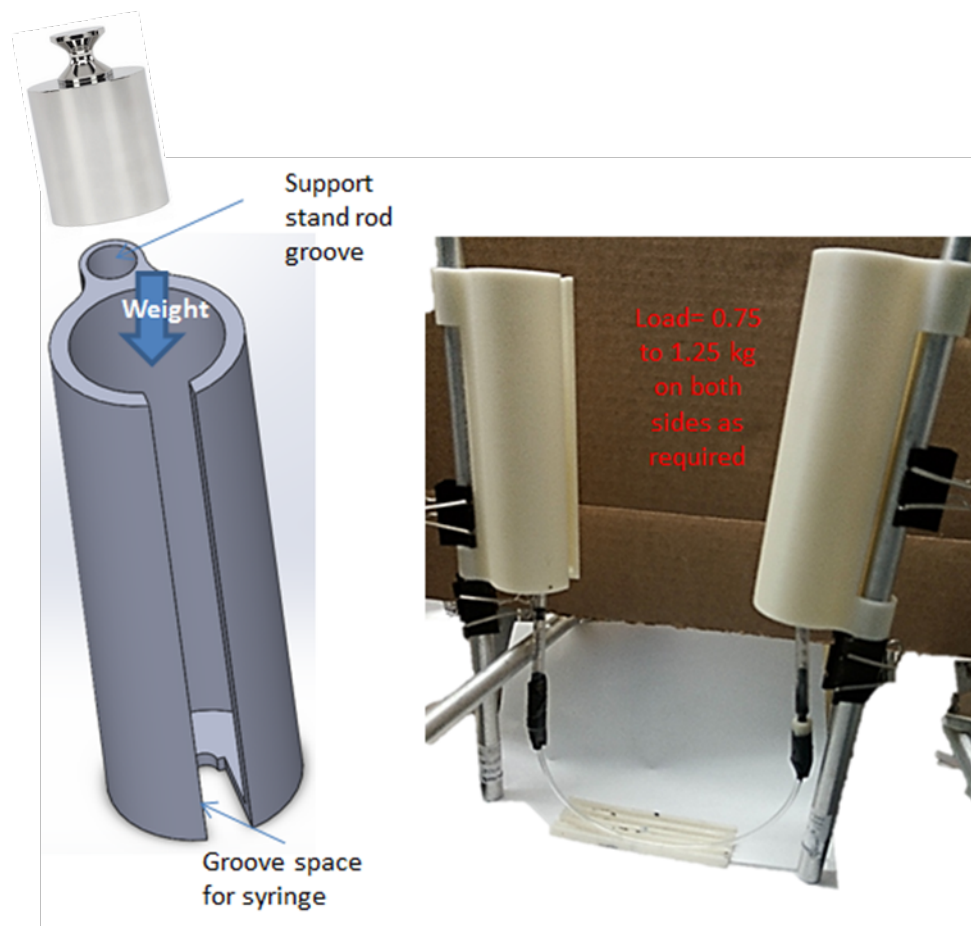


Figure 3.3. (a) 3D printed load carrier structures (b) Full horizontal drying setup with weights.

The cutting technique uses a 3D printed blade casing which cuts the rubber tube to its thickness on both sides with high precision. Figure 3.4 shows the SolidWorks 2014 CAD design of the cutting apparatus. This can be modified for different rubber tubes as required. This design is made for 1.75mm inner diameter rubber tubes obtained from McMaster. The apparatus is assembled using screws and bolts with Dewalt carbide utility blade. The design is made in such a way that the blade is firmly held in the groove exposing sufficient tip to cut. The tube is precut for about 20 mm before pushing through the hole for proper alignment of the blade tips to cut the tube. The protruded part of the tube can be used to firmly hold and pull the tube out. The tube is pulled out by an impulse movement with

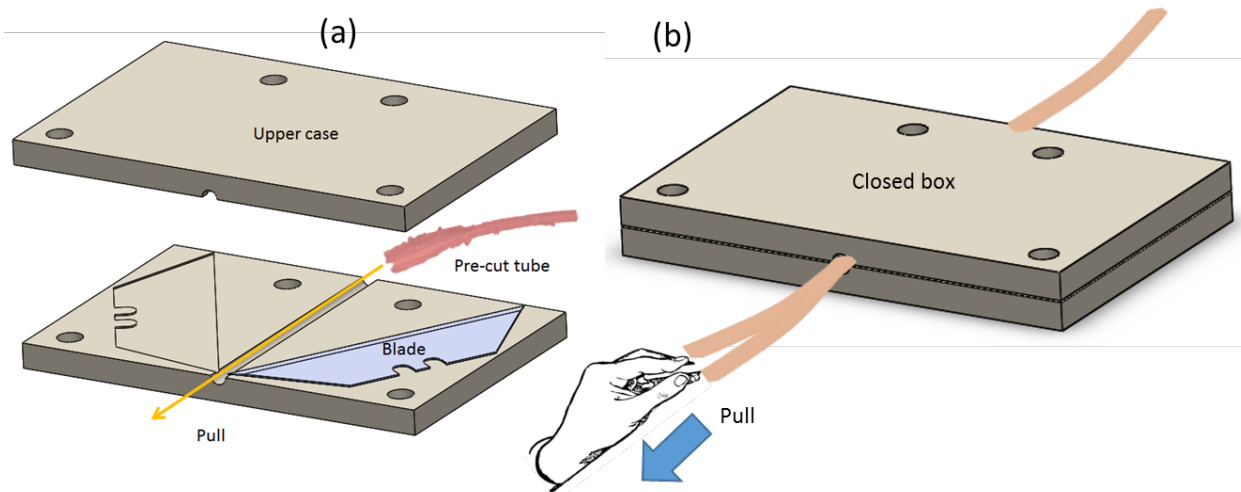


Figure 3.4. (a) SolidWorks 2014 CAD model of the cutting apparatus for splicing the rubber mold that has initial per-cut. (b) Assembled cutting apparatus when the rubber tube is pulled by hand.

sufficient force, which cuts the tube and leaves the filament untouched. The blades can be replaced when blunt and the technique needs minimum hand skills of the user, making the process extremely fast and simple.

3.2.4 Long Filament Fabrication

The longer filament of 1.5m length was made through implementation of spring-loaded mechanism with same holders as shown in figure 3.3 (a). The spring load mechanism is shown in figure 3.5 (a), where cuts were made using a Dremel at three different points, each representing the zero loads for 7 mL, 4 mL, and 0 mL solution. The spring load system was adapted for longer filaments, as calibrated weight loads required for long filaments were too heavy. The spring was held between spring holders and rubber bands to give more strength to withhold the tension caused by the spring on the 3D printed holder. The springs used were 22.2 mm. in diameter and 101.6 mm in size applied on both ends with a safe working load limit of 24.8 - 44.7 lbs. (11.8 - 20 kg). The holder was designed to hold 60 mL standard syringes. In the case of the longer filaments, in the middle along the length of 30 mm, a

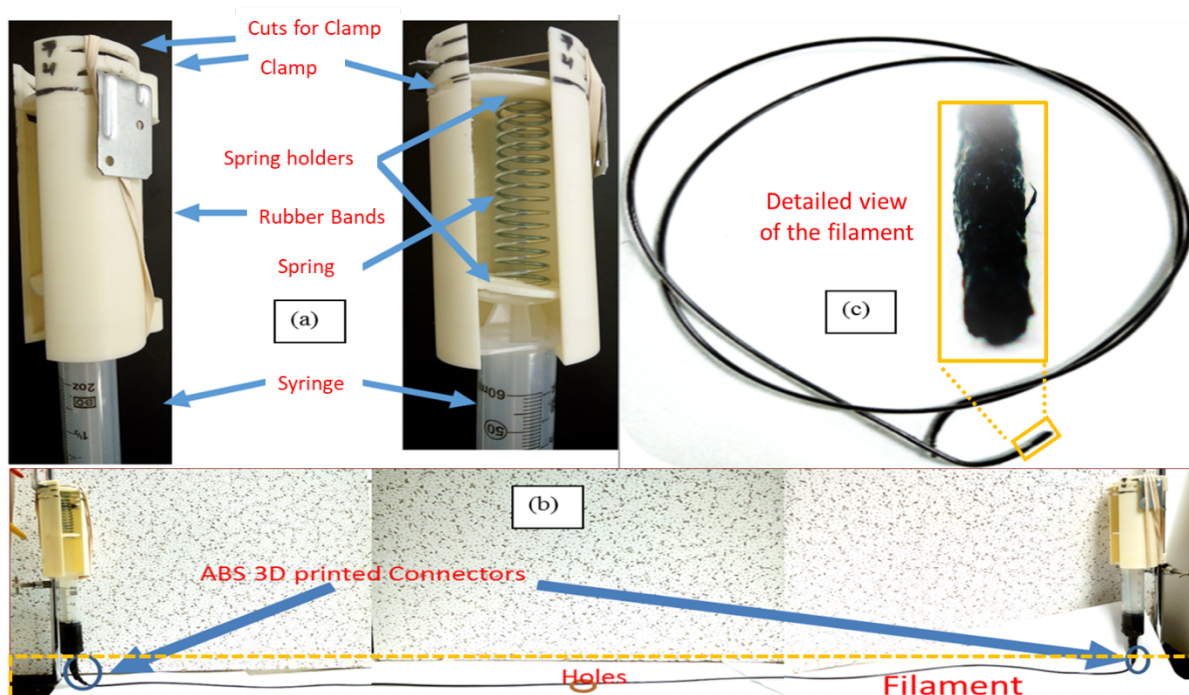


Figure 3.5. (a) The spring mechanism implemented in the holders for more load (b) 1.5m long filament preparation using spring mechanism and (c) prepared long filament.

cluster of pinholes were punched as it required more DCM to evaporate. Figure 3.5 (b) shows the complete setup of the injection and drying mechanism. In figure 3.5 (c), the reader can see the synthesized 1.5 m long filament for big size 3D prints. It took 4 days for drying compared to 1-2 days of drying for the smaller filaments. This can be controlled by the pin holes or by implementing forced drying techniques. The forced drying techniques can change the strength and properties of the formed filament. The fume hood used had the maximum exhaust flow of 645.5 CFM and average face velocity of 131.5 FPM. The current technique in this work illustrates the method of improving the properties of thermoplastic materials with the additive. The process can be scaled up for mass manufacturing by employing a good drying technique because the current longtime requirement for longer filament is due to the need of cooling techniques. Another issue was the 3D printed connectors, which were made of ABS, eroded during drying due to DCM exposure for long hours and needed to be

replaced several times to avoid leakages. This can be resolved by using porcelain connectors as it does not react with DCM.

3.3 Experimental Results

3.3.1 Viscosity of PLA, NC and DCM solution

Figure 3.6 shows the typical viscosity range of 0-15 wt.% of carbon nanoparticles in PLA within in 5-10 ml DCM solution as shown in table 3.2. These data were obtained from Brookfield DV2T viscometer. The typical viscosity, that can be used for solution casting is between 1400 - 2400 mPa-s (or cP) shown in transparent green box and the optimum range for proper filament samples was 1600 - 2200 mPa-s shown in the transparent orange box. Beyond this, the solution is out of viscosity range for preparation of solid filament which is visually and experimentally observed. This phenomenon is controlled by increasing the DCM volume as shown earlier in table 3.2. The 9 and 15 NC wt.% have a higher amount of DCM to control the viscosity in the favorable range. The variation implies that the viscosity increases as the percentage of nanocarbon increases, which matches with general observation as the volume of nanoparticles increases as percentage increases [193]. All the experiments were done under a chemical hood. If the optimum viscosity range is crossed, it will be too dry to suck through a syringe. If the solution is too viscous, after evaporation in the rubber tubing, it will reduce in volume leaving air cavities and eventually giving a hollow, brittle and weak filament which is unusable with the 3D printer.

3.3.2 Electrical property of the PLA and carbon nanoparticles composite filaments

Electrical conductivity tests of the composite filaments consisting of PLA and carbon nanoparticles were done using radio shack voltmeter to find the resistance at 10 mm apart across

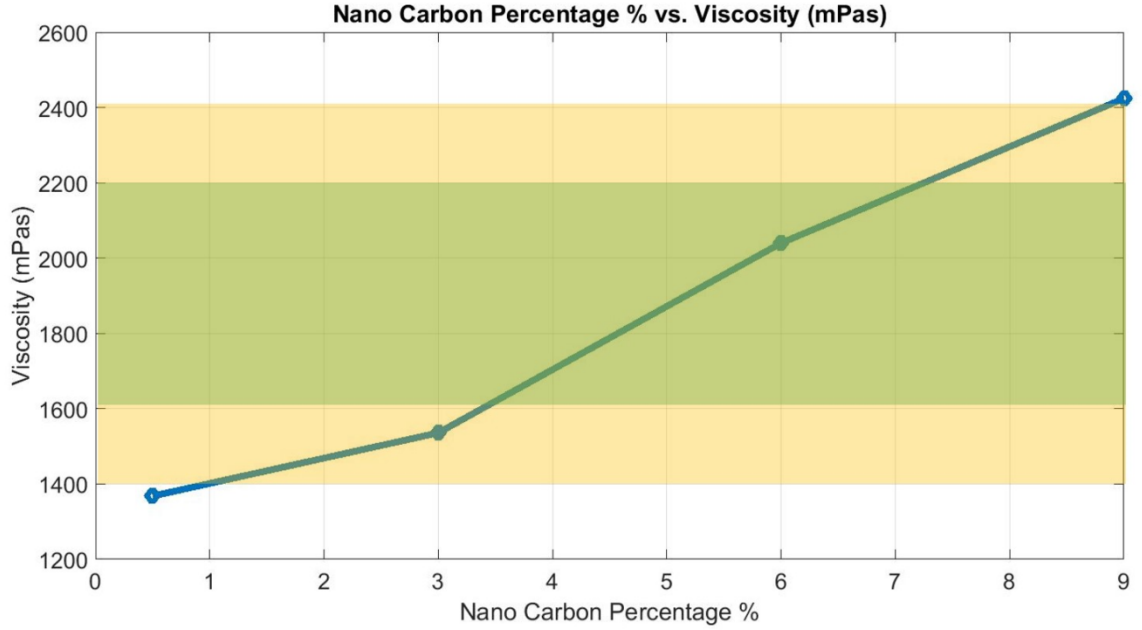


Figure 3.6. Viscosity (mPa-s) of carbon nanoparticles percentage for 1 g PLA and respective volumes of DCM from table 3.2 at 25 rpm and at room temperature for 1:5 wt. ratio.

the length of the sample and the average values were taken. The measurements were taken several times and on different dates as well. The average values and the standard deviations of both the resistivity and conductivity results are shown in figure 3.7. As expected the conductivity of the filaments increases as the percentage of the carbon nanoparticles increases.

The relationship of geometrical properties and material constant can be expressed by the following simple equation:

$$k = \frac{1}{\rho} = \frac{L}{RA} \quad (3.1)$$

Where k is the conductivity, ρ is the resistivity, R is the resistance, L is the length, and A is the area of the sample. In figure 3.7, the average electrical resistance of a filament with the diameter of 1.75 mm and measured at 10 mm distance along the longer filament made from at 15 wt.% NC was $6 \pm 2 \text{ k}\Omega$, which is equivalent to a resistivity of $1.44 \pm 0.48 \text{ }\Omega\text{m}$

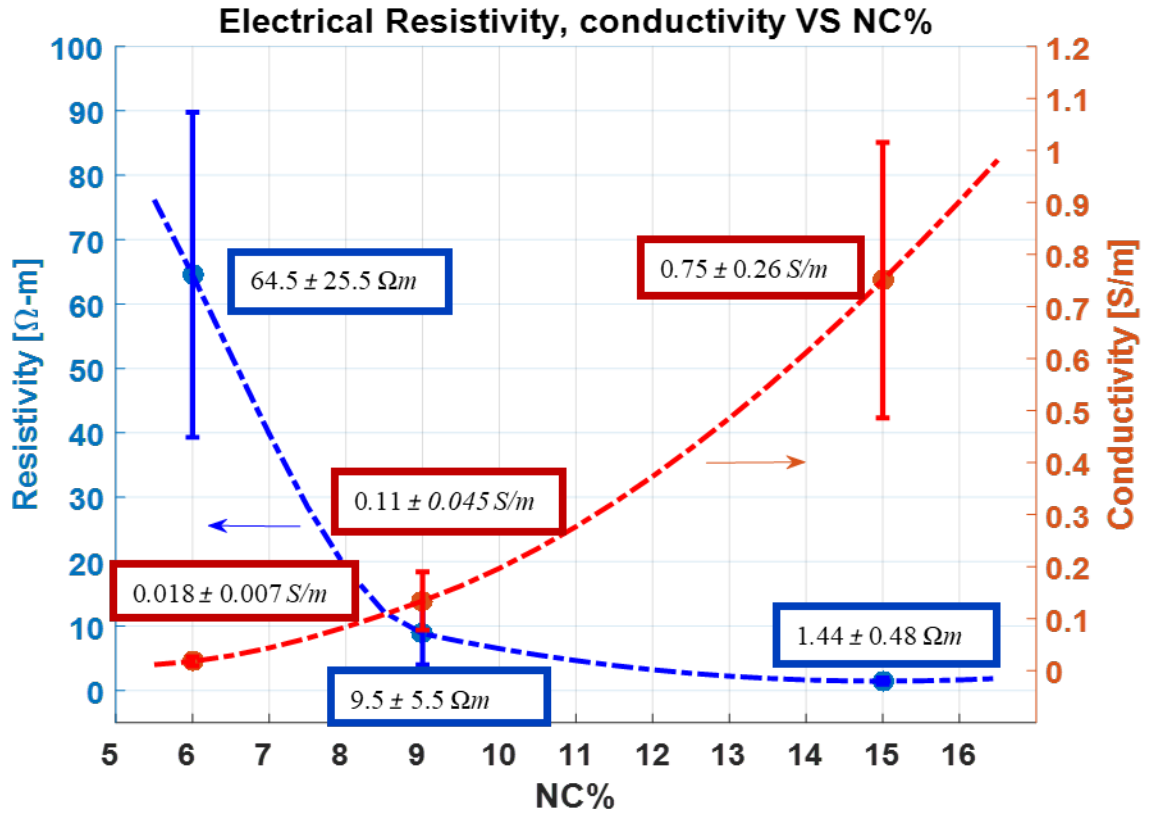


Figure 3.7. Resistivity and conductivity of the filaments made of various wt.% of carbon nanoparticles in PLA. The samples were 1.75mm in diameter and 100 mm long, where the resistances of each sample were taken at 10 mm distance along the filament, both the average and standard deviation of the measurement are shown.

and conductivity of 0.75 ± 0.26 S/m, which is significantly lower from infinite resistance as PLA is a pure insulator. In figure 3.7, the comparison is done under the same conditions for different percentages of the NC. The inconsistencies are due to non-uniform formations of the filament because of human error. The major error is due to measurement of the electrical resistivity which was done at different segments in a long filament and taking the average and standard deviation. Since the distribution of the conductive part was not uniform for a different composition, the large deviation is prevalent in figure 3.7. The electrical conductivity at a low weight percentage of the filler carbon nanoparticles was observed at 6 wt.%,

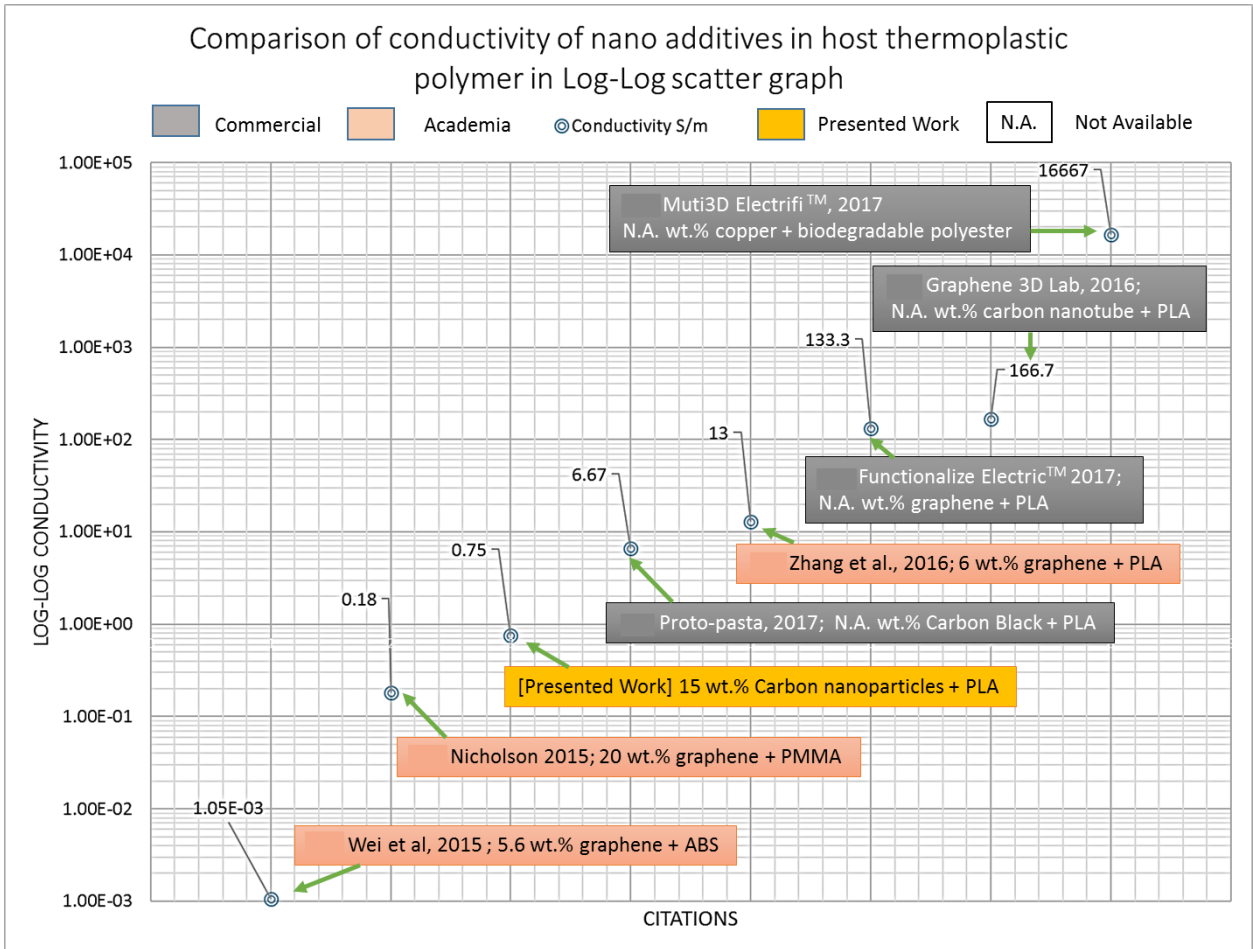


Figure 3.8. Comparison of the conductivity of nano-additives in host thermoplastic polymer. [242, 138, 227, 3, 6, 2, 135] . The commercially available filaments are shown in grey, the academically published filaments are shown in salmon color and the presented work is shown in mustard color.

which is low compared to the works presented by others.

The resistances shown by Nicholson [138] with graphene and PMMA composite were $1.5 \pm 0.4 \text{ M}\Omega$ and $60 \pm 7 \text{ k}\Omega$ for the 15 and 20 wt.% filaments of length 25.4 mm and diameter of 1.75 mm, which is equivalent to $142 \text{ }\Omega \text{ m}$ or $7 \times 10^{-3} \text{ S/m}$ for 15 wt. % sample and $5.7 \text{ }\Omega \text{ m}$ or 0.18 S/m for 20 wt. % sample. The resistance of their sample at 15 wt.% is very high compared to the presented results. Zhang *et al.* [242] at 6% wt. graphene and

PLA filament showed conductivity of 13 S/m whereas is 0.02 ± 0.01 S/m for 6 wt.% NC and PLA. In a similar study, Wei *et al.* [227] showed electrical conductivity of 1.05×10^{-3} S/m at 5.6 wt.% graphene and ABS composite, which is low compared to the presented work. The conductivity of molded resin (not 3D Printed) of Proto- pasta Conductive PLA is 6.67 S/m [6] which is better than the presented work but the weight percentage of carbon black used is not specified. Functionalize Electric™ PLA [2], a commercially available conductive filament has a 133.3 S/m which is better than the presented work, but as mentioned previously carbon nanotubes are expensive than carbon nanoparticles and the composition is not specified. 3DXNANO™ ESD CNT-PETG [31] has a high surface resistivity of 10^7 to $10^9 \Omega$ (tested using concentric ring test method) which is comparatively larger but this is not compared as the volume resistivity is not specified. Graphene 3D Lab [3], a commercial plastic/graphene composite filament used for 3D printing of graphene - enhanced plastic structures has a conductivity of 166.7 S/m which is better than the resistivity presented in this work but the composition and all properties are not disclosed. Similarly, Electrifi filament [135] is another commercially available conductive filament made with biodegradable polyester and copper with a conductivity of 16,667 S/m but they do not disclose its composition. In figure 3.8 a comparison of the conductivity of nano-additives in host thermoplastic polymer with the work presented in this work is shown.

3.3.3 Mechanical property of the PLA and carbon nanoparticles composite filaments

To study the mechanical strength of the filaments, Instron tensile tester (5960 Dual Column) was used to test their ultimate tensile strength and compared with original PLA (commercially obtained) and PLA samples prepared with DCM at various NC compositions (0 wt.%, 0.5 wt.% 1.5 wt.%, 9 wt.% and 15 wt.% NC: PLA). In figure 3.9, tensile testing of (a) clear PLA (right) and 15wt.% NC and PLA (left) are shown and in (b) clear PLA (left)

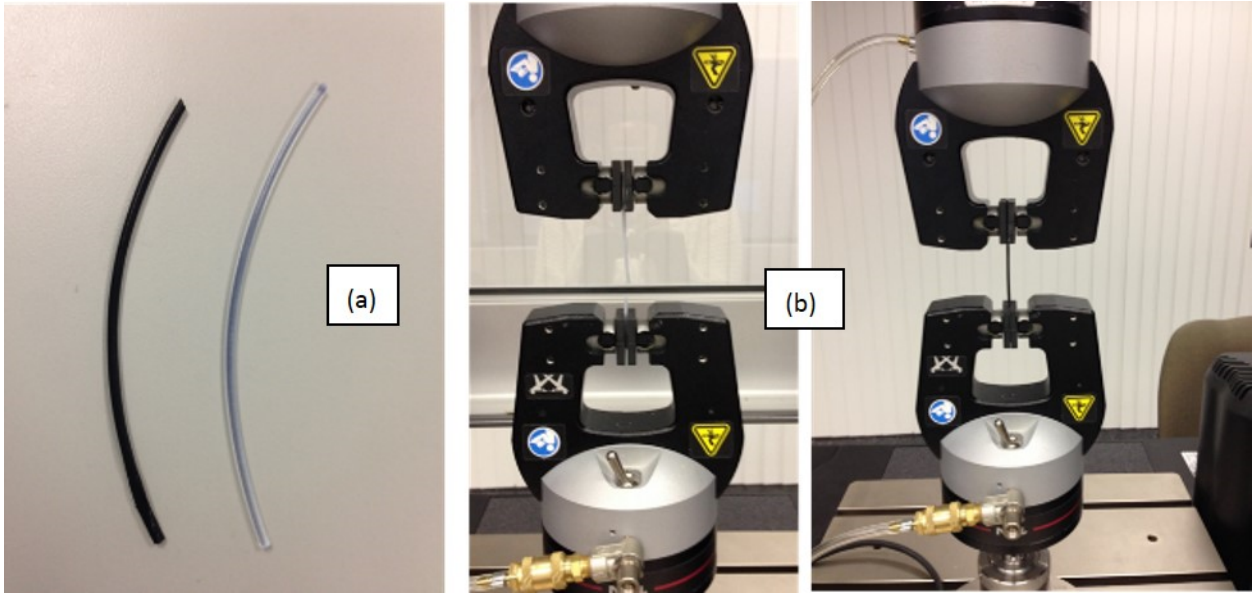


Figure 3.9. Tensile testing of (a) Clear PLA (right) and 15wt.% NC and PLA (left), (b) clear PLA (left) and 15wt.% NC and PLA (right).

and 15wt.% NC and PLA (right) are shown respectively. In figure 3.9, the tensile strength of NC1.5 is higher than that of NC0.5 which could be reinforcement provided by carbon at some small values and the role of DCM with plastic with NC filler needs to be further studied. The tensile test was quasi-static at a strain rate of 1 mm/min. In figure 3.10 (a), the stress-strain curves of all the samples along with a 3D printed dog bone structure (NC15 3D, printed with 15 wt.% NC filament) is shown. The inset of stress-strain is shown for all except PLA and 3D printed part. The pure PLA has the highest strength of 60 MPa, and most of the samples have below 15 MPa strength. However, the 3D printed structure using 15 wt.% NC: PLA filament has the 25MPa tensile stress. Using the presented manufacturing process from figure 3.10 (b) the reader can see a small drop in the mechanical strength as more carbon nanoparticles in PLA is added. The 3D printed part is stronger due to the dog bone structure printed in layers. Table 3.3 shows the values of ultimate tensile stress and strain respectively for each sample. There is a significant loss of tensile strength when DCM is used for dissolving the PLA and adding the NC using the presented manufacturing

process. Effect of strength using other solvents can be studied in future using this method. The 6% wt. filament was not tested because at this diameter the filament was non-uniform.

Table 3.3. Tensile test results of all the PLA/DCM/NC specimens of 1.75mm diameter.

S. No.	Specimen label	Tensile stress (Ultimate) [MPa]	Ultimate Tensile strain [mm/mm]
1	Pure PLA	54.2	0.069
2	NC 0	11.9	0.064
3	NC 0.5	8.5	0.032
4	NC 1.5	11.0	0.060
5	NC 9	7.5	0.058
6	NC 15	6.9	0.051

3.3.4 Micro-structure of Filaments

Scanning Electron Microscope (SEM) images of the samples were taken and shown in figure 3.11 (a). In figure 3.11 (a), that the dark structures are mostly insulating PLA and the bright structures are the conductive carbon. In figure 3.11 (b), the reader can observe a bar graph of particle distribution of nanoparticles in the respective SEM images that were processed in MATLAB image processing toolbox [5], where the number of the particles increases as the percentage of carbon nanoparticles in PLA increases. A similar representation of SEM imaging in particle distribution histogram was shown in another study of thermoplastic nanocomposites with carbon nanotubes [176]. A clear increase of the white formations is observed as the percentage of the carbon nanoparticles increases in the sample. One more observation is that the carbon nanoparticles are seen coagulated and the surface has platelet formation with the increase of carbon nanoparticles.

Low-resolution images of samples at lower NC concentration is observed. Figure 3.12 (a) shows the streaked surface of clear PLA made through commercial hot extrusion but in figure 3.12 (b) there are no streaks, rather a very smooth surface of PLA+DCM formed

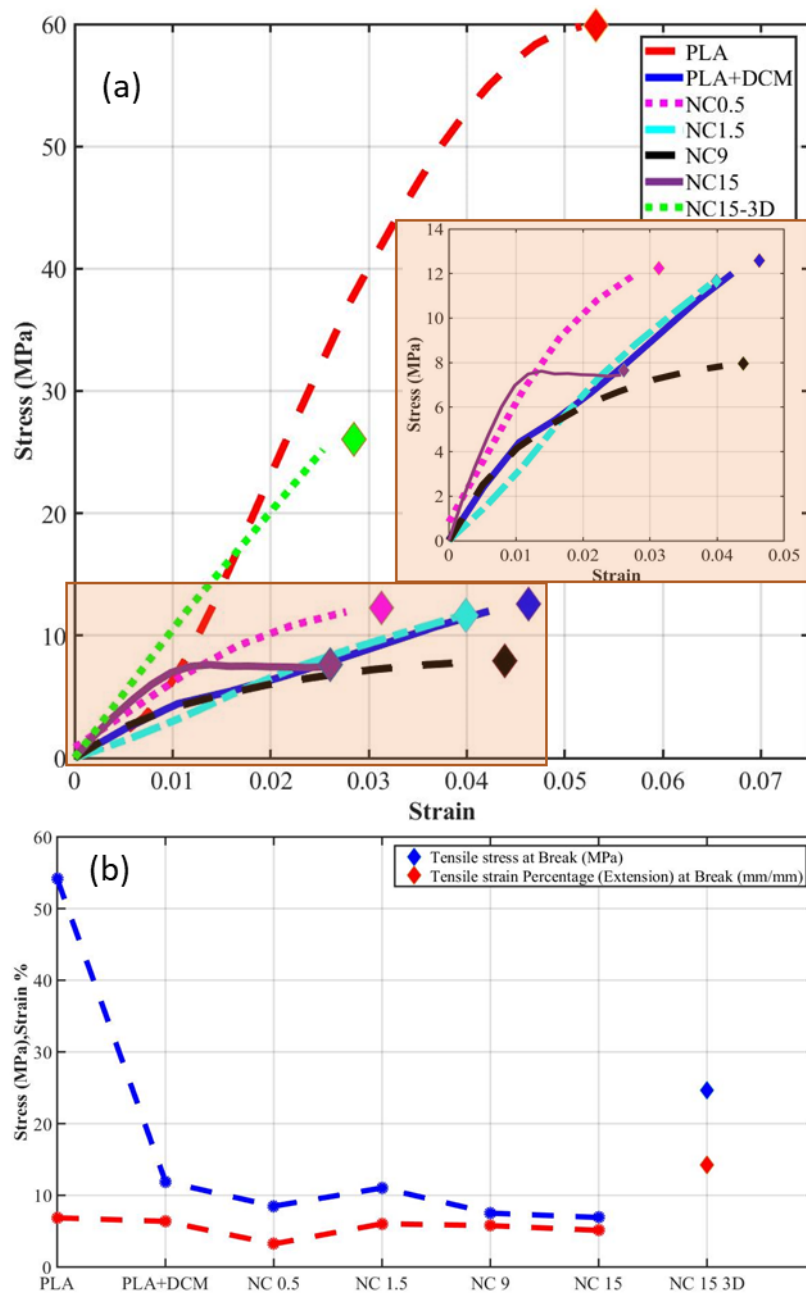


Figure 3.10. Mechanical property of filaments made of various compositions of wt.% NC in PLA (a) Tensile stress-strain curve (diamond marker shows breakpoint) and (b) magnitude of tensile stress (MPa) & tensile strain (%) at the break for all samples with along with a 3D printed structure.

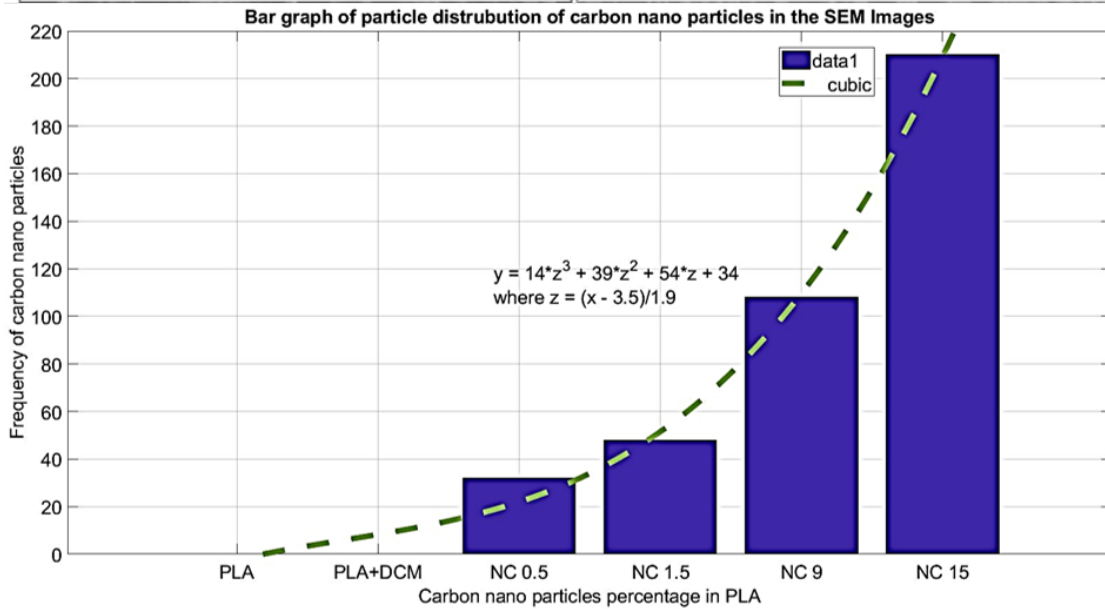
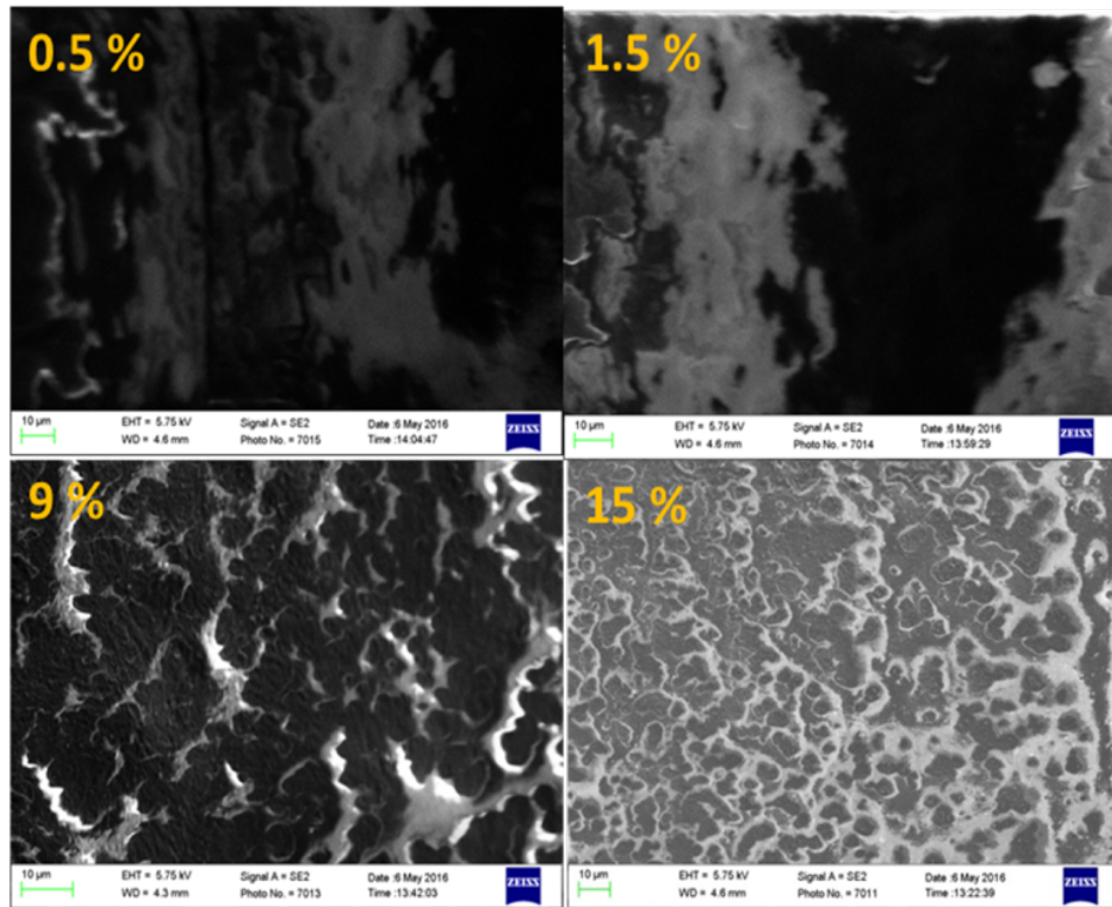


Figure 3.11. Microscopy and image analysis of various wt.% of NC in PLA along the surface: (Top) SEM images of the filaments of NC 0.5, NC 1.5, NC 9 and NC 15 at 10 μm resolution; and (Bottom) Bar graph of particle distribution of nanoparticles in the respective SEM images.

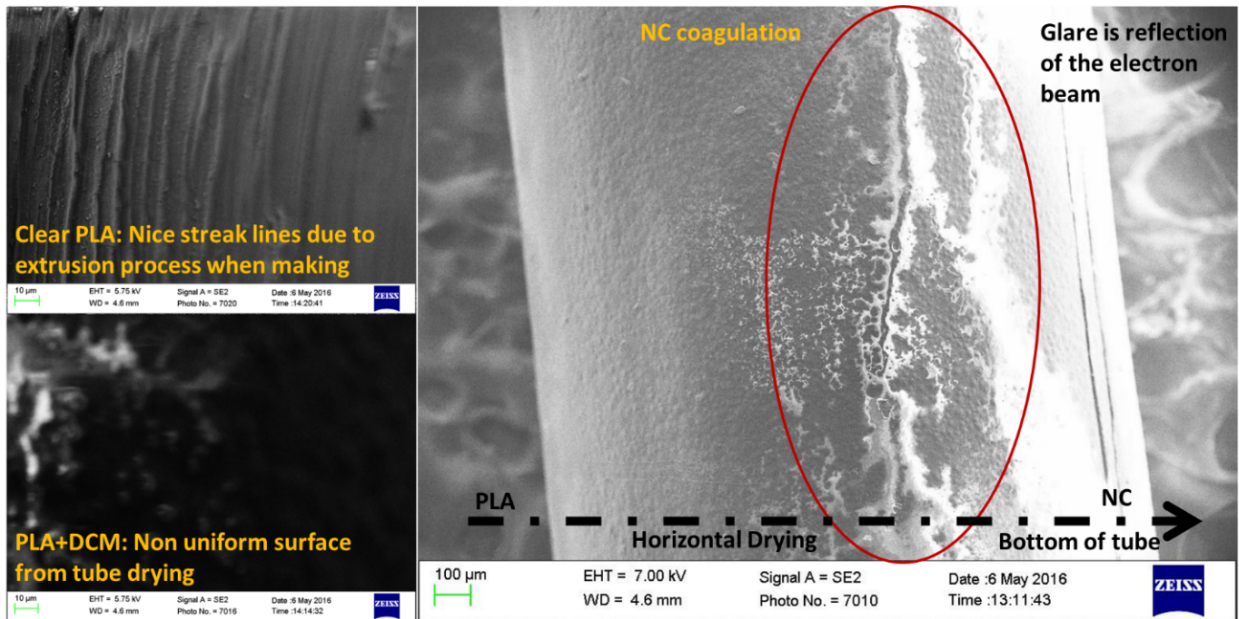


Figure 3.12. SEM Images of samples at the surface: (a) clear PLA, (b) PLA+ DCM through tube drying and (c) SEM image of NC15 lower resolution showing the effects of horizontal drying.

through tube drying (bar scale = $10\ \mu\text{m}$). Figure 3.12 (c) shows the 15% wt.NC (NC15) at a lower resolution (bar scale = $100\ \mu\text{m}$) where one can clearly see the NC coagulated structures. Due to horizontal drying, we can see the more NC concentration towards the right of the picture representing the bottom of the tube due to the weight of NC and vice versa, and more PLA towards the left or top of the tube can be observed. We should not be confused with a bright glare as NC, as it just represents the reflection of the electron beam in the SEM machine. SEM images of PLA and Arlcel 83 in a solvent of dichloromethane (DCM) and toluene were shown by Liu et.al. [116], where PLA micro-capsules formation and variable distribution exist due to the solvents and compositions. Similar SEM image as in figure 3.11 is presented by Haroosh *et al.* [70], where they showed for PLA: PCL blends in DCM: DFM except few fibrous structures due to electro-spinning and solution contents. Utilizing inkjet 3D printing, Jakus *et al.*, showed related SEM images of samples made of

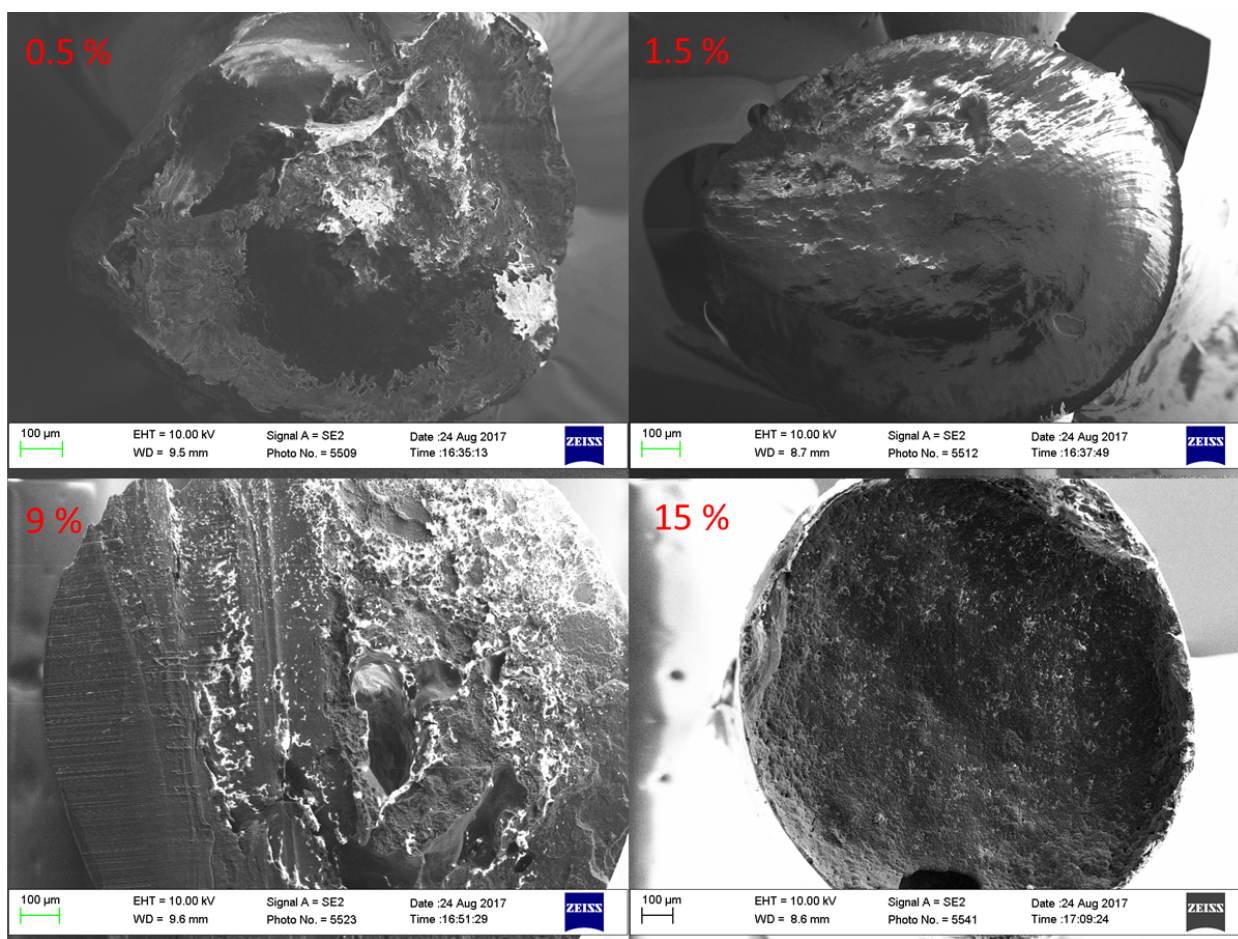


Figure 3.13. Microscopy and image analysis of various wt.% of NC in PLA: SEM images of the filaments of NC0.5, NC1.5, NC9 and NC15 at 100 μm resolution in cross-sectional view.

PLG- graphene using DCM [88]. The variation in texture in the presented work samples is because of the horizontal drying process in a tube that resulted in a smooth surface.

In figure 3.13, one can see the SEM images of the cross-section of the filament from NC0.5, NC1.5, NC9 and NC15 compositions at 100 μm resolution. The plasticity of NC0.5 and NC1.5 bent the filaments while slicing them for SEM images which can be observed in figure 3.13. The brittleness of NC9 and NC15 due to increased carbon helps in a cleaner cut. The SEM images are sharper as the NC percentage or conductivity of the filament increases.

3.4 Observations and Discussions

Several methods and approaches were investigated to successfully synthesize a solid filament with various percentages of carbon nanoparticles using a DCM solvent. The most successful method is described earlier in the section. Then the filaments are characterized for mechanical strength and electrical conductivity. As shown in figure 3.7 earlier, low percentage of NC (6 wt.%) showed large standard deviation in resistivity due to the variation of carbon distribution across the surface. However, the variation decreases with a higher concentration of NC. Among the samples, the 15% wt. NC filament was used to 3D print a dog bone structure for demonstration. Initially, several attempts with different filaments that have either void inside or not completely solid that brought difficulty in 3D printing using commercial 3D printers. The main issue was that the extrusion force between two gears damaged the filaments and created difficulty in extruding out the new filaments. Therefore, care was taken for fabrication of solid filaments. The 15 wt. % NC mixed in PLA solution was selected for 3D printing due to the relatively high conductivity of the filament as discussed previously.

The 15 wt. % NC PLA filaments had an average resistivity of $1.44 \pm 0.48 \Omega m$ or conductivity of $0.75 \pm 0.26 S/m$, whereas clear PLA had infinite resistance. Figure 3.14 shows the 3D printed dog bone structure of 30 mm in length, 5 mm in width and 1 mm in thickness (the measured resistance was $118 \pm 64 k\Omega$). The deduced resistivity and conductance of the dog bone structure was slightly higher ($20 \pm 10 \Omega m$ and $0.065 \pm 0.04 S/m$) as there was a rearrangement of carbon nanoparticles while 3D printing. This is lower than 476 S/m at 6% wt. of reduced graphene oxide (r-GO) in PLA after 3D printing is shown by Zhang *et al.* [242] but their filament conductivity was 13 S/m whereas the presented work is $0.75 \pm 0.26 S/m$ with the same 3D printer in both cases, but different chemicals and parameters were used during synthesis. The cost of PLA filament per g is roughly 0.6 cents from MakerBot Inc. and the cost of mesoporous carbon from SIGMA-ALDRICH is roughly \$30 per g. Hence

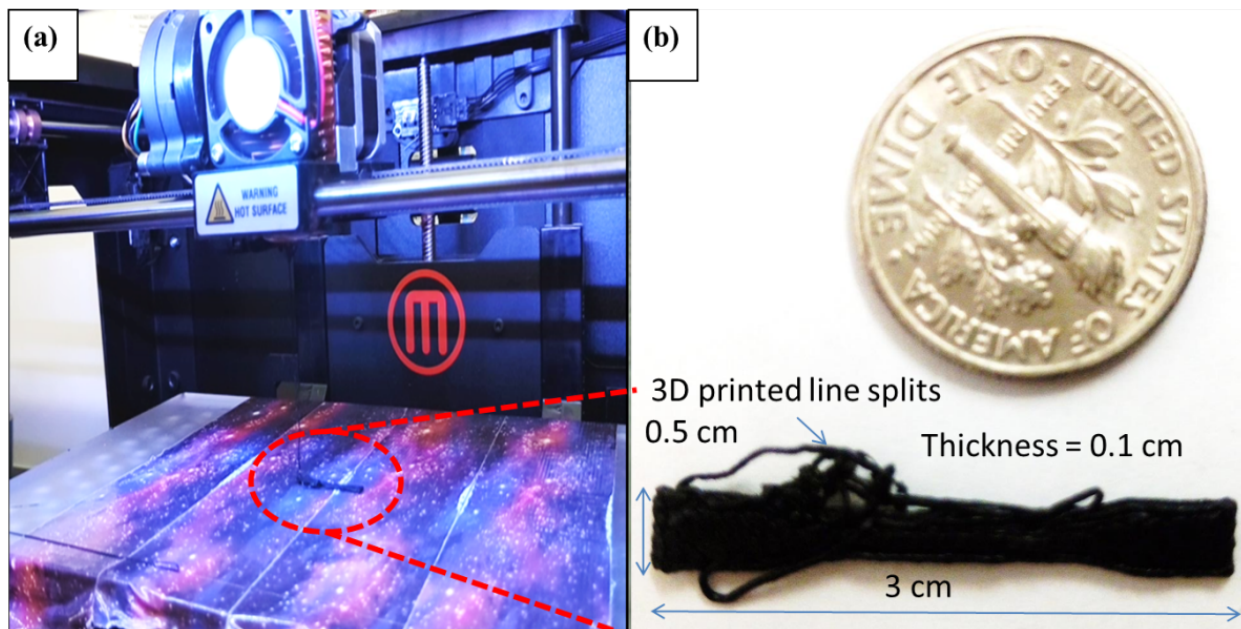


Figure 3.14. (a) MakerBot 3D printer test system and (b) 30 mm x 5 mm x 1 mm dog bone structure printed from a composition of 15 wt.% carbon nanoparticles and Polylactide fiber (PLA) using MakerBot 3D printer.

the NC15 material cost would be roughly \$5 per g. Reduced graphene oxide (r-GO) used by Zhang *et al.* [242] from SIGMA-ALDRICH roughly costs \$750 per g. Hence NC15 costs 9 times lesser than the 6% wt. of reduced graphene oxide (r-GO) in PLA of Zhang *et al.* [242]. While 3D printing the sample, the filament was melted in the 3D printer head without a proper distribution of carbon nanoparticles (uncontrolled) and resulted in a higher electrical resistance. On the other hand, Wei *et al.* [227] at 3.8 wt.% graphene in ABS composite showed a conductivity of $6.4 \times 10^{-5} S/m$ and after it was 3D printed into 10 mm x 10 mm x 1 mm rectangular model, the conductivity decreased to $2.5 \times 10^{-7} S/m$. Graphene and ABS cost roughly \$1200 per g from SIGMA-ALDRICH and 0.5 cents per g from MakerBot Inc., which brings their filament per g roughly 9 times costlier than NC15 presented in this work. This shows that the 3D printing process must be optimized for homogeneous melting for better conductive 3D printed parts. As mentioned before, the mechanical strength of the filaments is reduced as the amount of the carbon nanoparticles is increased, which has become

a challenge when 3D printing using MakerBot 3D printer. The problem was that the filament having more than 15% wt. carbon nanoparticles were not strong enough to pass through the extruder head. This was observed by Zhang *et al.* [242] and they could not go beyond 8% by wt. in their case. The major difference is that they used hot melt extrusion using HAAKE twin-screw melt mixer while in this work DCM solution blending is used. Solution blending may give more freedom of higher concentrations of the filler and more uniform distribution. As mentioned previously, carbon nanoparticles are 5 times cheaper than graphene, making the procedure presented in this work more cost-efficient.

The approach in this work could be a cheap alternative to regularly used gold-coated electrodes, with the advantage of 3D printable complex shape electrodes. The only limitation of this method is the clogging of the 3D printer head due to successive printing with coated NC and PLA filament which leaves a residue that is very adhesive in nature and becomes very hard after drying. To unclog the nozzle, DCM was used and the nozzle can be used again after several hours of soaking. A nano-lubricant inside the nozzle would solve this issue of clogging. The first layer of the printed structure (figure 3.14 b) did not stick to the base of the 3D printer, which left a dangling structure. This can be easily resolved by using adhesive tapes available in the market for the 3D printers.

3.5 Application in Humanoids

One application of the conductive filament is in the fabrication of robots and humanoids. Humanoids are robots, which look and perform like humans. They are often made of several mechanical and electrical parts having complex electrical wires running from the power sources, controllers and actuators. As the humanoids are expected to perform complex tasks using complex manner like humans, these complex network wires cause a major problem as they become dangled near the joints and along the whole body. In our experience, these

wires end up tangled and detach during complex human-like movements causing failure and repeatable maintenance and low productivity. The work presented in this work has high application in humanoids that use 3D printing as its major manufacturing technology. This can be implemented in the humanoids like Buddy [153, 155, 30] and HBS-1 [232] humanoid, which are mostly 3D printed using ABS plastic for various applications. As shown in figure 3.15, wires can be replaced by printing conductive filaments to complete the electrical circuits of components, which do not interfere or be a hindrance during the complex maneuver of the robot. Wires can run through the pipe segments to minimize tangling at the joints. NC printed wiring can solve the major problem of actuation, maintenance and connection issues, ultimately leading to advancement in humanoid manufacturing. This can be implemented on any 3D printed parts to avoid wiring and utilize the advantages of the concept. Due to higher resistance than regular copper wires, there can be a decrease in power efficiency which is a limitation. This can be solved by conducting more research in the fillers rather than carbon nanoparticles like gold, silver nanoparticles, etc. which have higher electrical conductivity, but this will increase the overall cost.

We tested on 3D printed ABS structure as shown in figure 3.16 which contains several grooves of various lengths. First, a 1:1 ration of NC and PLA mix paste was prepared and manually filled the grooves layer by layer (for about 10 to 15 times). This process can be automated in the future. A 45 sec gap between each layer was used for drying each layer. When we first filled the paste, due to the DCM in the solution, it fills the full groove but eventually gets dried and forms a thin solid layer. There can be small holes left over which will end up in discontinuity for electrical conductivity. These holes should be refilled with the solution when applying the second layer. Figure 3.16 (c) shows the 3D printed assembly with syringe and needle used for testing the principle for the humanoid application with CAD images including dimensions. The electrical conductivity and resistances of various grooves were measured and are shown in the figure 3.16 (d) which shows some promising results for good electrical conductivity without much loses.

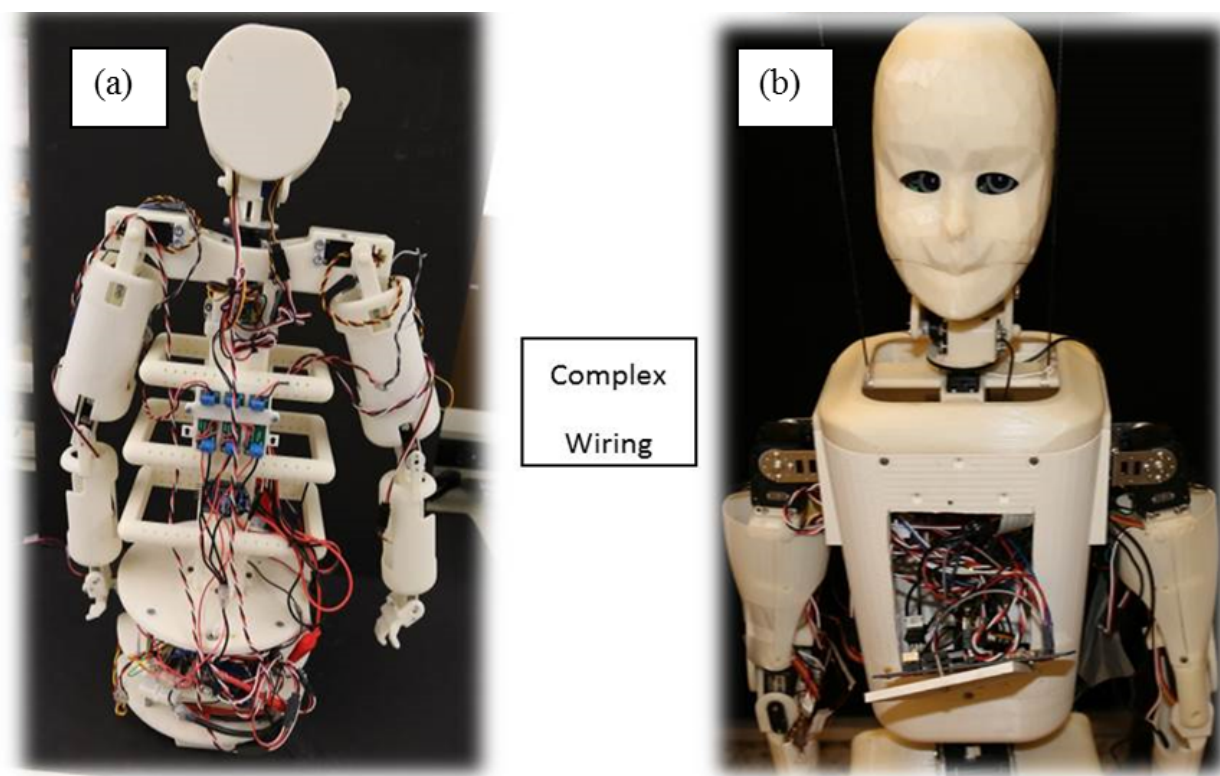


Figure 3.15. Complex wiring examples of 3D printed humanoid (a) Front side of Buddy-3D printed humanoid having mobile base [30], (b) a child-size humanoid, HBS-1 similar in size to a 7-year old, 3D printed in the laboratory [232].

3.6 Conclusion

A composite material consisting of carbon nanoparticle (NC), dichloromethane (DCM) and polylactide (PLA) was made for use as filament material for application in additive manufacturing and the material was characterized extensively. The electrical conductivity and mechanical properties of the filament material were experimentally measured for various weight percentages of mesoporous carbon nanoparticles in polylactide matrix. It was found that the synthesized filaments had a mechanical strength of 12 MPa than the original solid PLA filament (60MPa) but the electrical resistivity was improved from infinite to a range of 64 ± 25 to $1.4 \pm 0.48 \Omega\text{m}$ for 6 to 15 wt.% NC: PLA composition. A sample structure of $30 \times 5 \times 1 \text{ mm}^3$ was 3D printed and tested for mechanical strength and resistivity and found

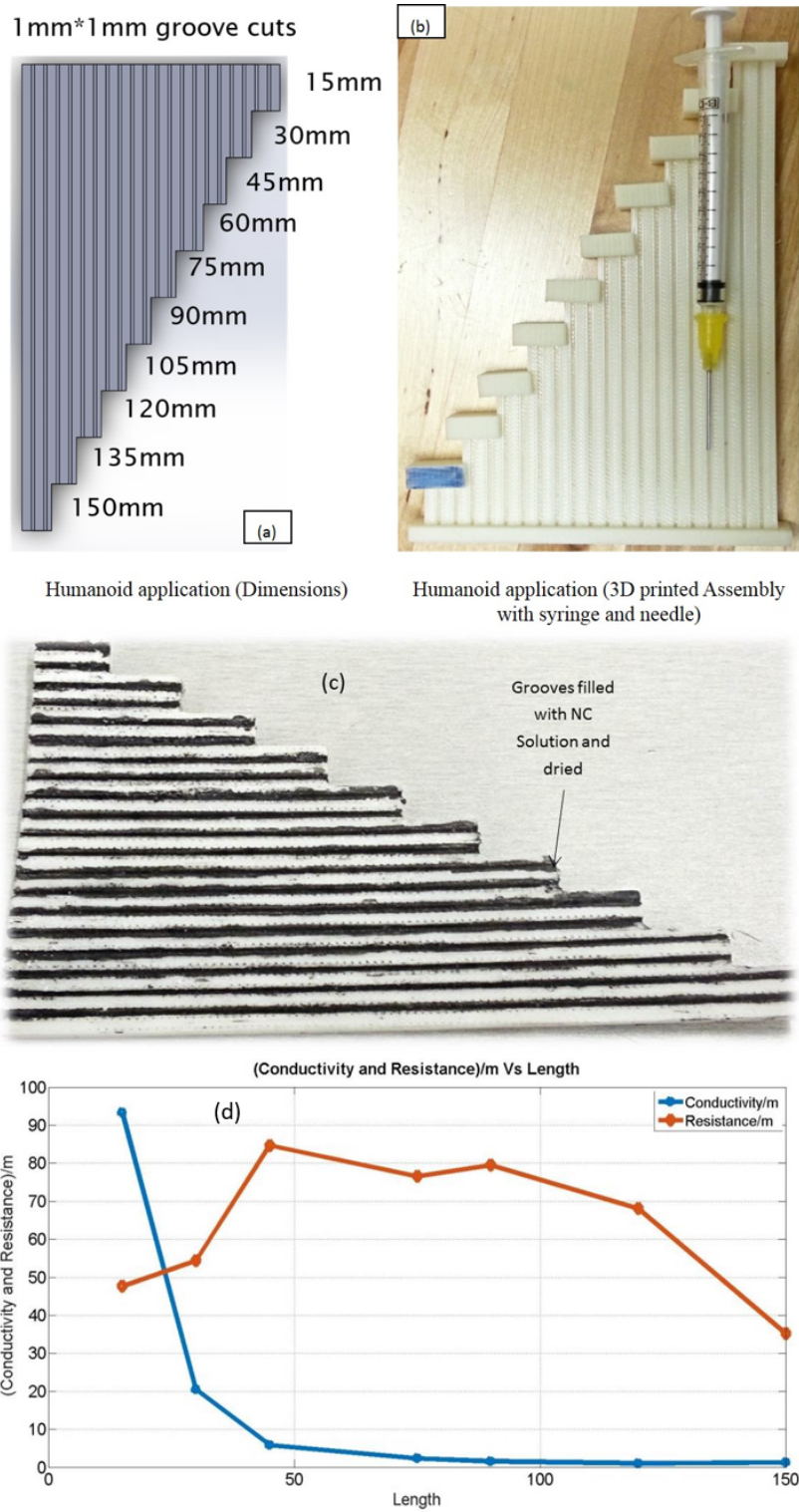


Figure 3.16. (a) Humanoid application dimensions , (b) the 3D printed assembly with the syringe and needle used and (c) 3D printed assembly with the ink jet (hand) printed cast

to be 25 MPa and $20 \pm 10 \text{ } \Omega\text{m}$ respectively. SEM images showed a relatively large number of particles distributed across the filament for a higher concentration of NC. The method can be used to build the robot structures with electrical circuitry except at the joints. The connection at joints can be made by a jumper that maintains continuous contact as discussed in the chapter. This approach reduces the problem of dangling and detachment of wires often encountered in many robotic systems. This work is easy to implement with any 3D printed structures that need electronic circuitry in an economical way using the most commercialized FDM 3D printers. Future of this project is the implementation of the technique presented in robotics and other complex wiring applications.

CHAPTER 4

FABRICATION AND CHARACTERIZATION OF COILED SHAPE MEMORY ALLOY (CSMA) ACTUATORS FOR SOFT ROBOTS

Soft robots need actuators with low profile, lightweight, high strain and relatively high frequency. Coiled shape memory alloy (CSMA) actuators satisfy these requirements, as SMAs are high-energy density actuators. There are a number of variables, which affect the performance of the CSMA actuators. This section presents the characterization of coiled SMA actuators mainly focusing on the spring geometry (spring diameter and number of coils per unit length). The manufacturing technique used in this section gives an added advantage for large strains. Relatively high frequency is an important requirement for soft robots, which can be achieved using liquid cooling under embedded conditions. In this section, we present a novel 2 step hot-cold water cooling to increase the frequency and performance of coiled SMAs in an artificial musculoskeletal (MS) joint and showed 24 ° rotation at a frequency of 0.125 Hz. We show CSMA that have 80% strain with respect to loaded length and > 1000% with respect to original length, when actuated with an input voltage of 4.2 V and 1.32 A with a frequency of 0.25 Hz, which can be used in many soft robots .

4.1 Introduction

Shape changing properties of materials is actively being researched for applications like artificial muscles, which mimic human muscle structure. These materials can be classified into shape memory alloys (SMAs), shape memory polymers (SMPs), dielectric elastomer actuators (DEAs), and ionic polymer metal composites (IPMCs) [121]. SMA actuators are known for their low mass, low volume, and large-stroke actuation. SMAs are metals which exhibit thermal and stress-induced shape recovery abilities from solid-state diffusion-less phase transformations [106]. At low temperatures, SMAs take a stable, face-centered

tetragonal lattice martensite phase and after heating above the transformation temperature, the material transforms to a high-temperature, body-centered cubic lattice austenite phase [75]. This transformation initiates a recoverable change in shape keeping external stress constant which can be used in the desired memory shape by annealing the material at high temperature [106]. The transformation temperature is specified by the composition of nickel and titanium used in the preparation of the material and the annealing condition. In this work, we present coiled SMAs performance and extensive characteristics by varying parameters like different diameters and a number of coils per unit length under different loads for constant current/voltage, SMA wire diameter and SMA wire length and discuss how the number of coils per unit length and spring diameters influence the SMA spring actuators.

Coiled SMAs have been implemented in several applications for soft robots and other fields due to their highest energy density, relatively high-frequency actuation, lightweight and low volume. Few examples of soft robots developed using CSMA are shown in figure 4.1. Several people have shown significant work, Paik and Wood [147] presented a low-profile bidirectional folding actuator based on annealed shape memory alloy NiTi sheets applicable for meso- and micro-scale systems that produce two opposing 180 ° motions. Song *et al.* [190] have shown a relatively high frequency of 35 Hz shape memory alloy actuator with bending-twisting mode at an applied current of 2.8 A for all SMA wires with the square wave input for a combination of multiple SMA wires, a soft polymeric matrix and an ABS layered reinforcement structure. The actuation speed of their actuator corresponds to its natural frequency and the resonant amplification of the actuator increases the amplitude of actuation of the actuator. Payload weights ranging from 0.3 g to 3.0 g were used where the resonance frequency of 10 Hz was obtained experimentally. The frequency reduces as the payload increases and the 35 Hz frequency they obtained is at 0.3 g which is low for practical applications. Their actuator is a complex network of SMAs which occupy more

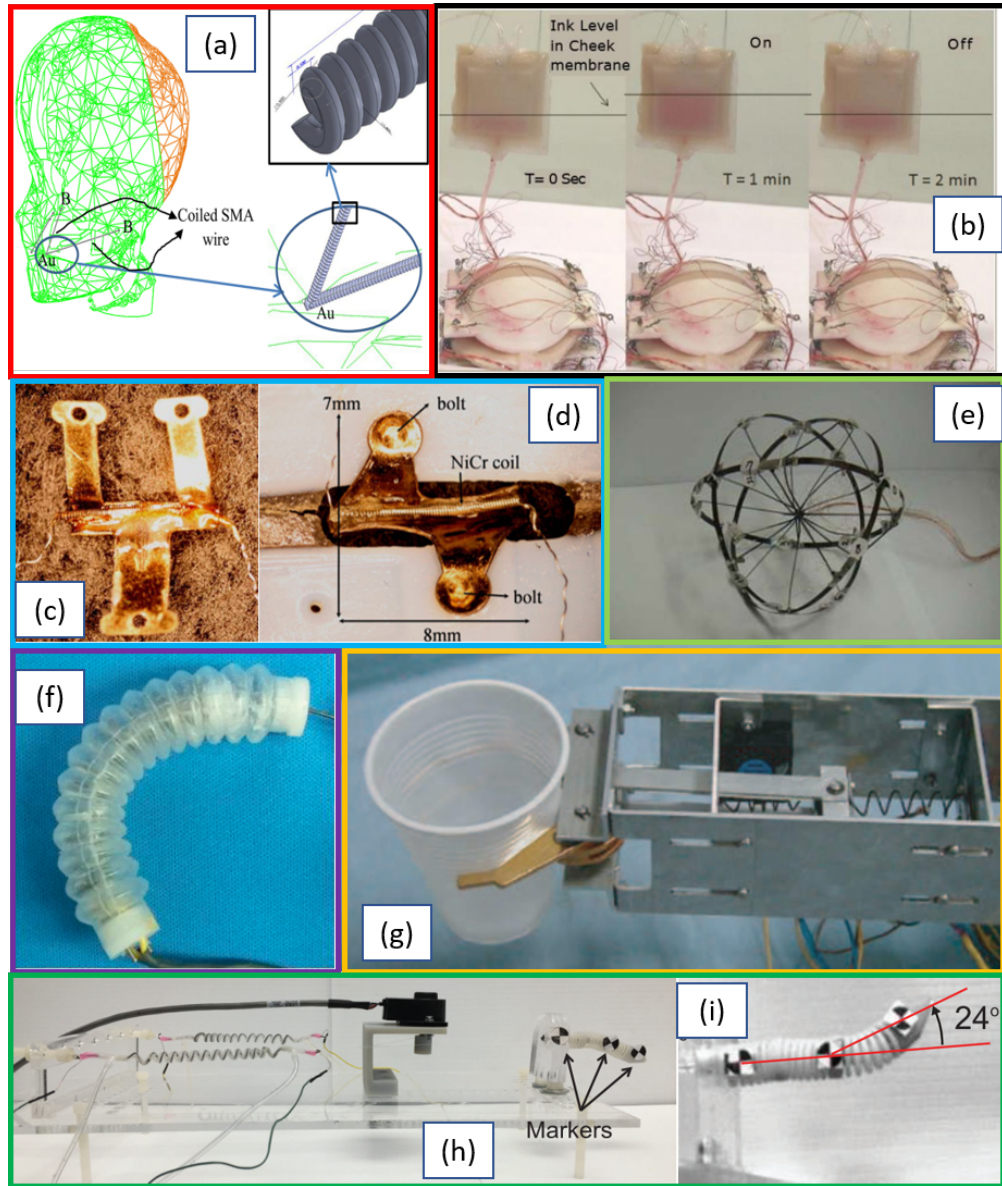


Figure 4.1. Coiled SMA actuator based applications: (a) Coiled SMA proposed for humanoid faces. [199]; (b) artificial heart for humanoid robot using coiled SMA actuators with sequential actuation of the robotic heart [161, 158]; SMA torsional actuators with Ni-Cr heating coil (c) Y-type and (d) Z-type bolted down front view [146]; (e) Spherical prototype for crawling and jumping [195]; (f) the bending of the Type B actuator [211]; (g) a gripper prototype holding an object [238] and (h) Side View of SMA springs in antagonistic configuration for actuating single robot joint [33], (i) The end segment of MINIR-II robot moves back and forth under active cooling of SMA actuators. [33]

volume than CSMAAs present in this section. Paik *et al.* [146] presented a fabrication process and experimental results of flat sheet torsional SMA actuators with high torque density, low profile, and improved response rates. Sugiyama *et al.* [195] proposed a deformable robot capable of crawling and jumping. They showed a circular prototype that moves about 65% of its diameter per second, climbs up a slope of 20°, and jump twice its diameter. Taniguchi [211] has shown a flexible artificial muscle actuator using coiled shape memory alloy wires where a guide case of the actuator is fabricated from silicone rubber which can bend up to 90°, but the displacement and force were both decreasing gradually with the increase in the bending angle.

Several works were published in coiled SMA and in this section, we present few relevant ones in table 4.1. Holschuh and Newman [75] have shown how low spring index (a ratio of coil diameter to wire diameter) influences the coiled SMA behavior for a wire diameter of 0.305 mm with spring diameter of 1.575 per mm. They have fabricated their SMA springs by motor coiling on a stainless steel core at room temperature, annealing it at 450° C and water quenching. They have shown that low spring index SMA actuators show large active forces as high as 99.56N using the largest commercially available SMA wire of wire diameter of 510 μm . Maximum strain was observed to be 173% with respect to original length L_0 of the CSMA with a force of 8.94N when actuated at 8 V at a frequency of 0.0083 Hz. The material they used was Ni (55-56%) Ti (44-45%) from Dynalloy inc [49] with critical actuation temperature of 70 °C. Santhanam *et al.* [175] worked on a SMA spring of wire diameter 0.78 mm and spring diameter of 6.4 mm with 19 coils to show that isothermal force-displacement experiment (IFDE) where force increases with increase in temperature and residual displacement decrease with the increase in temperature, in shape recovery force experiment (SRFE), they showed that shape recovery force increases with the increase in the initial deflection for the same temperature range. The stiffness of the spring, at austenite state was around 2.61 times the stiffness of the spring at martensitic state. The deduced

Table 4.1. Fabrication of CSMAs and characterization by various authors.

Reference	Wire Diameter	spring diameter	Di- number of Coils per unit length	Fabrication	Bias Mass	Power Settings	Max strain	Max Force at max strain	Critical activation temperature	Frequency	Material	Weight
Holschuh and Newman [75], 2014	0.305 mm	1.575 mm	N.A.	Motor coiling on to stainless steel core at room temperature and annealing it to 450°C and water quenching.	N.A	8V	173% (with respect to Lo)	8.94 N	70°C	1/120 = 0.0083 Hz (deduced)	N (55-56%) Ti(44-45%) [49]	N.A
Santhanam et al. [175], 2013	0.78 mm	6.4 mm	19 (Overall)	Commercially available NI-TI SMA springs	N.A	N.A	50*100 /382 = 13.1% (deduced with respect to initial length of the SMA wire)	14N	90°C	N.A	Ti-55.84 wt% Ni	N.A
Czarnocki et al. [37], 2013	0.2, 0.25, 0.3, 0.381 mm	1.19, 2.667, 4.75 mm	3.28 per mm (16 per 0.192 in)	motor coiled the wire on a mandrel and annealed at 500°C and quickly quenched in cold water	N.A	N.A	N.A	1.3N	70°C	N.A	N (55-56%) Ti(44-45%) [49]	12 mg; 12 mg; 42.4 mg; 75.4 mg; 26.9 mg; 61.1 mg ; 108.5 mg ; 43.4 mg; 98.5 mg; 507.4 mg(calculated)
An et al. [13], 2012	0.381 mm; 0.203 mm	2.36, 2.88 and 3.88 mm; 1.18, 1.68 and 2.16 mm	10 (Overall) and pitch angle 0°	annealed at 400 °C for 1 hr.	N.A	N.A	1 - 6% with respect to L_L	1.1N	70°C	N.A	N (55-56%) Ti(44-45%) [49]	54.4 mg, 66.2 mg, 89 mg ; 5.2 mg, 7.7 mg, 10.4 mg (calculated)

Table 4.1 continued

Reference	Wire Diameter	Spring Diameter	number of Coils per unit length	Fabrication	Bias Mass	Power Settings	Max strain	Max Force at max strain	Critical activation temperature	Frequency	Material	Weight
Bergamasco <i>et al.</i> [23], 1989	0.5 mm	1.5 mm	14	Commercially available Ni-Ti SMA springs [83]	N.A	N.A	100% with respect to L_0 (deduced 7mm /7mm)	5 N	N.A	1-2 Hz (submerged water cooling)	N.A	80 mg
Stebner <i>et al.</i> [194], 2009	0.5; 1; 1.5 mm	6.4, 12.7; 9.5, 12.7; 12.7, 19 mm	Different number of coils for all	coiled the wire on a screw thread with different threads and annealed at 515°C with a ramp rate of 10°C C/min for 1 hr and air cooled to room temperature.	N.A	N.A	4.52% with respect to L_L	2.36 N	100-300 °C (243 °C)	1/100 = 0.01 (deduced)	Ni19.5 Ti50.5 Pd25 Pt5 [49]	290.7 mg (calculated for geometry 1)
Yates and Kalamkarov [239], 2013	0.145, 0.192, 0.248, 0.375 mm	2.38, 3.175, 4.76, 6.35 mm	8, 12, 16, 20	500 °C Annealing temperate for 10 mins	20, 30, 40, 50 g	0.45, 0.5, 0.55, 0.6 A	20.7 % (relatively high frequency) ; 49.53% (high strain) with respect to L_L (deduced)	0.294N	70, 90 °C	0.1667 Hz (relatively high frequency); 0.05 Hz (high strain) (deduced)	N (55-56%) Ti(44-45%) [49]	16.9 mg - 101 mg (Calculated)
This section, 2018	0.2 mm	3.18 mm, 3.96 mm, 4.75 mm	1.26 per mm (32 TPI)(Threads per inch)), 1.406 per mm (36 TPI), 1.575 per mm (40 TPI)	motor coiled the wire on a screw thread with different threads and annealed at 350°C for 45 mins and air cooled to room temperature.	2 - 40 g (increments of 2)	0.66A; 4.2V	80% with respect to L_L ; 1166% with respect to L_0 , table 4.6 & 4.7	0.186 N, table 4.5	90°C	0.25 Hz (for all)	N (55-56%) Ti(44-45%) [49]	24mg

maximum strain is 13.1 % with respect to the initial length of the SMA wire with a force of 14 N. They used commercially available Ti-55.84 wt% Ni with a 90 °C critical actuation temperature. Czarnocki *et al.* [37] presented a parameter to study for different wire diameters of 0.2, 0.25, 0.3, 0.381 mm with spring coil diameters of 1.19, 2.667 and 4.75 mm, similar to the work presented in this section. They have shown that there is a strain increase with an increase in coil diameter and a decrease in force. They have used motor to coil the wire on a mandrel and annealed at 500° C and quickly quenched in cold water to fabricate the springs. They have shown actual strain of > 400% at 1.3N loads. Their actuators weight varies from 12 mg to 507.4 mg made from Ni (55-56%) Ti (44-45%) from Dynalloy inc [49] with critical actuation temperature of 70 °C. An *et al.* [13] have presented an engineering design framework to select parameters like the wire diameter, the rod diameter, the pitch angle and the number of active coils on the basis of the desired force and stroke. They have used two sets of wire diameter to spring diameter variations, (first with 0.381 mm wire diameter to 2.36, 2.88 and 3.88 mm spring diameters and 0.203 mm wire diameter to 0.8, 1.18, 1.68 and 2.16 mm spring diameters) with 10 coils and pitch angle 0°. They have shown a maximum shear strain of 6% and fabricated using annealing at 400° C for 1 hr. They have shown strains of 1% with respect to L_L at 1.1N. They used commercially available Ni (55-56%) Ti (44-45%) from Dynalloy inc [49] with a 70 °C critical actuation temperature.

Regarding frequency of actuation of SMAs, many studies are available. This work involves the study of actuation frequency with 2-step hot-cold water cooling during the cooling cycle which increases the actuation frequency. Cooling techniques like forced water cooling similar to this work for cylindrical SMAs were presented by Tadesse *et al.*[205]. Cheng *et al.* [33] showed how water cooling can increase the actuation frequency by threading a silicone tube through the spring coils. They used a SMA spring with a wire diameter of 0.75 mm, spring diameter of 8.5 mm and a number of coils of 13. Yan *et al.* [238] presented a gripper actuated by a pair of differential SMA springs of the wire diameter of 1 mm. They have shown some

preliminary results of increasing the actuation frequency by forced air cooling using a fan. In this work, we will focus on cooling only during the cooling cycle. Lee *et al.* [110] have shown how the forced air cooling using a fan can increase the actuation frequency and predicted the actuation cycle using a combination of SMA modeling and neural network. They have used a SMA wire of 0.38 mm and inside spring diameter of 2 mm with 11.5 turns. Cooling of coiled SMAs for robotic finger applications was shown in the late 1980's by Bergamasco *et al.* [23] where they kept the coiled SMAs in an aluminum container with an inlet and outlet for cold water for cooling. They have submerged the coiled SMAs in a heating cycle which inhibits their frequency and increase power consumption; they showed 1-2 Hz frequency of a robotic finger under submerged coiled SMA push-pull actuation. They have used a 0.5 mm diameter NiTi wire to make a 1.5 mm diameter coiled spring with the length of 7 mm and 14 rings. They have used commercially available CSMA from Innovative Technology International, Inc. [83] which weigh 80 mg. They have got 100% best strain with the original length of the CSMA at 5 N load with a 1-2 Hz relatively high frequency.

Stebner *et al.* [194] have shown the characterization of $Ni_{19.5}Ti_{50.5}Pd_{25}Pt_5$ helical actuators mechanical responses with respect to changes in geometrical parameters and training loads. They have used different screw thread profiles to produce the helical springs similar to the work presented in this section like 0.5 mm wire with spring diameters of 6.4 and 12.7 mm; 1 mm wire with spring diameters 9.5 and 12.7 mm and 1.5 mm wire with spring diameters of 12.7 and 19 mm with a different number of rings. They have coiled the wire on a screw thread with different threads and annealed at 515°C with a ramp rate of 10°C/min for 1 hr and air cooled to room temperature. They have not used constant wire length for all actuators or comparable spring diameter at a constant wire diameter as we present in this section and is difficult to compare with their work. Hence, they have normalized the results with a factor to compare between different geometry.

Yates and Kalamkarov [239] have investigated six variables of CSMA: wire diameter, spring diameter, bias force, number of active spring turns, direct current magnitude and

transition temperature. The results show that 4 out of 6 parameters affect heating cycle and a different set of 4 of the 6 affect the cooling cycle. All the 6 affect the stroke or strain of CSMA's. They have done a detailed investigation for CSMA's fabricated at an annealing temperature of 500 °C for 10 mins. The different wire diameters investigated were 0.145 mm, 0.192 mm, 0.248 mm and 0.375 mm; whereas the different spring diameters used were 2.38, 3.175, 4.76 and 6.35 mm and the different number of coils used were 8, 12, 16 and 20 respectively. The different bias loads were 20, 30, 40 and 50 g and the different input current values are 0.45, 0.5, 0.55, 0.6 A. The material used was from Dynalloy Inc. [49] with two critical activation temperatures between 70 and 90 °C. The maximum observed strain is 49.53% with loaded length at a frequency of 0.05 Hz and at the highest frequency of 0.17 Hz they showed a strain of 20.7 % with respect to loaded length. The strains and frequencies are lower than the work presented in this section.

A few other SMA modeling works include Frost *et al.* modeling of the mechanical response of NiTi SMA subjected to combined thermal and non-proportional mechanical loading on a case study of a helical spring loaded by a constant force and to a large variation of temperature [57]. Their model was particularly suitable for predictions of the material response to a multi-axial non-proportional mechanical and thermal loading. Kolyvas and Tzes [98] have designed and operated antagonistic SMA springs and examined for the cases of two and three actuators based on the phenomenological model. They linked the model to the elementary elastoplastic operator to produce a model with identifiable geometric features, in the force-deformation domain. Sousa *et al.* worked on a 2-DOF typical aeroelastic section with shape memory alloy (SMA) springs and modeled the mechanism of elastic restoring moment. The moment was considered (along with a linear unsteady aerodynamic model) and investigated the effects of pseudoelastic hysteresis on the aeroelastic behavior of the typical section, with the assumption of different sets of SMA properties [191]. Enemark *et al.* have shown through the justification of modeling , it is possible to use a single point (the star point) in the wire

cross section to represent the global behavior of the spring, despite strong material nonlinearities and complex stress-strain fields in the cross section of pseudoelastic shape memory alloy helical springs [52]. Huang *et al.* proposed a phenomenological model for simulating the superelasticity or pseudoelasticity of Nitinol SMA helical springs. The phenomenological model is based on force-displacement relationship consisting of a linear function as well as an exponential function, and the motion rules of the springs on loading and unloading are defined based on the results of the major loop and minor loop experiments. Spinella and Dragoni [192] have studied the mechanical, thermal, and electric performances of SMA helical springs with hollow round section by providing analysis equations. They presented a step-by-step design procedure leading to optimal hollow springs with minimum energy consumption. Yang and Gu [239] presented a new structure of compact flexible actuator based on shape memory alloy (SMA) springs where three SMA springs are trained to shrink as the phase transition occurs, which are embedded off-axially and movable in a silicone rubber rod solidified at room temperature. They showed that spatial bending through heating SMA springs by suitable current, could restore flexibly as soon as heating is stopped. Ho *et al.* [74] presented a new design of Minimally Invasive Neurosurgical Intracranial Robot (MINIR) actuated by SMA spring actuators and the tendon-sheath mechanism. The prototype has larger range of motion, larger output force, and has better compatibility with MRI.

Investigating CSMAAs at different manufacturing techniques and other parameters is important research in order to optimize the properties of CSMAAs for the required application. We have listed a few observed parameters, which play a role in the properties of the CSMAAs in material type, manufacturing, geometry and operational conditions, which is shown in table 4.2. The combinations of these variables just show the complication for finding the optimized parameters for strain and frequency.

Table 4.2. Observed parameters which influence the performance of CSMAs

Material	Manufacturing	Geometry	Operational
Composition	Annealing temperature, Θ_a	length of the SMA wire, l	Current
Critical actuation temperature	Annealing time, t_a	length of the SMA spring, L	Voltage
Resistance	Cooling technique after annealing	diameter of the wire	Frequency
Thermal conductivity, k	Tension in spring shape during annealing	diameter of the spring	Duty Cycle
Other material constants	Material of the spring shaft	spring shape angle, spring index and pitch	Cooling technique and Bias mass

4.2 Shape Memory Effect

Shape memory alloy materials exhibit shape memory and superelastic effects. These effects are associated with stress, strain and temperature state of the material. At low temperature, the shape memory effect is observed whereas, at high temperature, the superelastic curve will be observed. The shape memory effect (SME) is a result of temperature and stress dependent shift in the materials crystalline structure between the martensite and austenite phases, which can be understood from figure 4.2. The unique change in phase between the two crystalline structures enables the material to change its shape, and the material is used as an actuator or artificial muscle for numerous applications. It can operate in either the air or fluidic medium. The low-temperature phase, martensite is a soft structure and, on the other hand, the high temperature phase, austenite is hard structure [124]. At high temperature, the material changes to austenite phase, and when it cools down, it will transform to martensite. The shape memory effect (SME) is the recovery of large strain due to the application of thermal cycling (heating and cooling) [161, 157]. In figure 4.2, we see the 3D diagram of stress-strain-temperature relation of SMA phase transformation in both super elastic and shape memory effect.

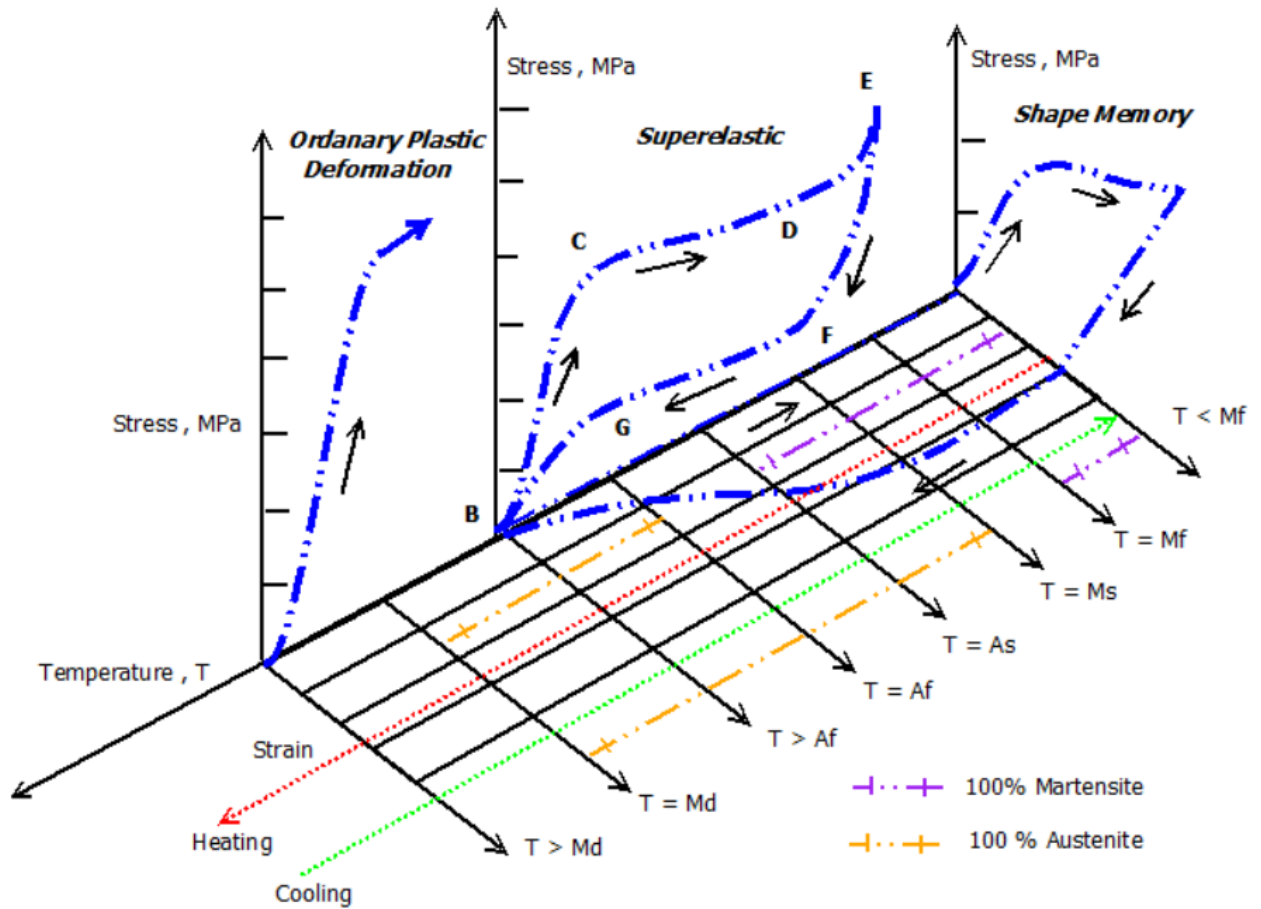


Figure 4.2. 3D stress-strain-temperature diagram of SMA phase transformation (Super elastic and Shape memory effect [11])

4.3 Influence of Annealing Temperature on CSMA's

The annealing temperature used in this work $350\text{ }^{\circ}\text{C}$ (623K) plays a significant role in the performance of the CSMA's. Several researchers worked on the effect of SMAs with respect to annealing temperatures. The most prominent is the work done by Huang and Liu [79], who have extensively studied the role of annealing temperatures on the transformation behavior and superelasticity of NiTi SMAs. They have studied annealing temperatures from 300 to $600\text{ }^{\circ}\text{C}$ on SMAs with 50°C increments and compared the influence of these temperatures on Differential Scanning Calorimetry (DSC) thermal and stress-strain curves. They have observed some interesting phenomenon at $350\text{ }^{\circ}\text{C}$ (623K). At that annealing temperature,

they have observed the highest intermediate phase transformation, Rs and Rf (R-phase). R-phase is an intermediate phase between martensite and austenite (rhombohedral crystal structure). They also observed that at the same conditions the material shows increments in Ms and Mf values as the annealing temperature increases. They also observed that under the same parameters the material also showed the highest transformation temperature values for Austenite Finish (Af), R-phase transformation start (Rs) and finish (Rf). Similar effect of an increase of the R-phase transformation temperatures (RTT) and Rp with increase in annealing temperatures below 350°C (623K) is also observed by Wang *et al.* [225] and Matsumoto [123]. The results presented in this work and the work done by Huang and Liu [79] and Wang *et al.* [225] show that annealing temperature affects the phase transformation temperature and hence, the properties of NiTi CSMA and its micro structure.

In this section, we first show the effect of spring geometry on the performance of CSMA and then present the effect of 2-step hot-cold water cooling on the frequency and performance of coiled SMAs in an artificial musculoskeletal joint that showed actuation at a 0.125 Hz with 22.5° angle. The artificial musculoskeletal joint presented in this section is from the biologically inspired muscle joint presented by Tadesse *et. al* [206, 231]. They have used recently introduced twisted and coiled polymer (TCP) muscles and a novel design of an artificial musculoskeletal system based on ball and socket joint, as well as their application in a 3-D printed humanoid robot. We have shown higher frequency in this section with coiled SMAs with 2-step hot - cold water cooling. Artificial musculoskeletal joints like structures were presented for a robotic endoscope as back as the mid-1980's [59] with coiled SMAs, but detailed investigation of frequency and performance with coiled SMAs and other actuators were not studied until recently.

In table 4.3, we compare our custom made CSMA actuator with commercially available CSMA from Dynalloy Inc. [49] and Toki Corporation [213] BMX150, which have similar

Table 4.3. Comparison to commercially available Coiled SMAs

	This work	Dynalloy Inc. (Spring) [49]	BMX150 (Toki Corporation) [213]
Spring Wire Diameter (mm)	0.203	0.203	0.15
Outer Diameter (mm)	1.6; 3.18, 3.96, 4.75	1.37	0.62
Strain with respect to Lo, ϵ_o (%)	1170; 850-1050, 960-1490, 1170-1400	900 (deduced)	200
Load at strain (g)	4.5; 25	16-40	20-40
Pitch (turns per mm)	3.15; 1.25-1.575	N.A.	N.A.
Current (A)	0.66	0.7	0.2-0.3
Cooling time (sec)	3 ; 2	3	N.A.
Service life (times)	N.A.	N.A.	10 ⁶
Electrical Resistance (Ω/m)	29	29.1	400
Voltage , V/m (deduced)	19.3	20.4	80-120
Power , W/m (deduced)	12.85	14.28	16-36
Transformation temperature [°C]	90	90	90
Frequency (Hz)	0.25	N.A.	N.A.

wire diameter. We can see that we have achieved strains with respect to original length ϵ_o maximum $> 1000\%$ at certain conditions, which is higher than any other commercially available CSMAs. Though we have purchased our precursor material from Dynalloy Inc. [49] our CSMAs has the lowest power consumption than all of them. It has the lowest cooling time, which makes it the highest frequency actuator among them, operating at 0.25 Hz. It is to be noted that the material composition is the same as Dynalloy Inc. [49] as we purchased the wire from them.

4.4 Experimental Setup for Actuation

4.4.1 Fabrication

SMA wire of 0.2 mm diameter is purchased from Dynalloy Inc.[49] and is coiled using a similar technique as used from our previous publication [158], where a low-cost bobbin winder is converted to SMA wire coiler with some mechanical and electrical modifications. Three different number of coils per unit length of 1.26 per mm (32 TPI), 1.406 per mm (36 TPI), and 1.575 per mm (40 TPI), per mm and three different diameters of 3.18, 3.96 and 4.75 mm were used to make a total of 9 samples. Table 4.4 shows the original spring length for different diameters and number of coils per unit length. The 9 samples are kept inside a furnace for 350 °C for 45 mins and air cooled to room temperature. The more the annealing temperature, the stiffer the actuators becomes, resulting in high load carrying capacity and low strain and

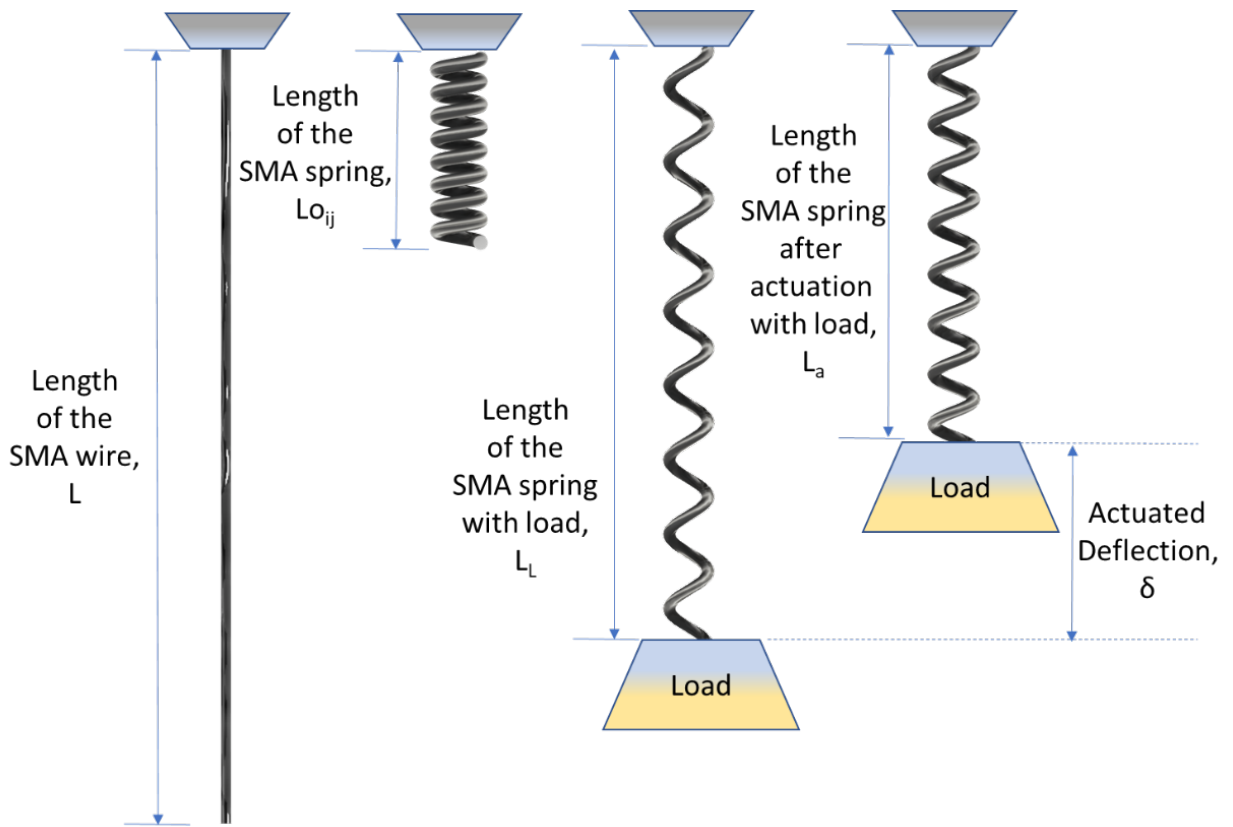


Figure 4.3. Fabrication (coiling and annealing) and testing of the SMA spring actuator. After motor coiling, all the 9 samples are kept inside a furnace for 350 °C for 45 mins and air cooled to room temperature. (Strain with respect to loaded length $\varepsilon_L = \delta/L_L$; Strain with respect to original length $\varepsilon_O = \delta/L_O$, where $\delta = L_L - L_a$)

vice versa. The most common temperatures of annealing in CSMA range from 400 °C to 550 °C for 10 to 30 minutes [37]. We have picked a lower annealing temperature to get higher strains but at the cost of load carrying capacity, as our application is soft robotics, which requires large actuation strain. For high load application, multiple actuators can be used as CSMA have low profile. The fabrication and testing of the SMA spring actuator is shown in figure 4.3.

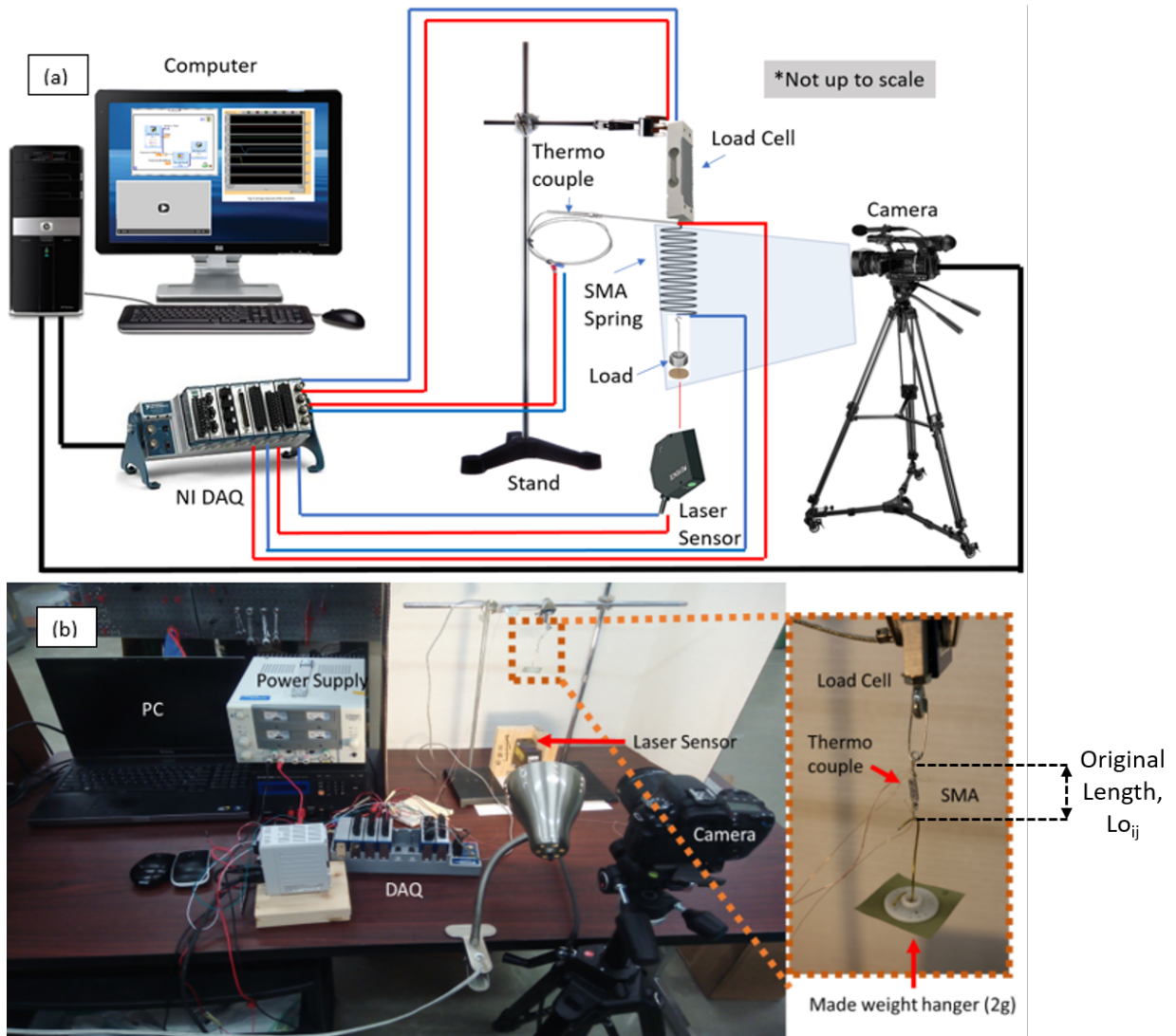


Figure 4.4. Experimental Setup used to characterize the coiled SMAs (a) Schematic and (b) Actual. The CSMA is connected to a load cell which is attached to a stand and a load weight is hanged. A thermocouple is attached on the top of the actuator to measure the temperature changes during actuation. A laser sensor is used to measure the displacement. All sensors are connected to the NI DAQ which is connected to computer with LabVIEW to measure the readings in real-time. A camera is used to record the actuation which is used for displacement measurement as a backup using Tracker software.

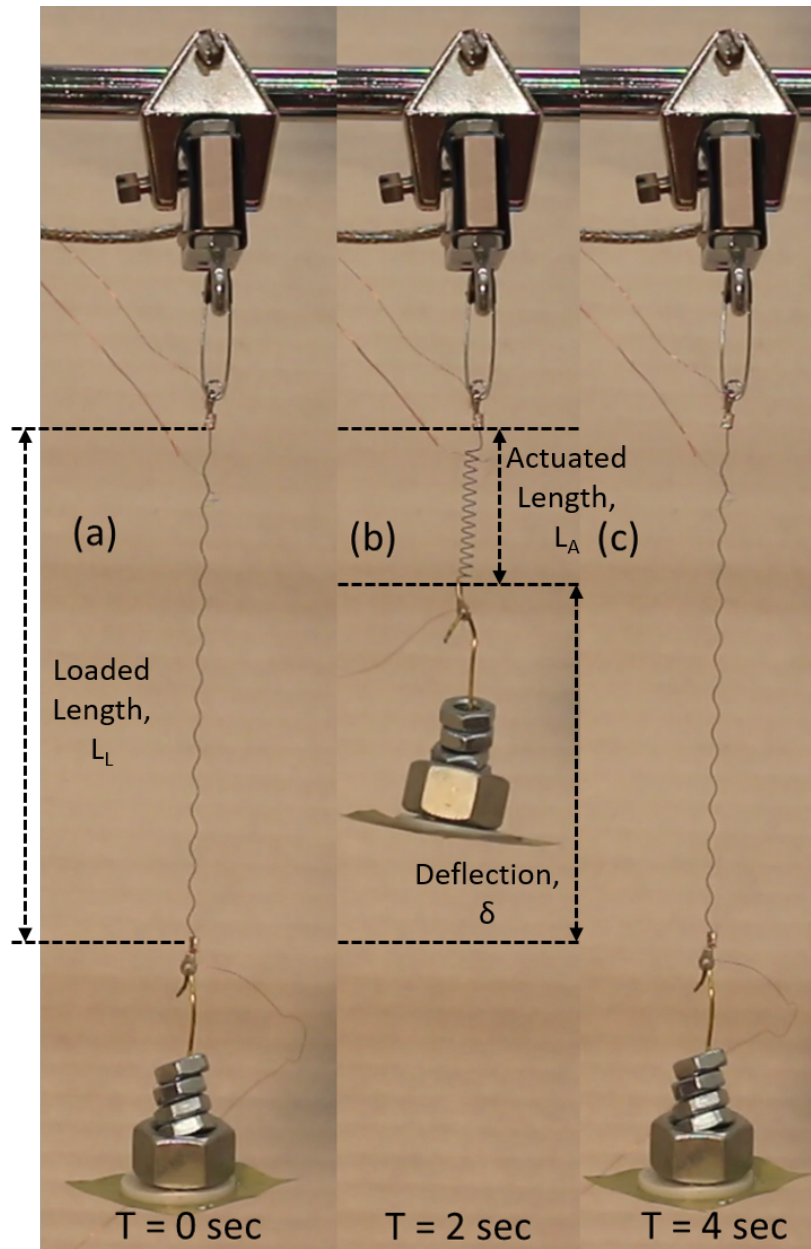


Figure 4.5. Actuation results for square input of 4.4 V with a frequency of 0.25 and duty of 50%. (a) at time = 0 sec, (b) at time = 2 sec and (c) at time = 4 sec showing 80% actuation. (Number of Coils, $N = 12$; length of actuator wire, $L_w = 120 * 10^{-3}$ m; length of the spring, $L_s = 10.06 * 10^{-3}$ m; Wire diameter, d_s or $d_w = 0.2 * 10^{-3}$ m [49]; spring diameter, $D_s = 3.175 * 10^{-3}$ m)

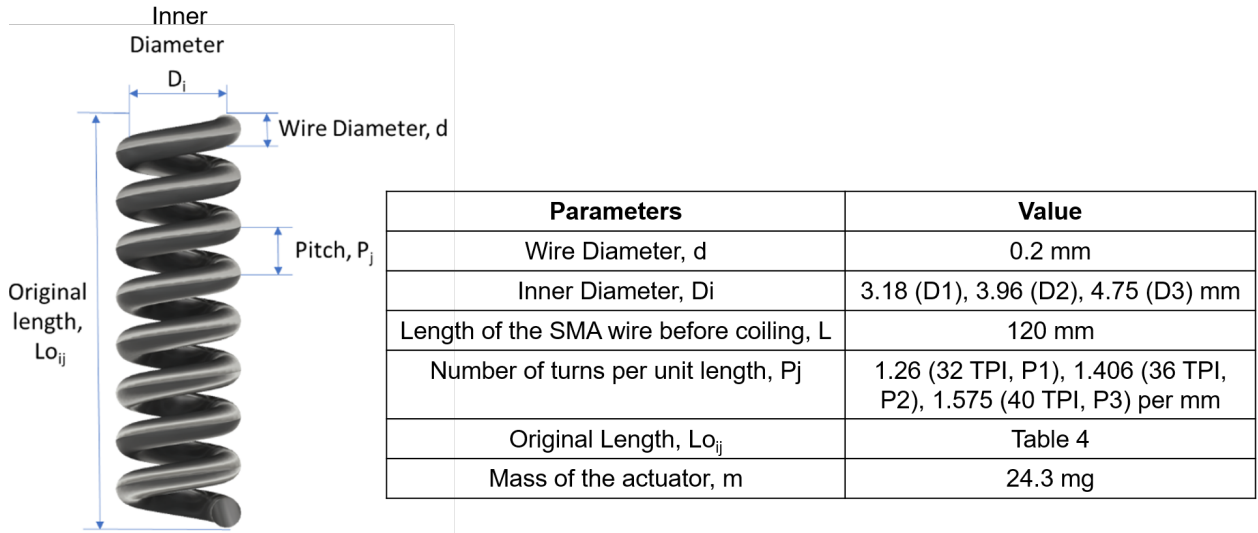


Figure 4.6. Parameters and values of the SMA springs used.

Table 4.4. Original spring length, $Lo_{i,j}$ for different diameters, Di and different no. of coils per unit length, Pj

	D1 = 3.18 mm	D2 = 3.96 mm	D3 = 4.75 mm
P1 = 1.26 per mm (32 TPI)	9.53 mm	7.65 mm	6.38 mm
P2 = 1.406 per mm (36 TPI)	8.54 mm	6.86 mm	5.72 mm
P3 = 1.575 per mm (40 TPI)	7.63 mm	6.12 mm	5.11 mm

Table 4.5. Load that provided maximum strain for different diameters, Di , and different no. of coils per unit length, Pj

	D1 = 3.18 mm	D2 = 3.96 mm	D3 = 4.75 mm
P1 = 1.26 per mm (32 TPI)	25 g (7.7 MPa)	20 g (6.16 MPa)	19 g (5.85 MPa)
P2 = 1.406 per mm (36 TPI)	25 g (7.7 MPa)	20 g (6.16 MPa)	19 g (5.85 MPa)
P3 = 1.575 per mm (40 TPI)	25 g (7.7 MPa)	20 g (6.16 MPa)	19 g (5.85 MPa)

4.5 Results and Discussion of Characterization of CSMAAs

4.5.1 Experimental Setup for the Testing Actuator

Precisely measured nuts were used as dead weights during a pulse actuation of 0.666 A current and a voltage magnitude of a 4.2 V using a power supply for 40 seconds actuation and with 20 seconds cooling time. Keyence LK-G152 laser displacement sensor and a digital



Figure 4.7. All 9 samples before actuation and after actuation.

Table 4.6. Maximum strain wrt. loaded length, $\varepsilon_L = \frac{\delta}{L_L}$ for different diameters, Di & different no. of coils per unit length, Pj

	D1 = 3.18 mm	D2 = 3.96 mm	D3 = 4.75 mm
P1 = 1.26 per mm (32 TPI)	75 %	70 %	80 %
P2 = 1.406 per mm (36 TPI)	76 %	71 %	73 %
P3 = 1.575 per mm (40 TPI)	76 %	70 %	66 %

Table 4.7. Maximum strain wrt. the original length, $\varepsilon_o = \frac{\delta}{L_{o_{ij}}}$ for different diameters, Di & different no. of coils per unit length, Pj

	D1 = 3.18 mm	D2 = 3.96 mm	D3 = 4.75 mm
P1 = 1.26 per mm (32 TPI)	842 %	962 %	1166 %
P2 = 1.406 per mm (36 TPI)	981 %	1001 %	1275 %
P3 = 1.575 per mm (40 TPI)	1047 %	1487 %	1405 %

camera at 60 frames per second combined was used to measure the displacement. A K type thermocouple was used to measure the temperature changes during the experiment, attached at the top of the actuator but due to the actuation, there was some slipping observed in the results. The laser displacement sensor, thermocouple, and load cell were read using a NI DAQ modules system using LabVIEW 2016 program and the results were plotted using Matlab 2017a.

This section covers the effect of spring geometry on CSMAAs, with respect to coil diameter and spring pitch. The results were smoothed exponentially using Microsoft Excel for cleaner graphs with a damping factor = 0.99 (smoothing constant alpha = 0.01) for displacement, temperature, and force and a damping factor = 0.49 (smoothing constant alpha = 0.51) for voltage and current. The length of the SMA is kept constant for all the samples at 120 mm. The current used 0.666 A is the recommended value by the manufacturer for optimized results. The static load is varied from 4 to 40 g in total of 10 readings done for each sample at 10 actuations for the fixed power settings. The voltage and current are recorded in the NI DAQ. The current is measured indirectly by connecting it through a resistor and measuring

the voltage in the NI DAQ. The weight of the SMA samples is constant 24.3 mg as the diameter and length are fixed for all samples as seen in figure 4.6.

Figure 4.4, shows the experimental setup where the coiled SMA is connected to an Omega Load cell of maximum 5-pound limit on the top and a static load is connected to the bottom end using a custom-made weight hanger which weighs around 2 g.

In figure 4.5, we see the time sequence actuation results of CSMA D3P1 with a square input voltage of 4.4 V with a frequency of 0.25 Hz and duty of 50% at time 0,2 and 4 seconds. In figure 4.7, all the 9 samples are shown before and after actuation as snapshots of time. Table 4.5, 4.6 and 4.7 show the static deflection at different loads, strain with respect to loaded length ε_L , strain with respect to original length ε_o corresponding to different loads. Figures 4.8, 4.9 and 4.10 show a comparison graph of static deflection at different loads, actuation strain with respect to loaded length and actuation strain with respect to original strain. The different CSMA geometries of 3 different diameters of 3.18 mm (D1), 3.96 mm (D2) and 4.75mm (D3) and different number of coils per unit length of 1.26 per mm (32 TPI) (P1), 1.406 per mm (36 TPI) (P2), and 1.575 per mm (40 TPI) (P3) mm respectively. Figure 4.8, shows the profile of loading the CSMA's, static deflection at different loads slightly varies but mostly remains constant (flatter) for all the diameters and pitches as the change is small between different diameters and pitches. When the load is increased from 15 g onwards, strain with respect to loaded length ε_L in figure 4.9 and strain with respect to original length, ε_o in figure 4.10, shows that the high strain falls towards lower loads when we increase the diameter or the pitch. In strain with respect to original length ε_o in figure 4.10, we see a better separation of strain between the parameters. The maximum strain with respect to loaded length ε_L almost remains constant with respect to number of turns per unit length and the change cannot be determined clearly with respect to diameter. It varies between 70-80%. The maximum strain with respect to original length ε_o increases mostly with an increment of number of coils per unit length and increases with respect to the increment in

diameter. Figure 4.11 shows a comparison graph of strain % with respect to loaded length ε_L , strain % with respect to original length ε_o and static deflection at different loads for SMA springs of 3 different diameters of 3.18 mm (D1), 3.96 mm (D2) and 4.75mm (D3) for 1.406 per mm (36 TPI) (P2) with original spring lengths of 8.54 mm Lo_{21} , 6.86 mm Lo_{22} and 5.72 mm Lo_{23} respectively. Increase in diameter of the spring produces more strain at lower loads of actuation as seen from the figure 4.11. Figure 4.12 shows a comparison graph of strain % with respect to loaded length ε_L , strain % with respect to original length ε_o and static deflection at different loads for SMA springs of 3 different number of coils per unit length as mentioned before with spring original lengths of 7.65 mm Lo_{12} , 6.86 mm Lo_{22} and 6.12 mm Lo_{13} respectively. Increase in pitch increases strain and the profile peaks move towards lower loads. Figure 4.13 shows a similar comparison graph of strain % with respect to loaded length ε_L , strain % with respect to original length ε_o and static deflection at different loads D1P3 SMA spring (number of coils per unit length 1.575 per mm (40 TPI) mm (P3) with spring original lengths of 7.63 mm Lo_{31} and spring diameter of 3.175 mm (D1)). This one out of nine samples graph helps to understand the strains and static deflections at different loads for increment of bias load. As we increase the bias load, strains first increase and then reduce and static deflections at different loads increases and remains flat. Figure 4.14 shows a time history graph of displacement at different load, voltage, current, temperature and force for D1P3 SMA spring (number of coils per unit length 1.575 per mm (40 TPI) mm (P3) with spring original lengths of 7.63 mm Lo_{31} and spring diameter of 3.175 mm (D1)). All SMA springs are made with 120 mm long cylindrical SMA wire of radius 0.1 mm which has a weight of 24 mg. All the SMA springs are actuated at a constant current of 0.666 A (recommended by the manufacturer Dynalloy Inc.[49]) with a voltage of 4.2V approximately. The time domain in figure 4.14 shows how the displacement increases with load initially and reaches maximum and then reduces back. The bumps in temperature graph is mostly due to the slipping of the temperature sensor during actuation. Force mostly stays constant as

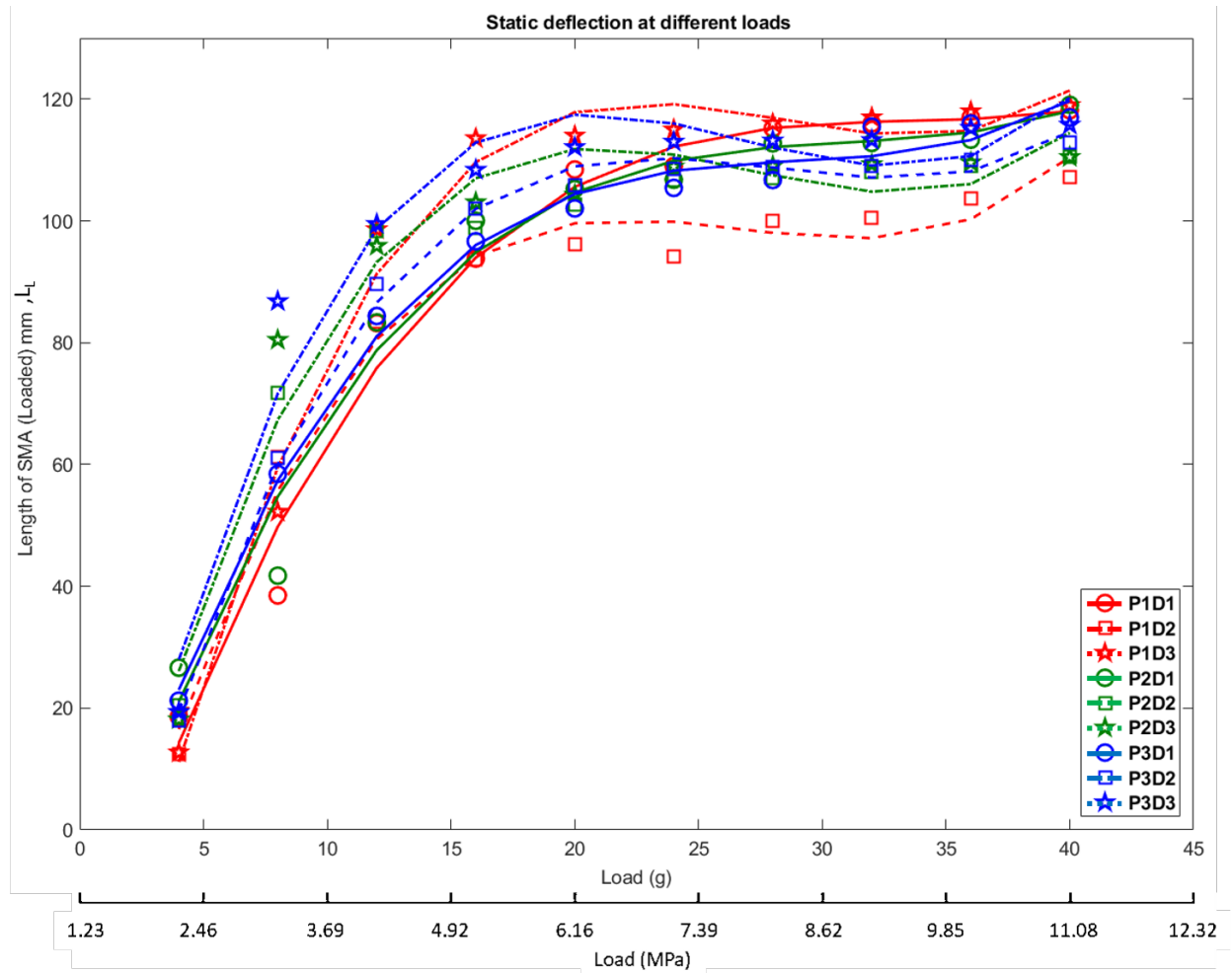


Figure 4.8. A comparison graph of static deflection at different loads for SMA springs of 3 different diameters of 3.18 mm (D1), 3.96 mm (D2) and 4.75 mm (D3) at a different number of coils per unit length of 1.26 per mm (32 TPI) (P1), 1.406 per mm (36 TPI) (P2), and 1.575 per mm (40 TPI) (P3) respectively. All SMA springs are made with 120 mm long cylindrical SMA wire of radius 0.1 mm, which has a weight of 24 mg. The lines represent polynomial fits of the data points.

the change during actuation is not significant. Both current and voltage have sharp peaks,

initially and then become more steady to a constant value.

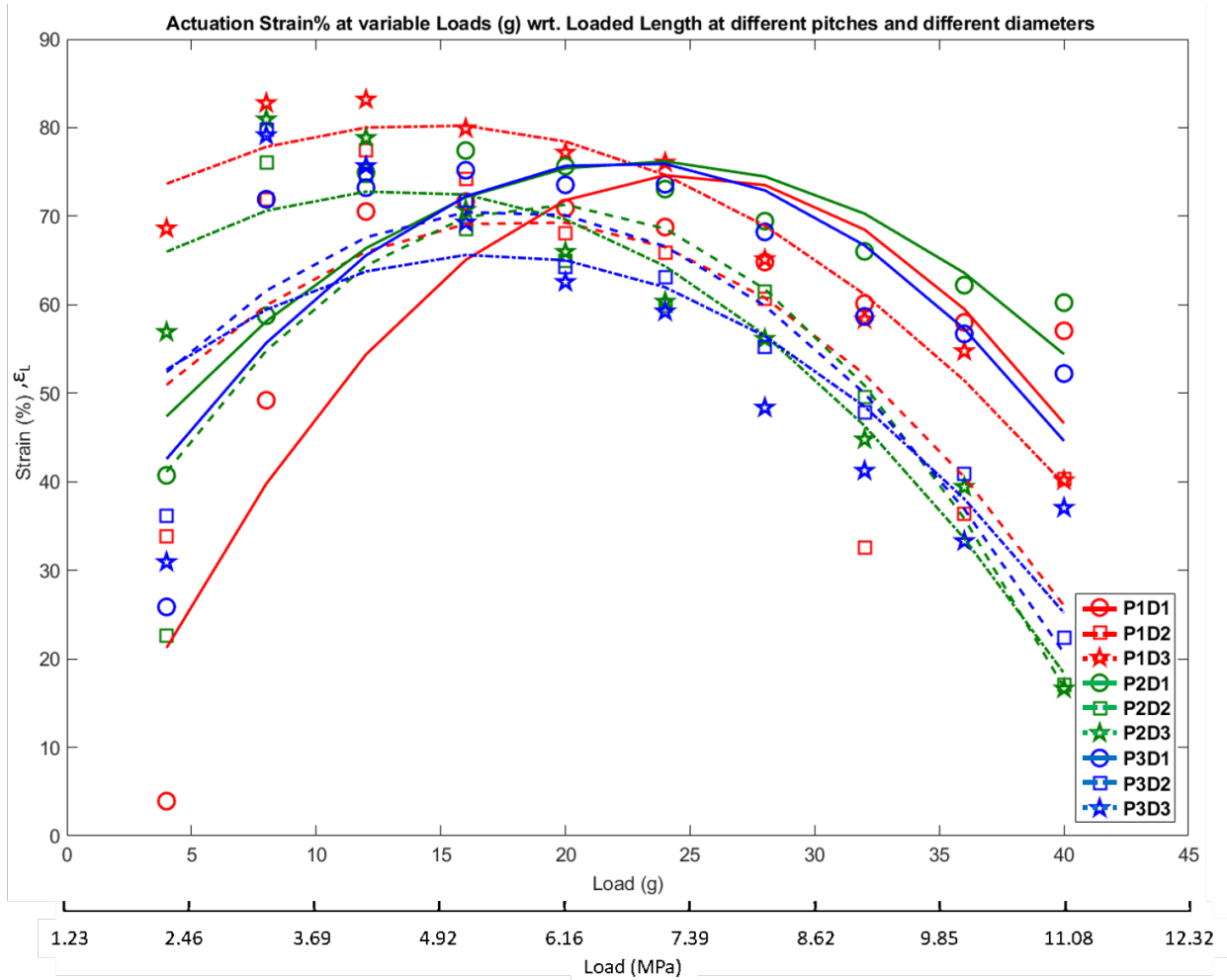


Figure 4.9. A comparison graph of actuation strain % with respect to loaded length ϵ_L for SMA springs of 3 different diameters of 3.18 mm (D1), 3.96 mm (D2) and 4.75 mm (D3) at a different number of coils per unit length of 1.26 per mm (32 TPI) (P1), 1.406 per mm (36 TPI) (P2), and 1.575 per mm (40 TPI) (P3) respectively. The lines represent polynomial fits of the data points.

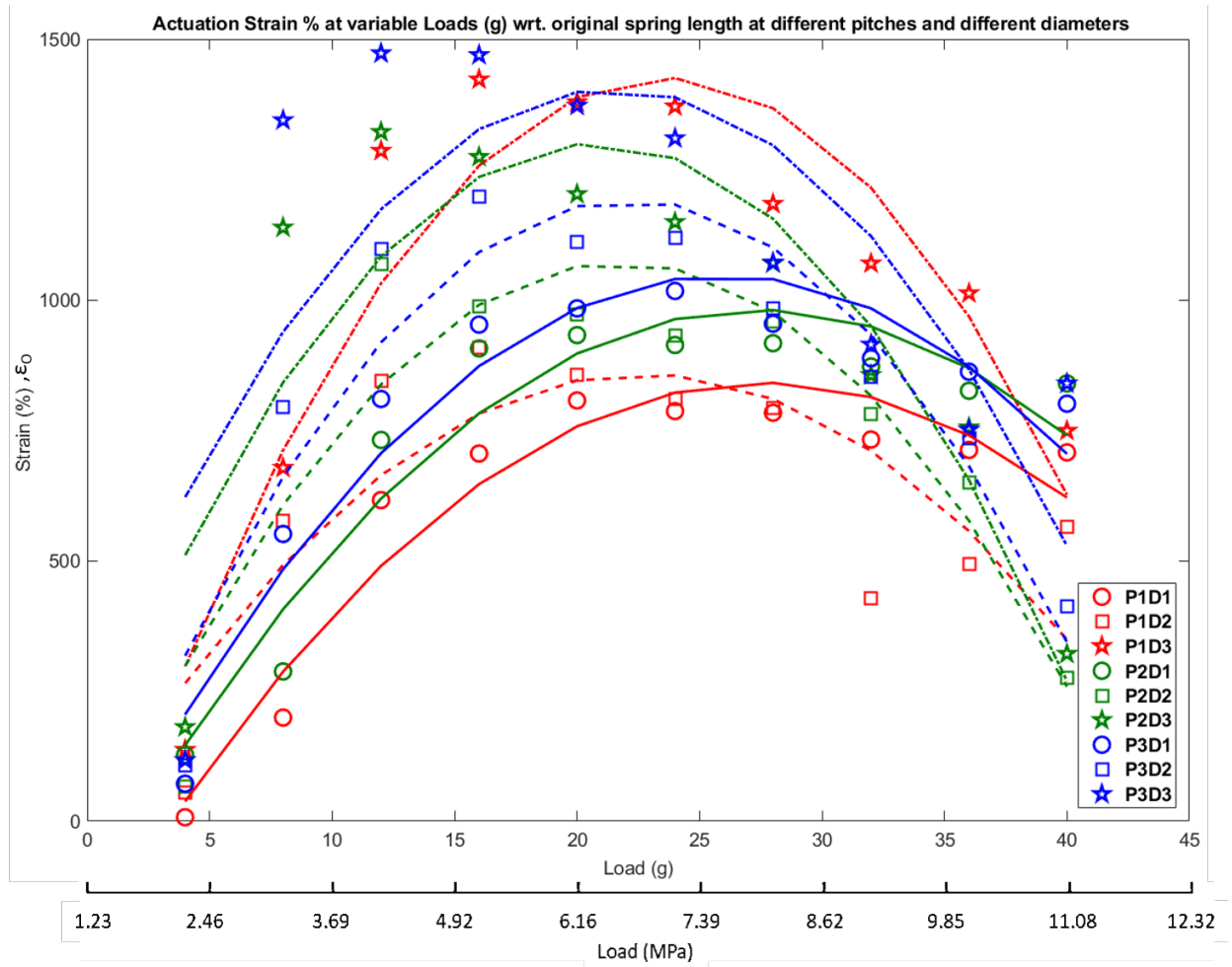


Figure 4.10. A comparison graph of actuation strain % with respect to original length ϵ_o for SMA springs of 3 different diameters of 3.18 mm (D1), 3.96 mm (D2) and 4.75 mm (D3) at a different number of coils per unit length of 1.26 per mm (32 TPI) (P1), 1.406 per mm (36 TPI) (P2), and 1.575 per mm (40 TPI) (P3) mm respectively. The lines represent polynomial fits of the data points.

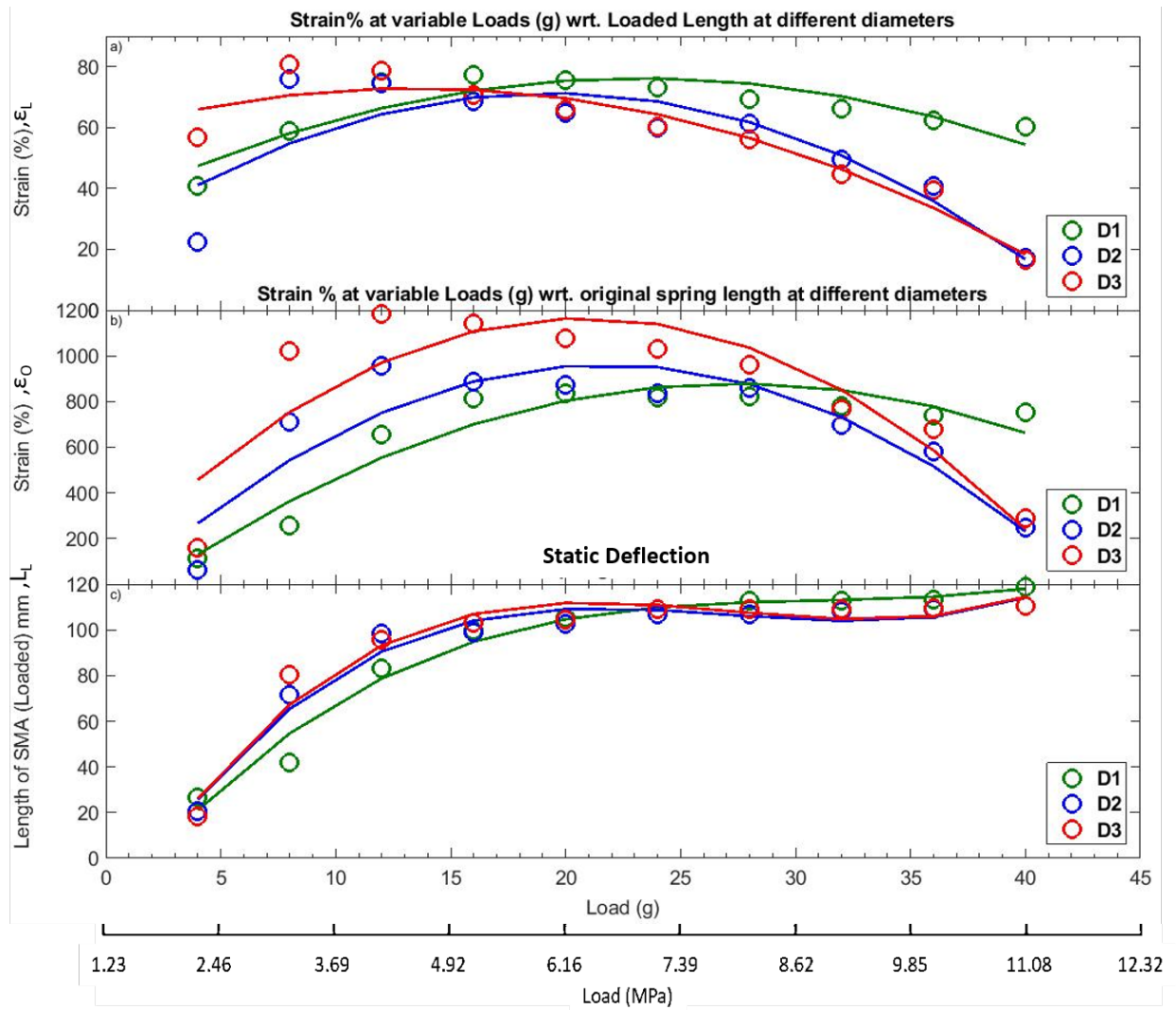


Figure 4.11. Effect of diameter for one pitch of 1.406 per mm (36 TPI) (P2), (a) strain % with respect to loaded length ϵ_L , (b) strain % with respect to original length and (c) static deflection at different loads for SMA springs of 3 different diameters of 3.18 mm (D1), 3.96 mm (D2) and 4.75mm (D3) with spring original lengths of 8.54 mm L_{o21} , 6.86 mm L_{o22} and 5.72 mm L_{o23} respectively. The lines represent polynomial fits of the data points.

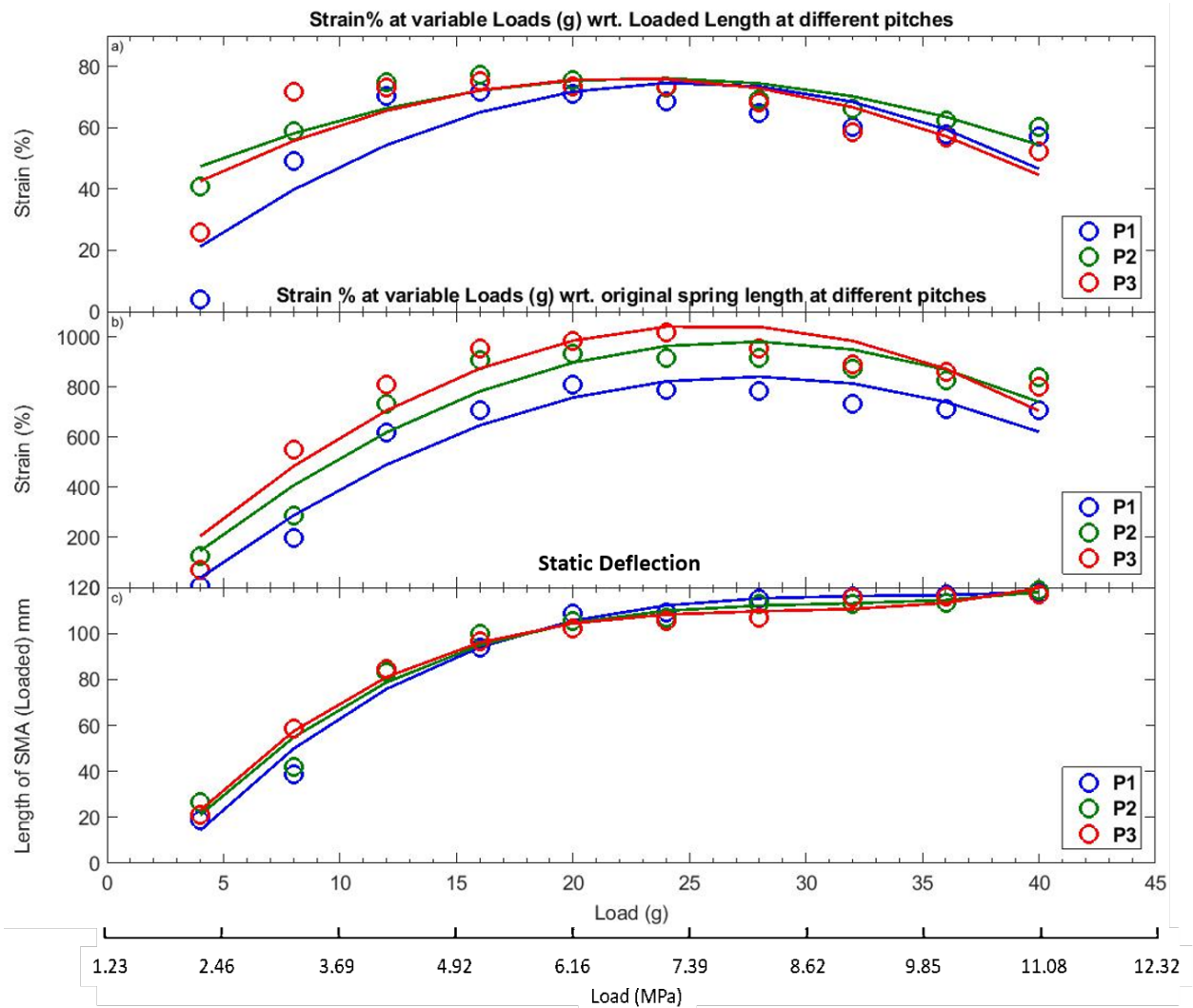


Figure 4.12. Influence of pitch for one diameter of 3.96 mm (D2), (a) strain % with respect to loaded length ε_L , (b) strain % with respect to original length ε_o and (c) static deflection at different loads for SMA springs of 3 different number of coils per unit length 1.26 per mm (32 TPI) (P1), 1.406 per mm (36 TPI) (P2), and 1.575 per mm (40 TPI) (P3) mm respectively with spring original lengths of 7.65 mm L_{o12} , 6.86 mm L_{o22} and 6.12 mm L_{o13} respectively. The lines represent polynomial fits of the data points.

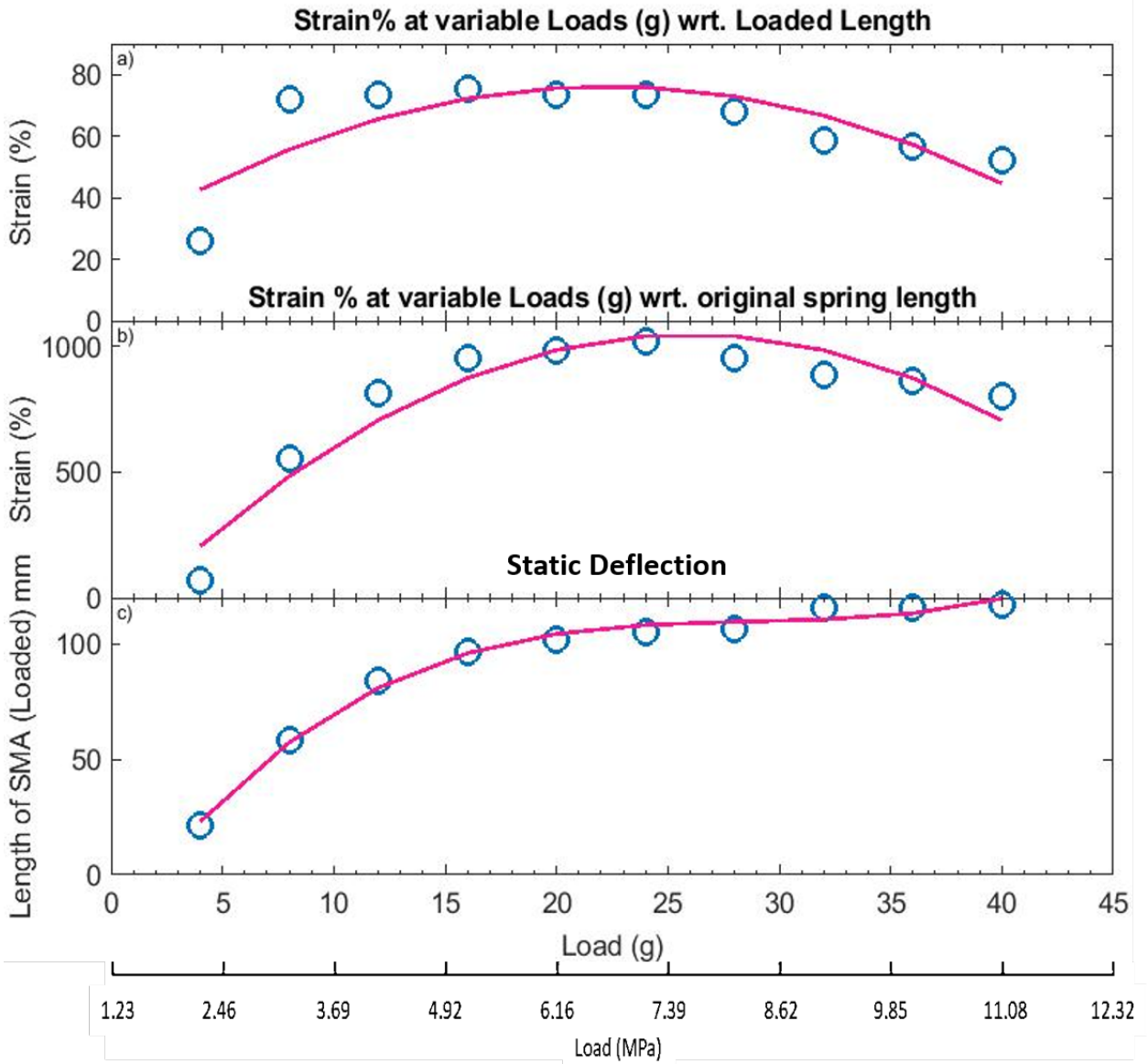


Figure 4.13. Representative sample D1P3, (a) strain % with respect to loaded length ϵ_L , (b) strain % with respect to the original length ϵ_o and (c) static deflection at different loads D1P3 CSMA spring (number of coils per unit length 1.575 per mm (40 TPI) mm (P3) with spring original lengths of 7.63 mm L_{o31} and spring diameter of 3.175 mm (D1).)

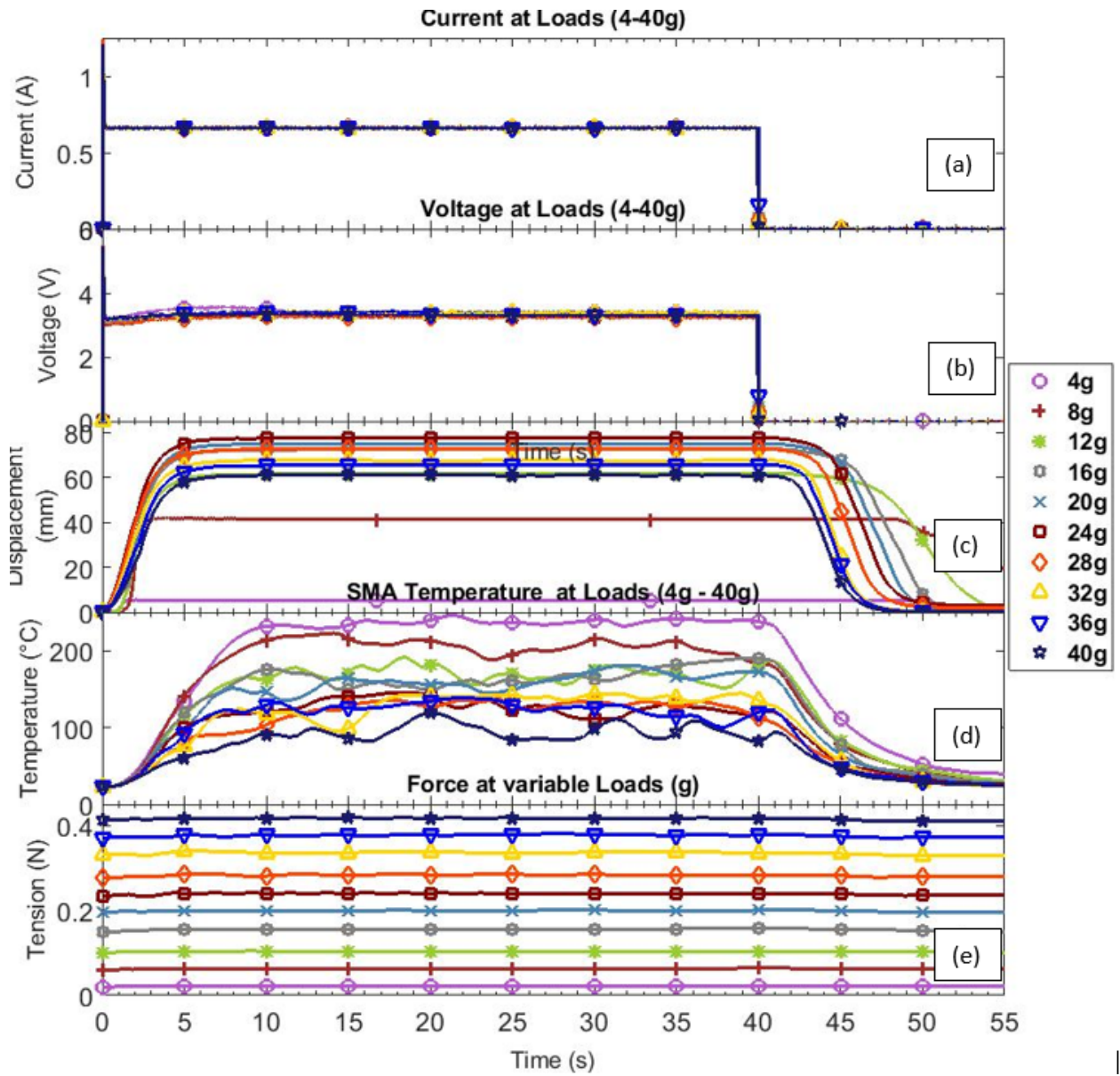


Figure 4.14. Time domain result of sample D1P3, (a) displacement at different loads, (b) voltage, (c) current, (d) temperature and (e) force for D1P3 CSMA spring (number of coils per unit length 1.575 per mm (40 TPI) mm (P3) with spring original lengths of 7.63 mm, L_{o31} and spring diameter of 3.175 mm (D1) respectively. All SMA springs are made with 120 mm long cylindrical SMA wire of radius 0.1 mm which has a weight of 24 mg. All the SMA springs are actuated at a constant current of 0.666 A (recommended by the manufacturer Dynalloy Inc. for cylindrical SMA) with a voltage of 4.2V approximately.)

4.6 Cyclic Testing of Coiled SMA Actuators

For this test, a SMA spring is made with 90 mm long cylindrical SMA wire of radius 0.1 mm which has a weight of 18 mg for the cyclic testing following the previous fabrication method. The SMA spring is actuated at a constant current of 0.666 A (recommended by the manufacturer Dynalloy Inc. [49] for cylindrical SMA) with a voltage of 3.3V at a load of 18 g (1000 times its weight). The maximum strain is not always observed at 1000 times its weight but it is closed to this magnitude. The 1000 times weight load is taken as testing standard in this work for cyclic testing. Similar experimental setup was used as seen in figure 4.4 but the camera here is not used for displacement measurement rather only the laser displacement sensor is used as the primary source of displacement measuring. From both frequency variation as seen in figure 4.15 and duty cycle variation as seen in figure 4.16, we can conclude that at 2 secs ON and 2 secs OFF with a frequency of $f = 0.25$ Hz and duty cycle of 50% is the fastest we can actuate the coiled SMAs for these particular parameters at natural cooling at room temperature with maximum strain. Fast actuation in embedded conditions is achieved by liquid cooling during the cooling phase of the actuator which is studied in next section of this work.

4.7 Artificial Musculoskeletal System Actuated by Coiled SMA with 2-Step Hot-Cold Water Cooling

An artificial musculoskeletal (MS) system is the fundamental structure that allows complex mobility of biological systems. The artificial MS joint as seen in figure 4.17 (a) was made using bone-like structure, soft tissue, artificial muscle based on Twisted Coiled Polymer (TCP) muscles [206, 231, 233]. The MS joint has 4 holes for muscle insertion and it is very flexible and to restrain the strain only in one direction we have used TCPs on the other 2 holes perpendicular to the motion to add stiffness. We do not use them as actuators in

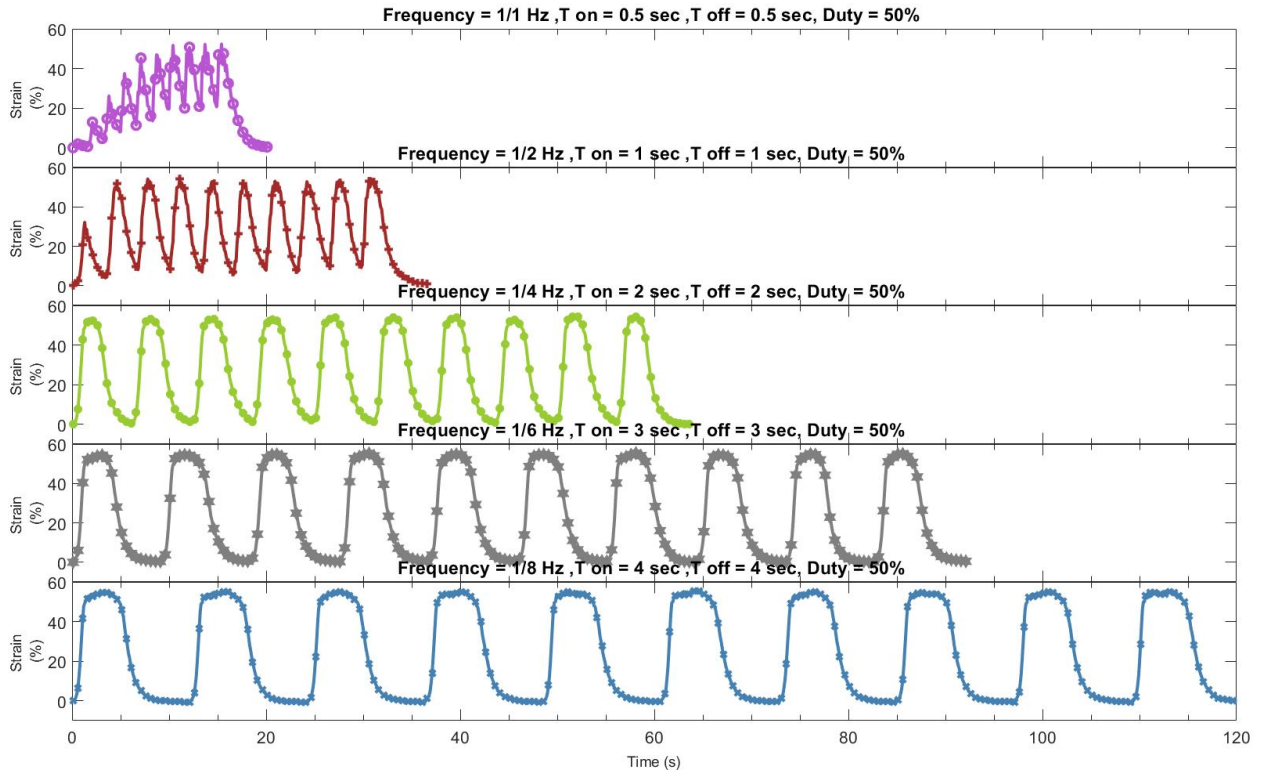


Figure 4.15. A comparison graph of different frequencies $f = 1 \text{ Hz}$, $f = 0.5 \text{ Hz}$, $f = 0.25 \text{ Hz}$, $f = 0.167 \text{ Hz}$ and $f = 0.125 \text{ Hz}$ for D2P2 CSMA spring (number of coils per unit length 1.406 per mm (40 TPI) mm (P2) with spring original lengths of 12 mm and spring diameter of 3.96 mm (D2) respectively. SMA spring is made with 90 mm long cylindrical SMA wire of radius 0.1 mm which has a weight of 18 mg. SMA spring is actuated at a constant current of 0.666 A (recommended by the manufacturer Dynalloy Inc. for cylindrical SMA) with a voltage of 3.3V approximately at a load of 18 g (1000 times its weight).)

this work rather were used as passive spring members. 4 SMA coiled actuators are used, 2 in each side. The CSMA's are prepared according to the previous section with geometrical properties of wire diameter 0.2 mm, spring diameter of 1.524 mm with 40 number of windings and a pitch of 3.15 turns per mm. The 2-step hot - cold cooling is used as only cold water quenches the coiled SMAs from high temperature to room temperature, which may lead to previous shape memory loss. Testing the SMA at 3 times the recommended voltage, the temperature of the SMA reaches close to annealing temperature used to make the coil structure, hence losing the memory of the coil shape under full load or completely stretched

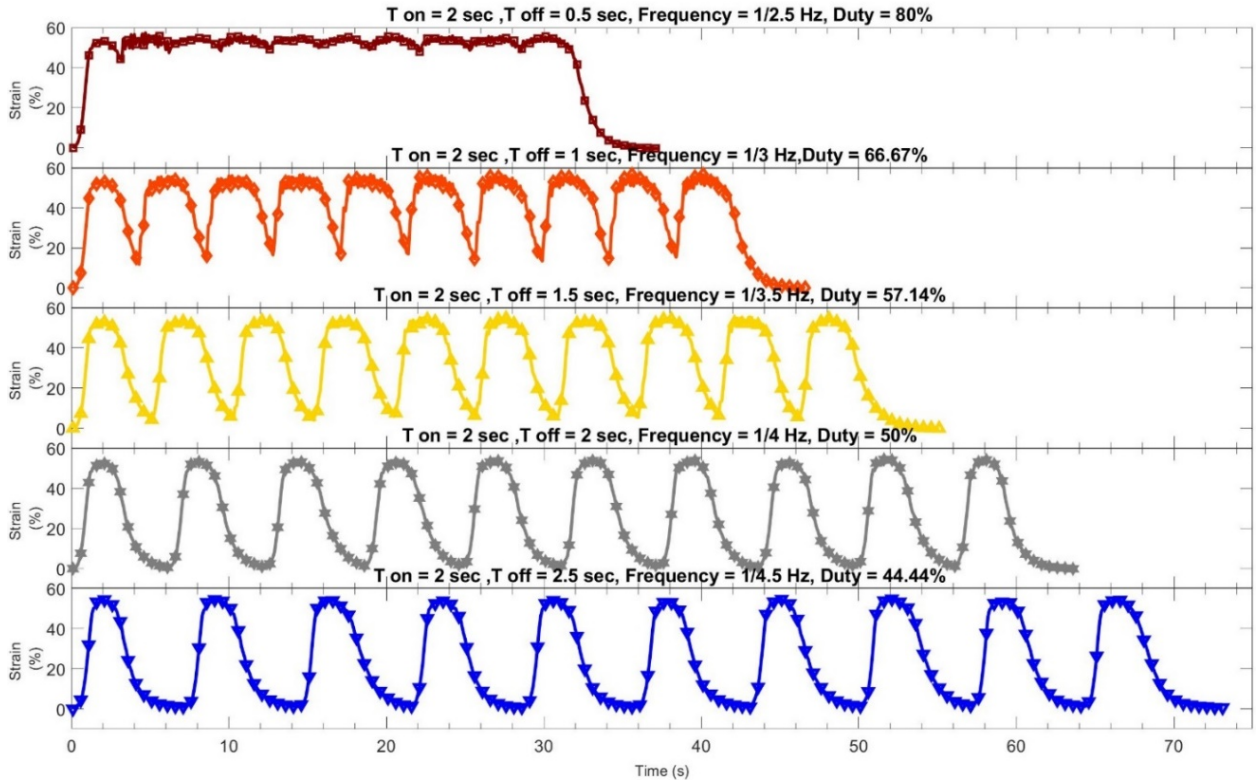


Figure 4.16. A comparison graph of different duty cycle and frequencies keeping ON time of 2 seconds constant, $D = 80\%$, $D = 66.67\%$, $D = 57.4\%$, $D = 50\%$ and $D = 44.44\%$ for D2P2 CSMA spring (number of coils per unit length 1.406 per mm (40 TPI) mm (P2) with spring original lengths of 12 mm and spring diameter of 3.96 mm (D2) respectively.)

due to load. A similar effect is observed by Holschuh and Newman[75]. The SMA still actuates as a cylindrical original SMA wire with to 4-7% strain. In figure 4.17 (a) and (b), we see the schematic diagram of the CSMA actuators in the MS joint. In (b) we see the angular measurement method used. In figure 4.17, we see MS joint actuation with 2 coiled SMAs in opposite sides for 1 cycle of 1.332 A constant current for both sides with a pulse actuation of 4 seconds on and off as shown in figure 4.17 (c) and (d) for left and right SMA actuators respectively. In figure 4.17 (e) we see the movement of the MS joint in the 1 cycle seen in figure 4.17 (f) as snapshots of the video at different time intervals showing extreme points. We get approximately 21.2° on both sides with a frequency of 0.125 Hz but we could not do for more cycles as the heat generated in the silicone chambers get entrapped raising

the temperatures and making the coiled SMAs always actuated. Sometimes the temperature reaches the annealed temperatures changing its memorized shape as discussed previously.

In figure 4.18, we see the schematic diagram of 2-step hot - cold cooling setup where we apply hot water (50 °C) for 2 seconds first and then cold water (23 °C) for 2 seconds. This procedure helps in not quenching the hot metal and make it stiff. We have used 4 pumps, 2 for hot water and 2 for cold water. The pipes and wires used for connecting the pumps to the MS joint are ultra-soft which do not keep any external stress on the joint against the actuation motion. The tubes used are ultra-soft tygon PVC tubing and the wires used are ultra-flexible miniature high-temp wire which are made of silicone with a shore hardness of 40A (McMaster Inc. Model No. 9564T3).

The pumps and the wires are connected using triple pipe connector as shown in figure 4.18, where firstly the CSMA's are actuated by resistive heating, then hot water was given followed by cold water according to the time sequence shown. The mixed water is dumped into a separate water tank. The cyclic digital signal is produced using NUCLEO F767ZI micro-controller and the MOSFET - resistor circuit as shown in figure 4.18. Video camera is used to record the movement and Tracker software is used to calibrate the time plots. In figure 4.19, we see the actual experimental setup and figure 4.20 shows experimental results of the 2-step hot - cold cooling actuation of coiled SMAs in the MS joint for 5 cycles. The temperatures never went close to annealing temperatures during the actuation due to the 2-step hot-cold cooling. The cooling helped in achieving higher degree actuation as much as 24°. The graphical results can be seen in figure 4.21 (g), the inconsistency of actuation in each cycle is due to the bad timing of pumps at high frequencies . The time domain plot is calibrated with Tracker software. Figure 4.20 shows snapshots of cyclic actuations on the extreme ends. The 2-step hot - cold cooling is used because cold water quenches the coiled SMAs from high temperature to room temperature drastically which may lead to previous shape memory loss. The frequency of actuation achieved is 0.125 Hz with a

duty cycle of 50%. In figure 4.21 (a) and (b), we see the pulse actuation of left and right actuators respectively. The major difference between the figure 4.17 and 4.20 is the cooling which increases its actuation angle from 21.2° to 24° and the frequency from only 1 proper cycle to 0.125 Hz for multiple cycles. The pulse actuation of the left hot - cold and right hot - cold pumps is shown in (c), (d), (e) and (f). The actuation angle achieved using CSMA in MS joint is 24° whereas the actuation angle achieved using fishing line TCPs is 20° [231, 233] and frequency of MS joint with CSMA is 0.125 Hz whereas the frequency of MS joint with fishing line TCPs is 8 mHz (15.625 times smaller) in normal actuation and 30 mHz (4.167 times smaller) with pulsed actuation. In both angular rotation or strain and frequency there is an increase from the performance of CSMA against fishing line TCPs for MS joint, frequency due to active cooling implementation on CSMA. An overhead reservoir system with fast response valves can help to get higher frequencies which is left for future of this project. The hot water is around $\sim 50^\circ\text{C}$ and cold water is at room temperature $\sim 23^\circ\text{C}$. One limitation of SMA over TCP is hysteresis in actuation and the additional cost of metal alloys over nylon precursor materials.

4.8 Conclusion on Actuation of CSMA

There are a number of variables that play a role in the performance of the CSMA actuators. Some play a significant role, and some have a moderate effect. This section presents the characterization of coiled SMA actuators mainly focusing on the spring geometry such as spring diameter and a variable number of coils per unit length. The manufacturing technique used in this section gives an advantage for large strains, relatively high frequency is an important requirement for soft robots, which can be achieved using liquid cooling under embedded conditions. In this work, we presented coiled SMAs performance and complete characteristics under different loads for constant current, voltage, SMA wire diameter and SMA wire length for different spring diameters and a number of coils per unit length and

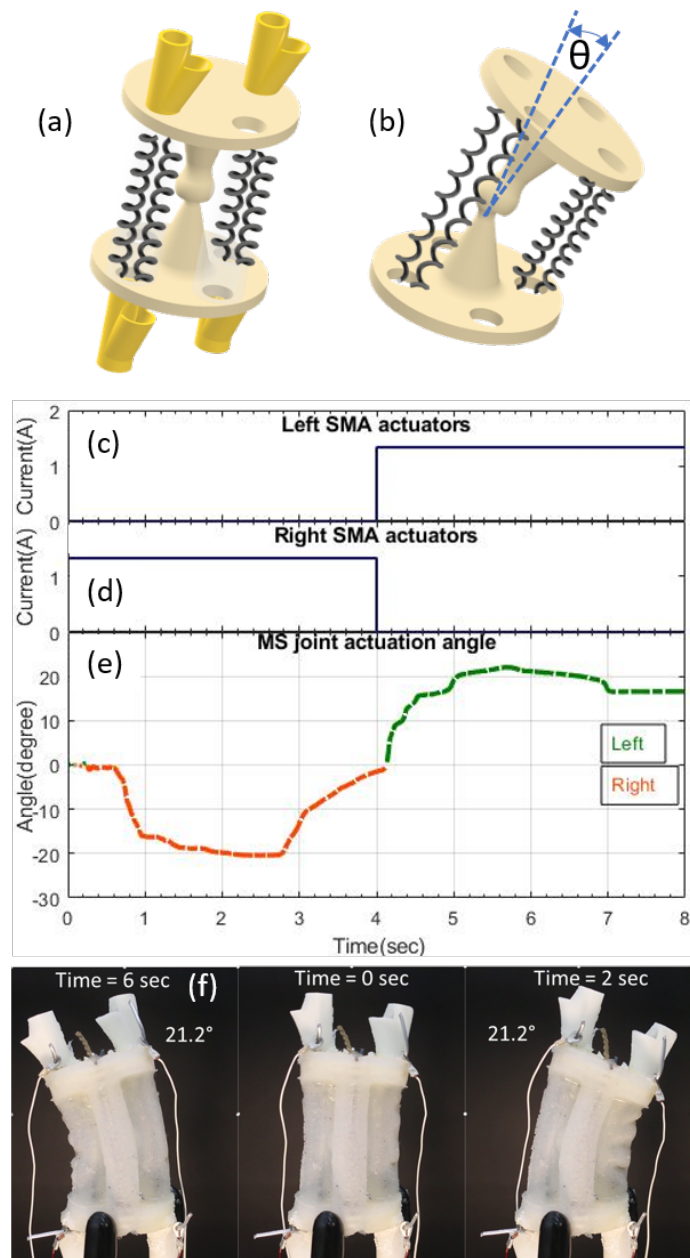


Figure 4.17. (a) and (b) we see the schematic diagram of the CSMA actuators in the MS joint. In (b) we see the angular measurement method used. MS joint actuation with 2 coiled SMAs in opposite sides for 1 cycle of 1.332 A constant current for both sides with a pulse actuation of 4 seconds on and off as shown in (c) and (d) for left and right SMA actuators respectively. In (e) we see the movement of the MS joint. The SMA coils used here are 2 on each side of wire diameter 0.2 mm, spring diameter of 1.524 mm with 40 rings and a pitch of 3.15 turns per mm. (f) MS joint actuation with 2 coiled SMAs in opposite sides for 1 cycle of 1.332 A constant current for both sides with a pulse actuation of 4 seconds ON and OFF (No active cooling). The video is supplied in supplementary material (Video: S2).

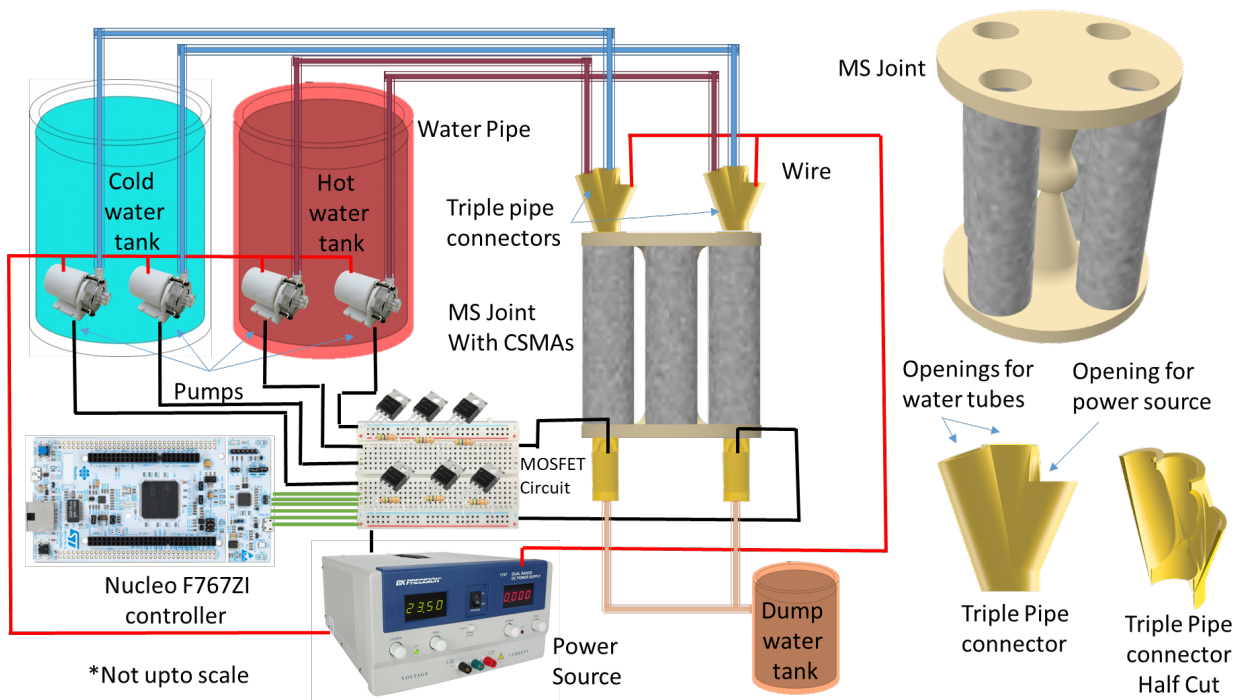


Figure 4.18. Schematic diagram of 2-step hot - cold cooling setup. We have used 4 pumps, 2 for hot ($\sim 50^\circ\text{C}$) water and 2 for cold ($\sim 23^\circ\text{C}$) water.

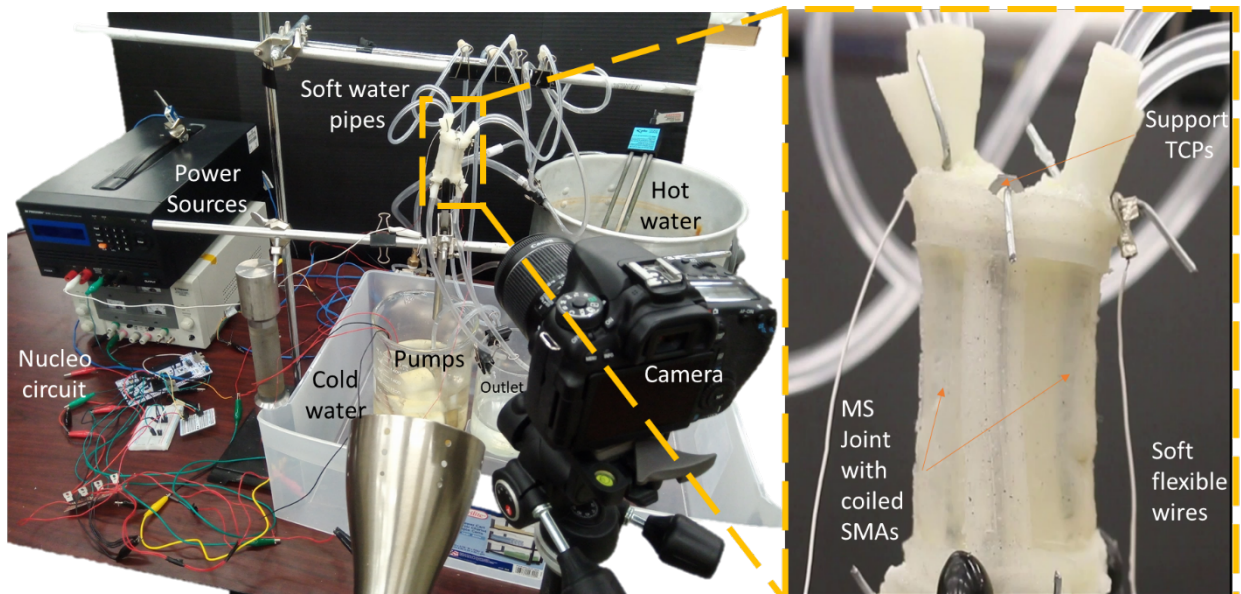


Figure 4.19. Experimental setup for 2-step hot - cold cooling. We have used 4 pumps, 2 for hot water and 2 for cold water. The pipes and wires used for connecting the pumps to the MS joint are ultra soft which do not keep any external stress on the joint against the actuation motion.

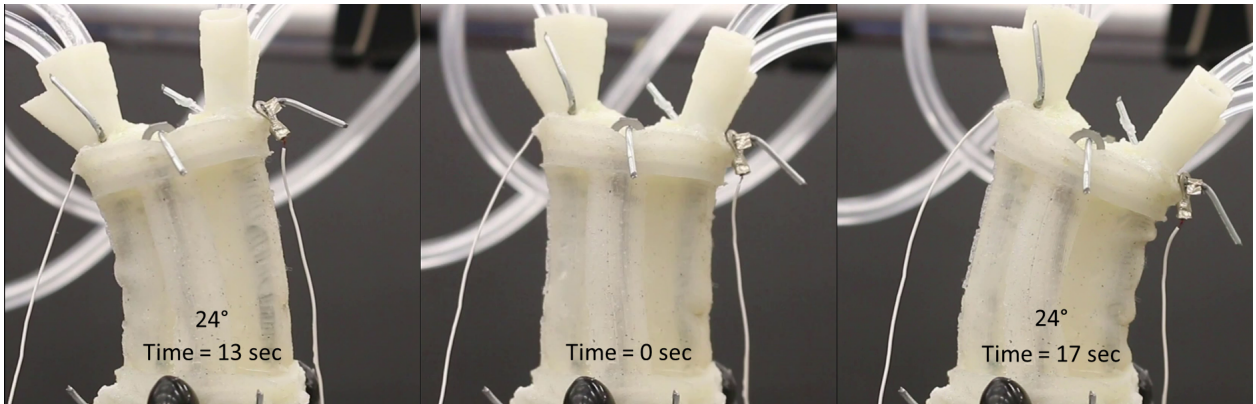


Figure 4.20. Experimental results of the 2-step hot - cold water actuation of coiled SMAs in the MS joint for 5 cycles. In figure 4.21 we see the graphical representation of the movement of the MS joint for 5 cycles.

discussed how the number of coils per unit length and spring diameters influence the SMA spring actuators. We can see that number of turns per unit length does not influence the maximum strain load but as we increase the diameter the load for maximum strain reduces. The maximum strain with respect to loaded length almost remains constant with respect to a number of turns per unit length, $\sim 75\%$ for 3.18mm diameter, 70% for 3.96 mm and between 70-80% for 4.15 mm and the change cannot be determined clearly with respect to diameter as it does not follow any pattern. It varies between 70-80%. The maximum strain with respect to original length increases mostly with an increment of a number of coils per unit length and increases with respect to the increment in diameter. The maximum strain with respect to original length is observed greater than 1000% at weights almost to 1000 times the actuator original weight. In this chapter, we present the effect of 2-step hot-cold water cooling to improve actuation frequency and performance of coiled SMAs in an artificial musculoskeletal joint. The actuation angle achieved using CSMA in the MS joint is $\sim 24^\circ$ whereas the actuation angle achieved using fishing line TCPs is 20° and frequency of MS joint with CSMA is 0.125 Hz whereas frequency of MS joint with fishing line TCPs is 30 mHz (4.167 times smaller) with pulsed actuation. In both angular rotation or strain and frequency there is an improvement in the performance of CSMA against fishing line TCPs

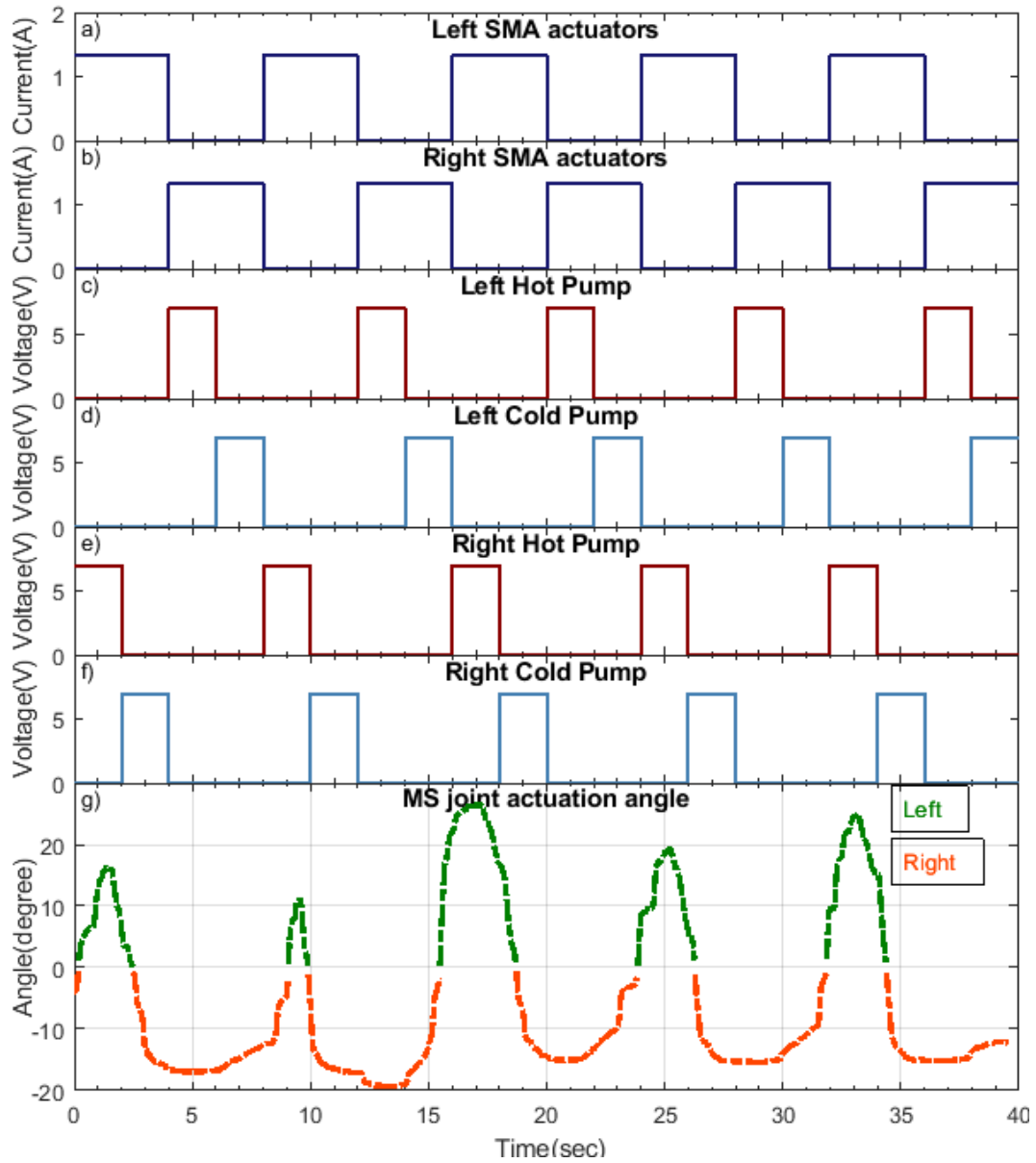


Figure 4.21. Sequential actuation of CSMA in MS joint and the 2-step hot - cold cooling system actuation of coiled SMAs in the MS joint for 5 cycles. The 2-step hot - cold cooling is used as only cold water quenches the coiled SMAs from high temperature to room temperature which may lead to previous shape memory loss. (a) and (b) represent the pulse actuation of left and right actuators respectively. The pulse actuation of the left hot and cold and right hot and cold is shown in (c), (d), (e) and (f).

for MS joint. One limitation of SMA over TCP is hysteresis in actuation and the additional cost of metal alloys over nylon precursor materials.

4.9 Modeling of CSMA based on only Temperature at Low Load Conditions ¹

In this section, we present modeling and characterization of CSMA actuators that are fabricated by coiling cylindrical SMA wires on to a threaded screw mandrel and applying heat treatment. Here, we evaluate a theoretical model that describes the actuation behavior of SMA springs based on the constitutive model. We have experimentally verified the theoretical model and analyzed various parameters with respect to temperature change during actuation. The model was coded in Simulink® and the effects of various parameters with respect to temperature change were investigated. Simulations were compared with experiments and good agreement was obtained. We show, how the high tension winding of SMA on the mandrel help in better performance and understanding of the fabricated coiled SMAs.

4.9.1 Heat Transfer Model

The input to SMA wire is provided by a manufacturer recommended amount of voltage depending on the length of the SMA wire. The governing differential equation of lumped capacitance heat transfer for SMA is obtained as in equation 4.1 [202].

$$mC_p \frac{dT}{dt} = I^2 R_w - hA(T - T_\infty) \quad (4.1)$$

where m is the mass of the actuator, h is the convective heat transfer coefficient, C_p is the specific heat capacity of the SMA alloy, I is the input current, A is the surface area of the SMA actuator, T is the temperature of the wire, and T_∞ is the ambient temperature.

¹Some parts are reprinted by permission from **Active and Passive Smart Structures and Integrated Systems: International Society for Optics and Photonics, Characterization of coiled SMA actuators for humanoid robot.** , Akshay Potnuru, Yonas Tadesse, ©2017

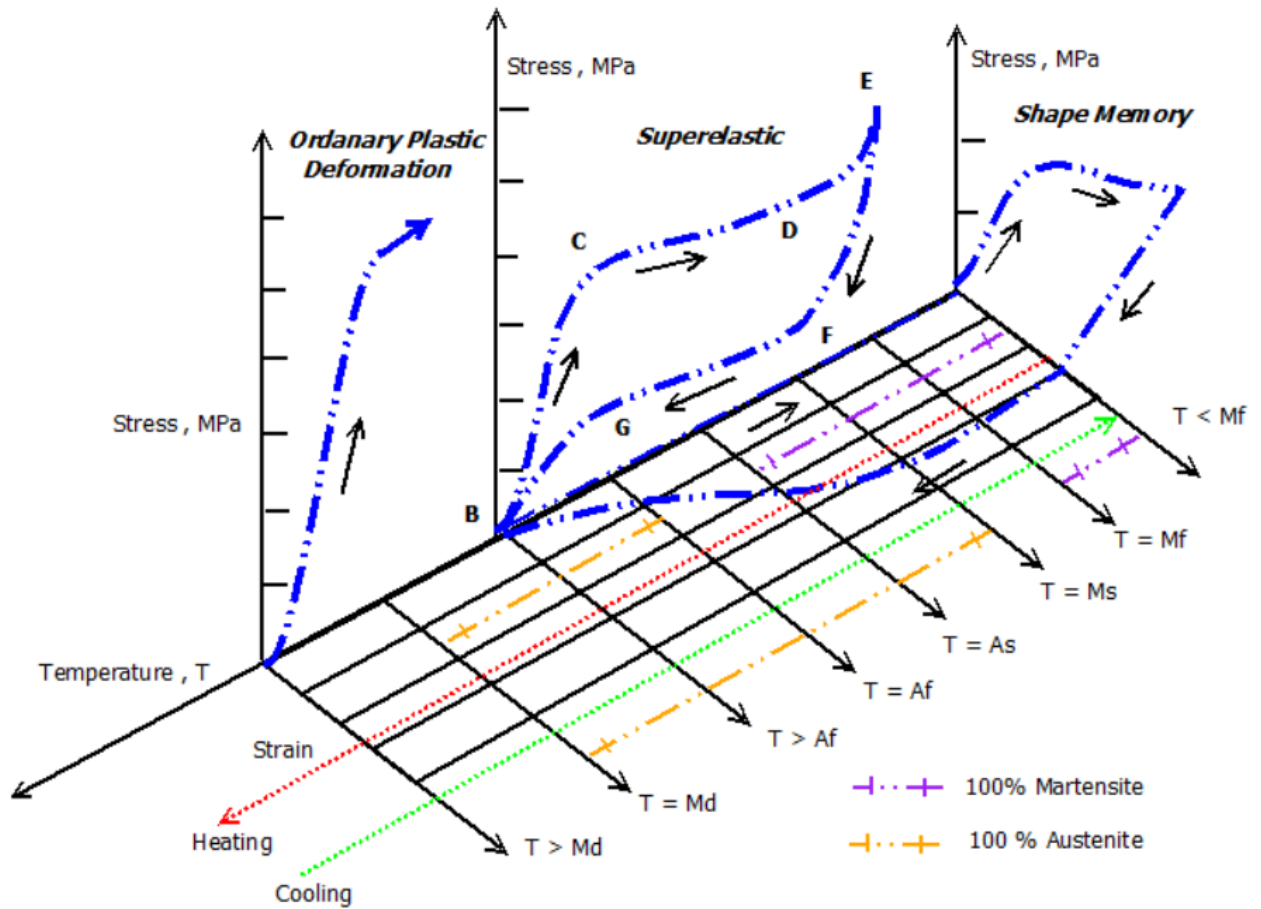


Figure 4.22. 3D stress-strain-temperature diagram of SMA phase transformation (Super elastic and Shape memory effect [11])

Shape memory alloy material exhibit shape memory and superelastic effects. These effects are associated with stress, strain and temperature state of the material. At low temperature, the shape memory effect is observed whereas, at high temperature, the superelastic curve will be observed. The shape memory effect (SME) is a result of temperature and stress dependent shift in the materials crystalline structure between the martensite and austenite phases, which can be understood from figure 4.22. The unique change in phase between the two crystalline structures enables the material to change its shape, and the material is used as an actuator or artificial muscle for numerous applications. It can operate in either the air or fluidic medium. The low-temperature phase, martensite is a soft structure and, on the other

hand, the high temperature phase, austenite is hard structure [124]. At high temperature, the material changes to austenite phase, and when it cools down, it will transform to martensite. The shape memory effect (SME) is the recovery of large strain due to the application of thermal cycling (heating and cooling) [161, 157]. In figure 4.22, we see the 3D diagram of stress-strain-temperature relation of SMA phase transformation in both super elastic and shape memory effect. Since the discovery of Shape Memory alloys (SMAs) in 1951 [145], researchers are extensively studying the material to understand its actuating behavior. Several constitutive models have been proposed to simulate the behavior and to improve the control of SMAs in the past 30 years [33]. SMAs are known for the properties like lightweight, low-cost and high power density, which made them ideal actuators for several applications in industry and academia. SMAs have few limitations such as non-linear behavior during the phase transformation, the repercussion of thermo mechanical cycles on the effective stress, strain and slow recovery actuation due to the low cooling rate under natural convection cooling. The slow recovery actuation can be solved by forced convection or conduction. Dynamics of SMAs are predominantly nonlinear since the energy conversion principle from thermal to physical properties depend on the phase transition of the material, which creates significant hysteresis in the model. On the other hand, the dynamic properties of the SMAs rely on their metallurgy content, fabrication process, training techniques, aging and ambient conditions [65]. Brinson and Huang [27] stated that most of the SMA constitutive models are composed of two main parts, the mechanical law governing the stress-strain behavior and the transformation kinetics that models the martensite phase transformation. Elahinia [50] has shown that for phenomenological SMA models, the critical aspect is the phase transformation kinetics law which defines the behavior of the model. The first SMA phenomenological models are developed by Tanaka [210], Liang and Rogers [114] and Brinson [28]. Some other SMA models are developed by Pence and Ivshin [86] and by Boyd and Lagoudas [25].

As the model we use in this section is a coiled SMA, which is annealed at high temperature to remain in the coiled state to attain higher strains, we need to consider SMA spring

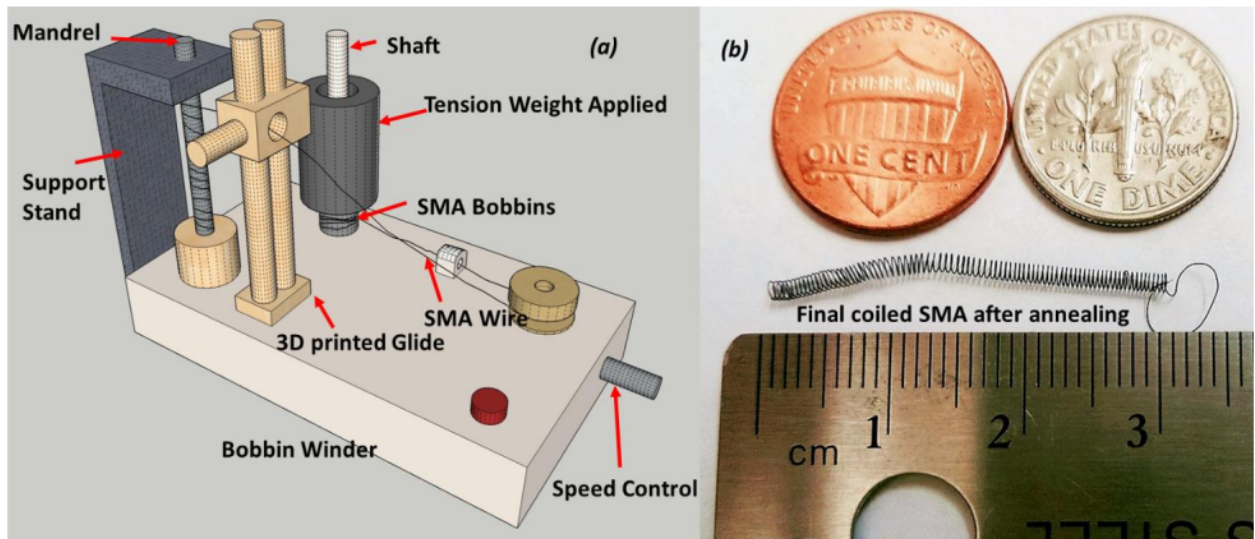


Figure 4.23. (a) Schematic Diagram of the bobbin winder made in Sketchup® (b) The final prepared coiled SMA after annealing.

phenomenological models. The most relevant one is proposed by Liang and Rogers [113], which considers shear stress due to the spring or helix structure. Several modifications of the Liang and Rogers models have been proposed later, which we will, incorporate in this work. The cylindrical geometry can contract 3-5 % strain and the coiled geometry can deform up to 200% [115]. This work is divided into seven major sections. The sections mainly comprise of coiled SMA preparation, characterization of coiled SMAs, coiled SMA modeling, Simulink® simulation of the model and finally discussion where we compare the Simulink® results with experiment results of characterization of coiled SMAs and conclusion.

4.9.2 Small Diameter Coiled SMA Preparation

Flexinol, shape memory alloy wire is bought from Dynalloy® of diameter size of 0.1 mm. The screw mandrel is bought from McMaster-Carr®, which is type 18-8 stainless steel fully threaded stud with 0-80 Thread, 50.8 mm Long and 1.59 mm diameter. Small wire end connectors on both sides clamp the coiled SMA. A coiling setup comprising of a custom modified Simplicity® SideWinder portable bobbin winder, 3D printed guide and tension

weights are used to coil the SMA on the screw mandrel as seen in figure 4.23. The bobbin winder motor is made to wind thread at high speeds under low tensions, but in SMA coiling, we need low speeds and high tensions. Therefore, we placed weight on the main SMA bobbin of 500 g to create more tension and modified the electronic circuit of the bobbin winder to control the speed of the motor for the application. The speed control knob from the placed potentiometer helps to reduce the speed to the right value for optimum coiling and can be varied for different mandrels and different SMA wire diameters. The electronic circuit is tested, soldered, and kept inside the bobbin winder with all its components in a way that only the potentiometer or speed control knob is visible outside on the right side of the bobbin winder through a drilled hole as seen in figure 4.23. The electric circuit is simple voltage regulating circuit consisting of a $10\text{ K}\Omega$ linear-taper potentiometer, transistor TIP122, $5\text{ K}\Omega$ resistor and microchip amplifier MCP6022. The coiled SMA on the screw mandrel in figure 4.23 is kept in Thermolyne industrial bench top muffle furnace (model number FD1535M) at $390\text{ }^\circ\text{C}$ for 45 mins and naturally cooled. The annealed coiled SMA is removed from the screw mandrel and is shown in figure 4.24 (b), which was used for characterization. In figure 4.24 (a) the schematic diagram of the customized bobbin winder shown in figure 4.23 is shown.

(a) Characterization of Small Diameter Coiled SMA

The SMA is actuated at 10.7 V at 0.2 A for optimum deformation, where the current is suggested by the manufacturer. The voltage is calculated based on the length of the SMA, which is 425 mm with resistivity of $128\ \Omega/\text{m}$ where resistance of the wire is calculated to be $54.4\ \Omega$. The SMA is fixed as seen the figure 4.26 (a) in the top end and the bottom end is free to actuate. Both ends are clamped with wire end connectors, which were soldered to very light copper wires, which are connected to power supply. Phantom[®] Miro eX digital high-speed camera captured the actuation at 50 frames per second. The point data recorded by the fast camera is used to calculate the deformation and strain using Microsoft[™] Excel[®]

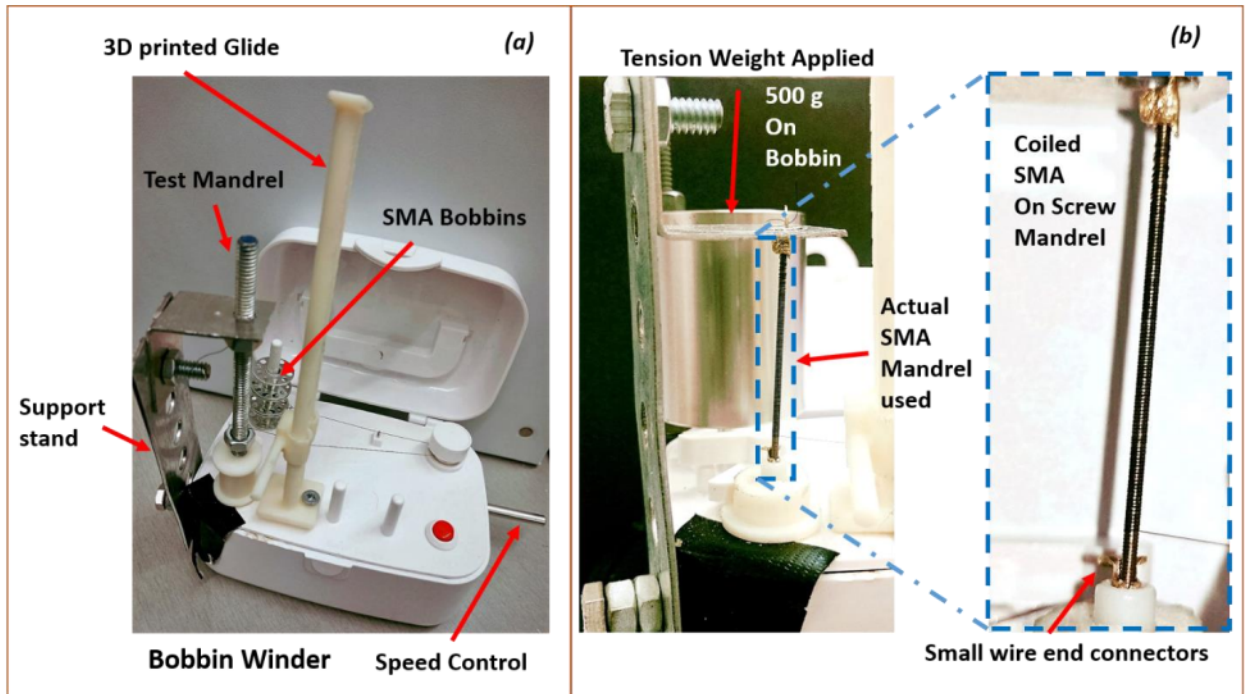


Figure 4.24. Experimental setup of the coiled SMA preparation (a) the complete setup (b) the detailed view of SMA wire on the mandrel.

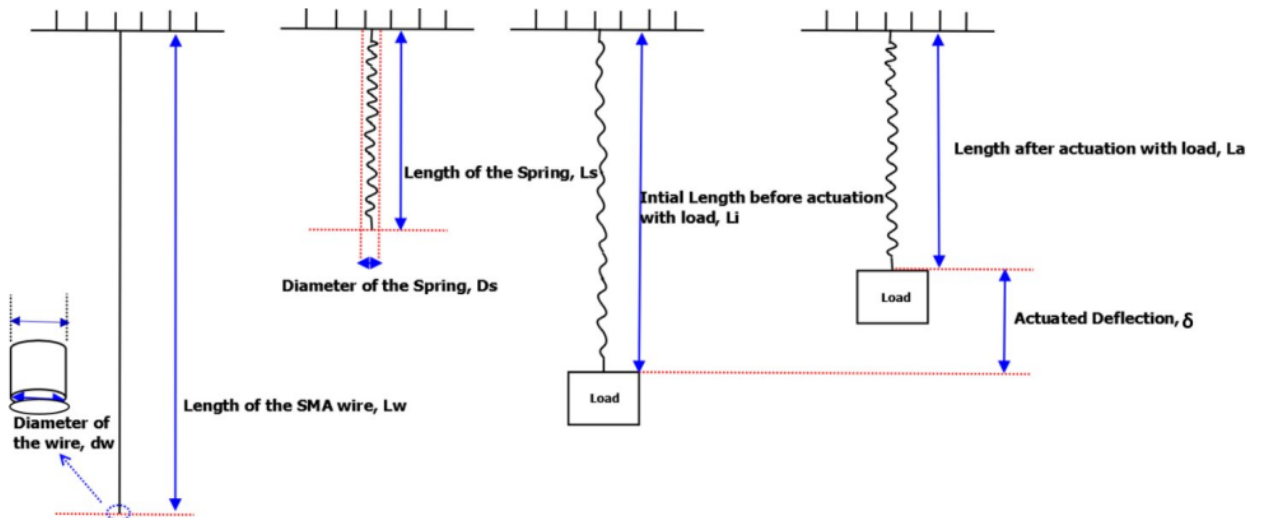


Figure 4.25. Fabrication (coiling and annealing) and Testing of the SMA Spring actuator

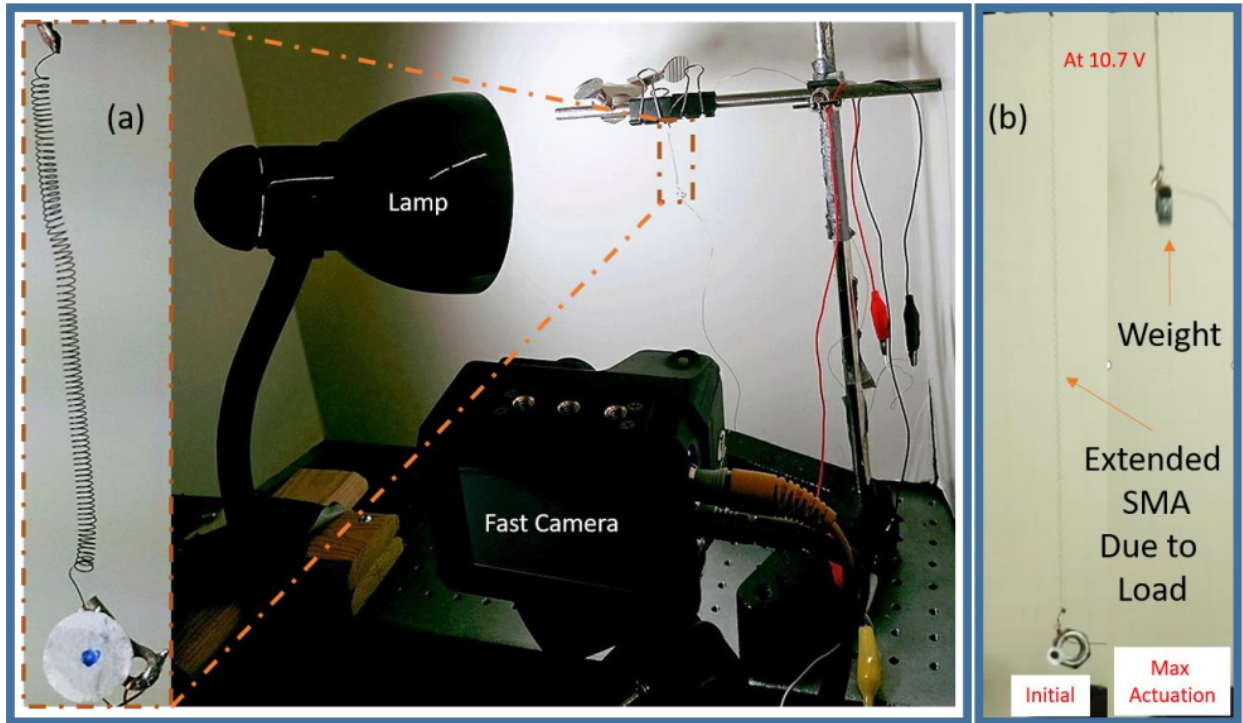


Figure 4.26. (a)SMA Experimental setup for characterization of small diameter CSMA ($d = 0.1 \text{ mm}$) (b) Best actuation at 10.7V and 0.2A at load at 4.375 g (200 times its weight) with 82.75 % strain at a square pulse voltage actuation with duty of $(300)/7 \%$ and a period of 7 seconds

. Figure 4.26 (b) shows the best actuation at 10.7V and 0.2A at load at 4.375 g with 82.75 % strain. In figure 4.27, we see the load against strain at 20 different loads. We can clearly see an increase and decrease as load increases. The coiled SMA has shown significant strains of 82.75% at load 4.375 g compared to just maximum 4% strain of cylindrical SMAs. The load against deformation and initial length is shown in figure 4.28. Load against initial length can be used to see the profile of the spring constant K . The characterization is done at 20 loads varying from 0 g (free load) up to 35 g. The actuation of the coiled SMA is pulsed wave actuation where its 3 seconds on at maximum voltage and current and 4 seconds off. It is a square wave pulse with duty of $(300)/7 \%$ and a period of 7 seconds.

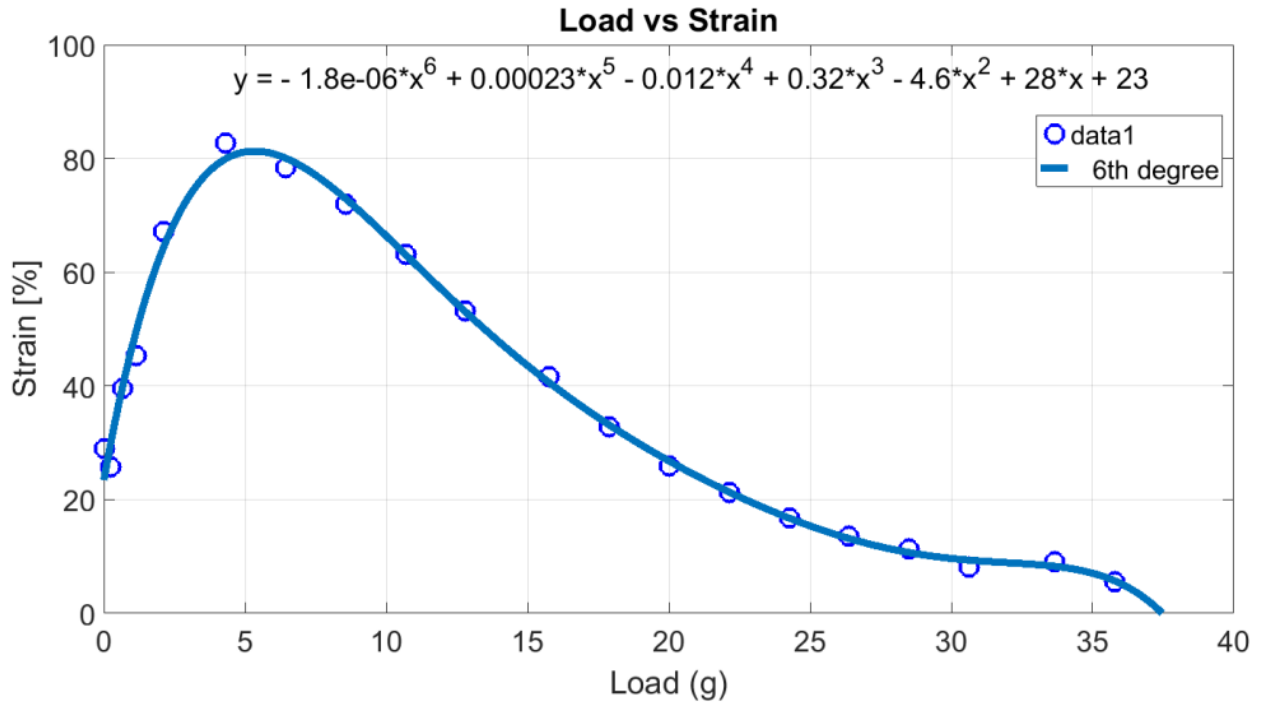


Figure 4.27. SMA Experimental results of characterization: Load Vs Strain

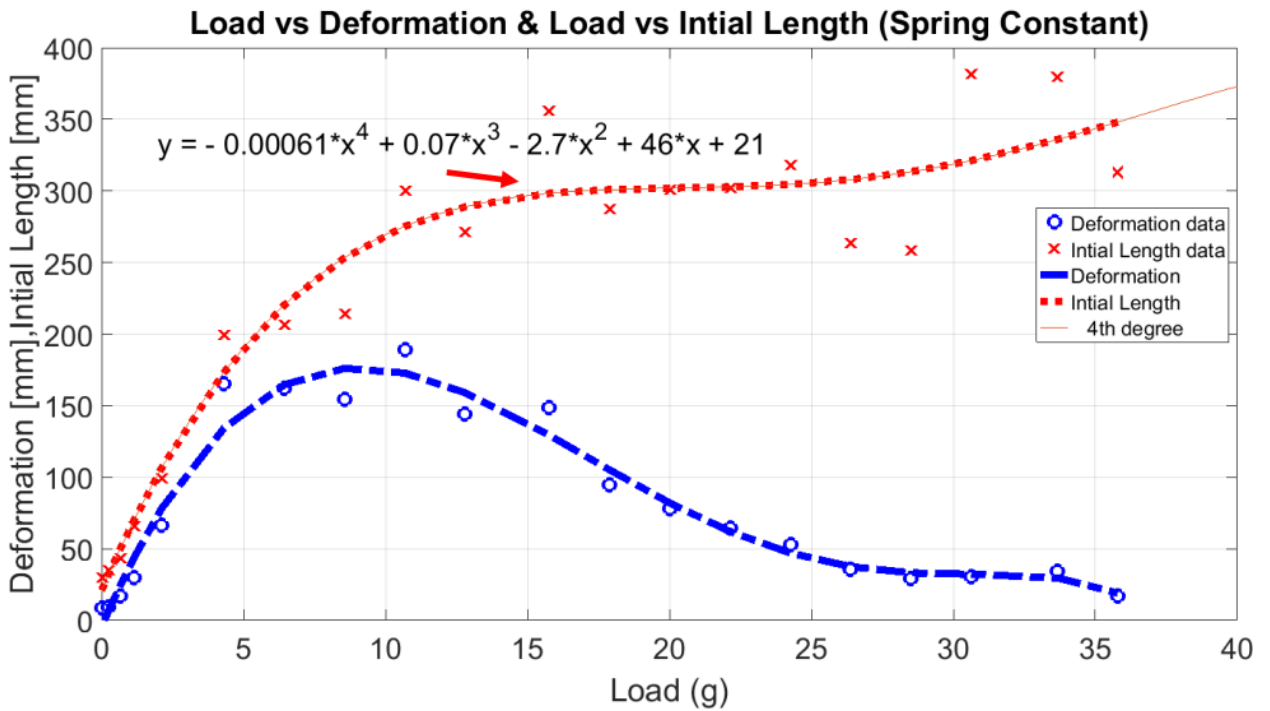


Figure 4.28. SMA Experimental results of characterization: Load Vs Deformation & Initial Length (Spring Constant)

4.9.3 Modeling Temperature of CSMA at Low Load

Several theoretical models to describe the actuation behavior of CSMA based on the constitutive model have been proposed previously for control of the SMAs . In the theoretical model, in this subsection, we have studied mathematical models and simulate the actuation of SMA spring with voltage as an input. In the further sub sections, we have explained different sub models like heat transfer, phase transformation, constitutive model and force and deflection based on constitutive model.

(a) Heat Transfer Model

The input to SMA wire is provided using the manufacturer's recommended amount of voltage depending on the length of the SMA wire. The governing differential equation of lumped capacitance heat transfer of SMA is obtained from equation 4.2 [202].

$$mC_p \frac{dT}{dt} = \frac{V^2}{R_w} - hA(T - T_\infty)$$

or

$$mC_p \frac{dT}{dt} = I^2 R_w - hA(T - T_\infty)$$
(4.2)

where m is the mass of the actuator, h is the convective heat transfer coefficient, C_p is the specific heat capacity of the SMA alloy, V is the input voltage, A is the surface area of the SMA actuator, T is the temperature of the wire, and T_∞ is the ambient temperature.

Using equation 4.2 and table 4.8, we did simulation of temperature of SMA to compare with experiment. The simulation is done using the parameters in table 4.8 in Simulink® Matlab™ . The simulation flowchart can be seen in figure 4.29.

In figure 4.30, we have the comparison of the simulated and experimental results at low load of 4 g for different spring geometries. The simulation agrees with the experiment for some spring geometries. The few discrepancies can be explained due to the loss of contact

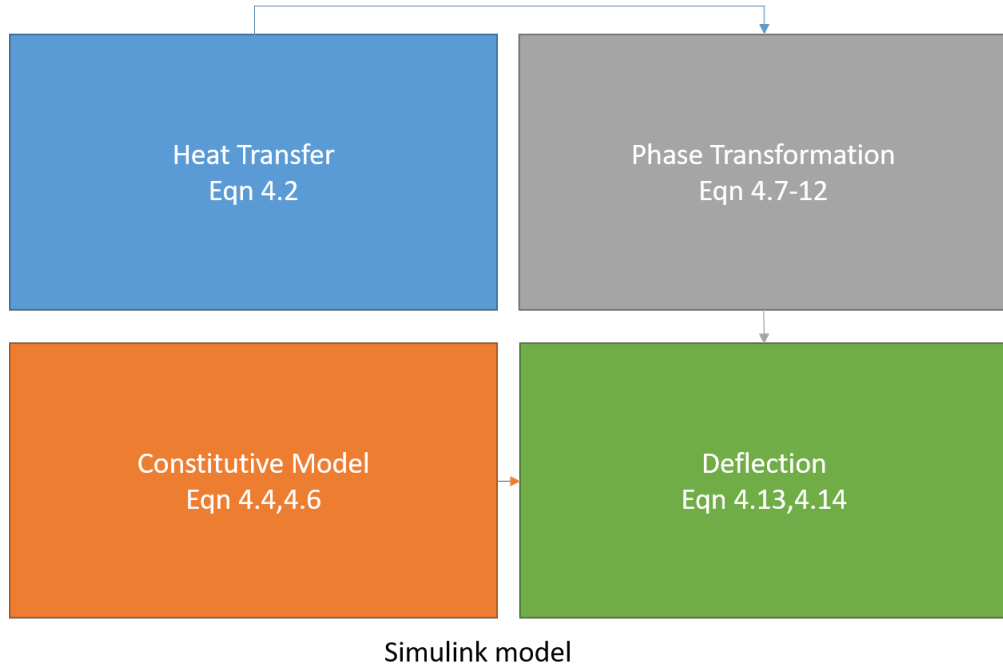


Figure 4.29. Simulink® Matlab™ simulation flowchart

of the thermocouple during experiment and the different convective heat transfer is due to uncontrolled thermal environment during characterization.

(b) Constitutive Model

It is important to model and characterize the SMA springs to understand their behavior. According to Liang and Rogers [113], the one-dimensional constitutive relation of SMAs can be expressed as shown in equation 4.3, where τ , γ , ξ , T , G , Ω , and θ are the shear stress, shear strain, martensite volume fraction, temperature, shear modulus, phase transformation coefficient and thermal expansion coefficient of the coiled SMA spring, respectively.

$$\tau = G\gamma + \frac{\Omega}{\sqrt{3}}\xi + \frac{\theta}{\sqrt{3}}T \quad (4.3)$$

The shear modulus G is given by equation 4.4, where GA is the shear Young's modulus of SMA in austenite phase and GM is the shear Young's modulus in martensite phase.

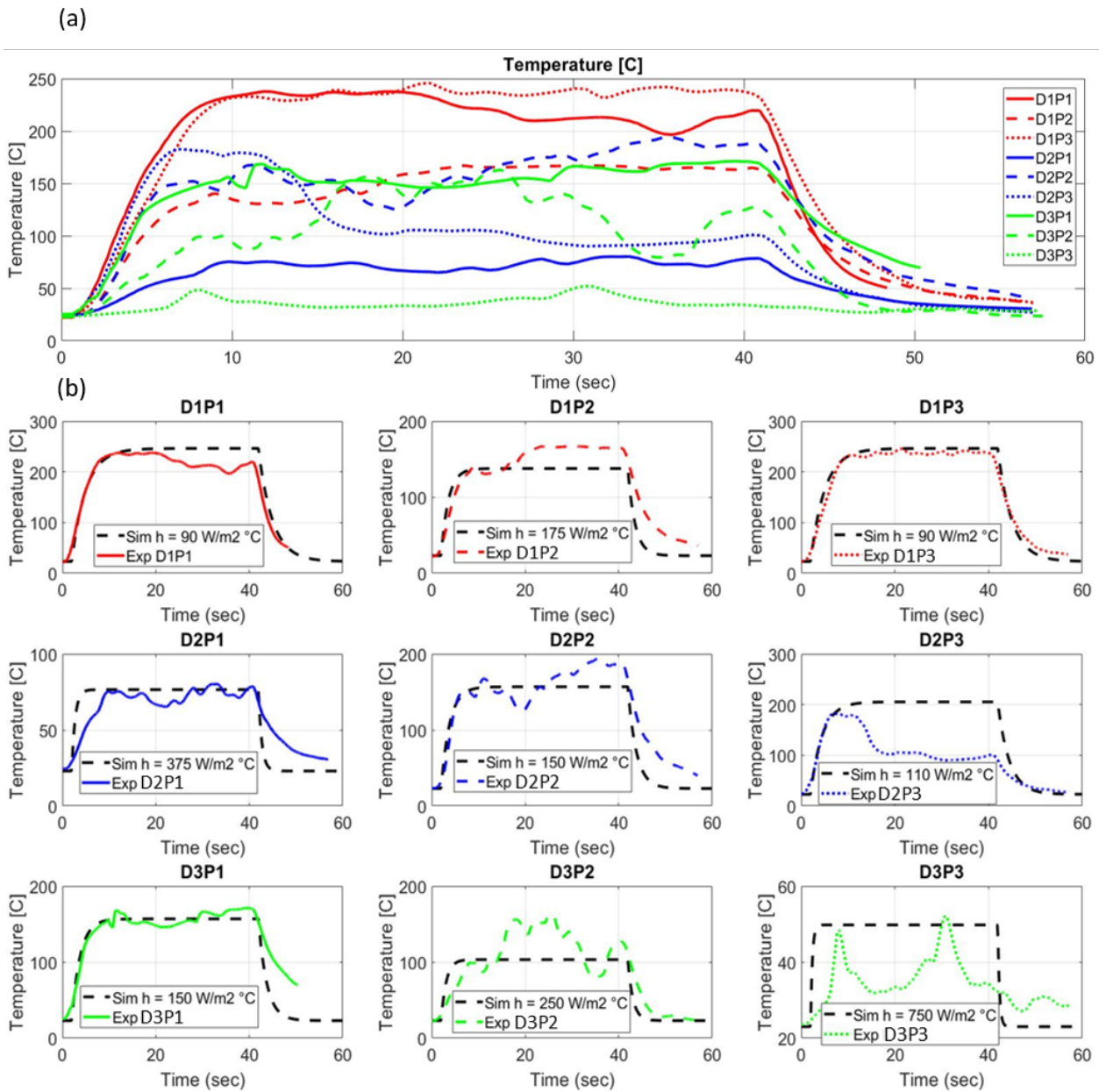


Figure 4.30. Simulink Matlab™ simulation results and experimental results for square input of 3.48 V, 0.66A at 4 g load. (a) Temperature in $^\circ C$ for all 9 samples experimental and (b) Temperature in $^\circ C$ for all 9 samples of different diameter and pitch individual comparison of experimental and simulation.

$$G = \frac{(GA + GM)}{2} \quad (4.4)$$

In equation 4.5, we see the shear strain of classical spring design based on Liang and Rogers and Hooke's law for torsion [191, 113]. This is for normal material or the first part of the constitutive model equation 4.3. F is axial load applied to the spring, d_w is the diameter, and D_s is the outer diameter of the coil.

$$\gamma = \frac{8FD_s}{\pi d_w^3 G} \quad (4.5)$$

Ω is given by

$$\Omega = -G\gamma_l \quad (4.6)$$

(c) Phase Transformation Model

The phase transformation model was presented by Jairakrean *et al.* [87], which was originally defined by Liang and Roger [113] to represent the relationship between the input temperature and the martensite fraction at low stress. Generally, the phase transformation model is modeled using both temperature and stress induction, but as Jairakrean *et al.* [87], we considered only the temperature induced phase transformation model by Liang and Roger [113] for simplifying the model and assuming low stress. Heating and cooling process causes the change of the martensite fraction between $0 \leq \xi \leq 1$. The equation of martensite fraction is a function of temperature and can be expressed as

For cooling process

$$\xi(T) = 0 \quad \text{for } T > M_s \quad (4.7)$$

$$\xi(T) = \frac{1}{2} \left[\cos \left[\frac{\pi(T - Mf)}{(Ms - Mf)} \right] + 1 \right] \quad \text{for } Mf < T < Ms \quad (4.8)$$

$$\xi(T) = 1 \quad \text{for } T < Mf \quad (4.9)$$

where Ms and Mf are the start and finish temperatures of martensitic.

For heating process

$$\xi(T) = 0 \quad \text{for } T > Af \quad (4.10)$$

$$\xi(T) = \frac{1}{2} \left[\cos \left[\frac{\pi(T - As)}{(Af - As)} \right] + 1 \right] \quad \text{for } As < T < Af \quad (4.11)$$

$$\xi(T) = 1 \quad \text{for } T < As \quad (4.12)$$

where AS and AF are the start and finish temperatures of austenitic.

(d) Deflection

The deflection δ of a spring is taken from Hadi *et al.* [65] as see in equation 4.13, where D_s, N, G, ds or dw, F, Ω, ξ are diameter of the spring, number of coils, shear modulus, diameter of the wire, the applied force, phase transformation coefficient, and fraction of martensite respectively.

$$\delta = \frac{8D_s^3 N}{Gd_w^4} F - \frac{\Omega N \pi D_s^{2*}}{\sqrt{3} G d_w} \xi \quad (4.13)$$

$$D_s^* = D_s * x \quad (4.14)$$

In equation 4.14, 'x' is the diameter reduction factor. We have considered the reduction of diameter due to the load extension before actuation. This plays a significant role in the deflection. The previous assumption of constant diameter during loading and unloading is defined for rigid structures, whereas CSMA's are more soft material. The diameter reduction factor varies for different geometry and load. For simulation we have ignored the non martensite part of equation 4.13 for displacement as we have measured the effective actuation in experiment.

4.9.4 Simulation

Table 4.8. Simulation parameters used in Simulink model

Parameter	Value
Length of actuator wire, Lw	$120 * 10^{-3}$ m
Wire diameter, ds or dw	$0.2 * 10^{-3}$ m [49]
Twinned martensite shear modulus, GM	$17 * 10^9$ Pa [65]
Austenite shear modulus, GA	$26.9 * 10^9$ Pa [65]
Austenite start temperature, AS	88 °C [202]
Austenite finish temperature, AF	98 °C [202]
Martensite start temperature, MS	72 °C [202]
Martensite finish temperature, MF	62 °C [202]
Martensite constant, CM	$10.3 * 10^6$ Pa/°C [202]
Austenite constant, CA	$10.3 * 10^6$ Pa/°C [202]
Maximum shear strain, γ_l	0.05 [65]
Ambient Temperature, T_∞	23 °C
Specific Heat of the SMA, CP	837.36 J/°C Kg [49]
Density of SMA, ro	$6.5 * 10^3$ Kg/m ³ [49]
Resistance per unit length of SMA, rho	29 Ω /m [49]
Mass of the actuator, M	ro*A*L = $2.43 * 10^{-5}$ Kg
Force Applied, F	4 g (0.039 N)
Resistance of the SMA wire, R_ω	$R_\omega = \text{rho} * L = 3.48 \Omega$

A Simulink® model was created that employs the equation such as heat transfer, phase transformation and constitutive model. The models are explained in the coiled SMA mod-

eling section. The same diameter reduction factor is used for the rest of the simulations and in figure 4.31 we see the martensite volume fraction change with respect to temperature for the same conditions. In figure 4.32, we see the voltage input, temperature, displacement and martensite volume fraction at 3.5 V, which was used for the experiment at 4g load and the simulated value at different diameter reduction parameters and a value of 0.3 fits closely. We have conducted the simulation at 3.5 V, 2.75 V, 2.05 V and 2 V with a square wave input with a frequency of 0.02 Hz to understand the phase transformation effect and the change as shown in figure 4.33, consisting of voltage input, temperature, displacement and martensite volume fraction. We can clearly see the time shift of strain and displacement with voltage or temperature variation from 2 V to 3.5 V. We see the change due to the phase transformation phenomenon as we increase temperature using voltage beyond the austenite and martensite finish and start temperatures. In figure 4.33, at 2 V we see a jump in martensite volume fraction due to the sharp change of temperature because of square voltage temperature input. In figure 4.34, we see similar time domain results for different pitches of the same spring diameter, and we see that higher pitch generally has higher strains. The compiler of simulation used is ode4 (Runge-Kutta) with fixed step of 0.0001, with a simulation time of 55 seconds. The input for the Simulink® is voltage, which is given into the heat transfer model whose output is the temperature. Then temperature is given as input to the constitutive model and the phase transformation model. Inside the constitutive model, we have shear stress and strain. In the phase transformation model, we have the martensite volume fraction, which acts as an input for constitutive model, force and deflection. The force and deflection models are nested in loop to each other as input and output with the martensite volume fraction as an additional input for both. In table 4.8, we have specified all the constants used in the simulation along with their magnitudes.

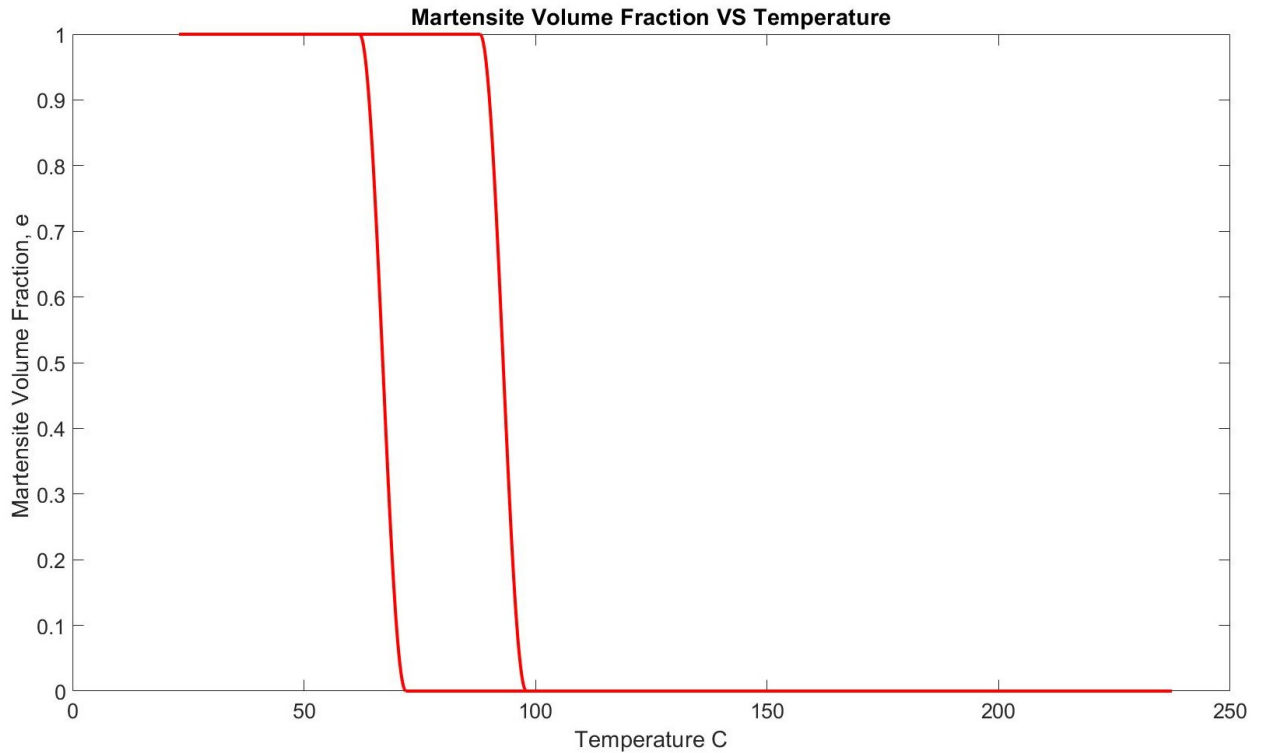


Figure 4.31. Martensite volume fraction Vs Temperature, Simulink® Matlab™ simulation results for square input of 3.5 V with a frequency of 0.02 for D1P3 sample. (Parameters are seen in table 4.8)

4.9.5 Discussion

In figs. 4.32 to 4.34, we see the experimental and simulation results of displacement (mm) for square input of 3.5 V at 4 g load with a period of 60 seconds, square wave that has a width of 66.667 % and phase delay of 2 seconds. We can clearly see that the Simulink® simulation and the experiment results with respect to the time are close. The cooling of the SMA is much slower in experiment compared to the cooling seen in the simulation due to external environmental conditions not introduced in the Simulink® model. We can see the switching between different phases of phase transformation, austenite and martensite in the simulation graph. The Simulink® model is tested under other conditions or constants and observed the variations accordingly. As we do not consider dynamic model in the simulation and assume that the martensite volume fraction is only temperature induced or dependent

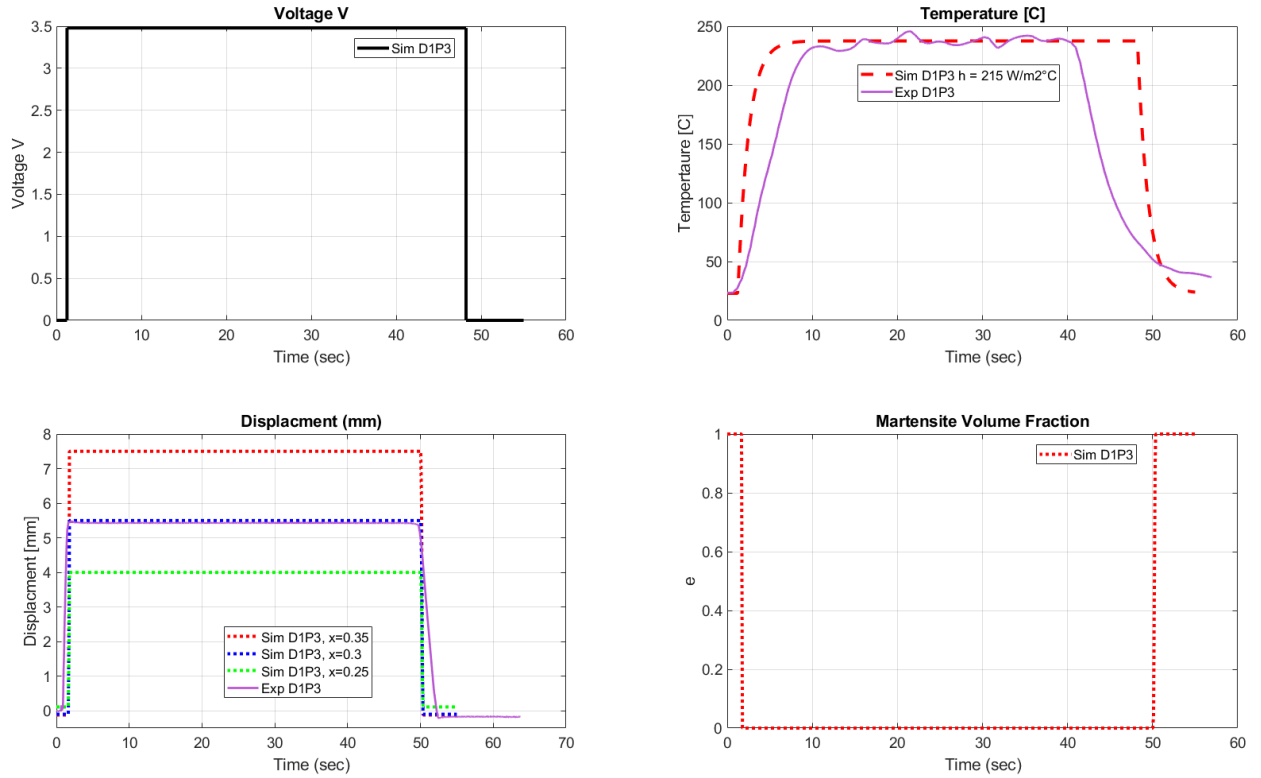


Figure 4.32. Simulink® Matlab™ simulation results for square input of 3.5 V with a frequency of 0.02 for D1P3 sample at different diameter reduction parameters. (a) Input Voltage in V, (b) Temperature in °C (c) Displacement in mm, (d) Martensite volume fraction, e. (Parameters are seen in table 4.8)

without stress induction, the model will have deviation from the experimental results at dynamic loading and heavy stress conditions.

In summary, we analyzed existing theoretical models, based on the phenomenological constitutive models to describe the actuation behavior of our SMA coiled springs and experimentally verified. We analyzed various parameters like strain and deflection with respect to temperature change during actuation. We have characterized the fabricated small diameter spring SMA actuator at different loads and quantified its actuation behavior at each load, to understand mechanical properties like strain and spring constant. We have shown 82.75 % strain when actuated with the spring SMA with a square of 10.7 V and 0.2 A, voltage

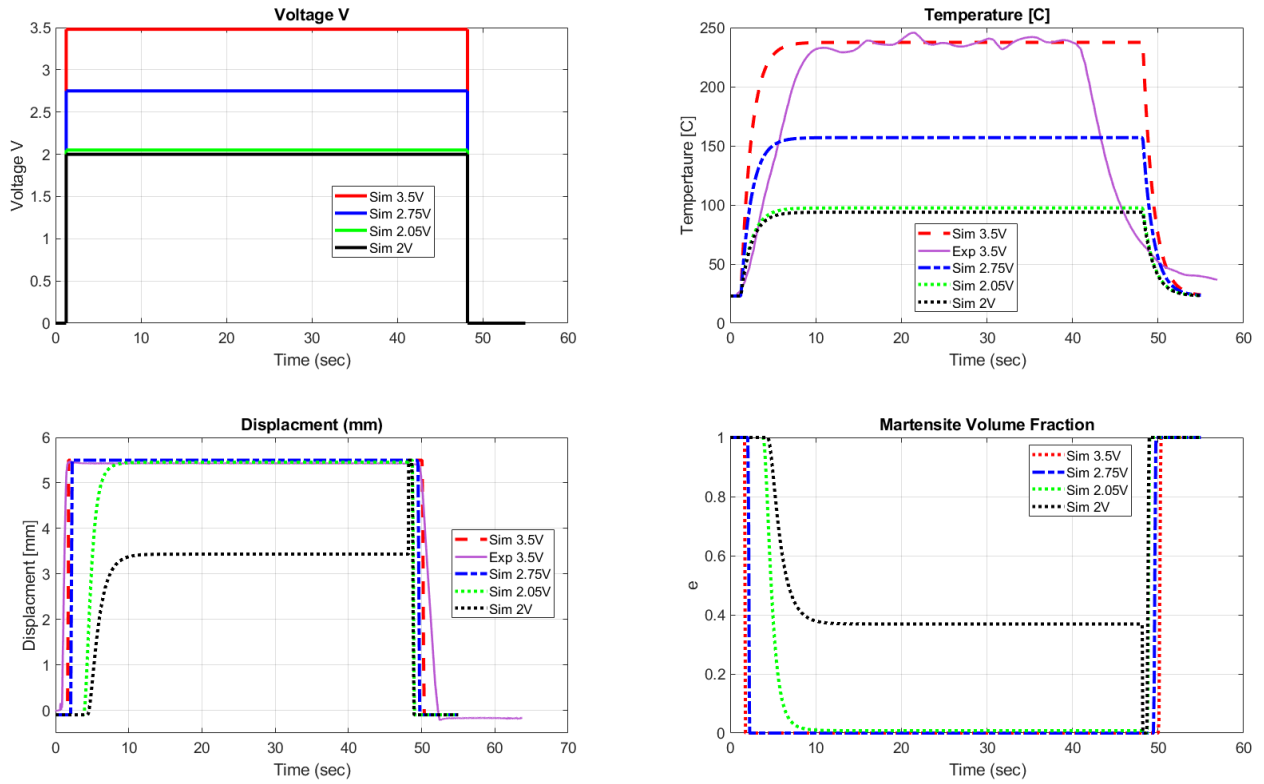


Figure 4.33. Simulink® Matlab™ simulation results for square input of 3.5 V, 2.75 V, 2.05 V and 2 V with a frequency of 0.02 for D1P3 sample. (a) Input Voltage in V, (b) Temperature in °C (c) Displacement in mm, (d) Martensite volume fraction, e. (Parameters are seen in table 4.8).

actuation with duty of $(300)/7$ % and a period of 7 seconds at a load of 4.375 g (200 times its weight). The higher strain rate in this section is due to high tension coiling used in fabrication, which ultimately will help in higher pumping of fluid in the artificial heart for humanoid robots.

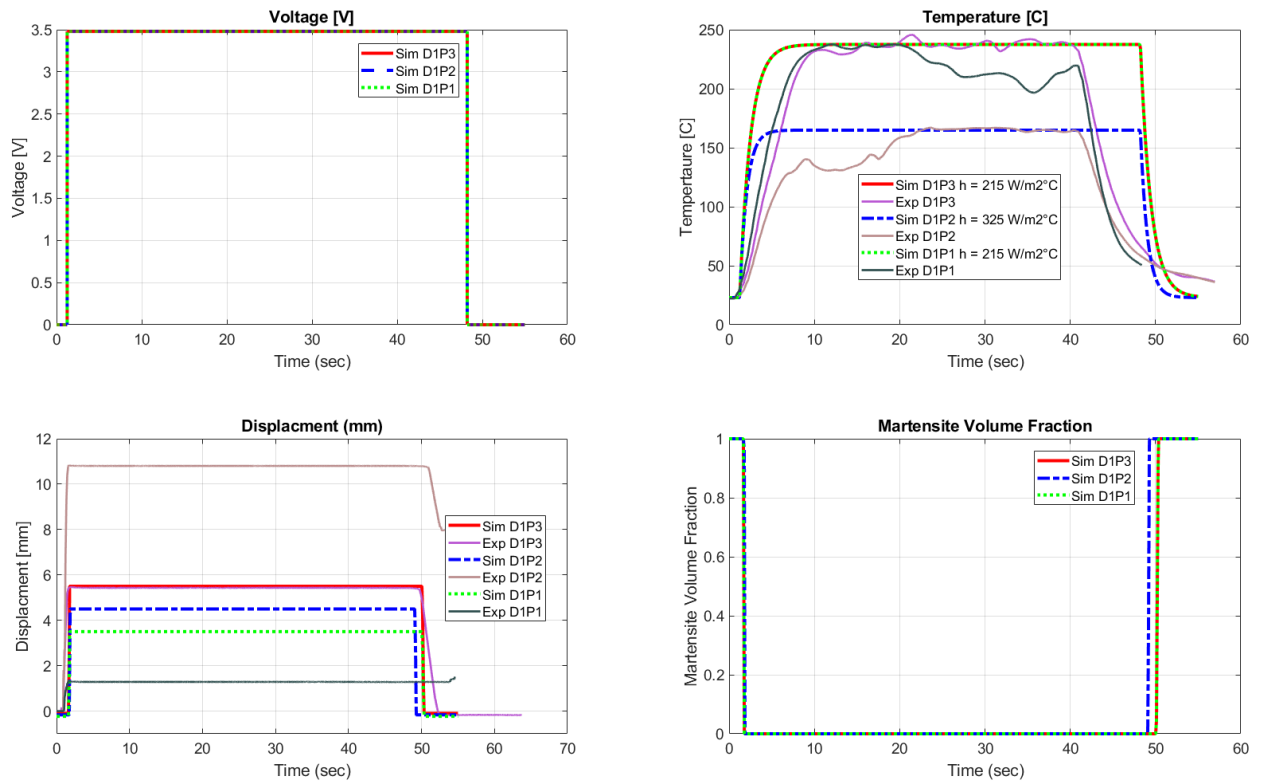


Figure 4.34. Simulink® Matlab™ simulation results for different pitches for square input of 3.5 V (a) Input Voltage in V, (b) Temperature in °C (c) Displacement in mm, (d) Martensite volume fraction, e. (Parameters are seen in table 4.8).

CHAPTER 5

APPLICATION OF COILED SMAS FOR HUMANOIDS AND HEALTH-CARE

5.1 Artificial heart for humanoid robot (SMAs Vs CSMA) ^{1, 2}

A soft robotic device inspired by the pumping action of a biological heart is presented in this study. Developing artificial heart to a humanoid robot enables us to make a better biomedical device for ultimate use in humans. As technology continues to become more advanced, the methods in which we implement high performance and biomimetic artificial organs is getting nearer each day. Research on development of artificial hearts for assisting the treatment of patients who are suffering from cardiac failure is being conducted for several decades [34]. In this section, we present the design and development of a soft artificial heart that can be used in a humanoid robot and simulate the functions of a human heart using regular SMAs and then CSMA and compare them. The robotic heart is designed to pump a blood-like fluid to parts of the robot such as the face to simulate blushing or anger by the use of elastomeric substrates with certain feature patterns for the transport of fluids. In the CSMA actuation , we present sequentially actuated robotic heart that is constructed with silicone elastomer, coiled SMA actuators and passive structures. The schematic diagram of the robotic heart is shown in figure 5.1 depicting the working principle of the device. Basically, the actuators integrated in the soft material are actuated one by one at certain interval of time, which is also known as sequential actuation. In this section we will introduce and discuss throughly the design, implementation and calibration of three soft pump artificial heart concepts and

¹Some parts are reprinted by permission from **Electroactive Polymer Actuators and Devices (EAPAD): International Society for Optics and Photonics, Artificial heart for humanoid robot** , Akshay Potnuru, Yonas Tadesse, ©2014

²Some parts are reprinted by permission from **Bioinspiration, Biomimetics, and Bioreplication: International Society for Optics and Photonics, Artificial heart for humanoid robot using coiled SMA actuators.**, Akshay Potnuru, Yonas Tadesse, ©2015

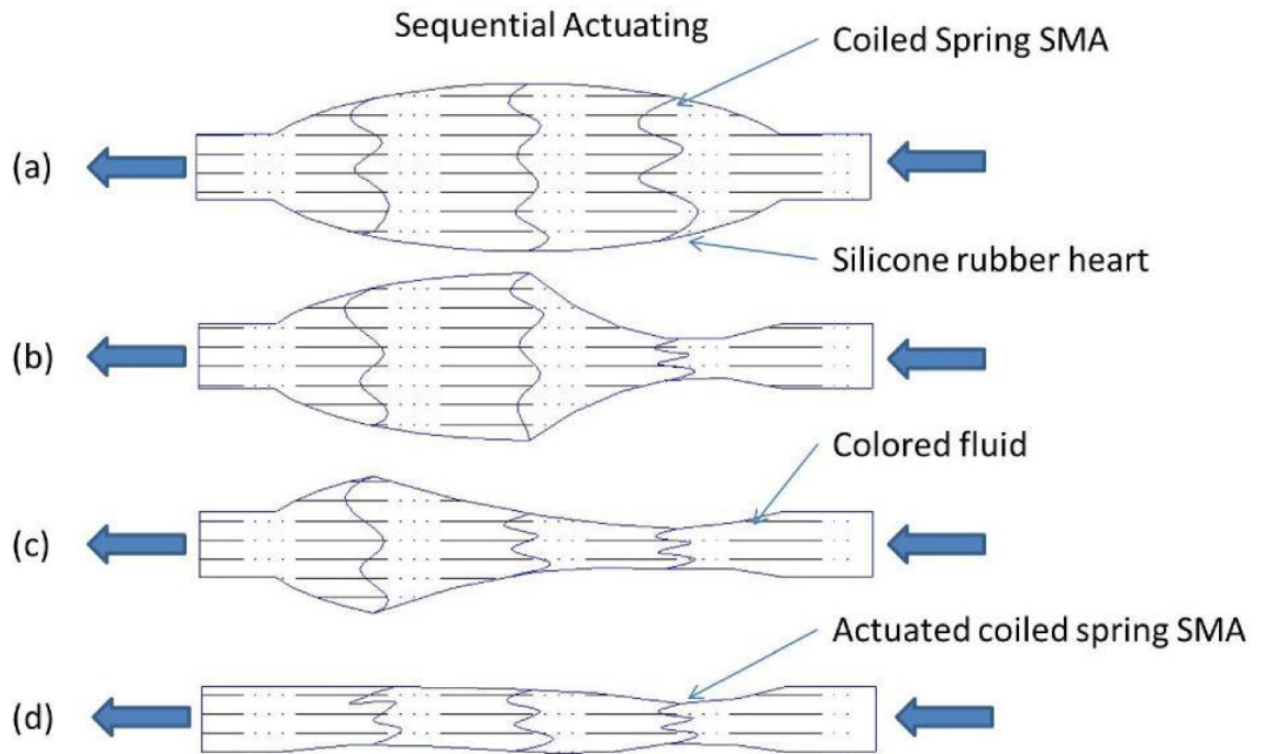


Figure 5.1. Peristalsis motion by sequential actuating (a-d) of the robotic heart

compare them. The first one is made with regular SMA wound around a soft heart structure, the second one is coiled SMA actuation of a curved rigid sleeve on the soft heart structure and the third is coiled SMA actuation of a flat rigid sleeve on the soft heart structure.

5.1.1 Biological Heart

Natural heart is a muscular organ which pumps blood through our body. It is the center of our circulatory system, which consists of a network of blood vessels like arteries, veins and capillaries, which carry blood to and from of all parts of the body [1]. Research has been done to show how facial color changes are an effective nonverbal communication and how it plays a significant role in expressing oneself [236]. Human heart plays a significant role in change of facial color as the flow of blood is regulated by the heart to face. The rate of human heart beat per minute plays an important role while expressing emotions like happy, sad, angry

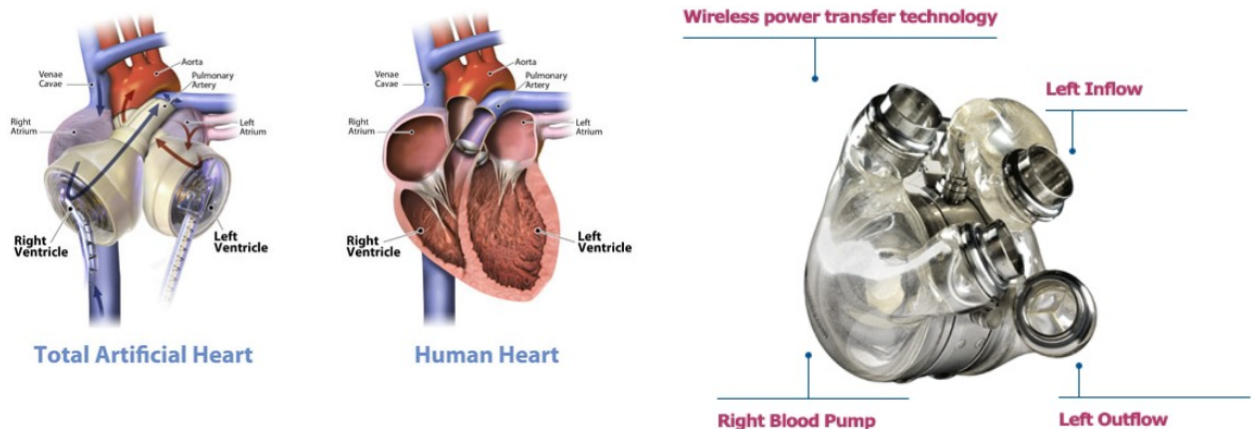


Figure 5.2. Artificial heart (a) CardioWest™ : Total artificial heart and human heart illustrations with detailed callouts (Courtesy of SynCardia Systems Inc.) [15] and (b) AbioCor® : World's First Artificial Heart (Courtesy of Abiomed Inc.)

and disgust [36]. Facial color change is unique human characteristic, which is not shown by other animals even though they possess cardiovascular apparatus which is first observed by Darwin in his studies [184, 39]. Humans mainly show facial coloration for anger, fear and embarrassment. In anger, we show reddening that is caused due to vasodilation, increased contractibility. In fear, we show blanching due to vasoconstriction and in embarrassment we show blushing due to vasodilation [20]. A study in various cultural groups showed that humans connect facial expressions with certain colors [38]. The study showed that anger and happiness are connected to the red color, as in the case naturally, we blush for happiness, anger and embarrassment. The green color is connected to disgust and sickness. Naturally these colors are exhibited in humans due to sudden variation in blood pumping to face from heart due to emotional changes experienced which are controlled by the brain. Facial coloration is prominent in specific areas of the face such as the cheeks where the blood vessels are wider in diameter and are nearer to the skin surface, and where there is less reduction of visibility due to tissue fluid [230].

5.1.2 History and Existing Artificial Hearts

The concept of artificial hearts originated in the 60's after the first heart transplantation in 1967 [63]. The first major breakthrough came out in 1965, where Kolff and Akutsu sustained a calf for almost forty four hours using a pendulum based artificial heart [89]. The first artificial heart transplantation was made in 1969 to Haskell Karp by Cooley and Liotta team where the artificial heart pumped 6 L/min and the patient lived with it for 3 days until a donor heart was available [63]. In 1970, Kolff and Javrik developed Javrik-7 prototype, which had two ventricles with air chambers and 6 titanium valves, with attachments to patients arteries [89]. In 1982, Javrik-7 was first implanted in a patient named Barney Clark who survived for 112 days [46]. Later Javrik was renamed as Cardiwest (shown in figure 5.2 (a)) and in 2001 Abiomed Inc. began its first Abiocor (shown in figure 5.2 (b)) artificial heart implants. The average life of the person after artificial heart was around 50 ± 42 days [15]. The starting models of the artificial heart had technical flaws and the need of huge power source made them impractical for permanent replacement [35]. This was a major reason for moving the artificial ventricles out of the body and transformed the artificial heart to a ventricular assist device [150]. Cleveland clinic's continuous-flow total artificial heart is one of the recent inputs to the science of artificial hearts which has one motor and one rotating assembly supported by a hydrodynamic bearing [97]. A completely simulated 3D thoracic anatomical model with implanted artificial heart was developed for testing and preoperational analysis in Japan [241]. An electro-mechanically actuated one piece artificial heart which can be completely implanted for permanent human use was developed by Takatani *et al.* [207]. An anatomically accurate, multi material, patient specific cardiac simulator with sensing and controls was developed which mimics the functionality of an artificial heart [168].

5.1.3 Shape Memory Alloy Artificial Muscles

Research on the development of artificial muscles, which can mimic natural muscles in performance, size and durability has been growing significantly in recent years due to their unique applications in the design of humanoid robotics and biomimetic systems [199, 202]. There are several kinds of actuators used as artificial muscles such as piezoelectric, electromagnetic, pneumatic, shape memory alloys(SMA) and electro active polymers (EAP) [198]. Shape memory alloys come under smart materials, which exhibit super elasticity and shape memory effects. The most widely used alloys in SMA actuators are nickel-titanium, copper-zinc and silver-cadmium at specific compositions. Shape memory effect can be described as the recovery of initial shape after deformation due to residual strain developed in the material by thermal cycling. There are several advantages of shape memory alloys such as: (1) small profiles generally around 100-150 μm in diameter, (2) high force to weight ratio, (3) utilizes simple current drive and (4) silent operation. The maximum operating frequency of SMA is less than 10 Hz, which limits its application as of their low operational frequency and narrow bandwidth, which is directly proportional to the time required for heating and cooling of the material [197]. Due to the benefits of SMA, a biologically inspired wet shape memory alloy actuated robotic pump was developed by Matthew *et al.* [152]. NiTi alloy was tested and showed a potential material to develop artificial muscles which can be used as a cardiac assistance device for dynamic cardiomyoplasty [196]. Nitinol, an alloy of nickel, titanium, cobalt was considered for actuating as an artificial muscle for the development of an artificial heart [178]. Covalent shaped shape memory alloy fibers were used for creating a sensorless control for a sophisticated artificial myocardial contraction by implementing PWM control method [187].

5.1.4 Related Robotic Heart Works

Recently, an artificial heart was developed which mimics the natural heartbeat. The device was actuated by NiTi (SMAs) artificial muscles powered by electrical power generated by microbial fuel cells (MFC's) [224]. An anatomically accurate, multi-material, patient-specific cardiac simulator with sensing and controls had been presented to mimic the functionality of an artificial heart [168]. Orejola et al. patented an autonomous artificial heart, which is a self-contained, totally implantable blood pump that replaces the whole heart with a small spherical device consisting of all the blood propulsion dynamics. The device can be controlled by a built-in micro controller [143]. One more recent patent by Kargakis presented an artificial heart comprising an energy storage device, an actuator and two pumping chambers. The chamber of the device has an inlet opening and an outlet opening, wherein each pumping chamber is bounded by at least one flexible wall and one rigid wall. The volume of each pumping chamber can vary by the deformation of the flexible wall by means of the actuator [93]. Frazier and Cohn recently presented a TAH (Total Artificial Heart) system for auto-regulating blood flow and maintaining the asymmetric pressure balance in the mammalian cardiovascular system. Their approach was based on reducing the resistance in blood flow and minimizing the pressure gradients to exploit the in-flow pressure sensitivities of continuous flow pumps [56]. Pelletier *et al.* showed a complete system overview of the fully implantable total artificial heart called ReinHeart-TAH. The device is still need to be tested on humans [149]. The other unique device presented is the one shown by Mohacsi and Leprince. They showed, the CARMAT total artificial heart that contains two chambers, each of which are separated by a membrane to form a blood and a fluid compartment where a viscous fluid is circulated by two electro-hydraulic pumps [130]. Most of the above studies are intended for human patients but our investigation will be focused on humanoids. We would like to design a robotic heart pump that changes the color of the face of a humanoid (shown in figures 5.3 and 5.4) and demonstrate facial expressions and emotions.

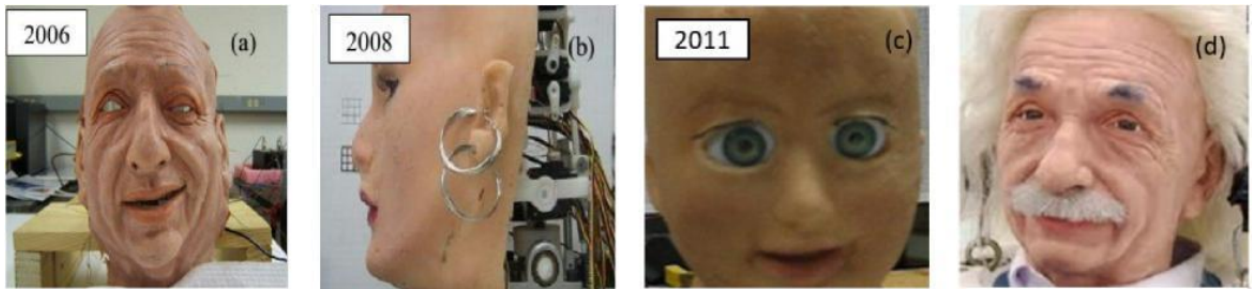


Figure 5.3. Facially expressive humanoid robots : (a) Albert-piezo: ultrasonic motors based humanoid head, (b) Lilly humanoid: servo motors and embedded piezoelectric sensors in the face, (c) Shape memory alloy based baby head, (d) Albert-HUBO, servo motors based humanoid (Courtesy of Hanson Robotics Inc.).

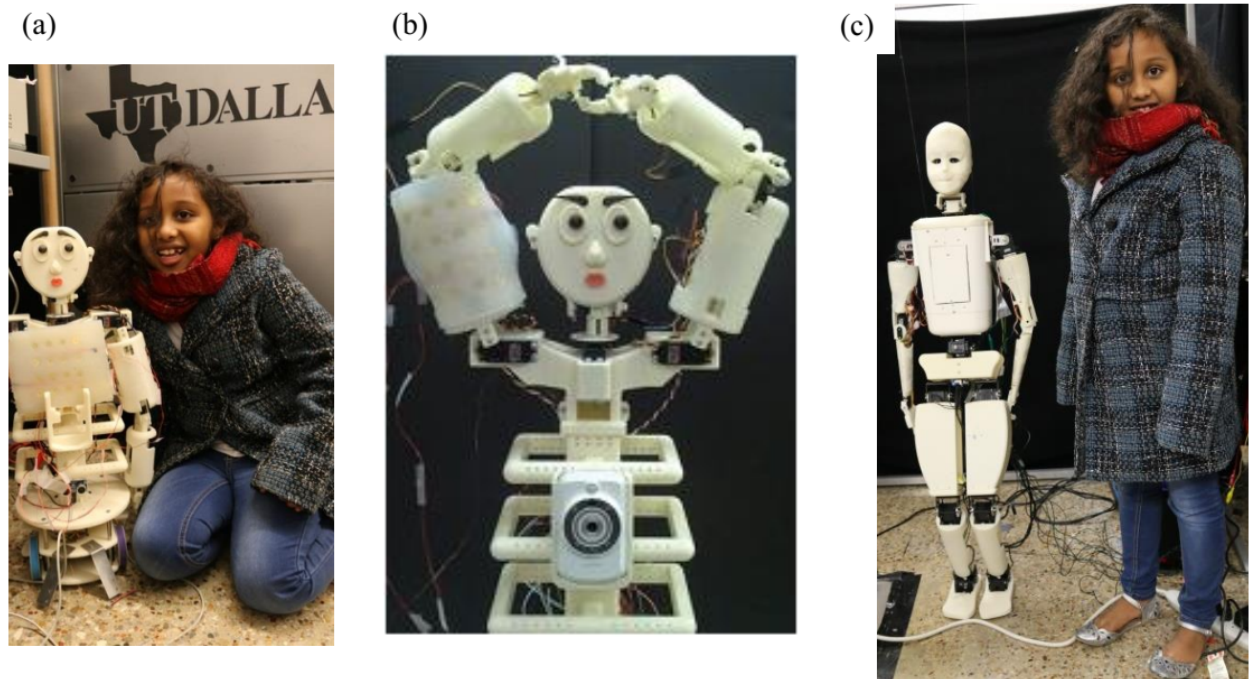


Figure 5.4. Humanoids developed in our laboratory (a) Buddy [153, 30], facially expressive but without skin in the face, (b) Buddy with embedded sensors in the skin and mounted in the arm and (c) HBS-1 a 7-year-old child size humanoid as compared to an eight-year-old child.

5.1.5 Humanoid Robots with Facial Expressions (HRwFE)

Study in androids, autonomous robotics, biomimetics and bionics such as humanoid robotics is being carried out worldwide extensively [9]. Humanoid robotics is a challenging and interesting area of research. It is related to the research of robots that mimics humans with regards to physical appearance and functioning. We categorized robots capable of displaying facial expressions by deforming their face as HRwFE. HRwFE is the acronym for Humanoid Robots with Facial Expressions. The research on humanoid robots with facial expressions (HRwFE) created a foundation in sociable communication between the robot and humans and vice versa [9, 199, 202, 198, 197, 152, 196, 178, 187, 68]. Many HRwFE prototypes have been presented in the past such as humanoid robot head ROMAN [24], Albert HUBO [141, 69], humanoid robot KOBIAN-R [215], Face Robot SAYA [71], F & H robot [228], Geminoid [139], WE-3RIV [128], ER-1 [226], and Baby-DARwln [202]. A few examples are shown in figures 5.3 and 5.4, Albert-piezo: ultrasonic motors based humanoid head [203], Lilly humanoid: servo motors and embedded piezoelectric sensors in the face [204], shape memory alloy based head [202], and servo motor based Albert Hubo [141, 69].

Unique capabilities of humanoids were demonstrated in the humanoid robot called WE-3RIV [128] that utilizes facial coloration to display emotions using red EL (Electro Luminescent) thin and light sheet device. In this section, we present a new robotic pump design to circulate fluids and hence change the color of a skin. For demonstration, a thin silicone piece (a representative of the cheek of a humanoid) is made by casting room temperature vulcanized soft rubber using 3D printed molds. The sample prototype will be discussed in the later section, can be easily applicable to the face robots shown in figures 5.3 and 5.4. We utilized washable colors that are used as the blood-like fluid contained in the artificial heart chamber. To demonstrate a proof of concept, a 50 mm square and 1 mm thick hollow silicone is casted representing a portion of a cheek membrane. A robotic pump is made by using coiled SMA actuators and connected to the silicone piece by thin pipes. As the actuators

are activated sequentially, bloodlike fluid from the chamber is pumped to the silicone piece and the fluid changes the color of the skin. Face coloration and facial expressions enhance the robot or humanoid capability; they enable the robot to have human-like appearance and function, which have diverse applications. For example, such robot or humanoid can be used as a humanoid patient simulator. The other major applications of humanoid robots with facial expressions (HRwFE) will be in education or entertainment. It can serve as communication personnel, as a press reporter that can read text effectively, as a receptionist at front desk, as a teacher in schools and in psychological rehabilitation for children with Autism [153, 199].

5.1.6 Design and Manufacturing

The human heart plays an important role in our metabolic system, which functions as a pump, providing the body with a steady flow of blood by means of regular rhythmic contractions. The outer wall of the heart is composed of three layers, the epicardium, the myocardium which is the muscle of the heart, and the endocardium . The muscle wall of the heart is responsible for pumping the blood through the systemic circulation. When pumping the blood out of the heart, the muscle wall of the heart contracts leading the decrease in the volume of the heart hollow cavity. The contractile elements in a comparable artificial heart should fulfill the function of the muscle wall of the mammalian heart. Due to the advantages of the shape memory alloy, it is anticipated that the SMA can be used as an efficient contractile element.

(a) Biologically Inspired Design (Design-1)

The design of the prototype heart is illustrated in figure 5.5. The heart is composed of a hollow body which is filled with colored fluid, a soft shell with inlet and outlet ports and a clamp. The material used for fabricating the heart is silicone, which enables the heart to

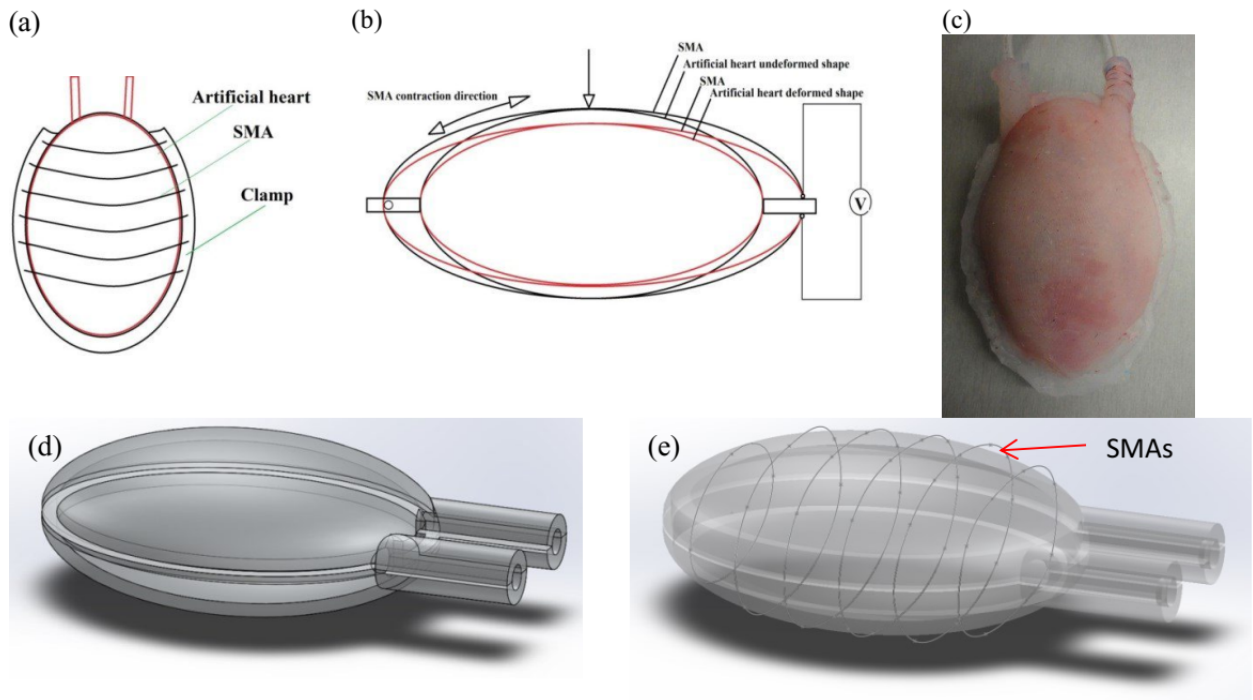


Figure 5.5. Artificial Heart (Design-1) (a) Schematic diagram of the front view of the artificial heart wrapped with SMA, (b) the section view of the artificial heart and (c) prototype, (d) CAD model and (e) SMA wrapped around the heart.

have a soft, flexible shell to be compressed by the contraction of the muscle wall. The shape memory alloy fibers (Flexinol® Actuator Wire) are employed as the contractile actuators of the heart. The Flexinol wires have two diameters, 130 and 200 μm . The smaller size actuator has less pulling force generating ability than the bigger size actuator while the smaller size actuator has quick response due to the less time needed to cool down. The SMA fiber undergoes a phase transformation from martensite phase to austenite phase when thermally activated by electrical current. During the phase transformation, the SMA fibers return to the original length, generating a 'recovery force' which can be harnessed to compress the soft heart.

In order to utilize the force generated by SMA fibers upon contraction, six shape memory alloys were anchored in parallel to the exterior of the heart (figure 5.5(a)). The SMA fibers have crimp ends, which are attached by screws to one side of the clamp. On the other side

of the clamp, small pulleys with a wheel diameter of 6.35 mm were placed. These pulleys help transmit the force generated by the SMA fibers through the body of the heart. When the SMAs are actuated, the liquid inside of the heart is forced out from the heart. Since the SMA fibers do not have a completely reversible contraction, a soft sponge consisting of porous material was employed inside of the heart to make the heart return its original shape. Once the electric current is removed from the SMA fibers, they require some time to cool down and relax. Two plastic tubes (internal diameter 2 mm) are attached to the inlet and outlet ports. The wall thickness of the artificial heart is 3 mm. The volume of the artificial heart is $1,16,631 \text{ mm}^3$. Figure 5.5 shows the schematic diagram, the CAD model and the sample artificial heart.

(b) Fabrication of the Robotic Heart

The workflow of the fabrication of the prototype heart is outlined step by step as shown in figure 5.6. In order to achieve the aim of our design, a total of four molds were designed in SolidWorks. Then these molds were exported as .stl (stereolithography) files to be fabricated by 3D printing using Stratasys Dimension Elite 3D printer. 3D printing, known as an additive manufacturing method, is a rapid prototyping technology which can fabricate a three dimensional object directly from computer-aided design data. While 3D printing has its limitations, 3D printing has several advantages compared with traditional manufacturing methods. Complex shape of the mold can be manufactured using the 3D printer. Another advantage is that 3D printing is time and cost saving for users. These molds are fabricated using ABS plastic rather than metal material that was often used in traditional casting mold method. After these molds are fabricated, they were assembled to cast elastomer that defines the outline of the artificial heart. Platinum cured silicone rubber (Ecoflex-10) was used to fabricate the artificial heart. At first, equal amount of part A and Part B were mixed thoroughly in a beaker for 3 minutes. It is recommended to do the mixing process in vacuum

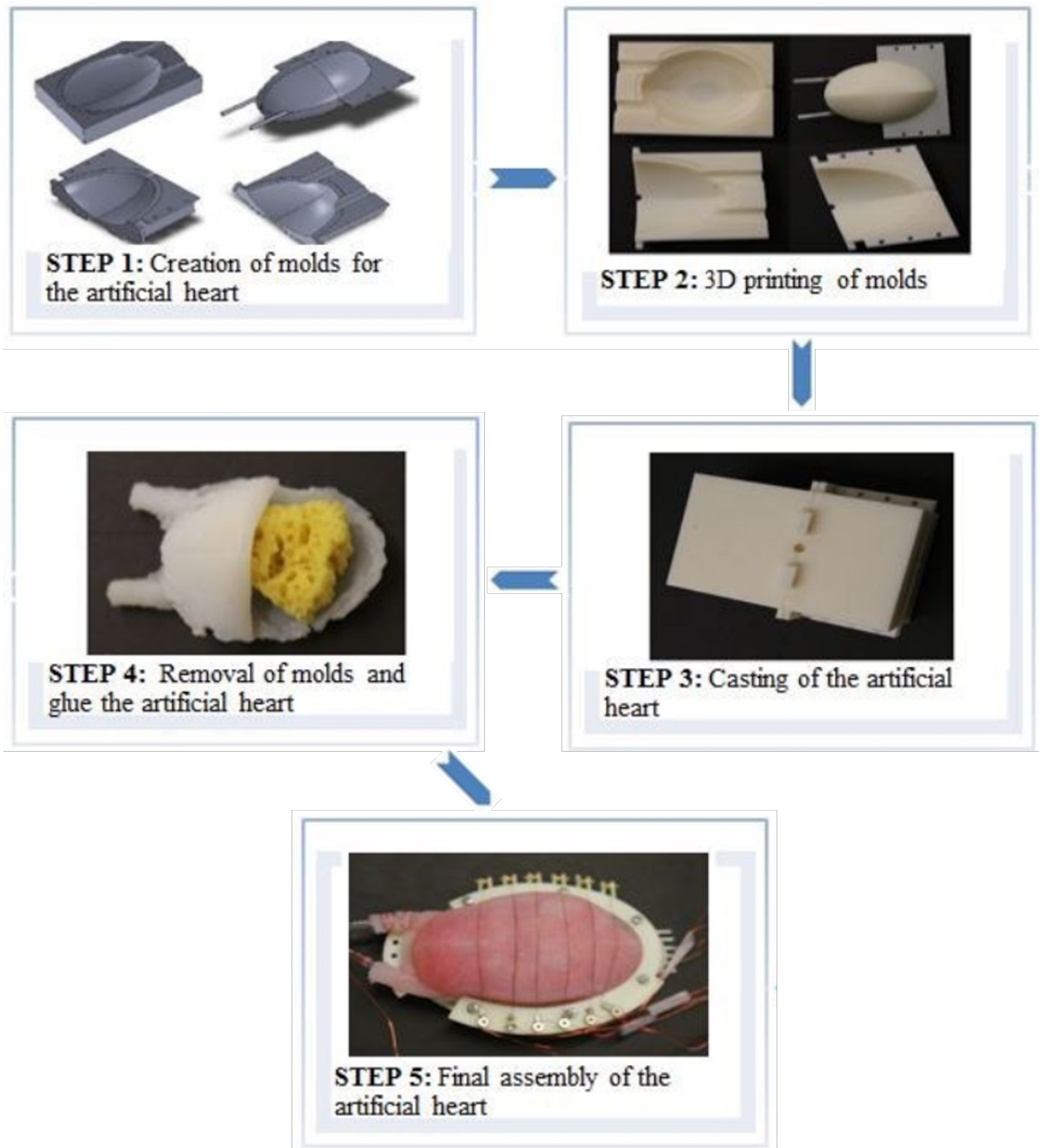


Figure 5.6. Manufacturing diagram for creation of artificial heart wrapping with SMA fibers.



Figure 5.7. Fabrication of coiled SMA wires: SMA wires wrapped around bolts and secured by nuts .

degassing to eliminate the air bubble in the mixture. A release agent was sprayed over the molds' surfaces to ensure a smooth demolding. After that procedure, the mixture is poured into the assembled mold slowly and continuously using a syringe in order to get rid of air bubble as much as possible. It took 4 hours for the rubber to cure at room temperature. In step 4, Sil-Poxy silicone adhesive was used to bond the silicone parts together. Finally, the SMA wires were routed around the heart in parallel pattern and the ends of SMA wires were fixed to a clamp. The clamp was designed to provide the SMA wire initial pre-stress.

5.1.7 Coiled Shape Memory Alloy (SMA) Actuators for the Robotic Heart

Shape memory alloy materials exhibit shape memory and super elastic effects. These effects are associated with stress, strain and temperature state of the material. At low temperature, the shape memory effect is observed whereas, at high temperature, the super elastic curve will be observed. The shape memory effect (SME) is a result of temperature and stress dependent shift in the material's crystalline structure between the martensite and austenite phases.

The unique change in phase between the two crystalline structures enables the material to change its shape, and the material is used as an actuator or artificial muscle for numerous applications. It can operate in either the air or fluidic medium. The low-temperature phase, martensite is a soft structure and, on the other hand, the high temperature phase, austenite is hard structure [125]. At high temperature, the material changes to austenite phase, and when it cools down, it will transform to martensite. The shape memory effect (SME) is the recovery of large strain due to the application of thermal cycling (heating and cooling).

Various shapes of SMA actuators can be made for various applications. The cylindrical geometry can contract 3-5 % strain and the coiled geometry can deform up to 200% [198]. The coiled SMAs in this section were prepared by manually winding 200 μm SMA wire over bolts and securing with nuts. This technique was done to create spring-like structures and the assemblies were annealed in a furnace (ThermolyneTM industrial bench top muffle furnace, model number FD1535M) at 390°C for 45 mins and naturally cooled. The annealing temperature was taken from the data presented by Kim *et al.* [96]. They presented a comparative study on the performance of coiled SMAs for different annealing temperatures. Figure 5.7 shows the fabricated coiled SMA wires. As geometrical parameters are the key factors that contribute to the performance of the actuators, we demonstrate the sizes and shapes of all samples that we test.

5.1.8 Characterization of Coiled SMAs

Experiments were carried out to test the performance of the coiled actuators. A 250 mm long SMA (Dynalloy Inc.) wire (200 μm diameter) was wrapped around a helical screw that has 2 mm in diameter and 25 number of turns. The resulting coiled SMA after annealing was 20 mm in length and 2 mm in diameter. The SMAs were tested first at no load condition, and the best-observed actuation was at 4V, resulting a strain of 39 %. Figure 5.8 shows a comparative deformation of the coiled SMA with respect to voltage at no load condition.

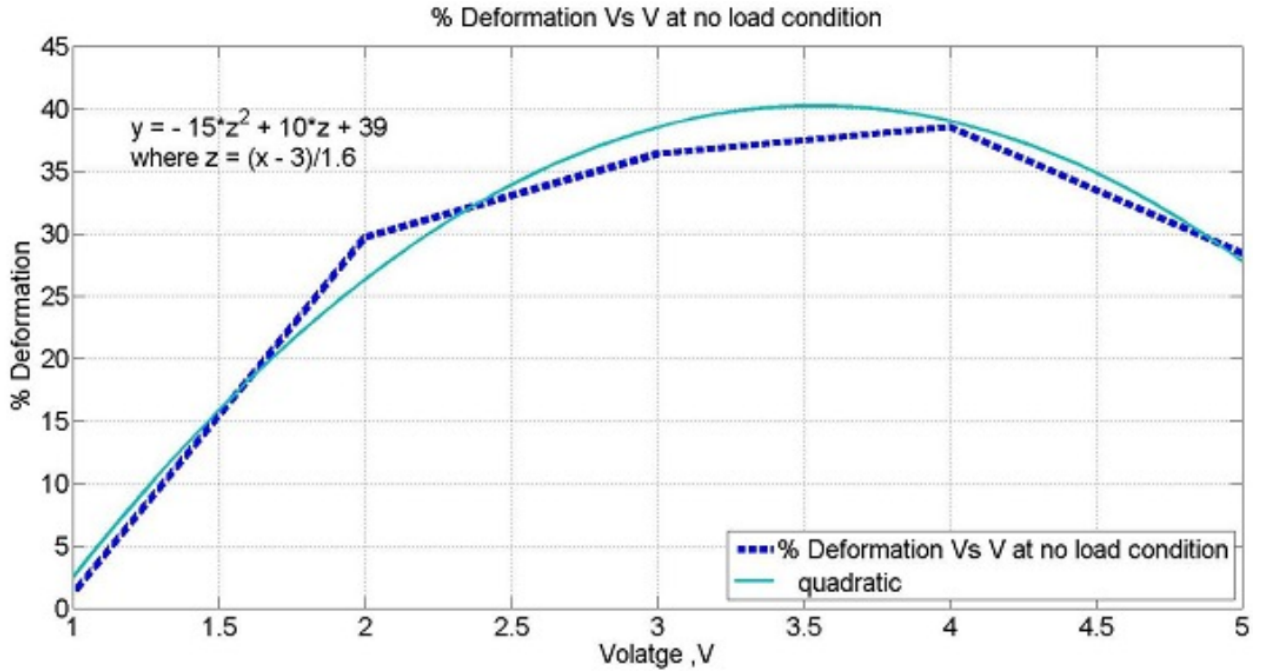


Figure 5.8. Deformation Vs. Voltage of the coiled SMA actuator at no load. (Length = 20 mm, $d = 200\mu\text{m}$, $D = 2\text{ mm}$)

Figure 5.9 shows snapshots of the video at different time sequence of the actuation at no load condition and 4V. The overlapped image of actuation is shown for simple comparison. Since the coil was under no load, it was able to freely move at any or most convenient direction to reduce stress in a nonlinear fashion. The characterization under load condition was done for 3 weights, 0.10 g, 0.22 g and 0.66 g using nuts as a dead weight. The deformation for an applied weight of 0.1 g was the best deformation with more than 92% as under a little tension. At 0.66g it had 34.6% which was significant as compared with 0.22 g load. This could be due to the repeatability issues of coiled SMAs, which needs further study and it can be due to geometric imperfections during fabrication. Figure 5.10 and 5.11 shows a timeline sequence of the actuation at 0.1 g and 0.66 g condition at 4V with an overlapped merged image of actuation respectively.

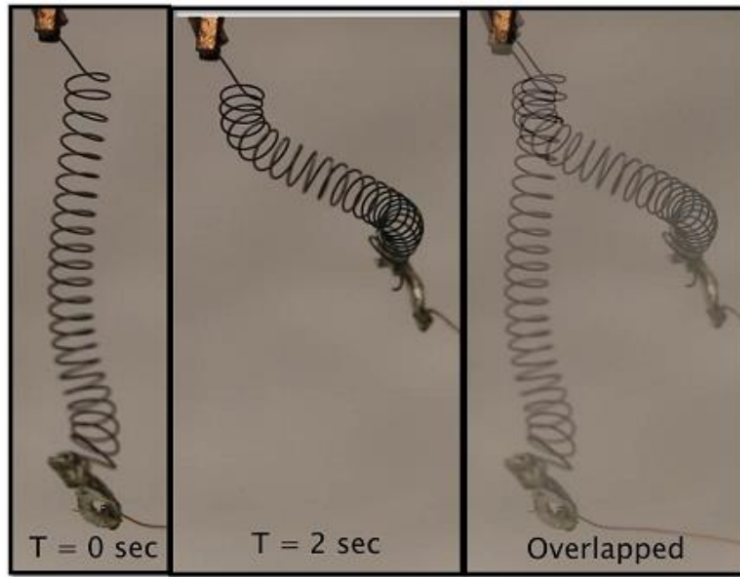


Figure 5.9. Timeline sequence of the actuation at no load condition at 4V at $T = 0$ sec and 2 sec and an overlapped merged image of actuation.

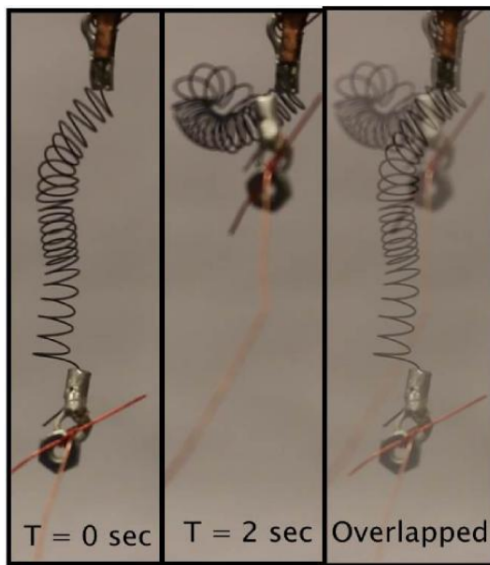


Figure 5.10. Timeline sequence of the actuation at 0.1 g load condition at 4V at $T = 0$ sec and 2 sec and an overlapped merged image of actuation.

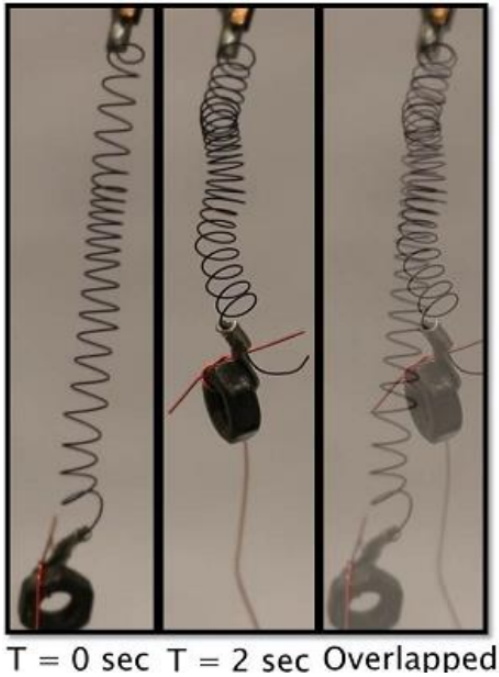


Figure 5.11. Timeline sequence of the actuation at 0.66 g load condition at 4V at $T = 0$ sec and 2 sec with an overlapped merged image of actuation.

5.1.9 Design and Manufacturing of the Robotic Heart (Design 2)

Bioinspired Design

Figure 5.12 illustrates the bio- inspired design of the robotic heart, which is composed of a hollow body filled with colored fluid, a soft shell with inlet and outlet ports, and a 3 mm diameter transparent tube. The fabrication material used for the heart is silicone that is soft and flexible. The silicone membrane is compressed by the contraction of SMA actuators that connect the top and bottom hard structures. The shape memory alloy fibers are used as the contractile actuators for the heart. The Flexinol wires come in several diameters from 25 to 500 μm . The smaller the diameter, the less the pulling force. On the other hand, the larger the diameter, the more the pulling force. On the contrary, the smaller diameter wires are quick to response due to faster cooling after actuation. In order to utilize the force generated by SMA fibers upon contraction, 18 coiled shape memory alloys of diameter

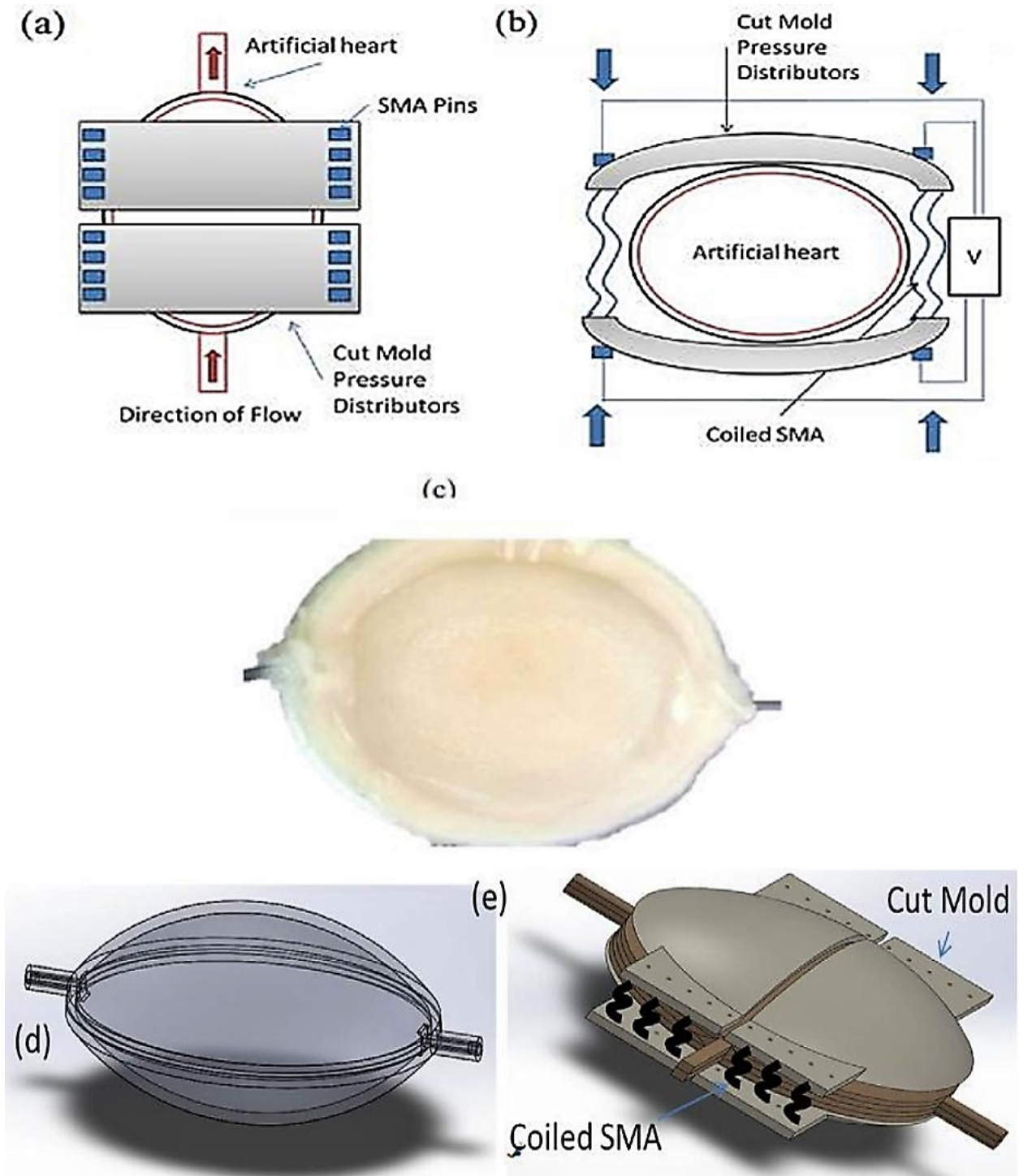


Figure 5.12. Artificial Heart (Design 2): (a) Schematic diagram of the top view of the artificial heart attached with hard structure pressure distributors, (b) the section view of the artificial heart and (c) prototype, (d) CAD model and (e) Coiled SMA attached to the side of the hard structures the cover the robotic heart.

200 μm were attached to the hard structures in perpendicular direction of the flow (figure 5.12(a)). The SMA fibers were attached to the hard structures using holes and pins. When the SMAs are actuated using the peristalsis motion by sequential actuation, the liquid inside of the heart will be pumped out from the heart towards a hollow silicone membrane. The silicone membrane is a representative part of a humanoid cheek. Since the SMA fibers take longer time to cool and come back to original shape, a finely cut soft sponge material pieces consisting of porous material was used inside of the heart. The sponge serves as a spring and helps in the return motion of the robotic chamber. Once the electric current is removed from the SMA fibers, they require some time to cool down and relax. Two plastic tubes with an internal diameter of 2 mm and outside diameter of 3 mm are attached to the inlet and outlet ports. The wall thickness of the artificial heart was 1-2 mm as it varies at the curve edges. The volume of the artificial heart is 1,16,631 mm^3 . Figure 5.12 shows the schematic diagram, the CAD model, and the new artificial heart design.

5.1.10 Fabrication of Design 2

The fabrication technique is similar to the previous design 1. The work-flow of the fabrication of the prototype heart (Design 2) is outlined step by step as shown in figure 5.13. Four molds were designed in SolidWorks 2014, two for the heart half section and two for cheek half section. These CAD mold parts were exported as STL files and fabricated by 3D printing using Stratasys Fortus 250 3D printer. After these molds are fabricated using the 3D printer, they were assembled to cast the silicone elastomer that forms the outer surface of the artificial heart and the cheek half sections. Platinum cured silicone rubber (Ecoflex-10) was used to fabricate the artificial heart. An amount of 3 drops of washable skin color is added to the mix to get a skin-like membrane for both heart and cheek. An equal amount of part A and Part B were mixed thoroughly in a container for 3 minutes, which is recommended to do under vacuum degassing to eliminate air bubbles. A release agent was sprayed over the molds'

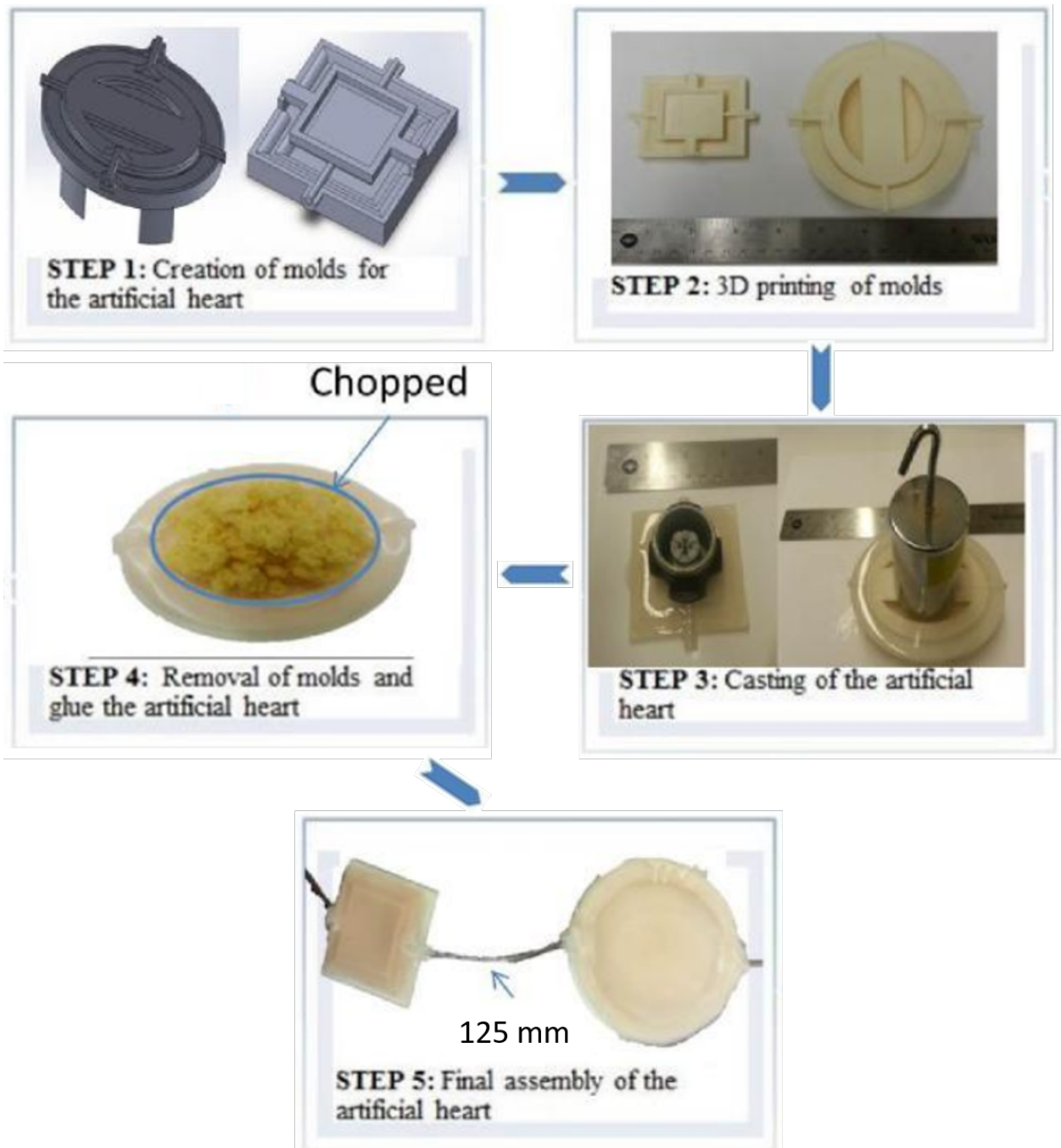


Figure 5.13. Manufacturing process diagram for creation of artificial heart.

surfaces to ensure a smooth removal of the formed molds. Then, the mixture is poured into the assembled mold slowly and continuously using a syringe in order to get rid of air bubble as much as possible. The elastomer takes 4 hours to cure at room temperature. Sil-Poxy silicone adhesive was utilized to bond the silicone half sections of heart and cheek together that took less than half an hour to cure. Finally, the CSMA wires were placed through the holes in the hard structures, and the assembly is made for actuation.

5.1.11 Modeling and Simulation of SMA Heart

This section describes the computer aided design (CAD) and analysis of the artificial heart using SolidWorks™ software. A hyperelastic stress analysis simulation is presented by varying pressure and using the simulation results, the volume of the fluid pumped at different pressures is calculated. Lastly, a flow simulation of the fluid inside the CAD model is shown to understand the flow pattern.

(a) Hyperelastic Stress Analysis

To calculate the volume of liquid that the heart model can pump using NiTi shape memory alloys, we conducted finite element analysis (FEA) to find the deformation under different pressures. The model material used for the heart model was silicone rubber which has a hyperelastic deformation. The finite element analysis (FEA) simulation was conducted using ABAQUS 6.13 (Dassault Systemes, France) and the hyperelastic simulation was conducted using Mooney-Rivlin model [131, 167].

Mooney-Rivlin model:

Continuum mechanics is a mechanics branch that studies deformation motion of a solid subjected to forces [58]. Mooney-Rivlin model is a continuum mechanics model that study deformation of a hyperelastic solid. The Mooney-Rivlin is an update of the Neo-Hookean

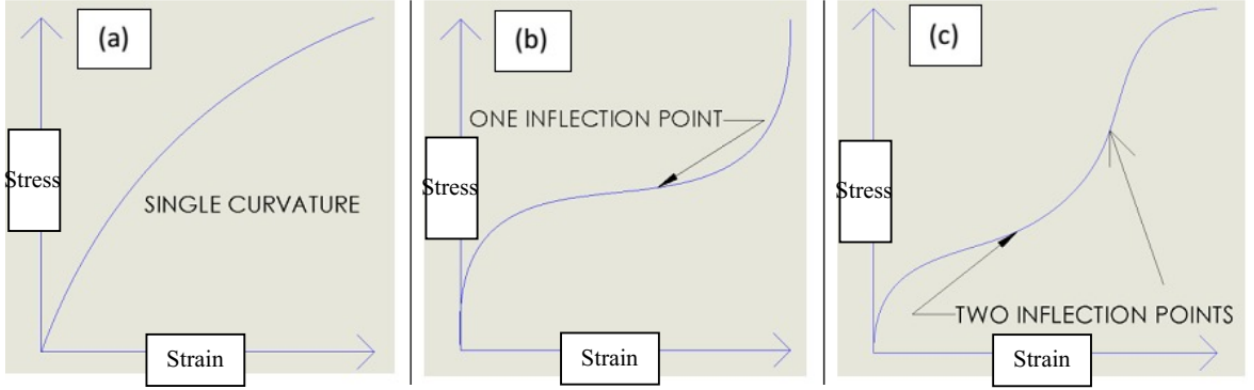


Figure 5.14. General hyperelastic material stress-strain curves (a) single curvature, (b) one inflection point and (c) two inflection points.

model and typically comes in two parameter, three parameter, five parameter or nine parameter [120]. The two parameter model is typically used for single curvature (no inflection points) materials in their stress-strain curve models. Five parameter and nine parameter forms are used if there is one or two inflection points in the material stress-strain curve models. This is shown in the figure 5.14 (a)-(c).

The two parametric form of Mooney-Rivlin model [72] is given by:

$$W = C_{10} (\bar{I}_1 - 3) + C_{01} (\bar{I}_2 - 3) + \frac{K}{2} (J - 1)^2 \quad (5.1)$$

$$\bar{I}_1 = J^{-\frac{2}{3}} I_1, I_1 = \lambda_1^2 + \lambda_2^2 + \lambda_3^2 \quad (5.2)$$

$$\bar{I}_2 = J^{-\frac{4}{3}} I_2, I_2 = \lambda_1^2 \lambda_2^2 + \lambda_2^2 \lambda_3^2 + \lambda_3^2 \lambda_1^2 \quad (5.3)$$

$$J = \det(F) = \lambda_1 \lambda_2 \lambda_3 \quad (5.4)$$

where C_{10} and C_{01} are constants derived from curve of the experimentally measured stress-strain of the material. \bar{I}_1 and \bar{I}_2 are the first and second invariant of the unimodular

component of the left Cauchy-Green deformation tensor. J is the determinant of deformation gradient F , and K is the distortional response. We used the two parametric form of Mooney-Rivlin model for the analysis. The EcoFlex-10 silicone material constants C_{10} and C_{01} were provided to the finite element analysis simulator using practical values. C_{10} and C_{01} were taken as 1 and 0.9 respectively from the experimental data published by Shergold *et al.* [185]. We used ABAQUS 6.13 as our Finite Element Analysis (FEA) simulator.

The finite element analysis results are shown in figure 5.15. The un-deformed model is shown in figure 5.15(a) depicting the center cross-section of the heart which has highest area. The cross-section was designed as a surface with surrounding faces to exact dimension of the prototype. The rectangular projections on the side were set to be the fixed in the model and to hold the SMAs in position. The expected deformations of the SMAs are in the tangential direction of curved model as the SMAs are wounded around the curved surface of the model. The applied load on the model was a uniform pressure acting inward to the outer surface which will eventually reduce the volume of the model and pump the liquid out as desired. So we considered the resultant uniform pressure for the simulation. The pressure load was varied from 0.001 MPa to 0.01 MPa. The analysis is not conducted beyond 0.01 MPa as the deformation is too large for ABAQUS to numerically calculate due the hyperelastic property of the material and the simulation failed. The boundary condition used for the simulation was given by fixing the two extreme sides of the rectangular projections as shown in figure 5.15 (b)-(f). The meshing size used was 3 with the free Quad-dominated element shape which created 75 elements. Figure 5.15 (b) and (c) show the contour plot of the resultant deformation of the model after the simulation with maximum and minimum x axis and y axis at applied pressure of 0.01 MPa. The maximum deformation in x axis is 0.32 mm at node 4 and the minimum deformation in x axis is -0.367mm at node 20, the negative sign depicts the opposite direction. The maximum deformation in y axis is 2.821 mm at node 24 and the minimum deformation is -2.71 mm at node 8. The minimum resultant deformation is 0 mm

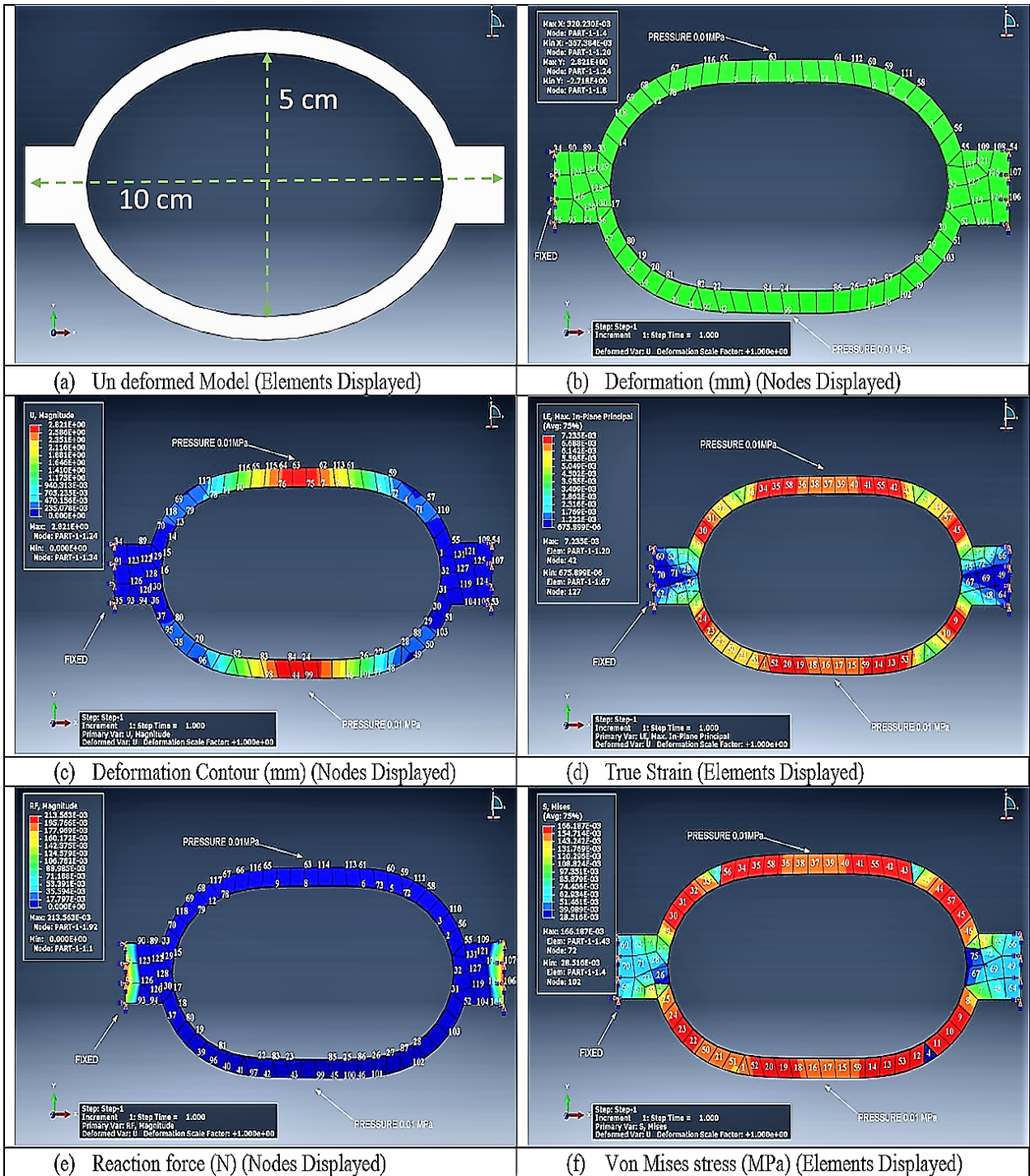


Figure 5.15. Hyperelastic stress analysis in ABAQUS 6.13 (a-f) at pressure of 0.01 MPa

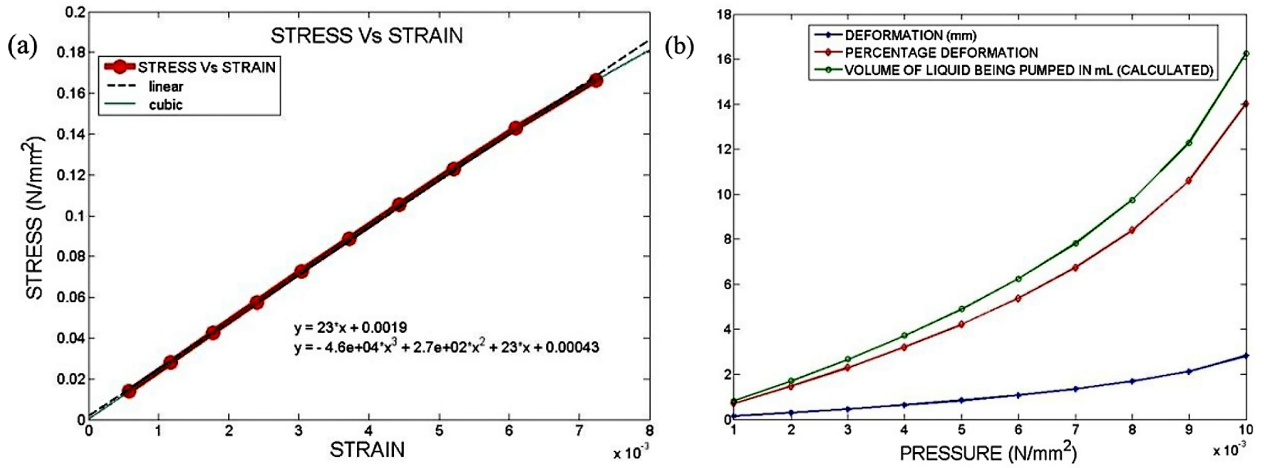


Figure 5.16. FEM simulation results plotted in MATLAB 2013b (a) Stress vs strain at center top (Node 37) and (b) Pressure Vs (Deformation, % deformation and volume of liquid being pumped in mL (calculated)) on one side of the model

at node 34(fixed end) as seen in figure 5.15 (c). Figure 5.15 (d) shows the maximum in plane principal true strain of average of 75% of all the elements in the contour deformed model with the maximum and minimum values $7.24x10^{-3}$ at element 20 and node 42 and $675.9x10^{-6}$ at element 67 and node 127 respectively. Figure 5.15 (e) shows the resultant reaction force of all the elements in the contour deformed model with the maximum and minimum values $213.56x10^{-3}$ N at node 92(fixed end) and 0 N at node 1 respectively. Figure 5.15 (f) shows the maximum von-Mises stress of average of 75% of all the elements in the contour deformed model with the maximum and minimum values $167.19x10^{-3}$ MPa at element 43(diagonal axis of the ellipse) and node 72 and $28.52x10^{-3}$ MPa at element 4 and node 102 respectively.

Figure 5.16 (a) shows the stress vs strain graph of the simulation obtained by varying pressure from 0.001 MPa to 0.01 MPa. The stress-strain curve shown in figure 5.16 is a linear relationship for the pressure considered. We can clearly see that figure 5.16 (a) and figure 5.14 (a) of the two parameter Mooney-Rivlin single curvature are similar as expected. The deformation analysis at the maximum possible pressure of 0.01 MPa was used to calculate the percentage deformation and provided approximately 14% on one side of the pressured model. Using this percentage deformation and integrating to the whole 3D model assuming

that the deformation is uniform and constant all through the body on both sides, we obtained the reduction of volume in the model due to compression. It was found out that the volume of liquid as $2 \times 16.26 = 32.52 \text{ mm}^3$ or 32.52 mL which is sufficient to clearly fill the cheeks of a humanoid with colored liquid (used as a blood). The actual pressure exerted by the SMAs will be much higher than the maximum pressure used in the simulation. This depends on directly on the length of SMA and maximum 4% deformation at maximum power conditions. The simulation results are in the range of experimental results and are in hyperelastic deformation neglecting hydrodynamic losses and inertial losses which can impact the performance of the actual pump.

(b) Flow Analysis

The flow simulation was done in SolidWorks 2014 using its FloWorks 2014 (Dassault Systemes, France) flow simulator. The inlet and outlet pressure conditions were taken from the results presented by Hayward *et al.* [72], the maximum pressure a regular small scale syringes can produce. From the previous hyperelastic simulation conducted at maximum possible load pressure of 0.01 MPa, we calculated the maximum volume that can be pumped and obtained approximately 32.52 mL. From the results of Hayward *et al.*[72], we best estimated the volume displaced assuming the heart model has similar pressure drop as the syringe and used a maximum pressure drop of approximately 32 psi (220.6 kPa). Therefore, we set the inlet pressure at 43 psi (296.48 kPa) and varied the outlet pressure from 11 psi (75.84 kPa), 17 psi (117.2 kPa), 23 psi (158.58 kPa), 29 psi (199.95 kPa) and 35 psi (241.32 kPa) to obtain different maximum velocities at five different pressure values. The analysis assumed that the robotic heart pump is already deformed due to actuation and the flow analysis was carried out assuming constant volume at certain period of time. This estimation was done mainly to see the variation of the velocities at different pressures and to see the flow path of the liquid inside the heart model using practical values. The simulation was

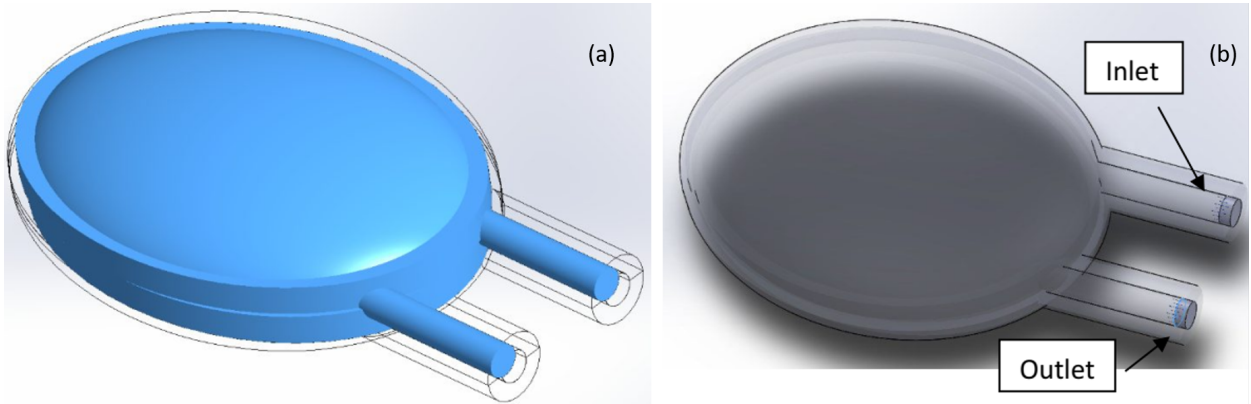


Figure 5.17. (a) Volume of the fluid inside the heart model during flow simulation = 116 mm^3 or 116 mL (b). Shows the inlet and outlet valves of the flow simulation

done at temperature of $68.09 \text{ }^\circ\text{F}$ (room temperature $20.05 \text{ }^\circ\text{C}$). Figure 5.17(a) and (b) show the volume of fluid (blue color), and the inlet and outlet of the heart model respectively.

Figure 5.18 shows the simulation results of the maximum velocity of the fluid with respect to the variation of pressure drop. We can clearly see that after a certain increase in pressure drop the curve becomes more linear. The values of the pressure drop were taken at five data points (8 psi (55.16 kPa) to 32 psi (220.63 kPa)) and the maximum velocities were in the range of 350- 700 in/sec (8.89 - 17.78 m/sec). Figure 5.19 shows the flow simulation at maximum pressure drop of 32 psi (220.63 kPa) (where inlet pressure is 43 psi (296.48 kPa) and outlet pressure is 11 psi (75.84 kPa)) and the corresponding maximum velocity is 691.6 in/sec (17.57 m/sec). The main purpose of the flow simulation is to observe how the fluid flows through the robotic heart chamber. A multi-physics simulation which can perform flow with deformation would give more accurate results but these results still show us a very clear concept on the nature of the fluid inside the artificial heart proposed in this work functions. The screen shot of the flow at 1, 1.5 and 2 seconds are shown in figure 5.19 where the fluid flow in the surface and continued to circulate inside the chamber and finally exits. It can be seen that the central portion has less velocity.

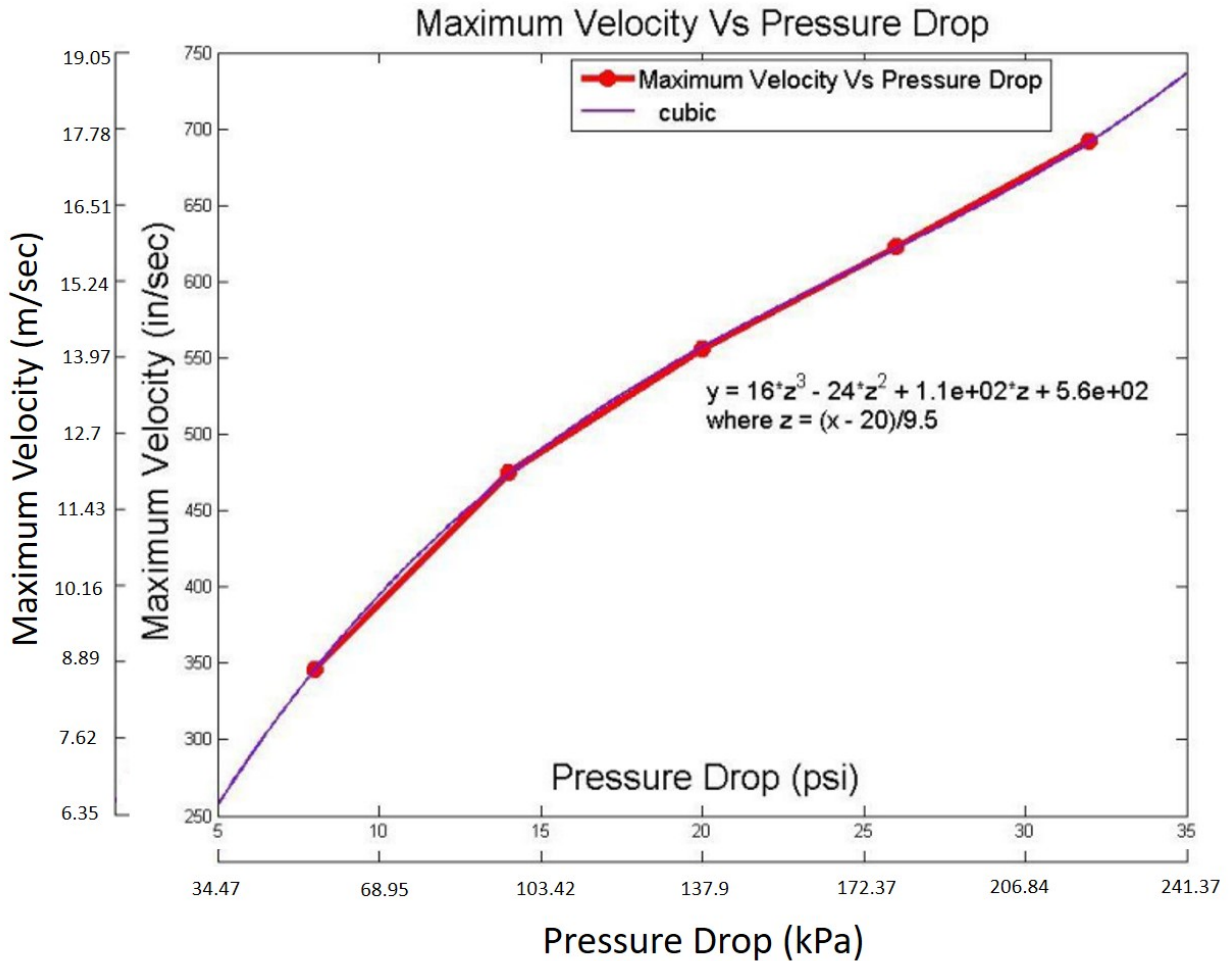


Figure 5.18. Plot of maximum velocity Vs pressure drop

5.1.12 Modeling and Simulation of CSMA Heart (Design 2 and Design 3)

This section describes the computer-aided design (CAD) model of the artificial heart using SolidWorks™ software. A hyperelastic simulation is presented by varying pressure. Using the simulation results, the volume of the fluid pumped at different pressures is calculated. As we are presenting the peristalsis motion by sequentially actuating SMAs, we compared the effects of actuation of two or three sections, to determine which is better and how the performance changes with respect to the number of sections actuated. Lastly, a flow simulation of the fluid flow inside the CAD model of robotic heart is shown to understand the flow pattern

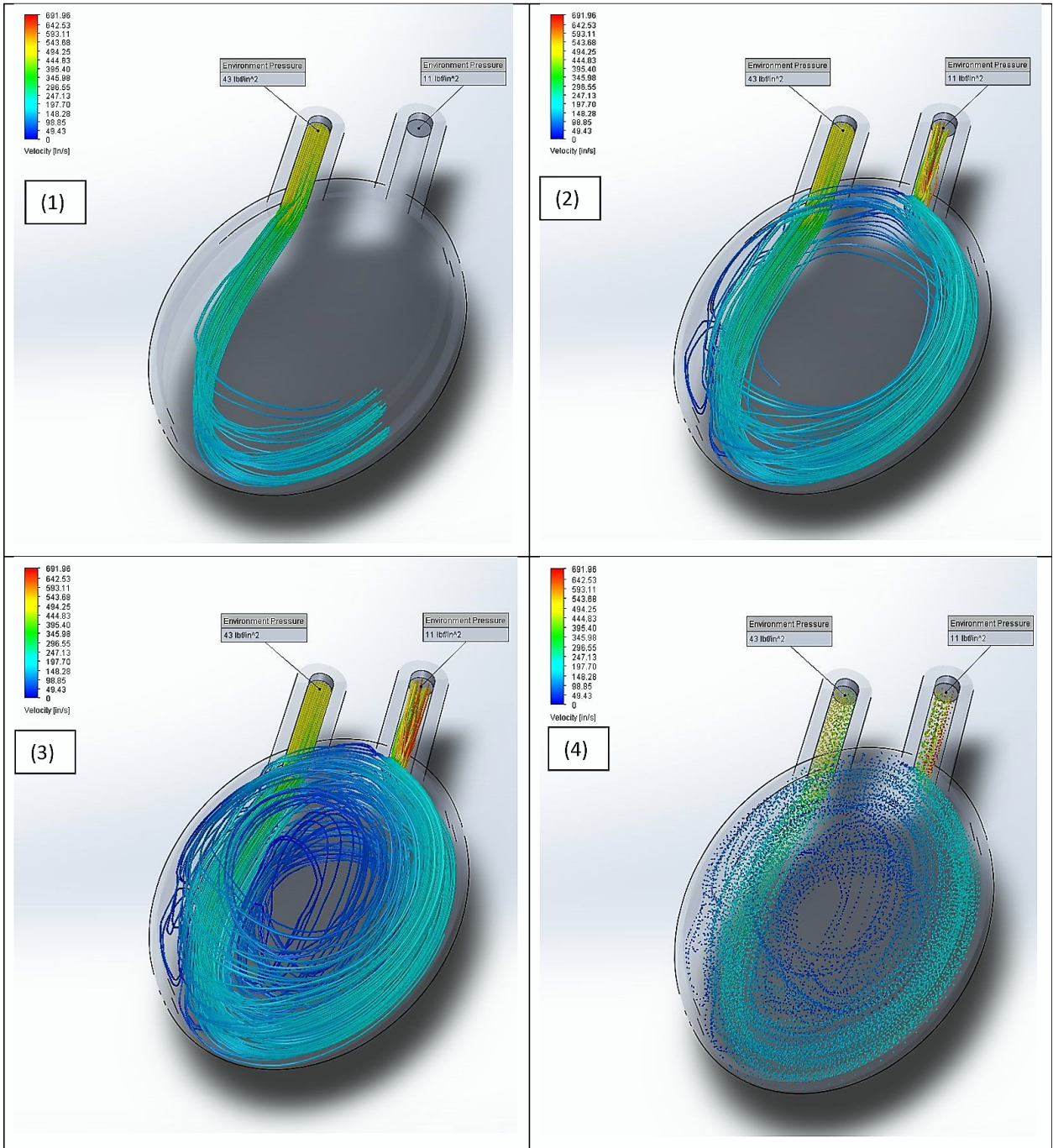


Figure 5.19. Flow analysis of computer aided design of the artificial heart in SolidWorks (1-3) in pipes in 1,1.5 and 2 seconds of simulation run respectively and (4) in balls for the maximum pressure drop of 32 psi (220.63 kPa) (where inlet pressure is 43 psi (296.48 kPa) and outlet pressure is 11 psi (75.84 kPa))

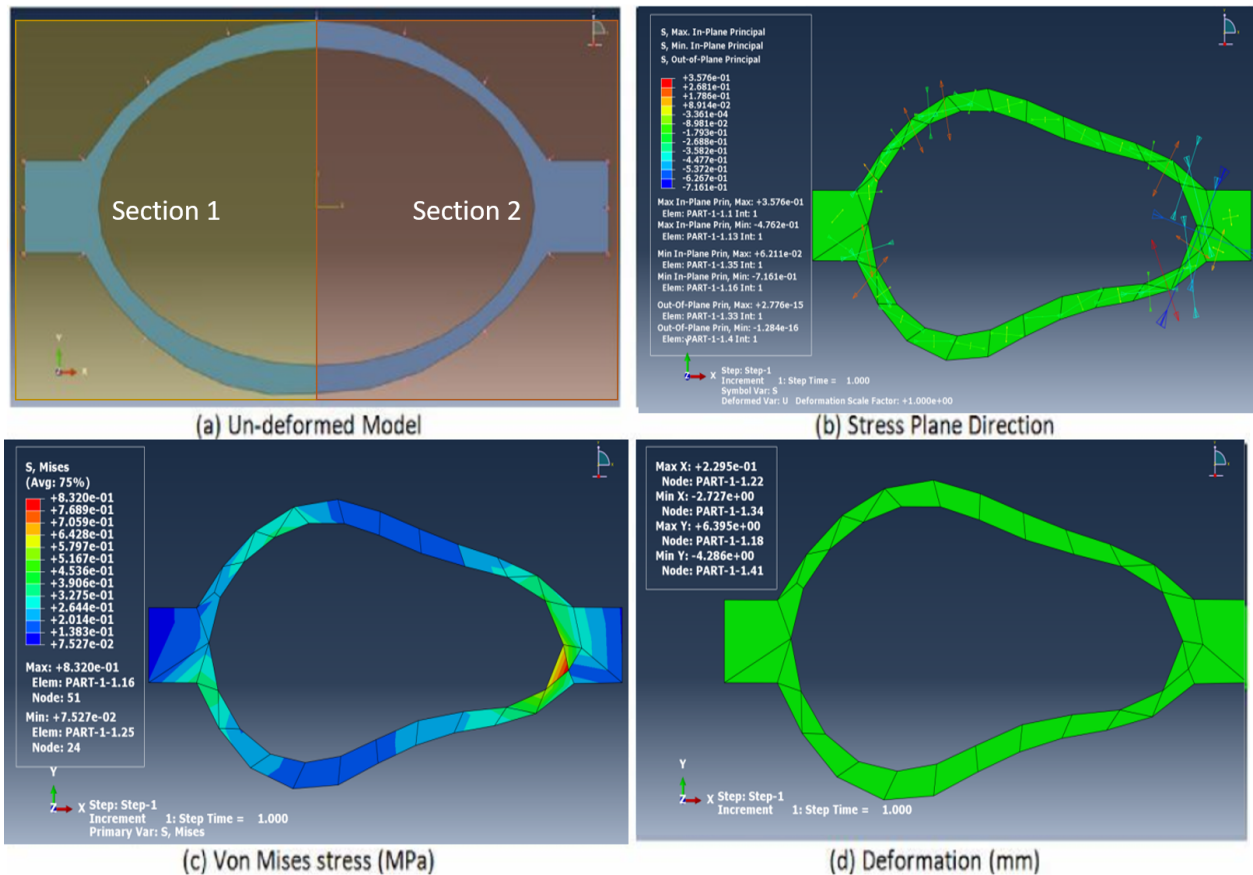


Figure 5.20. Hyperelastic Stress Analysis in ABAQUS 6.14 (a-d) at Pressure of 0.025 MPa for a two-section peristalsis motion by sequential actuating.

inside the model. The CAD model of the artificial heart was created using SolidWorks 2014 (Dassault Systemes, France) mimicking the outside dimensions of real human heart, so we can compare and observe how the human muscle like coiled SMAs actuate.

(a) Two-section Peristalsis Motion by Sequential Actuation

ABAQUS was used to simulate the deformation of sequential actuation of the robotic heart. The first simulation was carried out for two-section actuation. The undeformed model is shown in figure 5.20 (a) depicting the center cross-section of the heart. The applied uniform load on the model was on two sections from left to right at a time interval of 5 sec. The pressure load was varied from 0.005 MPa to 0.025 MPa. The analysis is not conducted

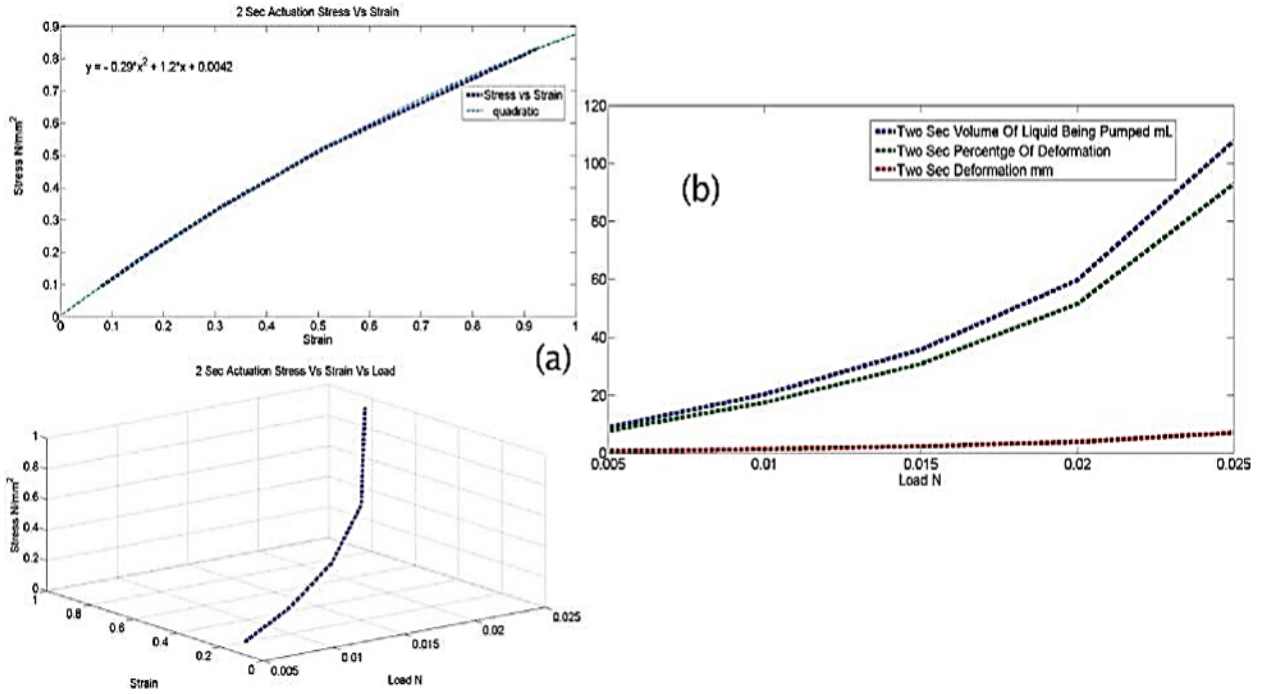


Figure 5.21. (a) Stress Vs Strain at a load of 0.25 MPa applied load and (b) Deformation, % deformation and volume of liquid being pumped in mL (calculated) on one side of the model for 2 section peristalsis motion by sequential actuating (c) Stress vs strain vs load applied in 3D of two section actuation .

beyond 0.075 MPa as the deformation is too large for ABAQUS to numerically calculate due the hyperelastic property of the material and the simulation did not converge. The meshing size was 3 with the free Quad-dominated element shape which created 35 elements. Figure 5.20 (b) shows the stress direction and figure 5.20 (c) shows the von-Mises stress where the maximum and minimum values are 0.83 MPa and 0.075 MPa respectively. In figure 5.20 (d), we see the deformation in mm where the maximum and minimum in x-axis are 0.23 mm and - 2.73 mm (negative sign showing direction). The maximum and minimum deformations in y-axis are 6.4 mm and -4.23 mm respectively.

Figure 5.21 (a) shows the stress vs. strain graph of the simulation obtained by varying pressure from 0.005 MPa to 0.025 MPa. The deformation analysis at the maximum possible pressure of 0.025 MPa was used to calculate the percentage deformation and provided approximately 92.7 % on one side of the pressured model. Using this percentage deformation

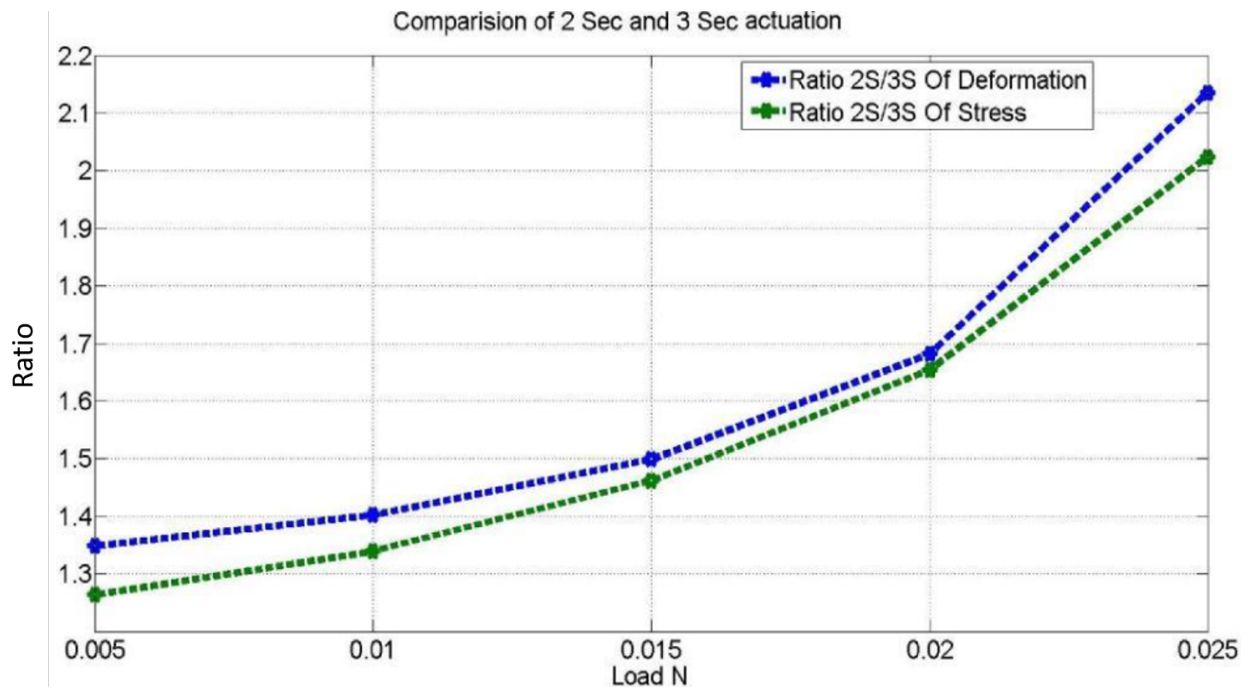


Figure 5.22. Comparison of three and two-section peristalsis motion by sequential actuation.

and integrating to the whole 3D model assuming that the deformation is uniform and constant all through the body on both sides, we obtained the reduction of volume in the model due to compression. It was found out that the volume of liquid as $107.5mm^3$ or 107.5 mL.

(b) Comparison of Three and Two Section Peristalsis Motion by Sequential Actuating

Similar simulation for two-section actuation was carried out for the three-section actuation. Essentially, three sections of the robotic heart were actuated one at a time in a time interval of 5 second. The comparative result is presented in figure 5.22. We can clearly see from the figure 5.22 that the stress and strain are higher for two-section actuation than three-section actuation at the same loads which shows that implementing two-section actuation on the heart will be more effective and that the more the sections the lesser the effectiveness. So, we implemented the two-section actuation on the heart.

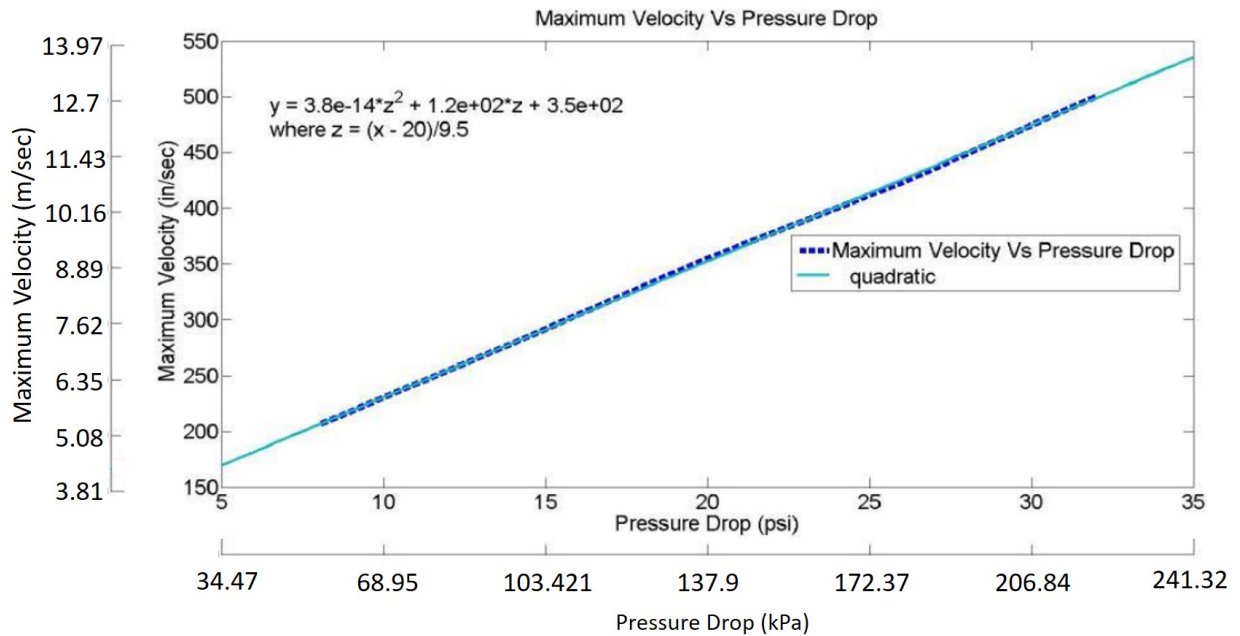


Figure 5.23. Plot of Maximum Velocity Vs Pressure Drop

(c) Flow Analysis

The flow simulation was done in SolidWorks 2014 using its FloWorks 2014 (Dassault Systèmes, France) flow simulator. The inlet and outlet pressure conditions were taken from the results presented by Hayward *et al.* [72], the maximum pressure a regular small scale syringes can produce. From the previous hyperelastic simulation conducted at maximum possible load pressure of 0.025 MPa, we calculated the maximum volume that can be pumped and obtained approximately 116 mL.

The analysis assumed that the robotic heart pump is already deformed due to actuation and the flow analysis was carried out assuming constant volume at a certain period of time. This estimation was done mainly to see the variation of the velocities at different pressures and to see the flow path of the liquid inside the heart model using practical values. The simulation was done at a temperature of 24 °C (room temperature). Figure 5.23 shows the simulation results of the maximum velocity of the fluid with respect to the variation of pressure drop. The volume of fluid is 116 mL. We can clearly see that after a certain

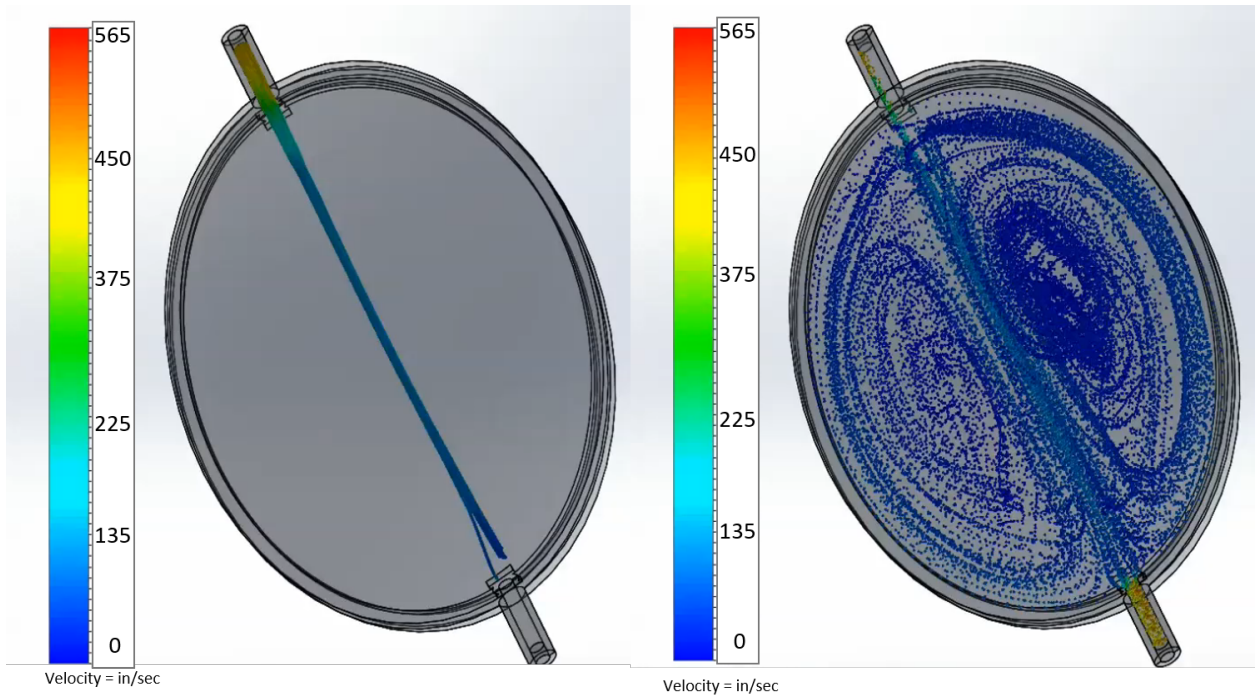


Figure 5.24. Flow analysis of computer aided design of the artificial heart in SolidWorks (a) in pipes and (b) in balls for the maximum pressure drop of 32 psi (where inlet pressure is 43 psi and outlet pressure is 11 psi)

increase in pressure drop the curve becomes more linear. The values of the pressure drop were taken at five data points (8psi to 32 psi) and the maximum velocities were in the range of 200- 600 in/sec. Figure 5.24 shows the flow simulation at maximum pressure drop of 32 psi (where inlet pressure is 43 psi and outlet pressure is 11 psi) and the corresponding maximum velocity is 12.7 m/sec (500 in/sec). This is not verified experimentally. The main purpose of the flow simulation is to observe how the fluid flows through the robotic heart chamber. A multi-physics simulation that can perform flow with deformation would give more accurate results. However, these results still show us a very clear concept on the nature of the fluid inside the artificial heart proposed in this work. It can be seen that the central portion has less velocity (figure 5.24). The flow analysis shows higher velocity at the inlet and outlet and symmetrical circulation at the center.

5.1.13 Experimental Setup

In this section, we describe the experimental setup to test the behavior of the artificial heart. The experimental setup is comprised of power supply (Topward 6306D) and National Instruments data acquisition system (NI 9201) with a computer interface and LabVIEW program. Schematic diagram of experimental setup is shown in figure 5.25. The heart was wrapped with the SMA fibers whose ring terminals were anchored to the surrounding clamp. The terminals of the SMA wires were connected to the power supply. The heart was filled with water mixed with red ink. Two small blocks was designed to support the clamp so that the artificial heart was unsupported to get realistic deformation for heart pumping testing. Two transparent plastic tubes were attached to the inlet and outlet ports. A drop of black ink was ejected into the transparent tube connecting to the outlet port for tracking purpose using image processing in MatLab™ . A steady camera was placed in front of the black ink to record its displacement. Once all preparation has been made, the tests were conducted by activating the SMA actuators.

The artificial heart operates as follows: power is supplied to the terminal of the SMA fibers; the SMA fibers are heated by the electric current and the rise in temperature causes them to undergo phase transformation, leading the contraction in length. The soft artificial heart is compressed due to the contraction of the SMA fibers. The water inside of the artificial heart is forced outwards through the hollow body of the heart. Meanwhile the camera records the displacement of the drop of black ink to track the water flow in the tube. Once the electric current is removed from the SMA fibers, the soft heart returns back to the rest position with the help of the 'recovery force' provided by the sponge.

The characteristics of the employed Flexinol wires are given in table 5.1. Since two different SMA wires were used in robotic heart, the actuation of SMAs was performed as follows. The SMA fibers (130 μm in diameter) were supplied with a current of 310 mA at 4.0 V, and the SMA fibers (200 μm in diameter) were supplied with a current of 520 mA at 3.0

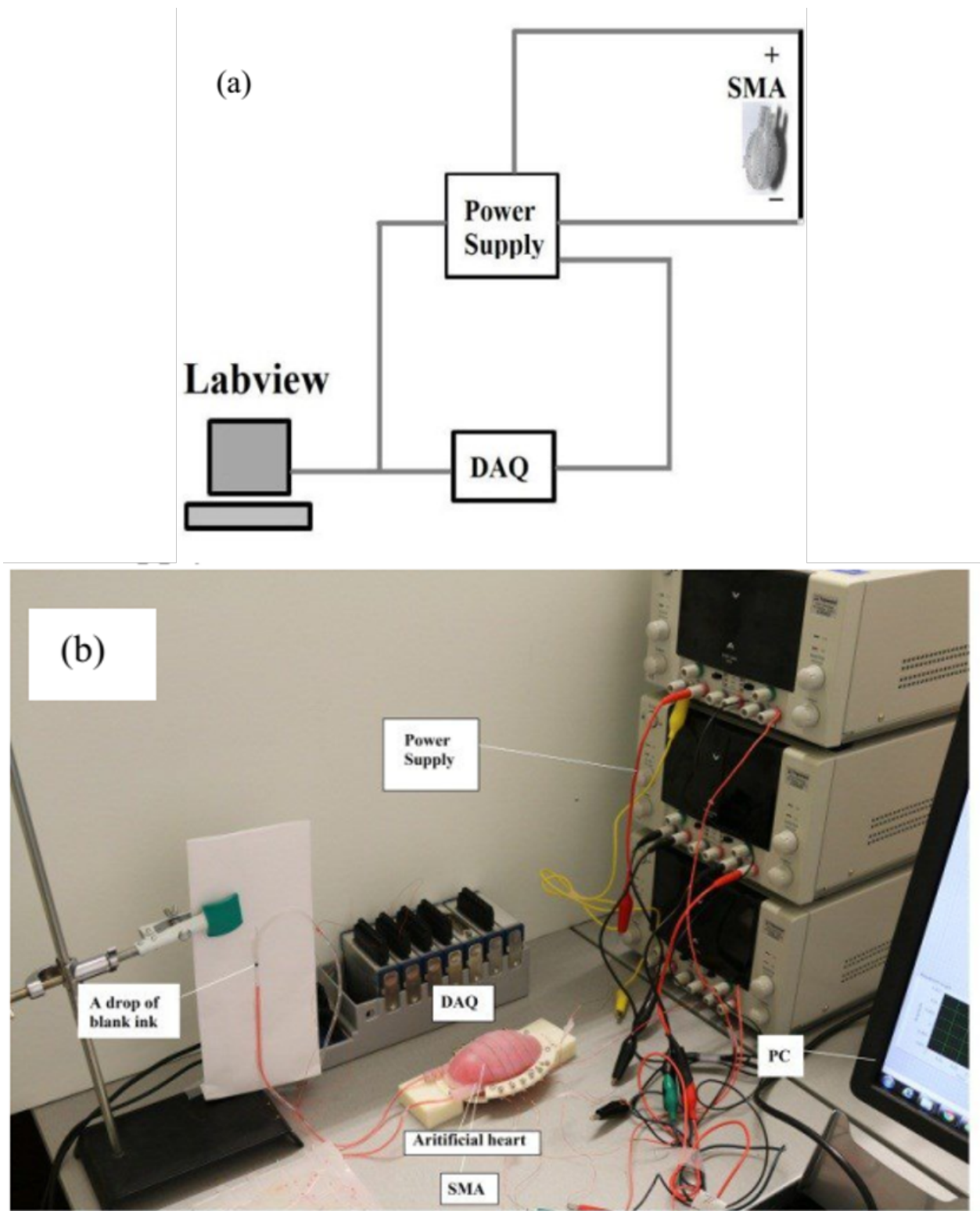


Figure 5.25. (a) Schematic diagram of the experimental setup, and (b) picture of the laboratory experimental setup

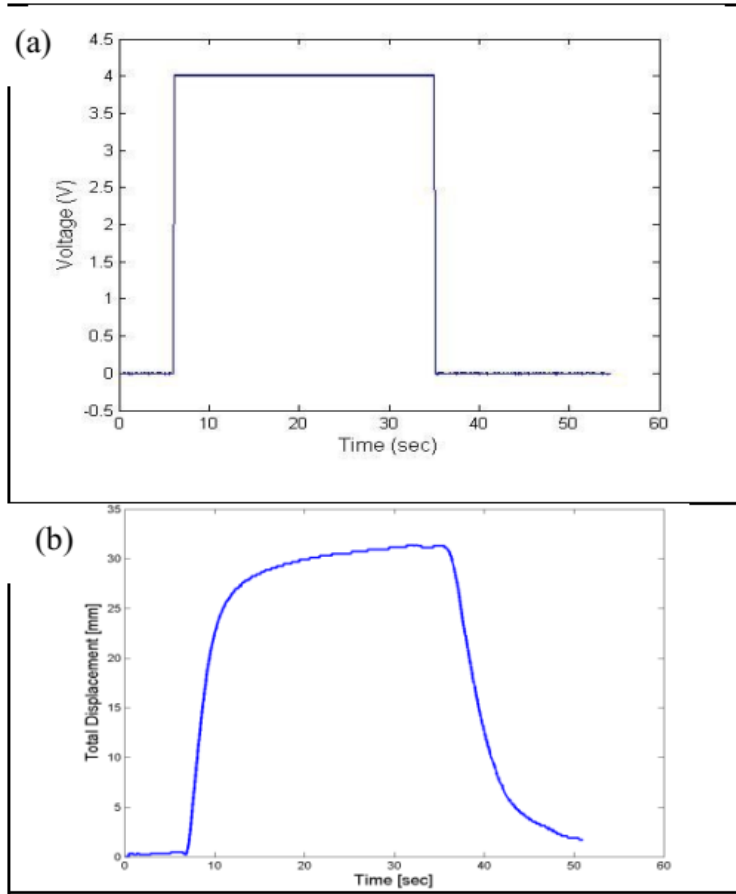


Figure 5.26. (a) Voltage applied to the SMA fibers(130 μm in diameter) and (b) the displacement of the drop of the black ink.

Table 5.1. Actuator parameters of SMA wires

Actuators parameters	Flexion wires	
Diameter(m)	130	200
Max force(grams)	223	570
Resistance (m)	75	29
Strain	3%-5%	3%-5%
Current(mA)	320	660

V. The artificial heart was compressed upon the SMA fibers' contraction. The results of this test are illustrated in figure 5.26 and 5.27 in terms of the displacement of the drop of black ink and the deformation of the heart. Figure 5.26 (a) shows only the voltage supplied to the SMA fibers whose diameter is 130 μm . Figure 5.26 (b) show the corresponding displacement

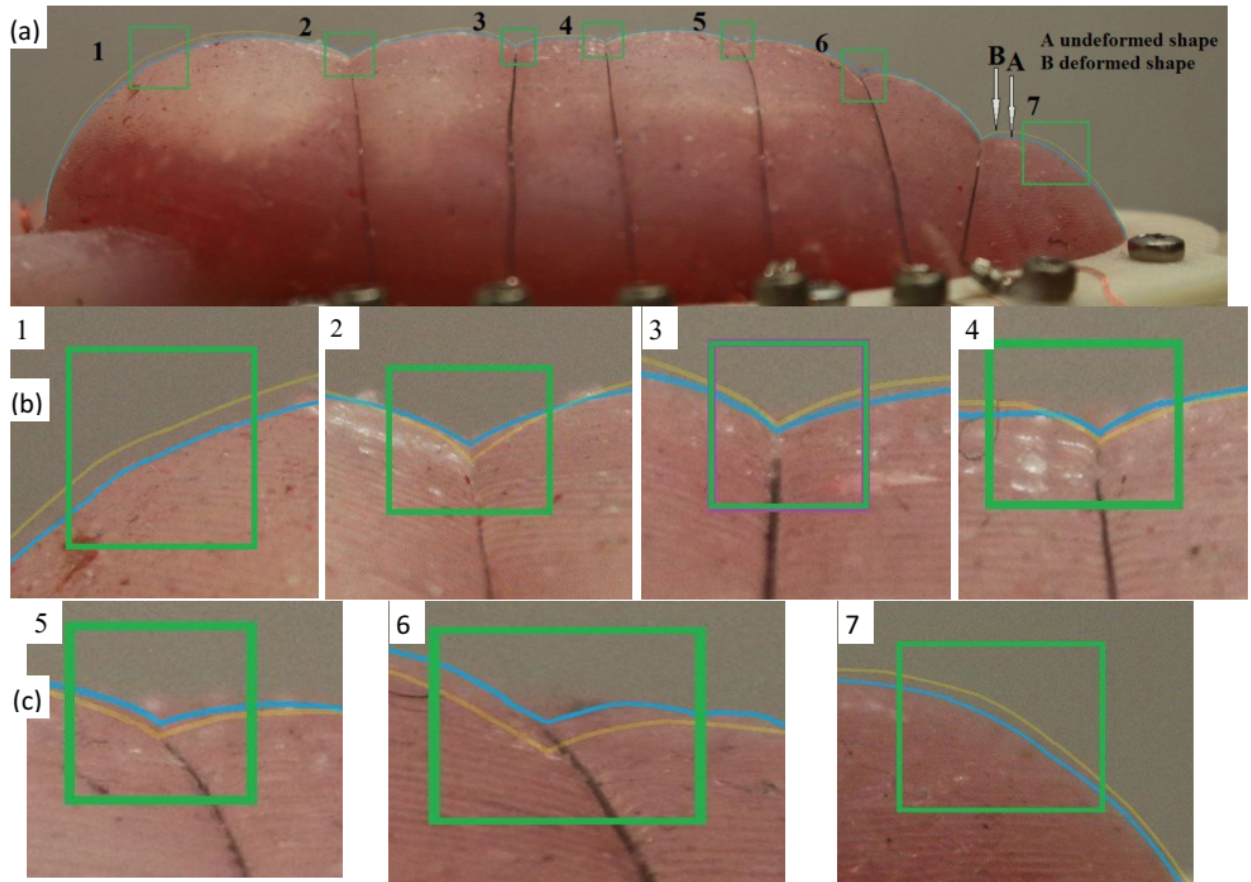


Figure 5.27. (a) Deformation of the artificial heart, and (b) & (c) magnified views of the deformation (No.1 No.7).

of the drop of the black ink in the tube under the action of the SMA fibers. It can be observed in this figure that in the rising stage, the displacement has a sharp increase at the beginning, indicating that the artificial heart is undergoing sudden deformation. Comparing the raising edge of displacement with the falling edge of displacement, it can be noticed that it takes much longer time for the ink to attain a steady position during the raising stage than the falling stage. Figure 5.27 shows the snap shots of the deformed artificial heart. It was noted here that the far left SMA fiber was not actuated. We compared the deformed shape and undeformed shape of the artificial heart and sketched the outline of the artificial heart to calculate the deformation. The deformation of the seven regions located in figure 5.27 (c) was magnified and the nut was used as scale. The displacement of these regions

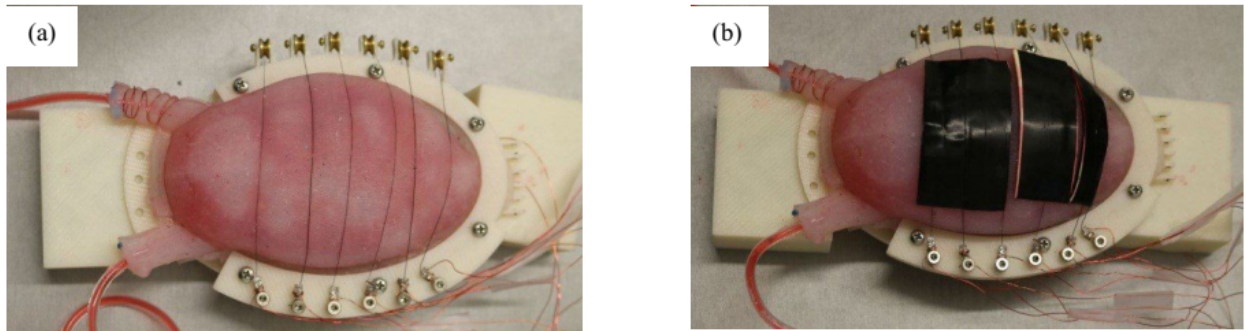


Figure 5.28. (a) Test 1: SMA fibers contact with artificial heart directly and (b) Test 2: Artificial heart covered with tape.

marked from No.1 to No.7 are 0.47 mm, 0.36 mm, 0.062 mm, 0.075 mm, 0.19 mm, 0.6 mm, 0.014 mm and 0.37 mm. It was observed that the force generated by SMA fibers had a local deformation on the artificial heart. Due to the liquid flow and the hyperelastic characteristic of the silicone, it can be noticed that the top and bottom end of the artificial heart were expanded.

In order to gain a better performance of the artificial heart, further experiment was carried out to compare the artificial heart pumping effect. In the previous test (shown in figure 5.28 (a)), test 1, it was shown that the contraction of SMA fibers was only caused localized deformation of the heart. In another test, test 2, the artificial was covered with the tapes to distribute the force generated by SMA fibers uniformly on the heart body (figure 5.28 (b)). These two experiments were carried out by applying the same voltage to the SMA fibers. The displacement of the drop of blank ink within the outlet pipe was recorded and the results are shown in figure 5.29, indicating that the one with tapes had much better pumping effect than that a bare SMA on the silicone. The magnitude of total displacement of the droplet was 30 mm and 75 mm for test 1 and test 2 respectively as shown in figure 5.29.

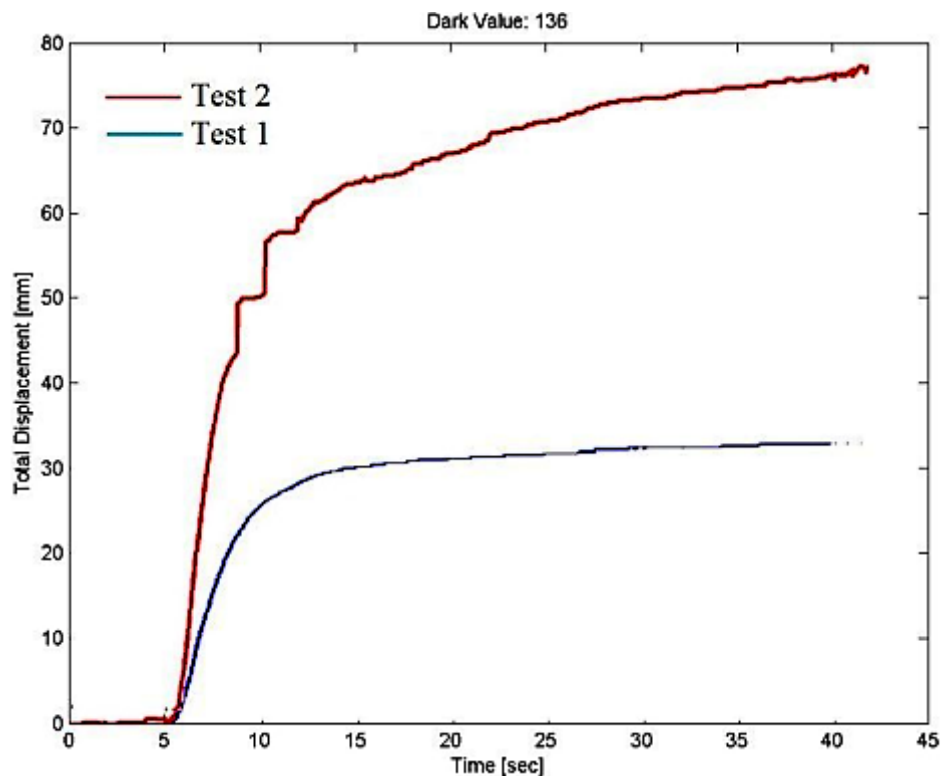


Figure 5.29. Displacement of the drop of blank ink using a tape on the silicone and without.

5.1.14 Applications

Facial color change is an effective nonverbal communication and it plays a significant role in expressing oneself. Human heart plays a vital role in change of facial color as the flow of blood is regulated by the heart to face. A study showed that humans connect facial expressions with certain colors [38]. The study showed anger and happiness are connected to the color red as in naturally we blush for happiness, anger and embarrassment and the color green is connected to disgust and sickness. Naturally these colors are exhibited in humans due to sudden variation in blood pumping to face from heart due to emotional changes experienced which are controlled by the brain. The prominent area of application is in humanoid robots with facial expressions (HRwFE). If these robots are provided with the ability to change colors while actuating their face muscles, better emotional expressions can

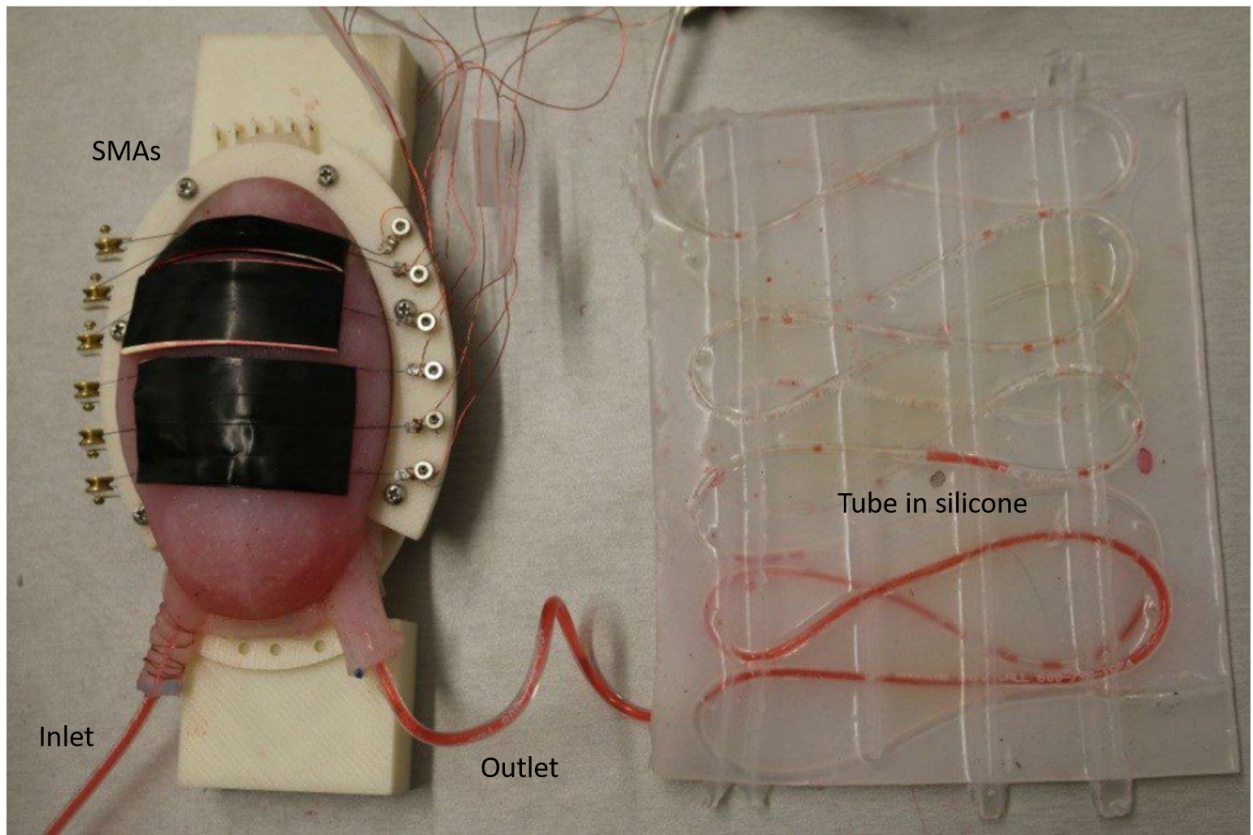


Figure 5.30. The transparent silicone layer embedded with tube for demonstrating the facial color change

be added obtained. This has an application in medical studies through the use of humanoids.

(a) SMA Artificial Heart (Design 1)

Figure 5.30 illustrates the basic idea of the application in humanoids. The general idea is to implement the artificial heart to pump a blood like fluid (red color water) to the humanoid robot face to mimic the human facial color changes. In figure 5.30, a transparent tube embedded in the silicone layer (much smaller size) was made and the inlet was connected to the robotic heart (Design 1). As the SMA actuators are activated the blood like fluid came out and passing through the channels. Although the spacing between the pipes is

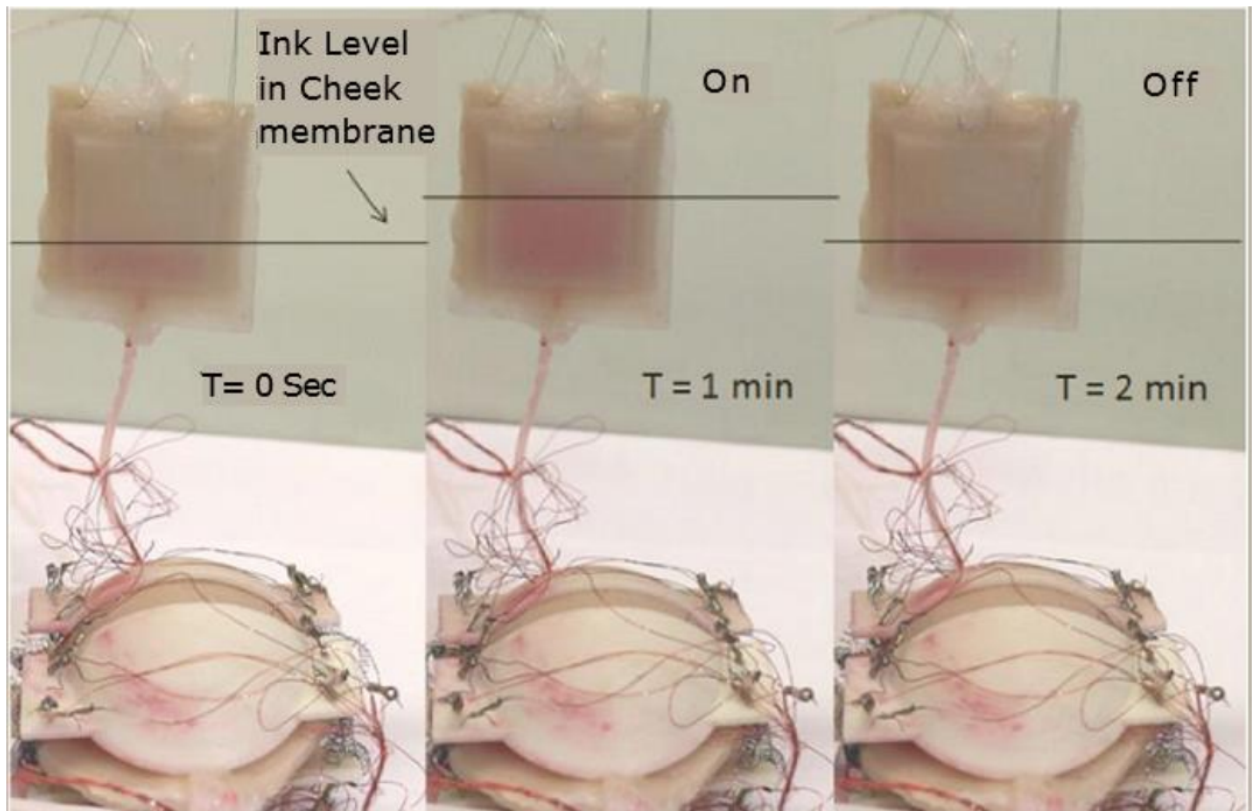


Figure 5.31. Sequential actuation of the robotic heart, results of trail 3 at time = 0 , 60 and 120 sec

not sufficient to make significant change in the color, the concept is applicable to use in humanoid robots. Particularly, the cheeks of a humanoid are an ideal area to implement on humanoid robot face. When the colorized water reaches the specific areas of the face, it will enable the robot to making facial expression in an effective nonverbal way.

(b) CSMA Artificial Heart (Design 2)

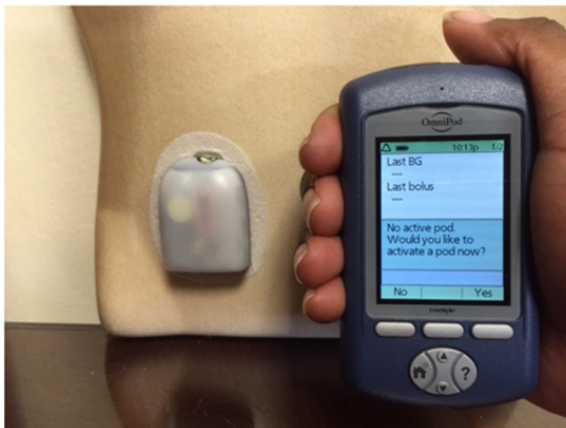
In figure 5.31 we see (Design 2), a cheek structure of 50 mm square with 1 mm hollow space and the inlet was connected to the robotic heart. As the SMA actuators are activated at 4V and 0.66A , the blood-like fluid is pumped out and passing through the cheek membrane. Particularly, the cheeks of a humanoid are an ideal area to implement on humanoid robot



A Medtronic Minimed Insulin Pump and a blood glucose meter that communicates blood glucose readings wirelessly with it. (\$5500+)



The T-slim Insulin Pump is popular with young patients due to its new touch-screen design. (\$6000+)



The OmniPod Tubeless Insulin Pump with a pod (right) and a handheld device that functions as a blood glucose meter and communicates wirelessly with the pod to deliver insulin based on the patient's personal settings. (\$1200+)



The Medtronic iPro2 Professional Continuous Glucose Monitor with its charger. (\$1200+)

Figure 5.32. A few examples of insulin pumps [126]

face. When the colorized water reaches the specific areas of the face, it will enable the robot to show facial expression in an effective nonverbal way.

(c) Application (Insulin Pumps)

Insulin pumps deliver insulin by continuous infusion through a single subcutaneous site which is replaced, generally, every three days. A pump delivers programmable basal insulin around the clock which is tailored to the patient's 24-h glucose profile. The insulin requirements are influenced by the individual's physiology, the type and duration of daily activity, work schedule, exercise, illness, concomitant medications, etc. Typical cartridge volumes are 200 to 300 units. A few examples of insulin pumps are shown in figure 5.32. The soft pump introduced in this chapter can be further developed to use in insulin pumps.

(d) Characterization of CSMA Artificial Heart as Soft Pump

The design of CSMA actuated artificial heart is slightly modified for better performance. Mainly the 3D printed curved plates (Design 2) used to compress the heart is replaced with flat rectangular plates (Design 3). The casing for the soft heart and spring geometry of the CSMA are modified to improve the performance of the soft pump artificial heart. The CSMA geometry is of wire diameter of 0.2 mm, spring diameter of 1.56 mm and with 10 number of turns with a pitch of 80 TPI (Threads per inch). The closely packed spring structure gives a better load carrying capacity and smaller profile than previously used geometry. The flatter casing as seen in experimental figure 5.33 would apply higher load than the previous curved shaped compression casing which was used in the previous section. The plates used are four 5 cm x 12 cm rectangular plates with small holes on the edges for crimping CSMA, which were made using the laser cutter as seen in figure 5.34 (c). The rectangular plates are designed to cover the whole heart as seen in figure 5.34 (a) and (b) schematically in top and side view schematically. A mannequin is used as a support for the cheek structure and would give a better understanding of implementation. With these changes, a higher frequency of 15 mHz is achieved and thoroughly characterized as seen in figure 5.35. A maximum flow of 3.65 cm^3 volume in 40 seconds is achieved when compressed with 8V and

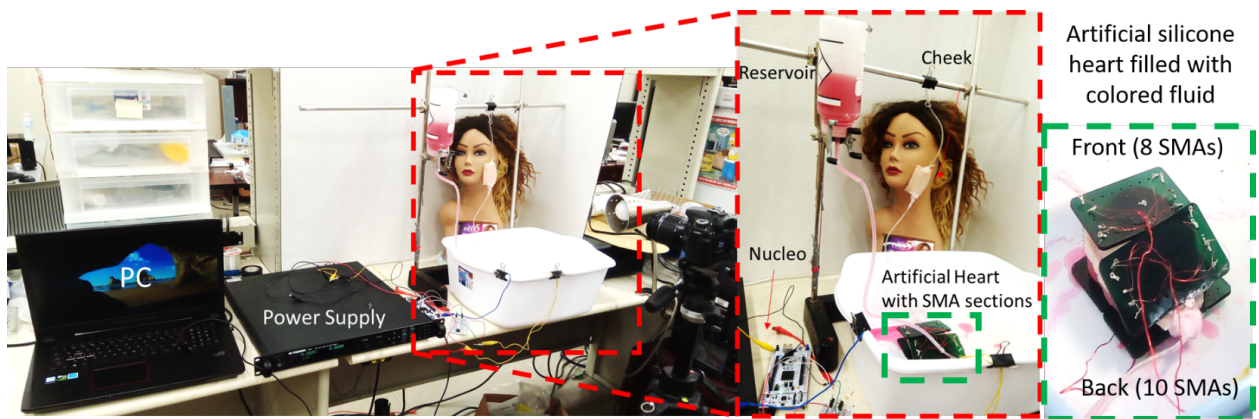


Figure 5.33. Experimental setup of the artificial heart soft pump actuation testing with cheek structure on a mannequin.

20A. The experiment is done using a NUCLEO F767ZI micro controller and the MOSFET - resistor circuit to produce a pulsed digital signal rather than manually switching it ON and OFF. The thickness of the inner cheek structure is 3 mm and 5 cm wide. The volume flow is calculated by multiplying the change of the height of the fluid with the area, which was obtained from video of the actuation. The time domain plot of voltage and current supply to back 10 SMAs and front 8 SMAs corresponding to volume flow of the soft pump is shown in figure 5.35. From this experiment, we can see the maximum volume flow vs time the soft pump can produce at its best frequency. The height vs time is obtained using a tracker software, and the volume is calculated by multiplying the height with length and breadth of the cheek structure assuming there is no bulging. The height of the cheek structure from ground also plays a some role. The height of the reservoir is around 500 mm from ground and the cheek structure is around 300 mm from ground. The soft pump can be used to pump fluids where low profile and low noise is a propriety, which cannot be achieved with regular electric pumps.

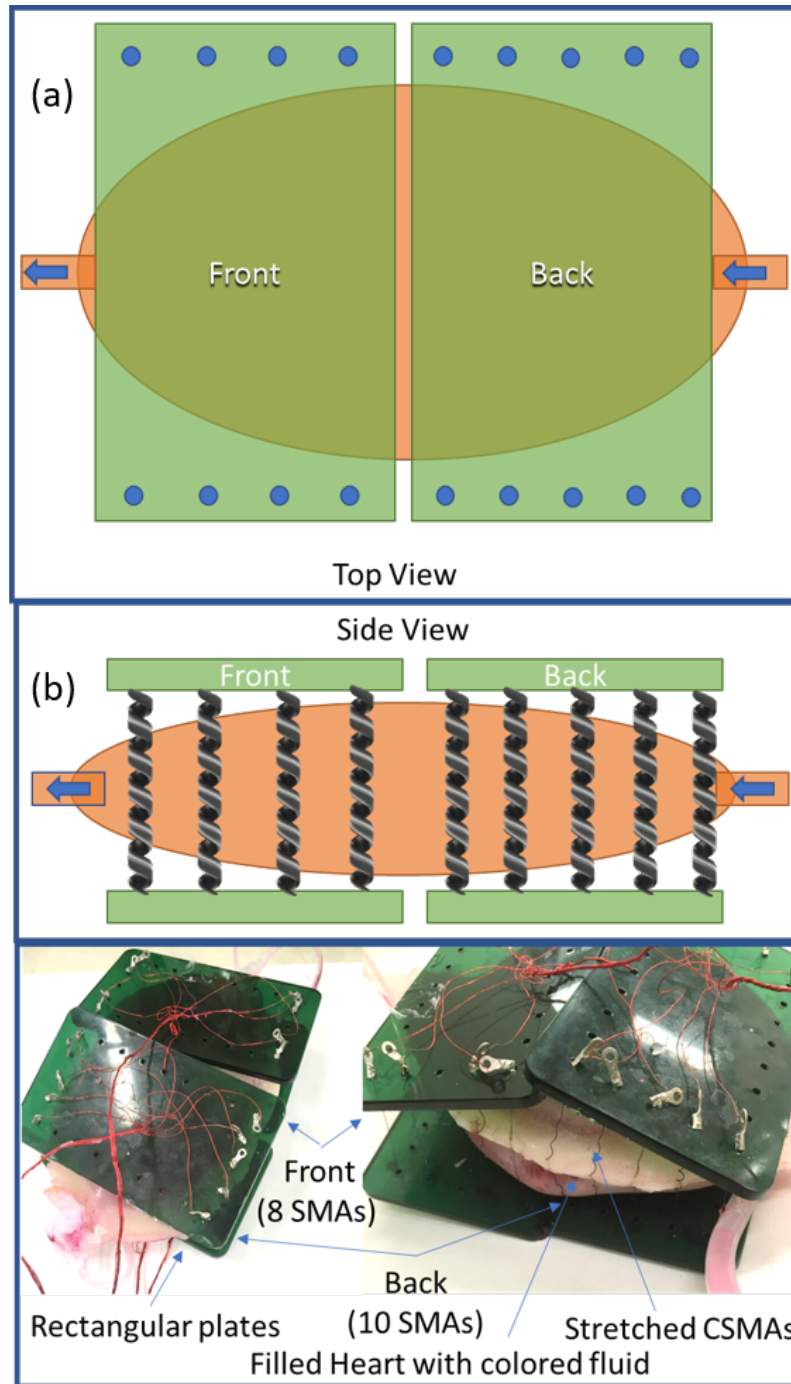


Figure 5.34. Schematic (Design 3) (a) Top View and (b) Side view of the soft pump with the rectangular plates showing the SMAs in the front and back section (c) Top and Side view of the soft pump with the rectangular plates and CSMAs.

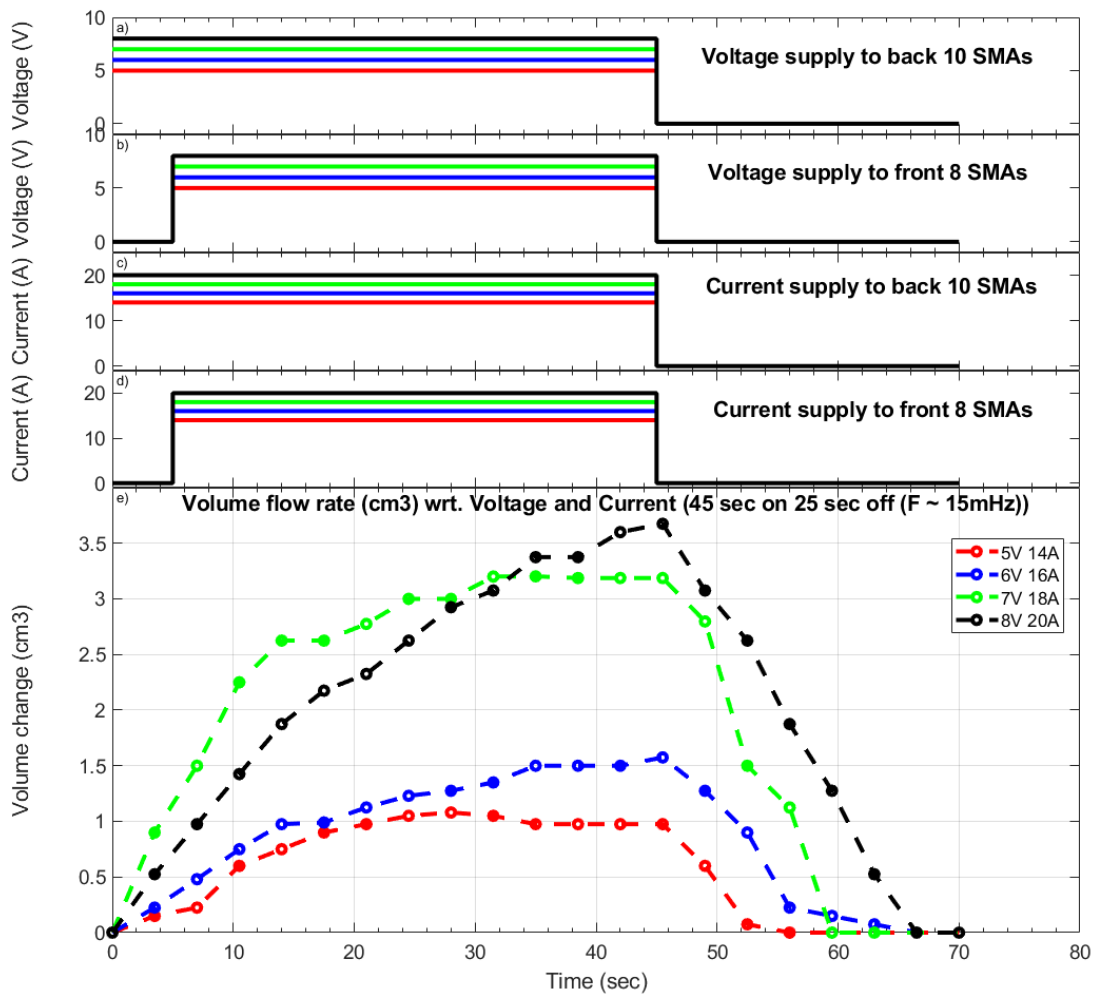


Figure 5.35. Time domain plot of voltage and current supply to back 10 SMAs and front 8 SMAs corresponding to the output volume flow rate of the soft pump (Design 3). (a) and (c) show the voltage and current for back 10 SMAs and similarly (b) and (d) show the voltage and current for front 8 SMAs. (e) shows the volume change (cm^3) with respect to time (sec) for four different voltage and current inputs.

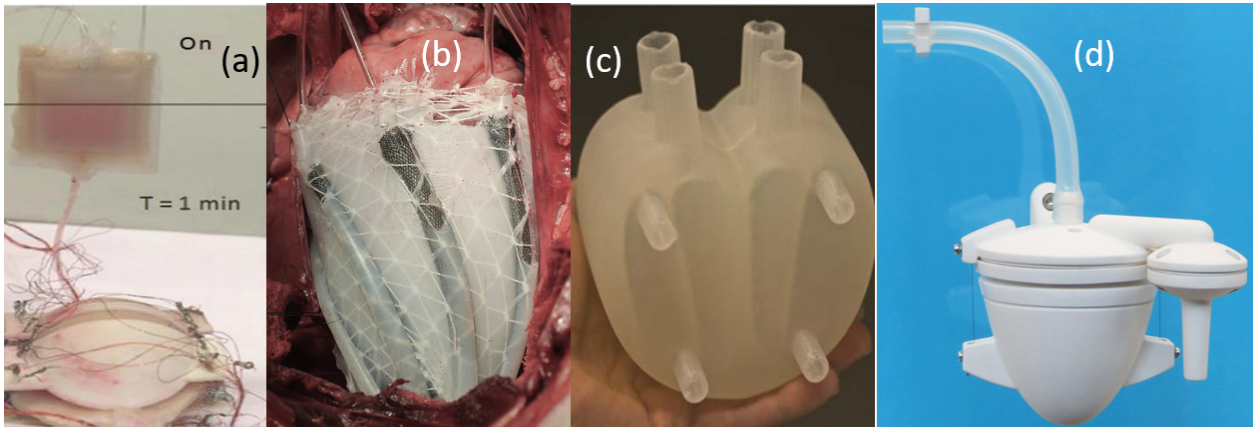


Figure 5.36. Comparison of the robotic heart (a) CSMA heart presented in this work with (b) pneumatic [169] ,(c) internal combustion heart [180] and (d) SMA artificial heartbeat [224]

(e) Comparison of the Heart with Other Published Soft Pumps

In figure 5.36, we can see the artificial CSMA heart compared with a soft pneumatic artificial muscle (PAM) heart [169] , an internal fuel gas combustion heart [180] and a SMA artificial heartbeat [224]. The main advantages of CSMA heart with respect pneumatic heart are that it does not need a compressor, silent, lightweight and low in profile. The CSMA heart is made with a softer Ecoflex-10 material rather than harder Ecoflex-30 material used for the pneumatic heart. On the other hand due to the high power of the pneumatic muscles and no cooling time, it has higher frequency and more than 50 mL volumetric displacements. The CSMA heart has lower frequency due to the cooling time and can pump upto 3.5 mL volumetric displacements. The other major difference is that the pneumatic heart is rather a soft sleeve on actual biological heart and the CSMA heart is a rigid sleeve on a soft silicone heart. The internal fuel gas combustion heart is made of polydimethylsiloxane (PDMS) elastomers which can withstand the heat and explosions of the combustion. It also has higher frequency and can pump volumetric displacements more than 30 mL. On the other hand, it reaches high temperatures due to loud explosions of the gas, risk of gas leaks and exhaust gases. The SMA artificial heartbeat has a small soft 3D printed structure, TangoPlus

within a rigid plastic 3D printed structure which is powered by electrical energy generated by microbial fuel cells (MFCs). The soft structure is compressed by NiTi wires, which are placed parallel to the structure. The SMA frequency is similar to CSMA frequency and they pumped more than 20 mL volumetric displacements, which is also dependent upon the size of the pump.

5.1.15 Conclusion on robotic heart

The design and fabrication of a soft artificial heart for a humanoid robot was presented in this section using a silicone elastomer and coiled shape memory alloy actuators. From this work, one can see the how CSMA's outperform cylindrical SMA. The deformation behavior of the heart model was studied under different pressures using finite element analysis. Mooney-Rivlin model was used to predict the deformation of the device. Simulations results showed that multiple sections in peristalsis motion by sequentially actuating affect the performance of the robotic heart pump. Three prototypes were developed and tested and we showed that the robotic heart can pump a blood-like fluid to parts of the robot face to simulate someone blushing or when someone is angry by the use of elastomeric substrates and certain features for the transport of fluids. A complete time domain characterization is performed to study the volume flow rate at different voltages and current. This study is not only useful in humanoids but applicable in the medical fields (medical training device). The device shows great potential in medical equipments like insulin pumps.

5.2 Case Study: Simulation and Experimental Study of NITI Double Helix Stents for Human Coronary Arteries ³

Despite new improvements in coronary artery stents, there is still great concern over the failure and life-cycle of stents in patients. In this work, we explore different models of existing stents fabricated using shape memory alloy and analyze them from the mechanical failure point of view and finally propose a novel double helix stent model for coronary arteries inspired from the structure of DNA. We conducted several simulations of the model under different conditions. The experiments are conducted using hyperelastic silicone rubber mimicking the human coronary arteries and the sample stent model made of superelastic NiTi shape memory material.

5.2.1 Introduction

Implantation of tubular endoprotheses (stents) in blood vessels to prohibit occlusion and restenosis of coronary arteries, and subsequently a percutaneous intervention such as angioplasty is being conducted since 1986 [188]. Stents are considered as a primary way of treating coronary stenosis with high reliability and testify to a reduction of minimum 30% of the restenosis rate after implantation in the patients [182, 54, 108]. Commonly used metallic stents fabricated with stainless steel or titanium have limitations due to their substandard radiopacity and mechanical properties, which may convolute the insertion and positioning of stents at location of blockage [61, 94]. On the contrary, NiTi alloy with superlative radiopacity, superelasticity, shape memory properties and bio- compatibility make it a potential material for stents [214]. As NiTi stents are widely used for short term and long term applications in clinical procedures, it is crucial to comprehend the mechanical behavior of

³Some parts are reprinted by permission from **Biomedical and Biotechnology Engineering: ASME International Mechanical Engineering Congress and Exposition, Simulation and Experimental Study of NiTi Double Helix Stents for Human Coronary Arteries**, Akshay Potnuru, ©2017

them thoroughly [174]. Finite element method (FEM) is widely used to simulate and study stents. The FEM analysis is done in two categories. The first category studies the mechanical behavior of stents during the process of free expansion without any external constraints and the second category studies the interaction between the stent and the vessel [235]. In this section, we present the study on the second category of the FEM analysis, which deals with in-stent restenosis and stent failure. In-stent restenosis is the narrowing of the artery again while the stent is in use. Stent failure is an imperative problem leading to serious complications after implantation, which can occur immediately or in the mid-late service time. Nakazawa *et al.* [137] observed that 78% of serious stent fracture cases had stent complications. Umeda *et al.* [219] statistically showed that restenosis rate increased from 3 to 15 % after stent failure. Similar observation has been presented by Aoki *et al.* [14] where an increase from 12.4% to 37.5% restenosis rate was seen after stent failure. The primary stimulations for stent failure are the contractions of the heart such as systolic and diastolic pressure, which instigate pulsation of vessels and vascular movements. Clinical results show that vascular movements have more impact than vascular pulsation (VP) on stent failure. Xu *et al.* [235] are one of the first few who studied the vascular dynamic bending (VDB) on stent models and showed how the effect of VDB is more than VP for stent failure. In this section, we perform FEM study based on the work presented by Xu *et al.* for our stent model, the double helix model. The difference between Xu *et al.* FEM simulation and the work presented in this work is that they used a friction between the stent and the artery, and we used a bonded constraint. In this work, we present the FEM modeling and simulation along with experimental verification for sustainability of double helix stent model. The superelastic NiTi material properties used for simulation are shown in 5.2 and figure 5.37 and the hyperelastic coronary artery material properties are shown in 5.3.

Table 5.2. Material properties of NiTi nitinol [234] as seen in figure 5.37

E (GPa)	ν	δ_{AM}^s (MPa)	δ_{AM}^f (MPa)	δ_{MA}^s (MPa)	δ_{MA}^f (MPa)	ξ_L	α
60	0.3	346	365	83	57	0.063	0.09

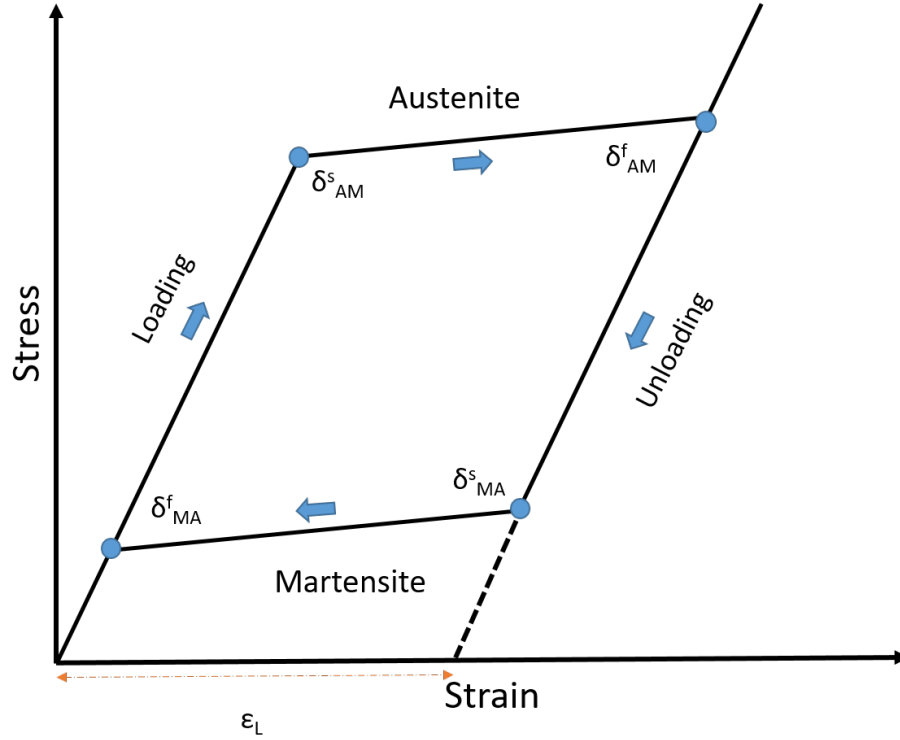


Figure 5.37. Superelastic effect of NiTi material

Table 5.3. Material properties of the coronary artery layers - coefficients of the strain energy density function [235]

Layer	C_{10} (MPa)	C_{20} (MPa)	C_{30} (MPa)
Plaque	$2.38e^{-3}$	$1.89e^{-1}$	$-3.88e^{-1}$
Intima	$6.79e^{-3}$	$5.4e^{-1}$	-1.11
Media	$6.52e^{-3}$	$4.89e^{-2}$	$9.26e^{-3}$
Adventitia	$8.27e^{-3}$	$1.2e^{-2}$	$5.2e^{-1}$

5.2.2 Simulation

ANSYSTM 17.1 was used for all FEM simulations in this work. The stent model was designed as double helix spring structure of length 16 mm, inner mean diameter of 1.78 mm with

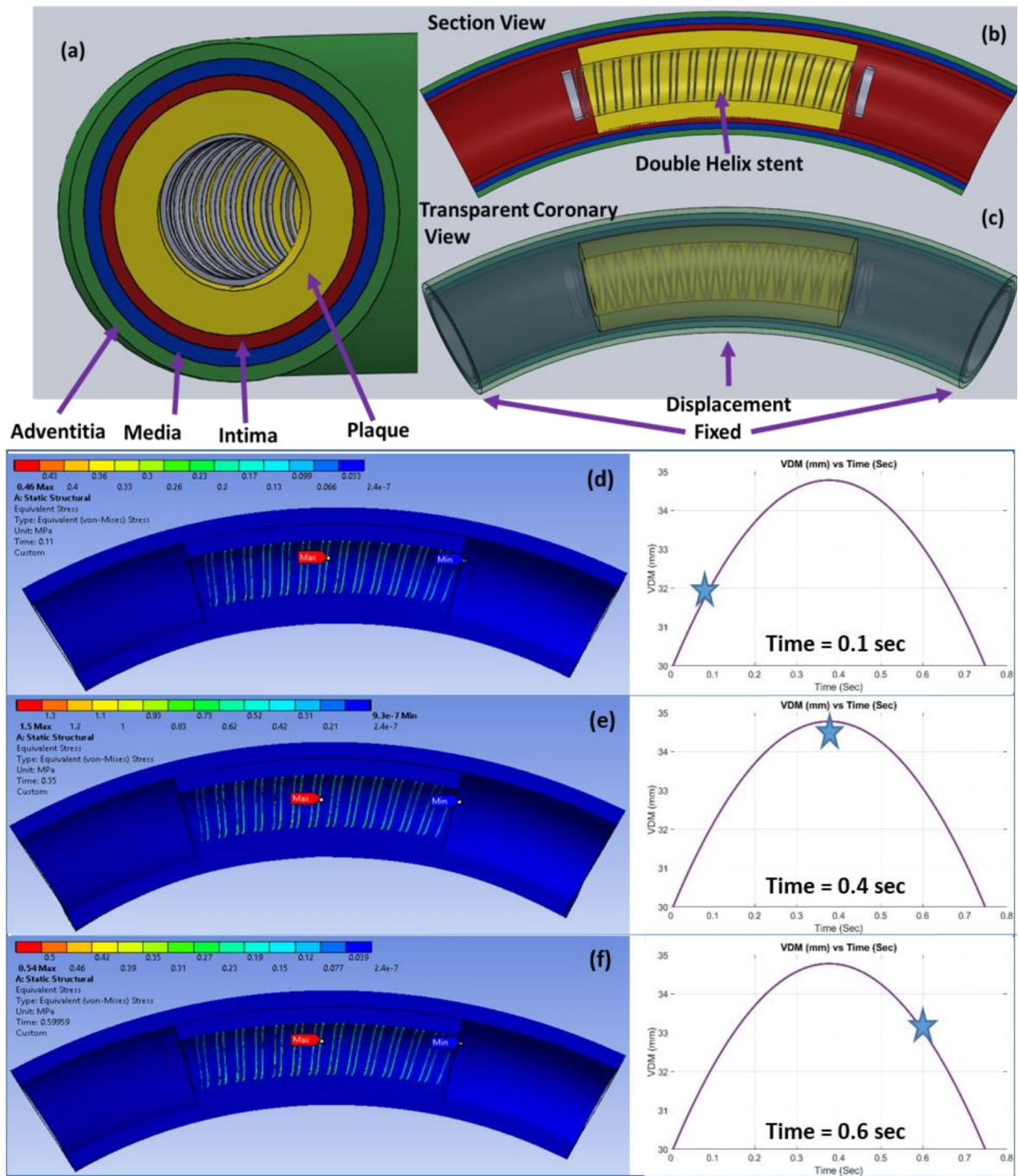


Figure 5.38. Double helix stent model : (a) side view of the coronary artery showing the different sections adventitia, media, intima, plaque and the double helix stent, (b) the section view with the double helix stent profile, (c) the boundary conditions of the simulation in a transparent view; Stress distribution in the vessel during artery moving process (d) is at time = 0.1 sec with maximum von-Mises stress of 0.45 MPa, (e) half of a cardiac cycle with maximum von-Mises stress of 1.5 MPa, (f) is 4/5 of a cardiac cycle, $t = 0.6$ sec with maximum von-Mises stress of 0.54 MPa.

16 number of coils and wire diameter of 0.1 mm. The model was created in SolidWorks™ 2016 and imported to ANSYS™ 17.1 using solid .iges format. The front and side view of the structures are shown in figure 5.38 (b) and (c). The material used for the stent was NiTi alloy with superelastic properties as shown in table 5.2 [234]. Wu *et al.* [234] used NiTi stents for carotid artery and their interactions using FEM. The coronary artery model was taken from Xu *et al.* [235] with an initial curvature radius of 30 mm, inner diameter of 3 mm, length of 30 mm and thickness of 0.9 mm as seen in figure 5.38 (a). A symmetric plaque of length 14 mm was applied at the center of the model. The coronary artery was composed of three layers, intima, media, and adventitia of thicknesses 0.28, 0.32, and 0.3 mm respectively. The mechanical behavior of the coronary artery was modeled using a homogeneous, isotropic and hyperelastic constitutive model, based on the works of Holzapfel *et al.* [77] and Xu *et al.* [235]. The constitutive model was based on reduced polynomial strain density function, U of sixth order but due to the limitation of ANSYS™ 17.1 software, we have reduced it to a third order Yeoh model of hyperelasticity,

$$U = \sum_{i=1}^3 C_{i0} (I_i - 3)^i \quad (5.5)$$

where, I_1 is the first invariant of the Cauchy-Green tensor:

$$I_1 = \lambda_1^2 + \lambda_2^2 + \lambda_3^2 \quad (5.6)$$

$$\lambda_i = J^{-\frac{1}{3}} \lambda_i \quad (5.7)$$

Here λ_i are the principal stretches and J is the determinant of deformation gradient of the hyperelastic material.

The coefficients of the strain energy density function for each layer of the coronary artery are presented in table 5.3 [235, 77]. It is assumed that the bending of the coronary artery is

driven by the artery movement. The input displacement used in this simulation was based on Xu *et al.* [235], Weydahl *et al.* [229] and Moore *et al.* [132] with variable radius curvature parameter. The maximum central displacement observed by Xu *et al.* [235] is 0.65 mm in time frame of 0.75 seconds in a gradual increment and reduction, with a peak in the center. It was used as the input to the FEM model and simulate the maximum stresses as seen in figure 5.38 (d), (e) and (f). In figure 5.38 (c), we see the boundary conditions provided to the solid model, where the two side ends are fixed and a displacement is given in the center of the assembly. In figure 5.38 (d), (e) and (f), we observe the von-Mises stress of the stent-artery assembly obtained from the simulation when the VDB amplitude varies at time 0.1, 0.4 and 0.6 seconds. We can see due to the profile of the stent the maximum stress concentration accumulated is observed to be as low as 1.5 MPa, which is very low.

5.2.3 Experiment

First a soft tube that mimic artery of human heart was created using elastomer materials EcoFlex. The EcoFlex™ 10 was cast in a 3D printed mold using Stratasys® Fortus™ 250mc with a thickness of 0.9 mm and a length of 30 mm similar to the dimensions used in the simulation as shown in figure 5.39 (a). The Part A and Part B of the EcoFlex™ 10 was mixed in equal proportions and poured into the opening of the mold with the caps fixed at the ends and a smooth metal shaft to create the hollow structure. It takes about 4 hours for different parts to cure and form the hollow silicone tube. Ni-Ti based shape memory alloy (SMA), Flexinol™ wire of 0.1 mm diameter was purchased from Dynalloy® , Inc., and used to create the helix stent using a screw as a mandrel as shown in figure 5.39 (b). The screw mandrel was placed in a customized bobbin winder to coil the SMA wire around it and annealed at 390°C as presented in our previous work [156]. The fabricated helix stent (single helix) is shown in figure 5.39 (c). The helix stent was then cut into 2 pieces of 16 coils each and using a safety pin as a shaft, it was stretched to 16 mm length to resemble the

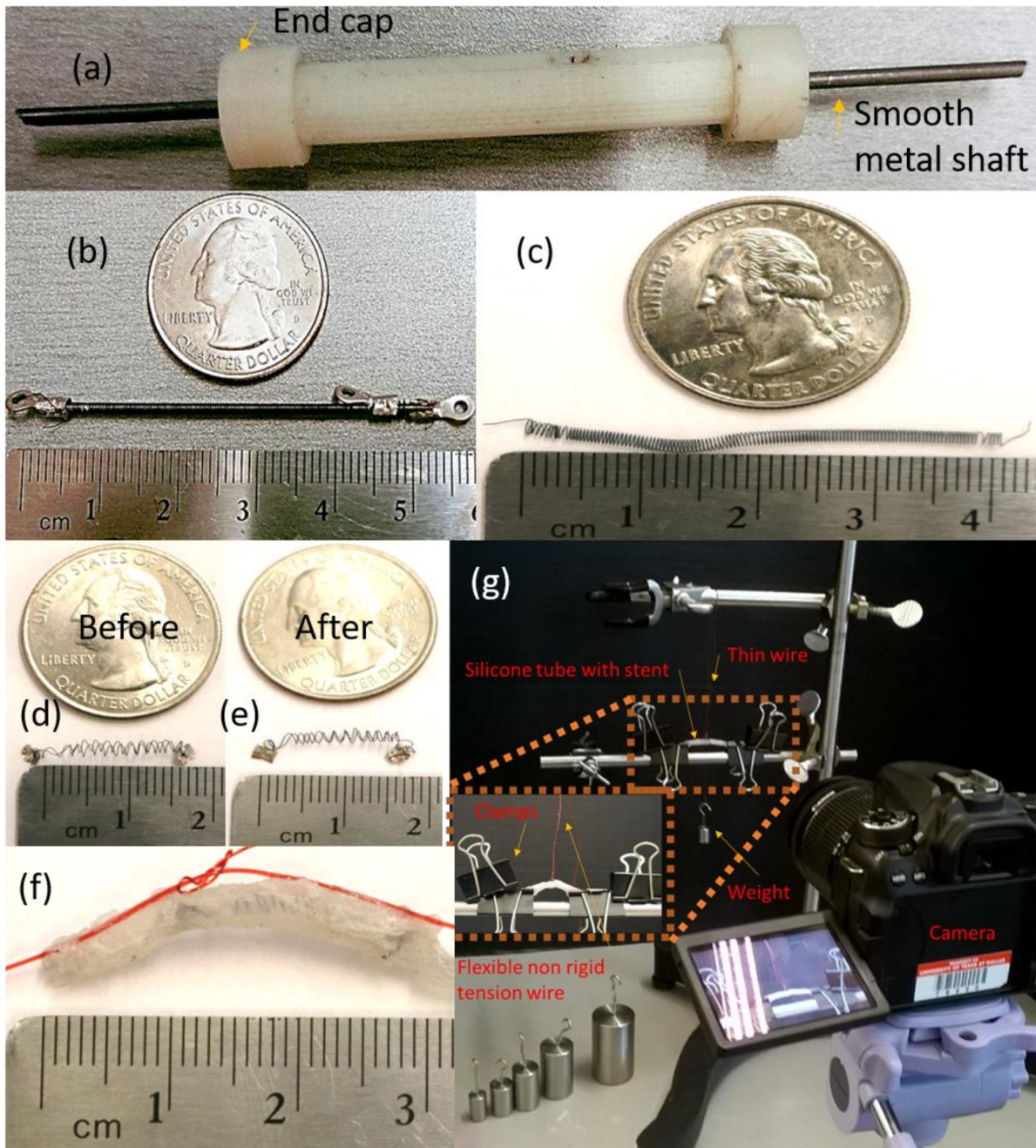


Figure 5.39. Simplified testing of double helix stent model (a) The EcoFlex™ 10 silicone coronary artery model, (b) the coiled and clamped Nitinol wire of diameter 0.1 mm around a metal screw in its thread, (c) the fabricated NiTi single helix stent after annealing at 390°C and removed from the screw (d) the double helix stent fabricated and clamped before the experiment, (e) slightly deformed double helix stent after the experiment where maximum deformation of about 6 times the simulation at a static load of 100 g, (f) the stent-coronary model, with the stent embedded carefully. The stent can be seen partially with the flexible non-rigid fishing line wire super-glued on both ends, not in center, (g) the experimental setup with stand with firmly fixed horizontal rods, calibrated weights and camera.

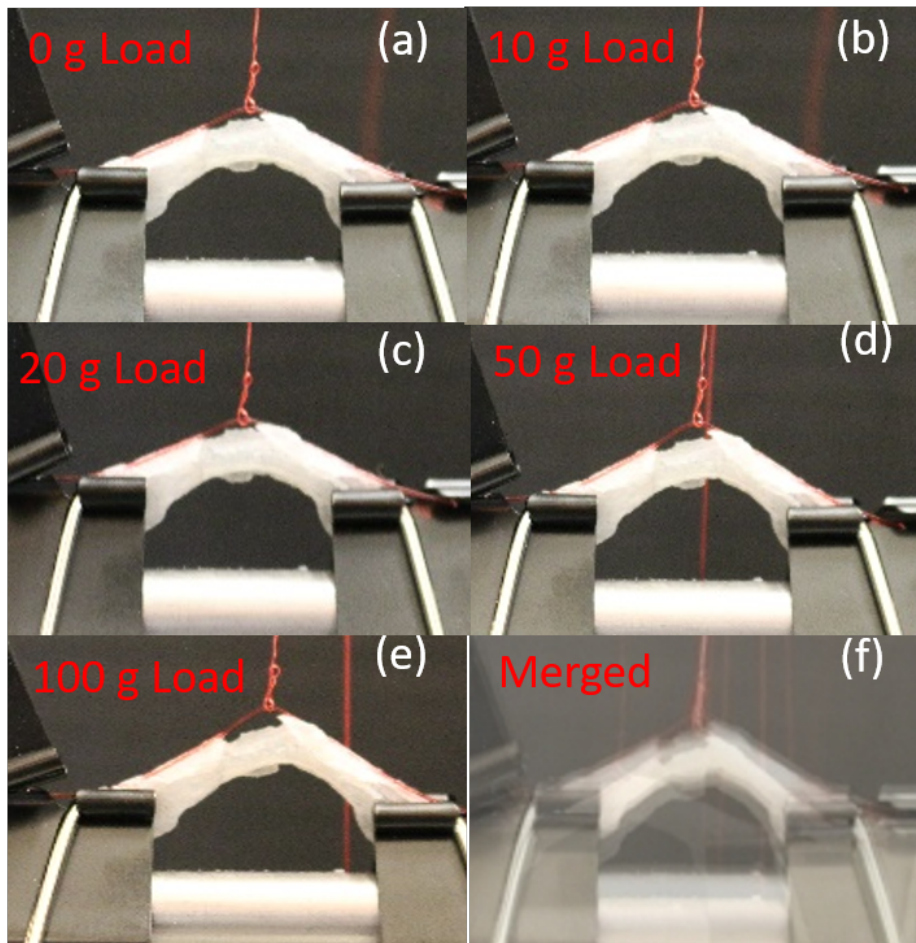


Figure 5.40. Experimental Results: (a-f) shows the snapshots of deformation when different loads are applied and with an initial curvature of 30 mm. The different loads are 0 or no load, 10 g, 20 g, 50 g, 100 g and merged picture of the all pictures.

simulation dimensions. Due to its shape memory property, the coil attains the new shape with a minimum stress application. Using the same safety pin as a shaft, we fixed one coil, inserted by rotating and pushing the other coil through the rings of the fixed coil, to make them a double helix, then crimp the ends. Then, the ends were clamped together using small metal clamps to maintain the position of the coils in the double helix form as shown in figure 5.39 (d-e).

The fabricated double helix stent was kept inside the silicone tube carefully using a tweezer not to destroy the double helix as shown in figure 5.39 (f). The process of fabricating

the double helix can be improved by automating the process. The experiment was conducted in static conditions rather than dynamic for simplicity, but with 5 times larger deformation than the simulation. The experimental setup consists of a stand with two horizontal rods firmly attached as shown in figure 5.39 (g). The bottom horizontal rod has clamps to hold the stent-coronary model in a fixed initial curvature position. The initial radius of curvature 30 mm was physically measured and was set to be fixed to maintain the curved geometry. A flexible non-rigid fishing line wire was super glued to the top curve of the stent-coronary model on both ends leaving the middle open. The open center was used to attach another wire for tensioning through a pulley system. Calibrated weights ranging from 10 g to 100 g were used to apply tension and displace the stent-coronary model. The central deformation achieved at 100 g weight was approximately 6 mm which is almost 5 times greater than the applied displacement in the simulation. There were no complications observed during testing after each load was applied for 30 seconds. A camera was used to take snapshots of the experiment at different loads as shown in figure 5.40 and the photos were calibrated for displacement and the results were plotted in a Matlab 2017a. The stent was carefully removed after the silicone coronary artery model was cut open to observe any stent failure as shown in figure 5.39 (e).

5.2.4 Simulation and Experimental Validation

The experiment conducted was using Ecoflex-10 rather than real human artery material. So similar simulation was conducted using Ecoflex-10 and compared with simulation for validation of the simulation. For the hyperelastic material constants of the Ecoflex-10 material, several uniaxial tensile tests were done using the Instron tensile tester (maximum load 50 kN) using the standard ASTM D412 Type C molded dog bone structures in 3D printed castings as seen in figure 5.41. The casted dog bone structures are stretched at standard 500 mm/min rate to get the uniaxial data as seen in figure 5.42. The average values of



Figure 5.41. Tensile testing silicone (a) shows the ASTM D412 Type C 3D printed casings for Ecoflex-10 silicone casting, (b) the casted dog bone structures, (c) and (d) show the Instron tensile tester (maximum load 50 kN) machine with the silicone dog bone structure.

the 6 samples from the tests was used to predict the hyperelastic constants using ABAQUS software using curve fitting. Even though ANSYS was used for simulation of the hyperelastic and superelastic multiphysics, ABAQUS was used for curve fitting of the hyperelastic uniaxial data as it was better fitting for experimental data. The curve fitting was done for 3 hyperelastic models, neo-hookean, yeoh 3rd order and polynomial 3rd order. The curve fitted hyperelastic constants can be seen in table 5.4. These constants are used to simulate the multiphysics hyperelastic and superelastic model in ANSYS for loads from 10 to 100g as same conditions as in the experiment as seen in figure 5.43. In figure 5.43, we see all the boundary conditions, loading conditions and model controlled meshing used. In figure 5.44, we see the simulated results along with the experimental ones from 10 - 100g load for all the hyperelastic models. We can see that yeoh 3rd order model is the closest to experimental results.

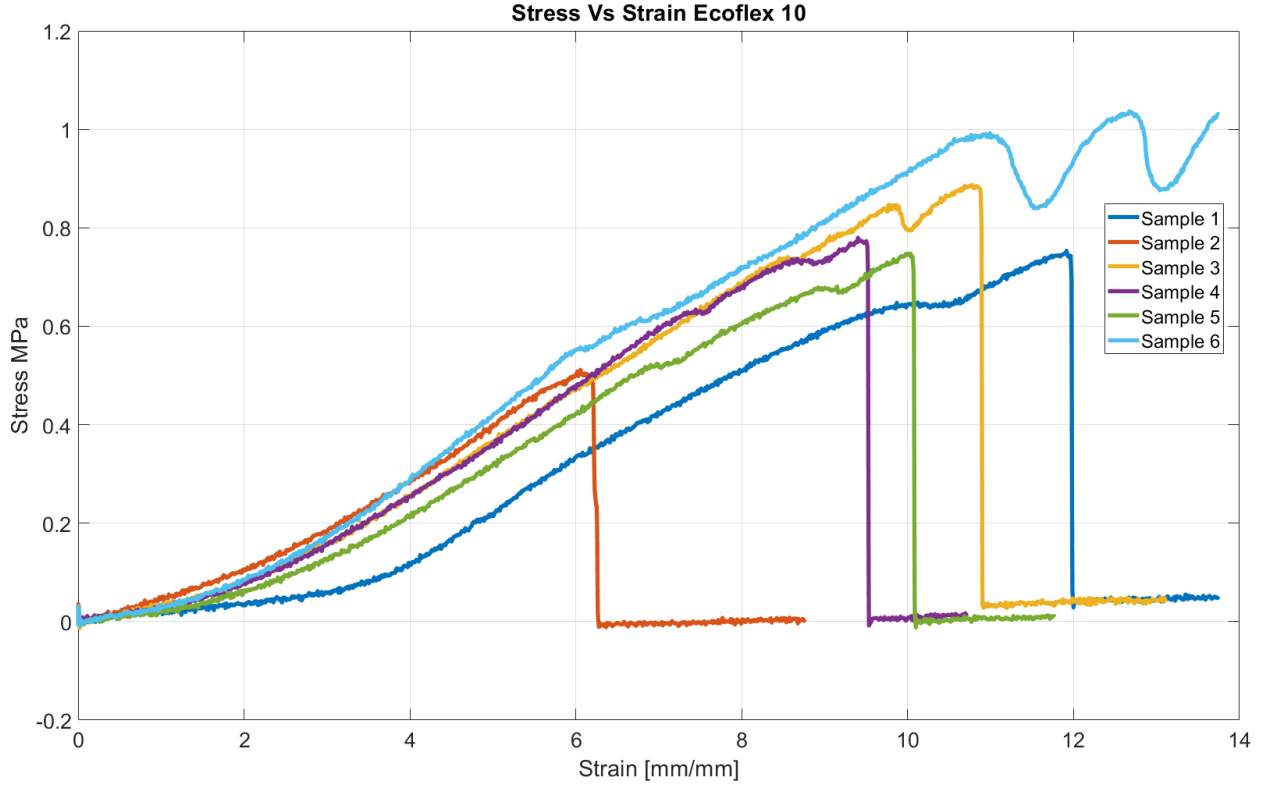


Figure 5.42. Uniaxial data (Stress vs Strain) of 6 samples Ecoflex-10 silicone ASTM D412 Type C casted dog bone structures using the Instron tensile tester (maximum load 50 kN) machine. Sample 3 result is used for simulation.

Table 5.4. Coefficients of the strain energy density function for each hyperelastic model [81], where W is strain energy potential; C_{ij} is material constants characterizing the deviatoric deformation of the material; I_i is deviatoric strain invariant

Hyperelastic Model	Constants	Strain energy potential equation
NEO-HOOKEAN	$C_{10} = 77e^{-4} MPa$	$W = C_{10}(I_1 - 3)$
YEOH (N = 3)	$C_{10} = 47e^{-4} MPa$ $C_{20} = 1e^{-4} MPa$ $C_{30} = 3e^{-7} MPa$	$W = \sum_{i=1}^N C_{i0}(I_1 - 3)^i$
POLYNOMIAL (N = 3)	$C_{10} = 4e^{-3} MPa$ $C_{20} = 2e^{-4} MPa$ $C_{30} = -7e^{-6} MPa$	$W = \sum_{i,j=1}^N C_{ij}(I_1 - 3)^i(I_2 - 3)^j$

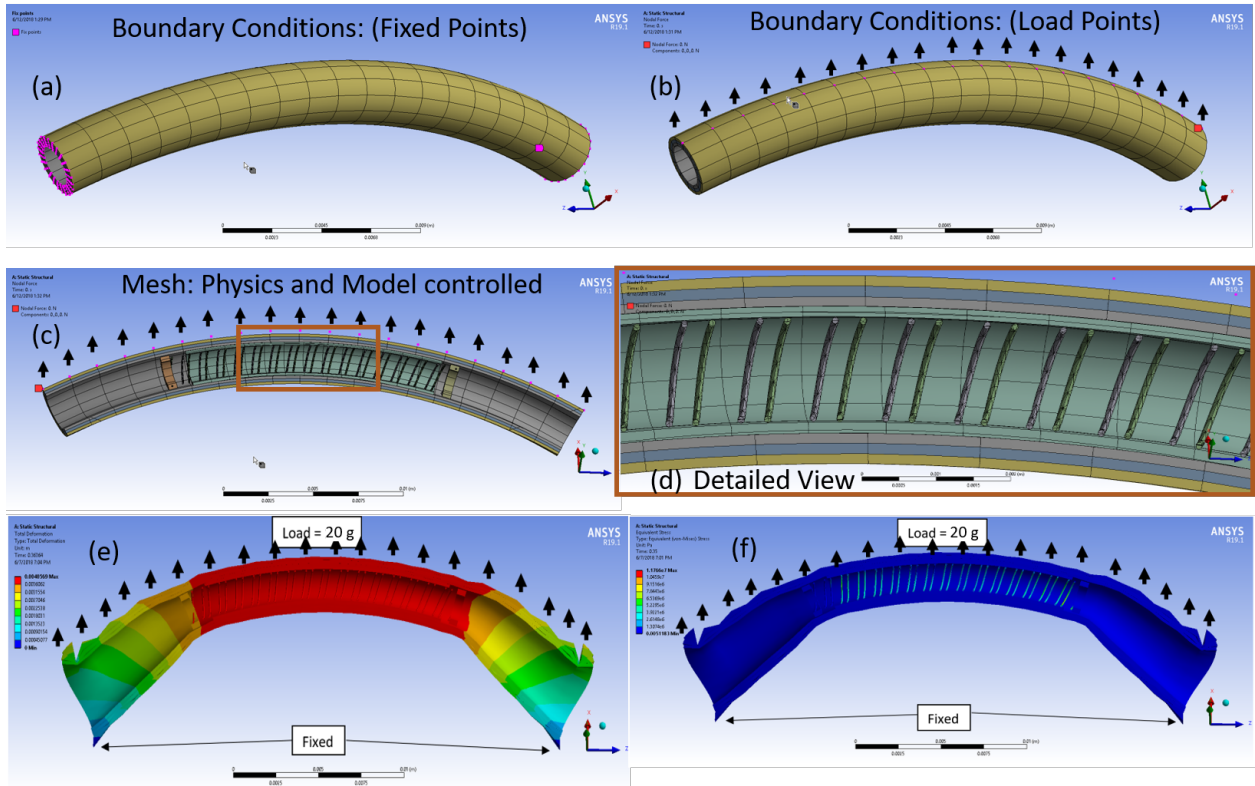


Figure 5.43. FEM Analysis: (a) and (b) show the boundary conditions (fixed and load points) used in ANSYS simulation to validate the experimental model ; (c) and (d) show the physics and model controlled meshing in ANSYS; Simulation results for uniformly distributed load of 20 g (e) deformation and (f) stress in the material.

5.2.5 Stent Implantation Techniques

In this section, we propose 2 feasible stent implantation techniques for the proposed double helix stent. The general stent implantation includes inflating of balloon and expanding the stent to desired position and locking it. We propose 2 methods in this section for our stent implantation, which is already in the expanded shape. The first method is using the shape memory property of the NiTi stent, where we use a NiTi SMA material with transition temperatures close to body heat. In this method, we can deform the stent in any shape desired for easy insertion to the location and then exposing it to the body heat to retain its original intended shape as seen in figure 5.45 (a) and (b). The annealing or exposing to

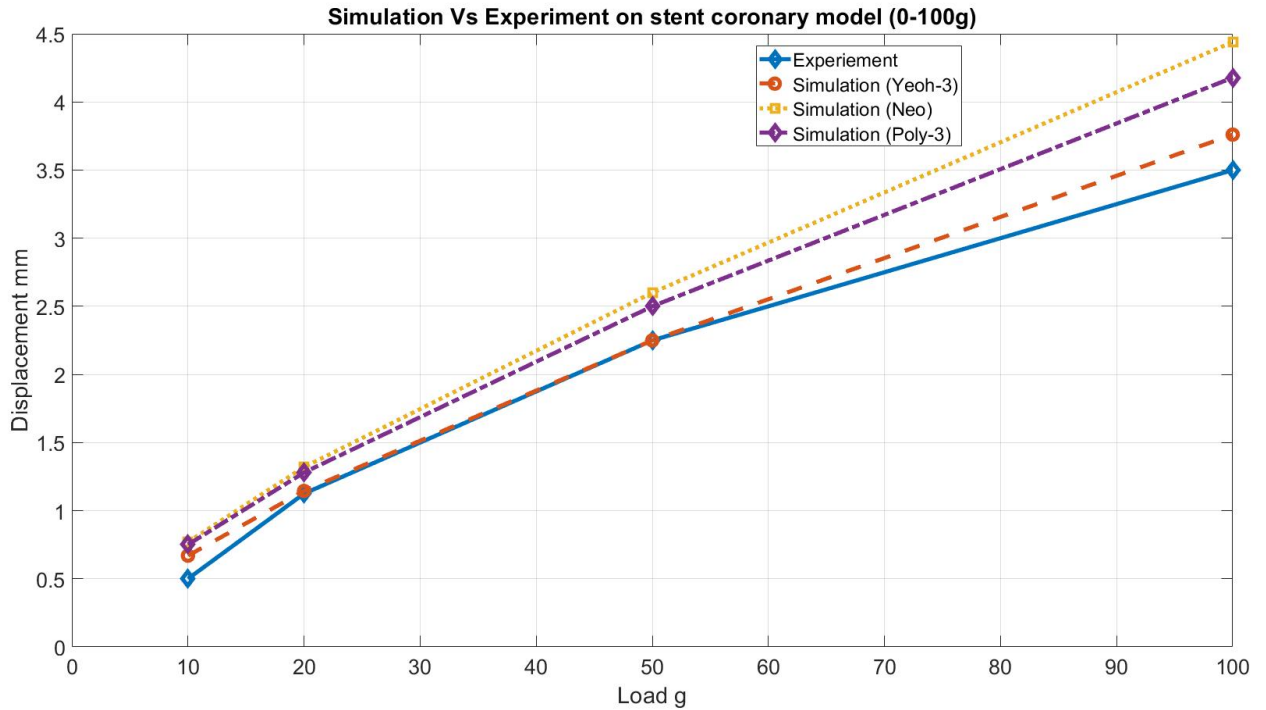


Figure 5.44. Matlab plot of experimental and simulated deformation with respect to 10 to 100g load with all the hyperelastic models. It shows the central deformation about 3.5 mm, which is almost 5 times more than the coronary artery deformation.

body heat process can be replaced by small voltage potential and considering low transition temperature of NiTi with different compositions. This process uses shape memory effect for insertion of the stent inside the coronary artery. The second method uses a little bit of torque to twist the spring model as seen in figure 5.46. the small torque will try to increase the number of turns and reduce the diameter of the spring. The reduced spring diameter under a small stress is transferred into a balloon which can be used to implant in inside the coronary artery as seen in 5.46 (d). Similar approach is used by Silkroad® medical which is coined as the TCAR procedure [8].

5.2.6 Discussion

In the simulation, at time 0.1 seconds we have a maximum von-Mises stress of 0.45 MPa at the central region of the stent model. At time 0.4 seconds, at the peak displacement (center

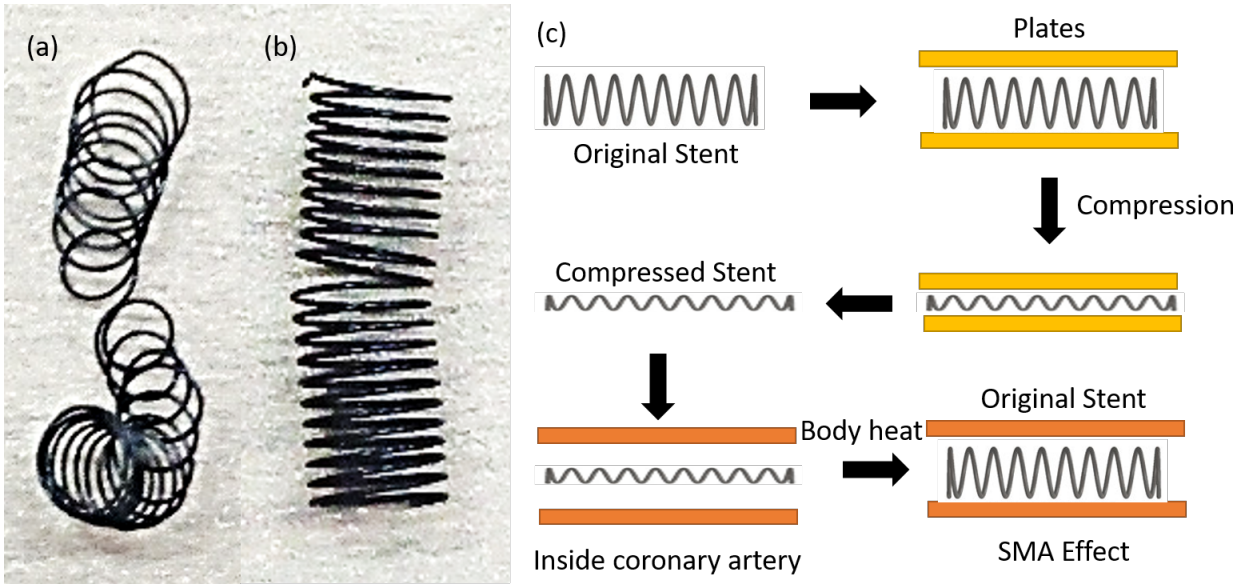


Figure 5.45. Stent implantation method 1: (a) The NiTi SMA stent is completely deformed to any desired shape for easy insertion, (b) annealing done in a furnace (exposing to body heat is possible for other composition) above transition temperature and (c) shows the schematic diagram of the insertion technique using the SMA effect.

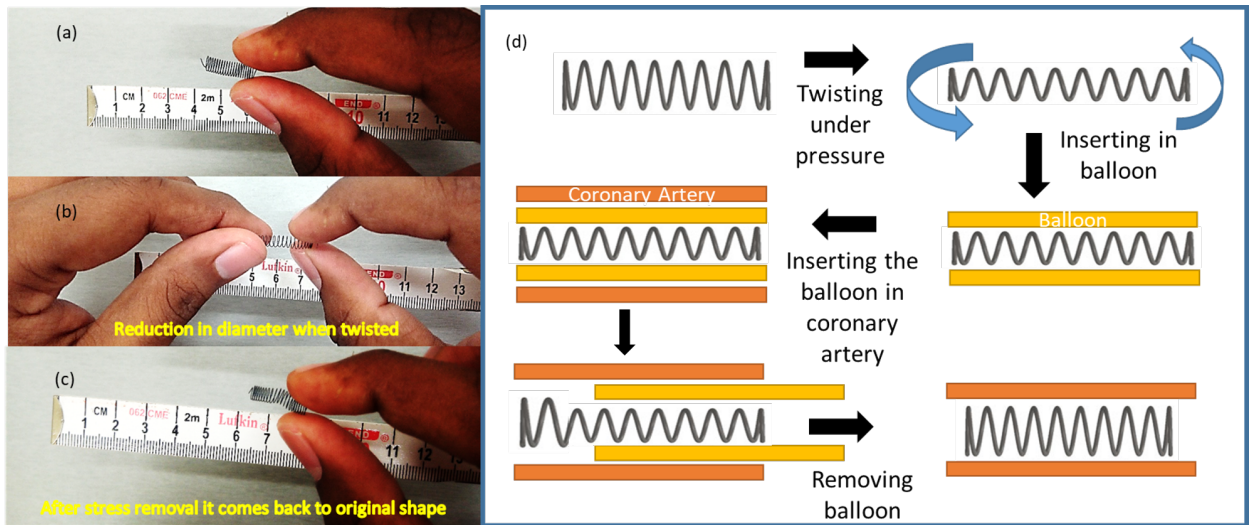


Figure 5.46. Stent implantation method 2: (a) shows a regular SMA spring stent, (b) slightly twisted SMA spring by hands showing reduction in diameter, (c) relaxed or torque released SMA spring stent and (d) shows the schematic diagram of insertion on the SMA spring stent inside the coronary artery using a compressive balloon for pre stress to reduce the diameter of the spring stent while insertion.

of the VDB cycle), we have the maximum von-Mises stress of 1.5 MPa at the central region of the stent model, which is 100 times smaller than 159.25 MPa observed by Xu *et al.* [235] for their model. Additionally, in contrary to the work presented by Xu *et al.*, there are no stress concentrations at any location of the stent which may lead to stent failure. At time 0.6 seconds, we have the maximum von-Mises stress of 0.54 MPa at the central region of the stent. We can conclude that the double helix model inspired by the DNA shape has higher potential to withstand the different cardiac cycles and the long service times without replacement making it highly reliable but the geometry may not be folded before inserted into the artery which can be a problem for deployment. Wu *et al.* [234] used NiTi stents for carotid artery which had maximum stress concentrations of approximately 400 MPa but we have to note that the location and boundary conditions are different from what presented in this work but the stents could sustain more pressure than what we have shown in this work.

In the preliminary experiment (static loading condition), there was no stent failure observed and only some rearrangement of the location helix rings was observed. The maximum weight used is 100 g, which might generate 63.6 MPa stress if the helix angles is ignored and assuming normal stress in the two helix ($\sigma = \frac{4F}{\pi d^2}$), for two helix cross section and ignoring the helix). We can conclude experimentally that the double helix stent may withstand higher load and remain in the shape and keep the coronary artery open.

Comparison of the NiTi Double Helix Stent with Other Published Geometries

In the cross cage 54/46 NiTi stent [76] (manufactured using raw materials NDC:CORDIS, Fremont, CA) the length of the stent is 23 mm and the expanded diameter is 9 mm. The double helix stent discussed in this work has a length of 14 mm, with a wire diameter of 0.1 mm, 14 rings and expanded diameter of 1.78 mm. Different stent dimensions are used for different locations of the body. We have designed the double helix stent for the coronary artery. Similarly, the single helix stent [162] which is designed for lung artery implantation

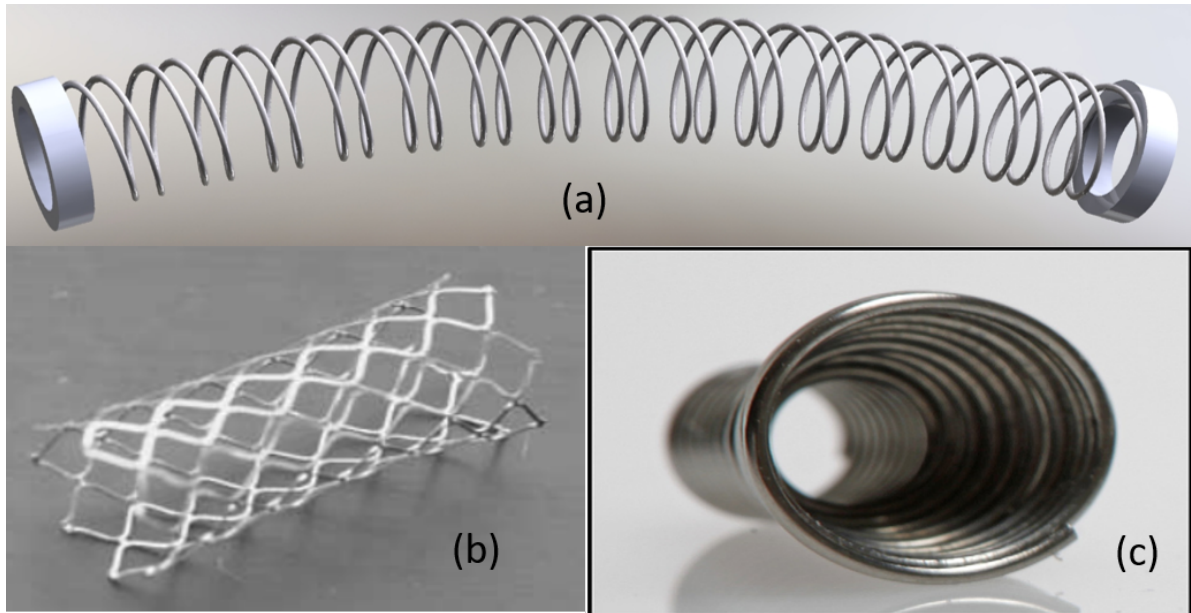


Figure 5.47. Comparison of the (a) NiTi double helix stent with (b)cross cage 54/46 NiTi stent [76] and (c) single helix NiTi stent [162]

has the length of 7 mm and the expanded diameter of 3.5-6 mm. In figure 5.47 we see the three models discussed, showing different shapes.

5.2.7 Conclusion

In this work, we presented a double helix NiTi based stent model for coronary arteries for treating coronary stenosis inspired from the model of DNA. We have shown that the double helix stent outperforms the commonly used stent model under vascular dynamic bending (VDB) by several order of magnitudes based on the finite element simulation. The maximum stress induced in the simulation is significantly small for stent failure and additionally there were no possible stress concentrations for mechanically weak locations in the model. We showed by experimentation that using a silicone coronary model with the NiTi double helix stent embedded inside does not fracture even with 5 times greater deformation with a maximum static load of 100 g which is equal to a light punch, which is much higher than the load the stent experiences in situ. After carefully removing the stent, we observed no

significant deformations to the stent. We have validated our simulation with experimental comparison with three hyperelastic models. We proposed 2 methods of insertion of the stent into the coronary artery. Therefore, we conclude that the double helix stent model might be reliable and is a potential solution to the stent fatigue problems in their clinical service time. More work should be done to develop the idea further.

CHAPTER 6

SUMMARY AND CONCLUSION

This dissertation is focused on conductive filament, NiTi based coiled shape memory alloy actuators (CSMA) and applications of CSMA. First, composite filaments consisting of nano-carbon PLA and 3D printing technique of the composites are introduced. The filaments were thoroughly explored in all parameters from fabrication, characterization and application. Second, coiled SMAs are extensively studied to use them as actuators to replace bulky, heavy and noisy servo motors that are used in robotic systems. CSMA are investigated from different perspectives like fabrication, characterization and application. Application of SMA and CSMA in soft robotic pump has been demonstrated. Case study on the use of CSMA as a stent was illustrated using a double helix CSMA stent.

6.1 Summary

The first chapter of the dissertation describes the motivation and the objectives of the study. Later, in chapter 2 we discuss the different humanoids present commercially and academically in categories of biped humanoids and human-like robots. Next, we introduce the humanoid “buddy” and give a brief description of its hardware and its capabilities.

The third chapter provides an insight on the novel nano-carbon PLA 3D printing technique for printing conductive circuitry for humanoids to solve detachable and tangling wires during actuation or movement. The detailed description of fabrication parameters, characterization of the filaments, a sample 3D printed part and possible application on humanoids are presented.

The fourth chapter shows the investigation of CSMA including fabrication at various parameters, characterization under different conditions, geometrical properties and application on artificial musculoskeletal joint. It discusses how CSMA are better actuators than TCPs

expect their limitations like higher hysteresis and cost.

The fifth chapter covers three applications of CSMAs. First, a soft pump artificial heart for humanoids for blushing. A detailed analysis on CSMAs', manufacturing, experimental setup and modeling using FEM software are presented. This section throws a contrast on the performance of CSMAs vs regular SMAs and how CSMAs outperform SMAs in performance. Second, a case study is presented that deals with a novel double helix CSMA stent for coronary arteries in health-care. Static simulation of the stent in the coronary artery is performed and a similar experiment is done to verify. It was shown that the stent model has low stress magnitude when VDB of heart is applied in coronary artery simulation.

6.2 Contributions

The major contributions of this dissertation are as follows:

6.2.1 Humanoids Buddy and HBS-1

Chapter 2 presents a 3D printed small and affordable human-like robots, humanoid “Buddy” and “HBS-1” that can serve as an assistive device or co-robot and at the same time entertain users. We present extensive literature review on humanoid robots focusing on Degrees of freedom (DOF) and the cost of humanoids from few dollars to millions. We briefly described the hardware, feasible movements, ballet dance synchronization, implementation of audio through open source Arduino board, color recognition of using the camera and finally the load carrying capacity of the arm. The 3D printing enables the flexibility and customizability according to the need of the subject. The audio synchronization with the dance makes it more lovely, whereas the color detection can help in checking the health condition of the subject by doing more work in color recognition. The important factor for the 3D printed robot, which is the load carry capacities of the arm were, determined both experimentally and via simulation. It was shown that the robot can easily handle commonly used objects and

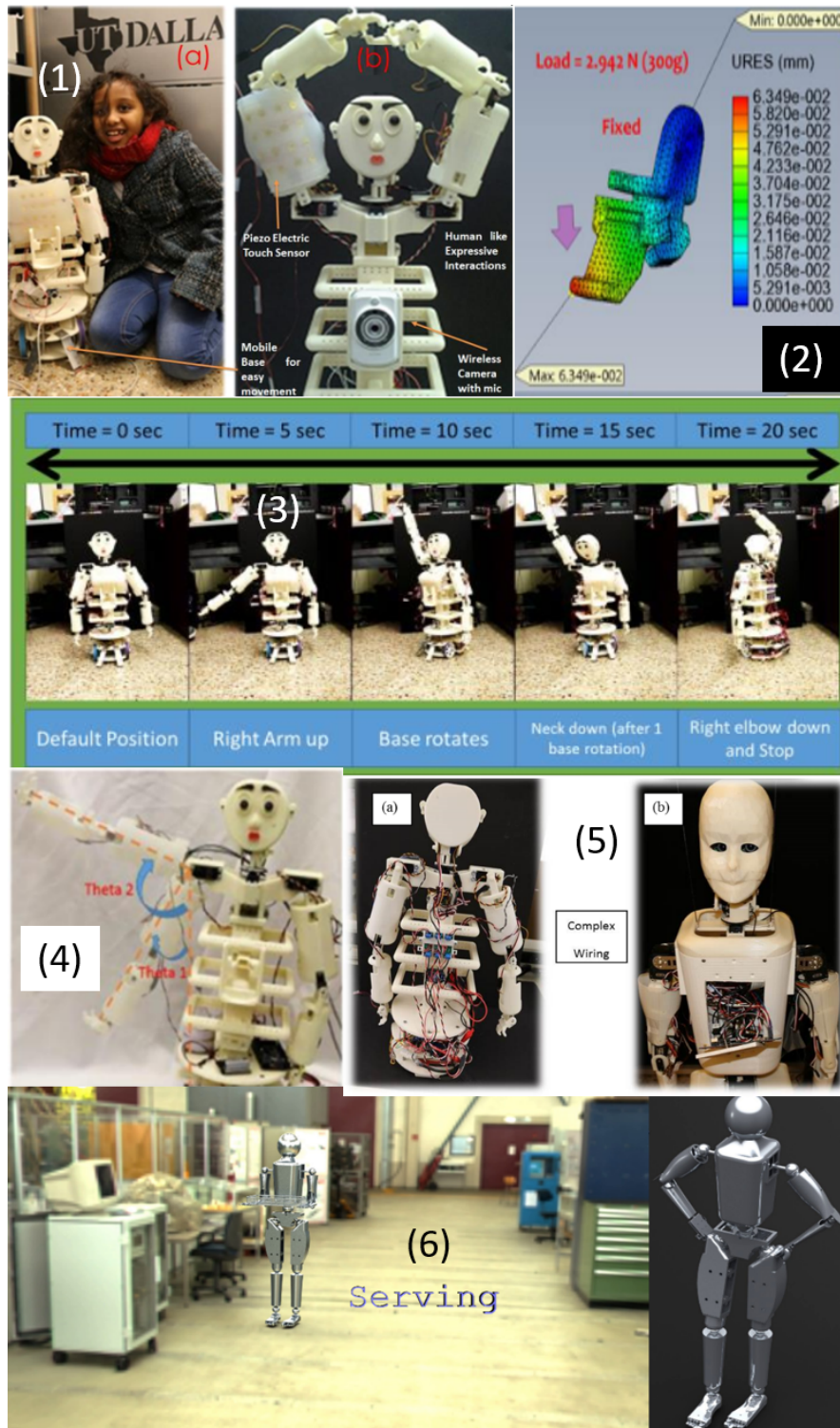


Figure 6.1. Overview of chapter 2: (1) Humanoid Buddy - 3D printed robot , (2) Simulation of load carrying capacity of humanoid Buddy arm,(3) “Ballet” dance performance by humanoid Buddy, (4) Experimental verification of load carrying capacity, (5) Complex wiring of Buddy and HBS-1 and (6) Humanoid HBS-1 initial design. [153, 155, 232]

help users in fetching and providing tools like thermometer, heart monitors, etc. Overview of chapter 1 is shown in figure 6.1.

6.2.2 Investigation of Polylactide and Carbon Nanocomposite Filament for 3D printing

A composite material consisting of carbon nanoparticle (NC), dichloromethane (DCM) and polylactide (PLA) was made for use as filament material for application in additive manufacturing and the material was characterized extensively and explained in chapter 3. The electrical conductivity and mechanical properties of the filament material were experimentally measured for various weight percentages of mesoporous carbon nanoparticles in polylactide matrix. It was found that the synthesized filaments had a mechanical strength of 12 MPa than the original solid PLA filament (60MPa) but the electrical resistivity was improved from infinite to a range of 64 ± 25 to $1.4 \pm 0.48 \Omega\text{m}$ for 6 to 15 wt.% NC: PLA composition. A sample structure of $30 \times 5 \times 1 \text{ mm}^3$ was 3D printed and tested for mechanical strength and resistivity, and it was found to be 25 MPa and $20 \pm 10 \Omega\text{m}$ respectively. SEM images showed a relatively large number of particles distributed across the filament for a higher concentration of NC. The method can be used to build robot structures with electrical circuitry except at the joints. The connection at joints can be made by a jumper that maintains continuous contact as discussed in the chapter. This approach reduces the problem of dangling and detachment of wires often encountered in many robotic systems. This work is easy to implement with any 3D printed structures that need electronic circuitry in an economical way using FDM 3D printers. Future of this project is the implementation of the technique presented in robotics and other complex wiring applications. Overview of chapter 3 is shown in figure 6.2.

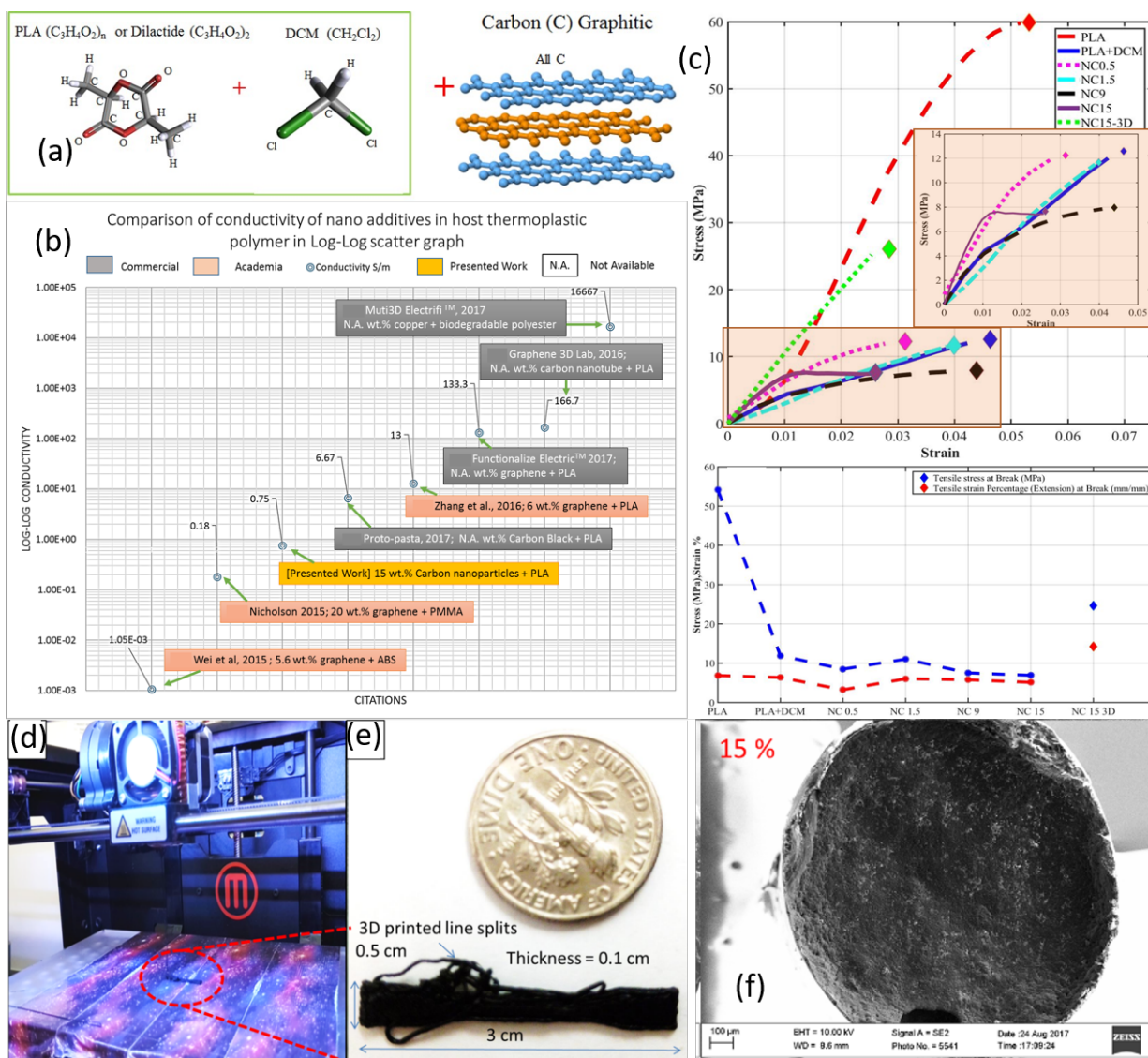


Figure 6.2. Overview of chapter 3: (a) molecular structure of PLA, DCM and graphitic carbon, (b) comparison of conductivity of the filament from the present work with other published or commercially available conductive filaments, (c) Tensile testing of the filaments with different weight percentage carbon nanoparticle filler and the 3D printed part, (d) 3D printing the NC15 filament, (e) 3D printed dog bone structure and (f) SEM images of cross-section of the NC15 filament. [160]

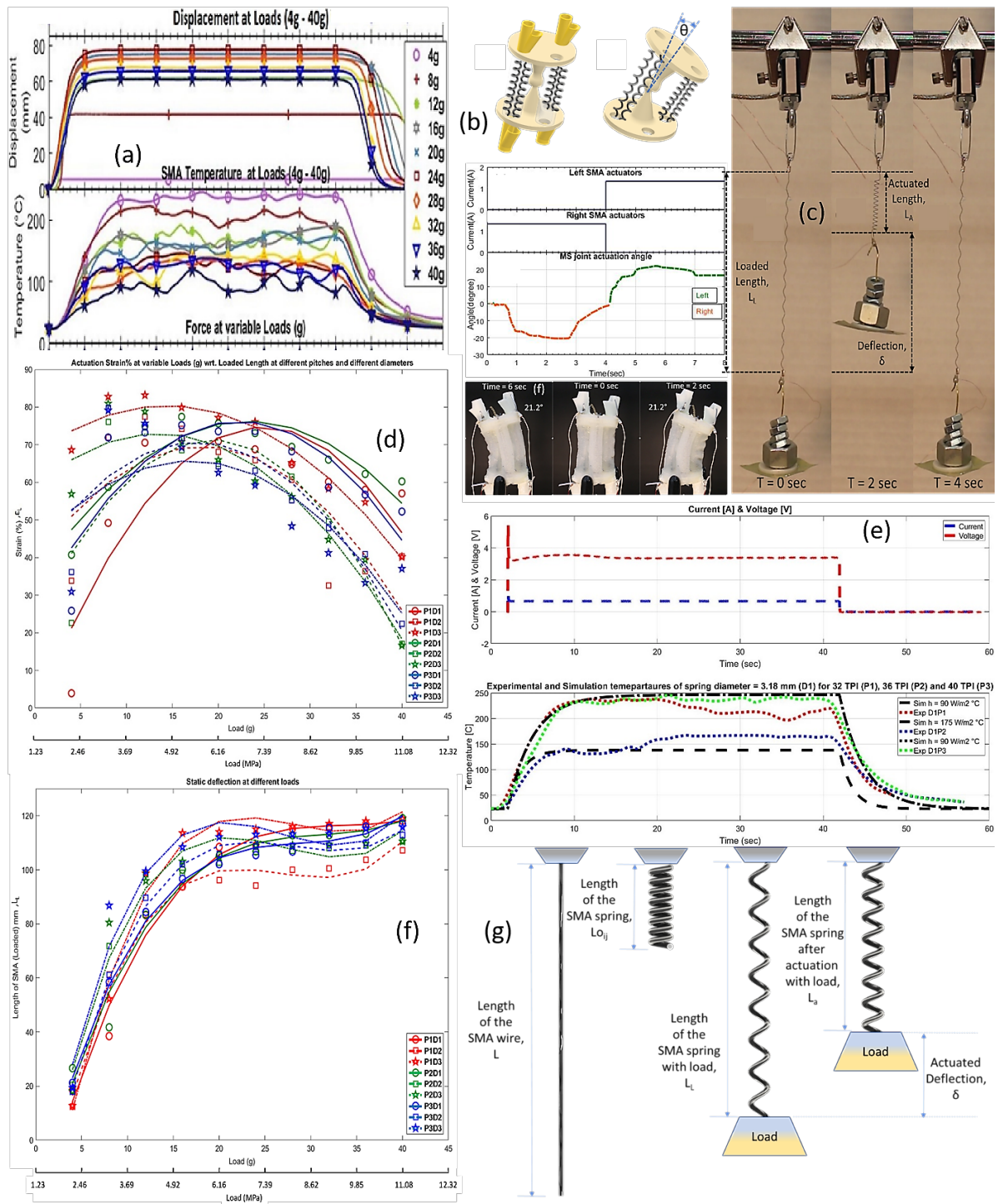


Figure 6.3. Overview of chapter 4: (a) Time domain characterization of D1P3 CSMA sample, (b) MS joint actuation using CSMA, (c) CSMA actuation time sequence, (d) 9 samples strain with respect to loaded length at different loads (strain > 80%) , (e) Simulation and experimental comparison of thermal profile of the CSMA actuation, (f) Initial deflection of the SMA spring with respect to load and (g) fabrication method and parameters used. [159]

Table 6.1. Typical profile of CSMA

Wire Diameter	Spring Diameter	Pitch	Strain	Frequency	Length of Spring	Length of SMA Wire	Load at max Strain	Operating conditions
0.2 mm	4.75 mm	32 TPI	80 %	0.25 Hz	6.38 mm	120 mm	19 g (5.85 MPa)	0.66 A; ~3.4 V; ~2.25 W

6.2.3 Fabrication and characterization of coiled shape memory alloy (CSMA) actuators for soft robots

There are a number of variables that play a role in the performance of the CSMA actuators. Some play a significant role, and some have a moderate effect. Chapter 4 presents the characterization of coiled SMA actuators mainly focusing on the spring geometry such as spring diameter and a variable number of coils per unit length. The manufacturing technique used for the fabrication of CSMA gives an advantage for large strains. Relatively high frequency is an important requirement for soft robots, which can be achieved using liquid cooling under embedded conditions. In this work, we presented coiled SMAs performance and complete characteristics under different loads for constant current, voltage, SMA wire diameter and SMA wire length for different spring diameters and a number of coils per unit length and discussed how the number of coils per unit length and spring diameters influence the performance of SMA spring actuators. We can see that number of turns (32-40 TPI) per unit length does not influence the maximum strain load but as we increase the diameter the load for maximum strain reduces. The maximum strain with respect to loaded length almost remains constant with respect to a number of turns per unit length, 75% for 3.18mm diameter, 70% for 3.96 mm and between 70-80% for 4.15 mm and the change cannot be determined clearly with respect to diameter as it does not follow any pattern, it varies between 70-80%. The maximum strain with respect to original length increases mostly with an increase in number of coils per unit length and increases with respect to the increase in diameter. The

maximum strain with respect to original length is observed greater than 1000% at weights almost to 1000 times the actuator original weight. In this chapter, we present the effect of 2-step hot-cold water cooling to improve actuation frequency and performance of coiled SMAs in an artificial musculoskeletal joint. The actuation angle achieved using CSMA in the MS joint is 24° whereas the actuation angle achieved using fishing line TCPs is 20° and frequency of MS joint with CSMA is 0.125 Hz whereas frequency of MS joint with fishing line TCPs is 30 mHz (4.167 times smaller) with pulsed actuation. In both angular rotation or strain and frequency there is significant increase from the performance of CSMA against fishing line TCPs for MS joint in this configuration. One limitation of SMA over TCP is hysteresis in actuation and the additional cost of metal alloys over nylon precursor materials. Overview of chapter 4 is shown in figure 6.3 and the typical profile of CSMA is shown in table 6.1.

6.2.4 Design and characterization of artificial heart for humanoid robot (SMAs Vs CSMA)

The design and fabrication of a soft artificial heart for a humanoid robot was presented in this chapter using a silicone elastomer and coiled shape memory alloy actuators. From this work, one can see the how CSMA outperform cylindrical SMA. The deformation behavior of the heart model was studied under different pressures using finite element analysis. Mooney-Rivlin model was used to predict the deformation of the elastomer used in the device. Simulations results showed that multiple sections in peristalsis motion by sequentially actuating affect the performance of the robotic heart pump. Three prototypes were developed and tested and we showed that the robotic heart can pump a blood-like fluid to parts of the robot face to simulate someone blushing or when someone is angry by the use of elastomeric substrates and certain features for the transport of fluids. Time domain characterization is performed to study the volume flow rate at different voltages and current. This

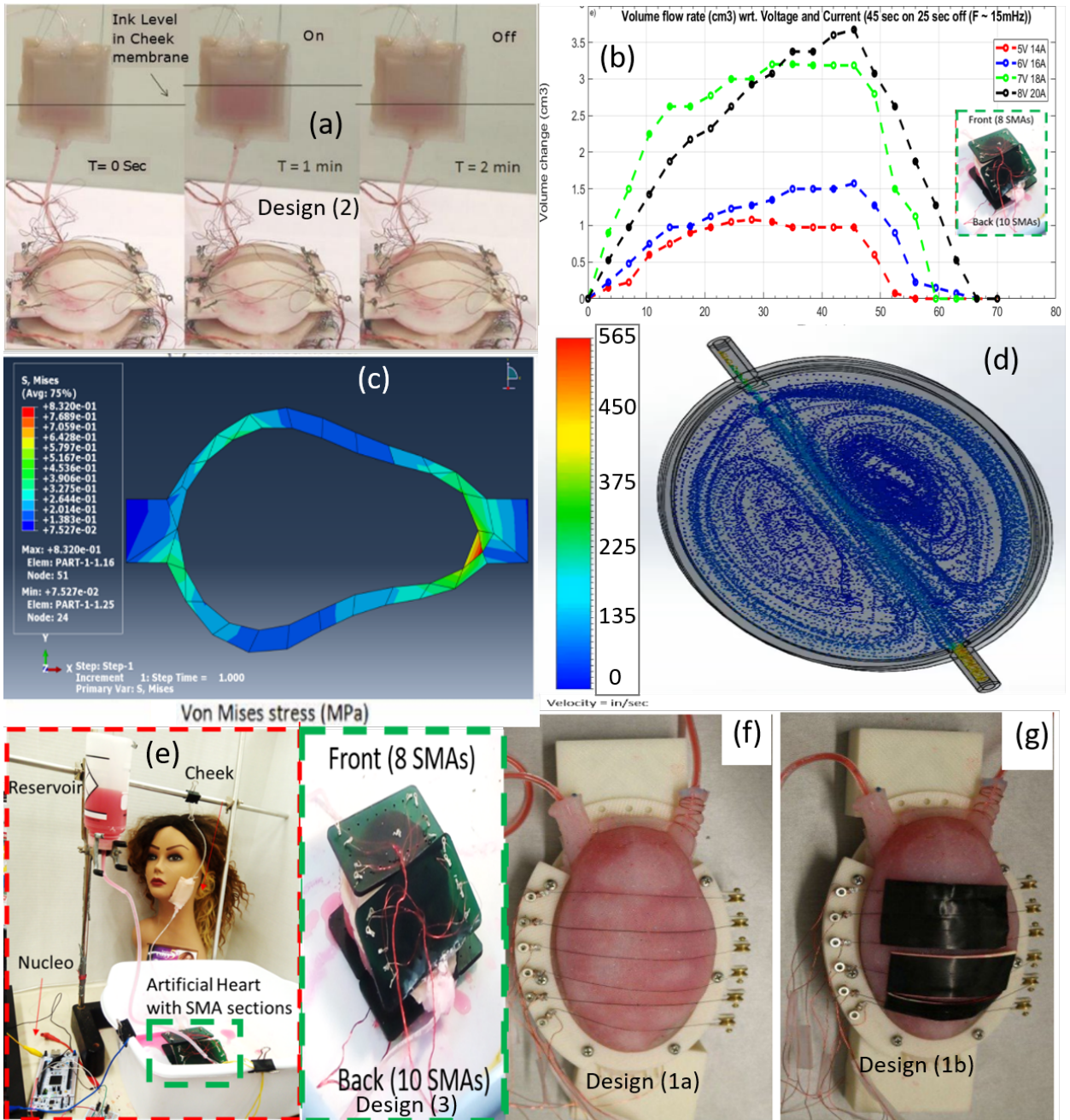


Figure 6.4. Overview of chapter 5 (a): (a) Time sequence of CSMA (Design 2) artificial heart pumping fluid into cheek structure, (b) characterization of CSMA (Design 3) artificial heart pumping (time domain), (c) ABAQUS simulation of 2 section peristalsis motion (Design 2), (d) SolidWorks flow simulation of the CSMA (Design 2 & 3) artificial heart pumping fluid, (e) Experimental Setup of CSMA (Design 3) artificial heart pumping, (f) and (g) show the design 1. [161, 157]

study is not only useful in humanoids but applicable in the medical fields (medical training device). The device can also be further developed to use in medical equipments like insulin pumps. This device can also be used to fabricate soft robot which can camouflage to the surroundings with change in color. Overview of chapter 5 (a) is shown in figure 6.4.

6.2.5 Simulation and experimental study of NiTi double helix stents for human coronary arteries

In this work, we presented a novel double helix stent model for coronary arteries for treating coronary stenosis inspired from the model of DNA. We have shown that the double helix stent outperforms the commonly used stent model under vascular dynamic bending (VDB) by several order of magnitudes based on the finite element simulation. The maximum stress induced in the simulation is significantly small for stent failure and additionally there were no possible stress concentrations for mechanically weak locations in the model. We showed by experimentation that using NiTi double helix stent embedded inside a silicone coronary model does not fracture even with when greater deformation is applied with a maximum static load of 100 g, which is much higher than the load the stent experiences in situ. After carefully removing the stent, we observed no significant deformations to the stent. We also conducted tensile testing of EcoFlex-10 and used the uniaxial data to simulate the hyperelastic material in ANSYS and also experimentally verified the simulation. Therefore, we conclude that the double helix stent model might be reliable and is a potential solution to the stent fatigue problems in their clinical service time. This work needs further investigation to identify and solve any issues associated with proposed idea. Overview of chapter 5 (b) is shown in figure 6.5.

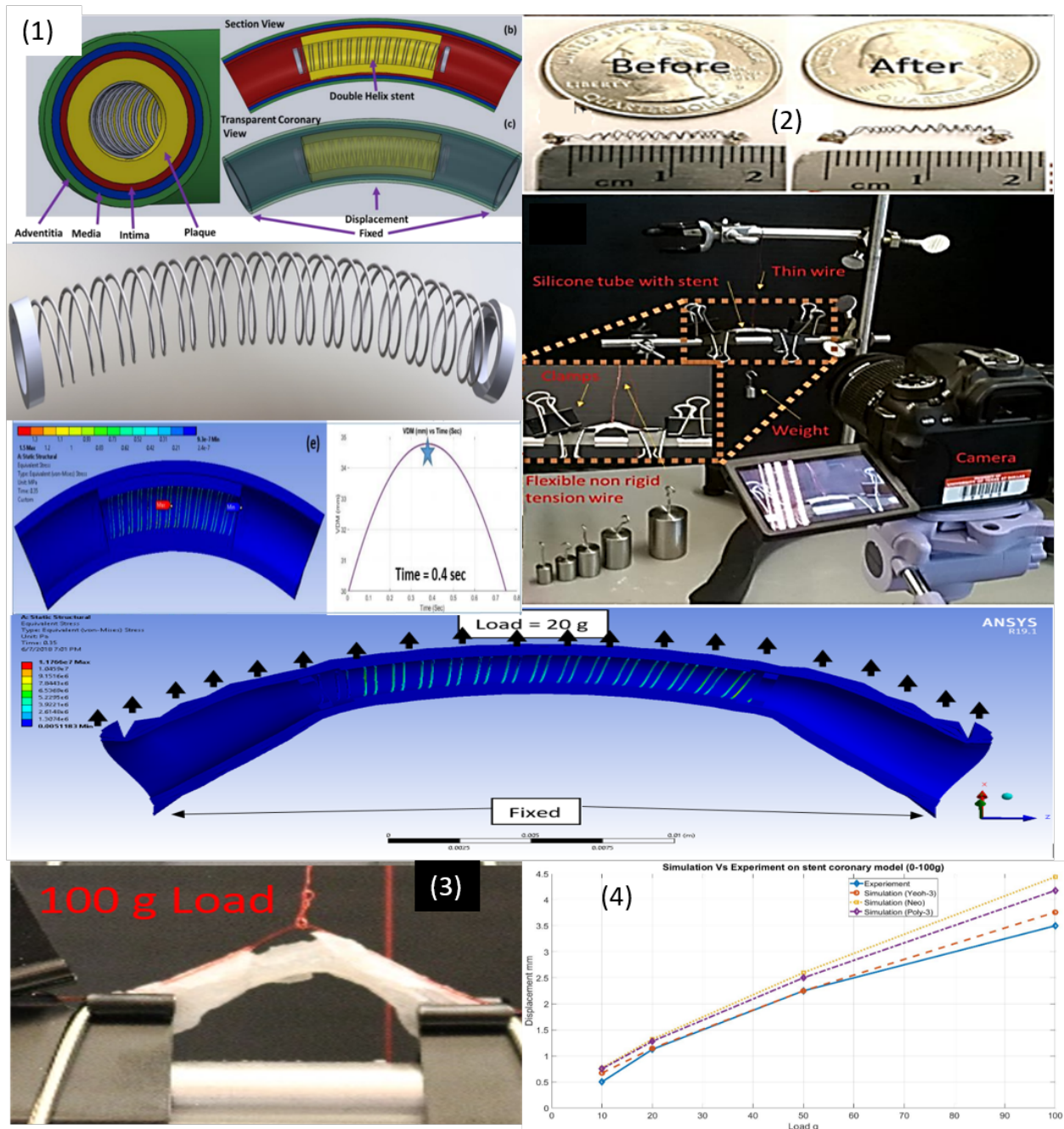


Figure 6.5. Overview of chapter 5 (b): (1) ANSYS multiphysics (hyperelastic and superelastic) simulation of the stent modal in the coronary artery, (2) Experimental setup and the custom made NiTi double helix stent in soft EcoFlex-10 silicone material, (3) Experimental results of the deformation with respect to load and (4) ANSYS simulation and experimental verification of the custom made NiTi double helix stent in soft EcoFlex-10 silicone material. [154]

BIBLIOGRAPHY

- [1] American heart association's complete guide to heart health: American heart association (1996).
- [2] Functionalize -electric™ pla. accessed august 8 2017. <http://functionalize.com/about/functionalize-f-electric-highly-conductive-filament/>.
- [3] Graphene, 3d lab inc., conductive, graphene, filament, accessed september 30 2016. <http://www.graphene3dlab.com/s/filament.asp..>
- [4] Hanson, robotics, ltd., sophia accessed june 22, 2018. <http://www.hansonrobotics.com/robot/sophia/>.
- [5] Meister s, 2012. accessed 9-26 2014, grain and particle analysis with line intersection method - file exchange - matlab central. <http://www.mathworks.com/matlabcentral/fileexchange/35203-grain-and-particle-analysis-with-line-intersection-method..>
- [6] Proto-pasta conductive pla. accessed august 20 2017. <https://www.proto-pasta.com/pages/conductive-pla.>
- [7] Robot scientist pushes limits of virtual reality, accessed on 30 july 2014. In <http://www.koreaherald.com/view.php?ud=20131225000122>.
- [8] Silk road medical, the tcar procedure. <http://silkroadmed.com> ,accessed june 14, 2018.
- [9] Acton, Q. (2013). *Robotics—Advances in Research and Application: 2013 Edition*. ScholarlyEditions.
- [10] Ahn, H. S., D.-W. Lee, D. Choi, D.-Y. Lee, M. Hur, and H. Lee (2012). Appropriate emotions for facial expressions of 33-dofs android head ever-4 h33. In *RO-MAN, 2012 IEEE*, pp. 1115–1120. IEEE.
- [11] Alam, M., M. Youssef, and M. Nehdi (2007). Utilizing shape memory alloys to enhance the performance and safety of civil infrastructure: a review. *Canadian Journal of Civil Engineering* 34(9), 1075–1086.
- [12] Ambrose, R. O., R. T. Savely, S. M. Goza, P. Strawser, M. A. Diftler, I. Spain, and N. Radford (2004). Mobile manipulation using nasa's robonaut. In *Robotics and Automation, 2004. Proceedings. ICRA'04. 2004 IEEE International Conference on*, Volume 2, pp. 2104–2109. IEEE.
- [13] An, S.-M., J. Ryu, M. Cho, and K.-J. Cho (2012). Engineering design framework for a shape memory alloy coil spring actuator using a static two-state model. *Smart Materials and Structures* 21(5), 055009.

- [14] Aoki, J., G. Nakazawa, K. Tanabe, A. Hoyer, H. Yamamoto, T. Nakayama, Y. Onuma, Y. Higashikuni, S. Otsuki, A. Yagishita, et al. (2007). Incidence and clinical impact of coronary stent fracture after sirolimus-eluting stent implantation. *Catheterization and Cardiovascular Interventions* 69(3), 380–386.
- [15] Arabia, F., J. Copeland, R. Smith, M. Banchy, B. Foy, R. Kormos, A. Tector, J. Long, W. Dembitsky, M. Carrier, et al. (1999). Cardiowest total artificial heart: a retrospective controlled study. *Artificial Organs-Cambridge* 23(2), 204–207.
- [16] Arjun, A., L. Saharan, and Y. Tadesse (2016). Design of a 3d printed hand prosthesis actuated by nylon 6-6 polymer based artificial muscles. In *Automation Science and Engineering (CASE), 2016 IEEE International Conference on*, pp. 910–915. IEEE.
- [17] Averous, L., L. Moro, P. Dole, and C. Fringant (2000). Properties of thermoplastic blends: starch–polycaprolactone. *Polymer* 41(11), 4157–4167.
- [18] Bak, D. (2003). Rapid prototyping or rapid production? 3d printing processes move industry towards the latter. *Assembly Automation* 23(4), 340–345.
- [19] Bar-Cohen, Y. and D. Hanson (2009). *The coming robot revolution: Expectations and fears about emerging intelligent, humanlike machines*. Springer Science & Business Media.
- [20] Barrett, L. F., M. Lewis, and J. M. Haviland-Jones (2016). *Handbook of emotions*. Guilford Publications.
- [21] Batliner, A., C. Hacker, S. Steidl, E. Nöth, S. D’Arcy, M. J. Russell, and M. Wong (2004). “you stupid tin box”-children interacting with the aibo robot: A cross-linguistic emotional speech corpus. In *LREC*.
- [22] Belter, J. T. and A. M. Dollar (2015). Strengthening of 3d printed fused deposition manufactured parts using the fill compositing technique. *PloS one* 10(4), e0122915.
- [23] Bergamasco, M., F. Salsedo, and P. Dario (1989). A linear sma motor as direct-drive robotic actuator. In *Robotics and Automation, 1989. Proceedings., 1989 IEEE International Conference on*, pp. 618–623. IEEE.
- [24] Berns, K. and J. Hirth (2006). Control of facial expressions of the humanoid robot head roman. In *Intelligent Robots and Systems, 2006 IEEE/RSJ International Conference on*, pp. 3119–3124. IEEE.
- [25] Boyd, J. G. and D. C. Lagoudas (1994). Thermomechanical response of shape memory composites. *Journal of intelligent material systems and structures* 5(3), 333–346.

- [26] Bridgwater, L. B., C. Ihrke, M. A. Diftler, M. E. Abdallah, N. A. Radford, J. Rogers, S. Yayathi, R. S. Askew, and D. M. Linn (2012). The robonaut 2 hand-designed to do work with tools. In *Robotics and Automation (ICRA), 2012 IEEE International Conference on*, pp. 3425–3430. IEEE.
- [27] Brinson, L. and M. Huang (1996). Simplifications and comparisons of shape memory alloy constitutive models. *Journal of intelligent material systems and structures* 7(1), 108–114.
- [28] Brinson, L. C. (1993). One-dimensional constitutive behavior of shape memory alloys: thermomechanical derivation with non-constant material functions and redefined martensite internal variable. *Journal of intelligent material systems and structures* 4(2), 229–242.
- [29] Broekens, J., M. Heerink, H. Rosendal, et al. (2009). Assistive social robots in elderly care: a review. *Gerontechnology* 8(2), 94–103.
- [30] Burns, A. and Y. Tadesse (2014). The mechanical design of a humanoid robot with flexible skin sensor for use in psychiatric therapy. In *Electroactive Polymer Actuators and Devices (EAPAD) 2014*, Volume 9056, pp. 90562H. International Society for Optics and Photonics.
- [31] carbon nanotube reinforced polyethylene terephthalate glycol copolymer 3D printing filament., D. E. C.-P. Accessed august 23 2017. <http://www.sigmaaldrich.com/catalog/product/aldrich/>.
- [32] Cheng, G., S.-H. Hyon, J. Morimoto, A. Ude, J. G. Hale, G. Colvin, W. Scroggin, and S. C. Jacobsen (2007). Cb: A humanoid research platform for exploring neuroscience. *Advanced Robotics* 21(10), 1097–1114.
- [33] Cheng, S. S., Y. Kim, and J. P. Desai (2017). Modeling and characterization of shape memory alloy springs with water cooling strategy in a neurosurgical robot. *Journal of intelligent material systems and structures* 28(16), 2167–2183.
- [34] Coghlan, A. (2013). Life savers: a history of the artificial heart. *New Scientist* 220(2945), 26–27.
- [35] Cooley, D. A., D. Liotta, G. L. Hallman, R. D. Bloodwell, R. D. Leachman, and J. D. Milam (1969). Orthotopic cardiac prosthesis for two-staged cardiac replacement. *American Journal of Cardiology* 24(5), 723–730.
- [36] Critchley, H. D., P. Rotshtein, Y. Nagai, J. O’doherly, C. J. Mathias, and R. J. Dolan (2005). Activity in the human brain predicting differential heart rate responses to emotional facial expressions. *Neuroimage* 24(3), 751–762.

- [37] Czarnocki, I., W. Kim, B. Utter, J. Luntz, D. Brei, and P. Alexander (2013). Design of sma helical actuators: An experimental study. In *ASME 2013 Conference on Smart Materials, Adaptive Structures and Intelligent Systems*, pp. V001T04A017–V001T04A017. American Society of Mechanical Engineers.
- [38] Da Pos, O. and P. Green-Armytage. Facial expressions, colours and basic emotions. *JAIC-Journal of the International Colour Association 1*.
- [39] Darwin, C. and P. Prodger (1998). *The expression of the emotions in man and animals*. Oxford University Press, USA.
- [40] Dautenhahn, K. (2002). Design spaces and niche spaces of believable social robots. In *Robot and Human Interactive Communication, 2002. Proceedings. 11th IEEE International Workshop on*, pp. 192–197. IEEE.
- [41] Dautenhahn, K., C. L. Nehaniv, M. L. Walters, B. Robins, H. Kose-Bagci, N. A. Mirza, and M. Blow (2009). Kaspar—a minimally expressive humanoid robot for human–robot interaction research. *Applied Bionics and Biomechanics 6*(3-4), 369–397.
- [42] Davis, D. R., F. N. Permenter, and N. A. Radford (2012, August 28). System and method for calibrating a rotary absolute position sensor. US Patent 8,250,901.
- [43] Davis, D. R., N. A. Radford, F. N. Permenter, A. H. Parsons, and J. S. Mehling (2011, November 29). Method and apparatus for electromagnetically braking a motor. US Patent 8,067,909.
- [44] Davis, D. R., N. A. Radford, F. N. Permenter, M. C. Valvo, and R. S. Askew (2013, May 14). Integrated high-speed torque control system for a robotic joint. US Patent 8,442,684.
- [45] Devaux, E., C. Aubry, C. Campagne, and M. Rochery (2011). Pla/carbon nanotubes multifilament yarns for relative humidity textile sensor. *Journal of Engineered Fabrics & Fibers (JEFF) 6*(3).
- [46] DeVries, W. C. (1988). The permanent artificial heart: four case reports. *Jama 259*(6), 849–859.
- [47] Diftler, M., T. Ahlstrom, R. Ambrose, N. Radford, C. Joyce, N. De La Pena, A. Parsons, and A. Noblitt (2012). Robonaut 2—initial activities on-board the iss. In *Aerospace Conference, 2012 IEEE*, pp. 1–12. IEEE.
- [48] Diftler, M. A., J. Mehling, M. E. Abdallah, N. A. Radford, L. B. Bridgwater, A. M. Sanders, R. S. Askew, D. M. Linn, J. D. Yamokoski, F. Permenter, et al. (2011). Robonaut 2—the first humanoid robot in space. In *Robotics and Automation (ICRA), 2011 IEEE International Conference on*, pp. 2178–2183. IEEE.

- [49] DYNALLOY, I. Flexinol® actuator wire technical and design data. <http://www.dynalloy.com/>.
- [50] Elahinia, M. (2004). *Effect of system dynamics on shape memory alloy behavior and control*. Ph. D. thesis, Virginia Tech.
- [51] Endo, G., J. Nakanishi, J. Morimoto, and G. Cheng (2005). Experimental studies of a neural oscillator for biped locomotion with qrio. In *Robotics and Automation, 2005. ICRA 2005. Proceedings of the 2005 IEEE International Conference on*, pp. 596–602. IEEE.
- [52] Enemark, S., I. F. Santos, and M. A. Savi (2016). Modelling, characterisation and uncertainties of stabilised pseudoelastic shape memory alloy helical springs. *Journal of Intelligent Material Systems and Structures* 27(20), 2721–2743.
- [53] Espalin, D., D. W. Muse, E. MacDonald, and R. B. Wicker (2014). 3d printing multifunctionality: structures with electronics. *The International Journal of Advanced Manufacturing Technology* 72(5-8), 963–978.
- [54] Fischman, D. L., M. B. Leon, D. S. Baim, R. A. Schatz, M. P. Savage, I. Penn, K. Detre, L. Veltri, D. Ricci, M. Nobuyoshi, et al. (1994). A randomized comparison of coronary-stent placement and balloon angioplasty in the treatment of coronary artery disease. *New England Journal of Medicine* 331(8), 496–501.
- [55] Foulger, S. H. (1999). Electrical properties of composites in the vicinity of the percolation threshold. *Journal of Applied Polymer Science* 72(12), 1573–1582.
- [56] Frazier, O. H. and W. E. Cohn (2012, July 24). Total artificial heart system for auto-regulating flow and pressure. US Patent 8,226,712.
- [57] Frost, M., P. Sedlák, L. Kadeřávek, L. Heller, and P. Šittner (2016). Modeling of mechanical response of niti shape memory alloy subjected to combined thermal and non-proportional mechanical loading: A case study on helical spring actuator. *Journal of Intelligent Material Systems and Structures* 27(14), 1927–1938.
- [58] Fung, Y.-c. (1977). A first course in continuum mechanics. *Englewood Cliffs, NJ, Prentice-Hall, Inc., 1977. 351 p.*
- [59] Furuya, Y. and H. Shimada (1991). Shape memory actuators for robotic applications. *Materials & Design* 12(1), 21–28.
- [60] Gao, Y., H. Li, and J. Liu (2012). Direct writing of flexible electronics through room temperature liquid metal ink. *PLoS One* 7(9), e45485.
- [61] Garg, S. and P. W. Serruys (2010). Coronary stents: current status. *Journal of the American College of Cardiology* 56(10), S1–S42.

- [62] Giszter, S. F., K. A. Moxon, I. Rybak, and J. K. Chapin (2000). A neurobiological perspective on humanoid robot design. *IEEE Intelligent Systems and their Applications* 15(4), 64–69.
- [63] Gray, N. A. and C. H. Selzman (2006). Current status of the total artificial heart. *American heart journal* 152(1), 4–10.
- [64] Guo, S.-z., X. Yang, M.-C. Heuzey, and D. Therriault (2015). 3d printing of a multi-functional nanocomposite helical liquid sensor. *Nanoscale* 7(15), 6451–6456.
- [65] Hadi, A., A. Yousefi-Koma, M. M. Moghaddam, M. Elahinia, and A. Ghazavi (2010). Developing a novel sma-actuated robotic module. *Sensors and Actuators A: Physical* 162(1), 72–81.
- [66] Haines, C. S., M. D. Lima, N. Li, G. M. Spinks, J. Foroughi, J. D. Madden, S. H. Kim, S. Fang, M. J. de Andrade, F. Göktepe, et al. (2014). Artificial muscles from fishing line and sewing thread. *science* 343(6173), 868–872.
- [67] Hans, M., B. Graf, and R. Schraft (2002). Robotic home assistant care-o-bot: Past-present-future. In *Robot and Human Interactive Communication, 2002. Proceedings. 11th IEEE International Workshop on*, pp. 380–385. IEEE.
- [68] Hanson, D. (2006). Exploring the aesthetic range for humanoid robots. In *Proceedings of the ICCS/CogSci-2006 long symposium: Toward social mechanisms of android science*, pp. 39–42. Citeseer.
- [69] Hanson, D., R. Bergs, Y. Tadesse, V. White, and S. Priya (2006). Enhancement of eap actuated facial expressions by designed chamber geometry in elastomers. In *Smart Structures and Materials 2006: Electroactive Polymer Actuators and Devices (EAPAD)*, Volume 6168, pp. 616806. International Society for Optics and Photonics.
- [70] Haroosh, H. J., D. S. Chaudhary, and Y. Dong (2012). Electrospun pla/pcl fibers with tubular nanoclay: morphological and structural analysis. *Journal of Applied Polymer Science* 124(5), 3930–3939.
- [71] Hashimoto, T., S. Hitramatsu, T. Tsuji, and H. Kobayashi (2006). Development of the face robot saya for rich facial expressions. In *SICE-ICASE, 2006. International Joint Conference*, pp. 5423–5428. IEEE.
- [72] Hayward, W., L. Haseler, L. Kettwich, A. Michael, W. Sibbitt Jr, and A. Bankhurst (2011). Pressure generated by syringes: implications for hydrodissection and injection of dense connective tissue lesions. *Scandinavian journal of rheumatology* 40(5), 379–382.

- [73] Helal, A. and B. Abdulrazak (2006). Tecarob: Tele-care using telepresence and robotic technology for assisting people with special needs. *International Journal of ARM* 7(3), 46–53.
- [74] Ho, M. and J. P. Desai (2009). Characterization of sma actuator for applications in robotic neurosurgery. In *Engineering in Medicine and Biology Society, 2009. EMBC 2009. Annual International Conference of the IEEE*, pp. 6856–6859. IEEE.
- [75] Holschuh, B. and D. Newman (2014). Low spring index, large displacement shape memory alloy (sma) coil actuators for use in macro-and micro-systems. In *Reliability, Packaging, Testing, and Characterization of MOEMS/MEMS, Nanodevices, and Nanomaterials XIII*, Volume 8975, pp. 897505. International Society for Optics and Photonics.
- [76] Holton, A., E. Walsh, A. Anayiotos, G. Pohost, and R. Venugopalan (2002). Comparative mri compatibility of 316l stainless steel alloy and nickel–titanium alloy stents: Original article technical. *Journal of Cardiovascular Magnetic Resonance* 4(4), 423–430.
- [77] Holzapfel, G. A., G. Sommer, C. T. Gasser, and P. Regitnig (2005). Determination of layer-specific mechanical properties of human coronary arteries with nonatherosclerotic intimal thickening and related constitutive modeling. *American Journal of Physiology-Heart and Circulatory Physiology* 289(5), H2048–H2058.
- [78] Horvath, J. (2014). A brief history of 3d printing. In *Mastering 3D Printing*, pp. 3–10. Springer.
- [79] Huang, X. and Y. Liu (2001). Effect of annealing on the transformation behavior and superelasticity of niti shape memory alloy. *Scripta Materialia* 45(2), 153–160.
- [80] Hwang, S., E. I. Reyes, K.-s. Moon, R. C. Rumpf, and N. S. Kim (2015). Thermo-mechanical characterization of metal/polymer composite filaments and printing parameter study for fused deposition modeling in the 3d printing process. *Journal of Electronic Materials* 44(3), 771–777.
- [81] Hyperelasticity. Hyperelasticity.<https://www.sharcnet.ca/software/ansys/>.
- [82] Inaba, M., T. Igarashi, S. Kagami, and H. Inoue (1997). Design and implementation of a 35 dof full-body humanoid that can sit, stand up and grasp an object. *Advanced robotics* 12(1), 1–14.
- [83] Innovative Technology International, I. Specializing in nitinol technology and products.<http://www.itinitinol.com/>.

- [84] Irfan, M. (2012). *Chemistry and technology of thermosetting polymers in construction applications*. Springer Science & Business Media.
- [85] Ishiguro, H. and S. Nishio (2007). Building artificial humans to understand humans. *Journal of Artificial Organs* 10(3), 133–142.
- [86] Ivshin, Y. and T. J. Pence (1994). A thermomechanical model for a one variant shape memory material. *Journal of intelligent material systems and structures* 5(4), 455–473.
- [87] Jairakrean, S. and T. Chanthasopeephan (2009). Position control of sma actuator for 3d tactile display. In *Rehabilitation Robotics, 2009. ICORR 2009. IEEE International Conference on*, pp. 234–239. IEEE.
- [88] Jakus, A. E., E. B. Secor, A. L. Rutz, S. W. Jordan, M. C. Hersam, and R. N. Shah (2015). Three-dimensional printing of high-content graphene scaffolds for electronic and biomedical applications. *ACS nano* 9(4), 4636–4648.
- [89] Joyce, L., W. DeVries, W. Hastings, D. Olsen, R. Jarvik, and W. Kolff (1983). Response of the human body to the first permanent implant of the jarvik-7 total artificial heart. *Transactions-American Society for Artificial Internal Organs* 29, 81–87.
- [90] Kahn, P. H., N. G. Freier, B. Friedman, R. L. Severson, and E. N. Feldman (2004). Social and moral relationships with robotic others? In *Robot and Human Interactive Communication, 2004. ROMAN 2004. 13th IEEE International Workshop on*, pp. 545–550. IEEE.
- [91] Kajita, S., K. Kaneko, F. Kaneiro, K. Harada, M. Morisawa, S. Nakaoka, K. Miura, K. Fujiwara, E. S. Neo, I. Hara, et al. (2011). Cybernetic human hrp-4c: A humanoid robot with human-like proportions. In *Robotics Research*, pp. 301–314. Springer.
- [92] Kamyshny, A., J. Steinke, and S. Magdassi (2011). Metal-based inkjet inks for printed electronics. *The Open Applied Physics Journal* 4(1).
- [93] Kargakis, S. (2014, November 20). Artificial heart. US Patent App. 14/262,028.
- [94] Katz, G., B. Harchandani, and B. Shah (2015). Drug-eluting stents: the past, present, and future. *Current atherosclerosis reports* 17(3), 11.
- [95] Khaing, M., J. Fuh, and L. Lu (2001). Direct metal laser sintering for rapid tooling: processing and characterisation of eos parts. *Journal of Materials Processing Technology* 113(1-3), 269–272.
- [96] Kim, S., E. Hawkes, K. Choy, M. Joldaz, J. Foley, and R. Wood (2009). Micro artificial muscle fiber using niti spring for soft robotics. In *Intelligent Robots and Systems, 2009. IROS 2009. IEEE/RSJ International Conference on*, pp. 2228–2234. IEEE.

- [97] Kobayashi, M., D. J. Horvath, N. Mielke, A. Shiose, B. Kuban, M. Goodin, K. Fukamachi, and L. A. Golding (2012). Progress on the design and development of the continuous-flow total artificial heart. *Artificial organs* 36(8), 705–713.
- [98] Kolyvas, E. and A. Tzes (2018). Model based design of antagonistic shape memory alloy spring devices. *Journal of Intelligent Material Systems and Structures*, 1045389X18770880.
- [99] Kozuki, T., Y. Motegi, T. Shirai, Y. Asano, J. Urata, Y. Nakanishi, K. Okada, and M. Inaba (2013). Design of upper limb by adhesion of muscles and bones—detail human mimetic musculoskeletal humanoid kenshiro. In *Intelligent Robots and Systems (IROS), 2013 IEEE/RSJ International Conference on*, pp. 935–940. IEEE.
- [100] Krzyzanowski, M., D. Svyetlichnyy, G. Stevenson, and W. M. Rainforth (2016). Powder bed generation in integrated modelling of additive layer manufacturing of orthopaedic implants. *The International Journal of Advanced Manufacturing Technology* 87(1-4), 519–530.
- [101] Kubota, N. and A. Yorita (2008). Structured learning for partner robots based on natural communication. In *Soft Computing in Industrial Applications, 2008. SMCia'08. IEEE Conference on*, pp. 303–308. IEEE.
- [102] Kumar, B., M. Castro, and J.-F. Feller (2012). Poly (lactic acid)–multi-wall carbon nanotube conductive biopolymer nanocomposite vapour sensors. *Sensors and Actuators B: Chemical* 161(1), 621–628.
- [103] Kumar, P. K., D. C. Lagoudas, K. J. Zanca, and M. Z. Lagoudas (2006). Thermomechanical characterization of high temperature sma actuators. In *Smart Structures and Materials 2006: Active Materials: Behavior and Mechanics*, Volume 6170, pp. 617012. International Society for Optics and Photonics.
- [104] Kwon, W., H. K. Kim, J. K. Park, C. H. Roh, J. Lee, J. Park, W.-K. Kim, and K. Roh (2007). Biped humanoid robot mahru iii. In *Humanoid Robots, 2007 7th IEEE-RAS International Conference on*, pp. 583–588. IEEE.
- [105] Ladd, C., J.-H. So, J. Muth, and M. D. Dickey (2013). 3d printing of free standing liquid metal microstructures. *Advanced Materials* 25(36), 5081–5085.
- [106] Lagoudas, D. C. (2008). *Shape memory alloys: modeling and engineering applications*. Springer Science & Business Media.
- [107] Lapeyre, M., P. Rouanet, and P.-Y. Oudeyer (2013). Poppy: A new bio-inspired humanoid robot platform for biped locomotion and physical human-robot interaction. In *Proceedings of the 6th International Symposium on Adaptive Motion in Animals and Machines (AMAM)*.

- [108] Lau, K. W. and U. Sigwart (1992). Novel coronary interventional devices: an update. *American heart journal* 123(2), 497–506.
- [109] Lee, D. D., S.-J. Yi, S. McGill, Y. Zhang, S. Behnke, M. Missura, H. Schulz, D. Hong, J. Han, and M. Hopkins (2011). Robocup 2011 humanoid league winners. In *Robot Soccer World Cup*, pp. 37–50. Springer.
- [110] Lee, H. J. and J. J. Lee (2000). Evaluation of the characteristics of a shape memory alloy spring actuator. *Smart Materials and Structures* 9(6), 817.
- [111] Leigh, S. J., R. J. Bradley, C. P. Pursell, D. R. Billson, and D. A. Hutchins (2012). A simple, low-cost conductive composite material for 3d printing of electronic sensors. *PloS one* 7(11), e49365.
- [112] Liang, C., Z. Li, and S. Dai (2008). Mesoporous carbon materials: synthesis and modification. *Angewandte Chemie International Edition* 47(20), 3696–3717.
- [113] Liang, C. and C. Rogers (1993). Design of shape memory alloy springs with applications in vibration control. *Journal of Vibration and Acoustics* 115(1), 129–135.
- [114] Liang, C. and C. A. Rogers (1997). One-dimensional thermomechanical constitutive relations for shape memory materials. *Journal of intelligent material systems and structures* 8(4), 285–302.
- [115] Lin, P.-h., H. Tobushi, K. Tanaka, T. Hattori, and A. Ikai (1996). Influence of strain rate on deformation properties of tni shape memory alloy. *JSME international journal. Ser. A, Mechanics and material engineering* 39(1), 117–123.
- [116] Liu, R., G. Ma, F.-T. Meng, and Z.-G. Su (2005). Preparation of uniform-sized pla microcapsules by combining shirasu porous glass membrane emulsification technique and multiple emulsion-solvent evaporation method. *Journal of Controlled Release* 103(1), 31–43.
- [117] Looije, R., F. Cnossen, and M. A. Neerinx (2006). Incorporating guidelines for health assistance into a socially intelligent robot. In *Robot and Human Interactive Communication, 2006. ROMAN 2006. The 15th IEEE International Symposium on*, pp. 515–520. IEEE.
- [118] Loomis, A. (2017). *Figure drawing for all it's worth*. EDITORA BIBLIOMUNDI SERVIÇOS DIGITAIS LTDA.
- [119] Love, L. J., V. Kunc, O. Rios, C. E. Duty, A. M. Elliott, B. K. Post, R. J. Smith, and C. A. Blue (2014). The importance of carbon fiber to polymer additive manufacturing. *Journal of Materials Research* 29(17), 1893–1898.

- [120] Mac Donald, B. J. (2007). *Practical stress analysis with finite elements*. Glasnevin publishing.
- [121] Madden, J. D., N. A. Vandesteeg, P. A. Anquetil, P. G. Madden, A. Takshi, R. Z. Pytel, S. R. Lafontaine, P. A. Wieringa, and I. W. Hunter (2004). Artificial muscle technology: physical principles and naval prospects. *IEEE Journal of oceanic engineering* 29(3), 706–728.
- [122] Marieb, E. N. and K. Hoehn (2007). *Human anatomy & physiology*. Pearson Education.
- [123] Matsumoto, H. (1993). Transformation behaviour of niti in relation to thermal cycling and deformation. *Physica B: Condensed Matter* 190(2-3), 115–120.
- [124] Mavroidis, C., C. Pfeiffer, and M. Mosley (1999). Conventional actuators, shape memory alloys, and electrorheological fluids.
- [125] Mavroidis, C., C. Pfeiffer, and M. Mosley (2000). 5.1 conventional actuators, shape memory alloys, and electrorheological fluids. *Automation, miniature robotics, and sensors for nondestructive testing and evaluation* 4, 189.
- [126] McAdams, B. H. and A. A. Rizvi (2016). An overview of insulin pumps and glucose sensors for the generalist. *Journal of clinical medicine* 5(1), 5.
- [127] Michalowski, M. P., S. Sabanovic, and H. Kozima (2007). A dancing robot for rhythmic social interaction. In *Human-Robot Interaction (HRI), 2007 2nd ACM/IEEE International Conference on*, pp. 89–96. IEEE.
- [128] Miwa, H., T. Umetsu, A. Takanishi, and H. Takanohu (2001). Human-like robot head that has olfactory sensation and facial color expression. In *Robotics and Automation, 2001. Proceedings 2001 ICRA. IEEE International Conference on*, Volume 1, pp. 459–464. IEEE.
- [129] Mizuuchi, I., T. Yoshikai, Y. Sodeyama, Y. Nakanishi, A. Miyadera, T. Yamamoto, T. Niemela, M. Hayashi, J. Urata, Y. Namiki, et al. (2006). Development of musculoskeletal humanoid kotaro. In *Robotics and Automation, 2006. ICRA 2006. Proceedings 2006 IEEE International Conference on*, pp. 82–87. IEEE.
- [130] Mohacsi, P. and P. Leprince (2014). The carmat total artificial heart.
- [131] Mooney, M. (1940). A theory of large elastic deformation. *Journal of applied physics* 11(9), 582–592.
- [132] Moore, J. E., E. S. Weydahl, and A. Santamarina (2001). Frequency dependence of dynamic curvature effects on flow through coronary arteries. *Journal of biomechanical engineering* 123(2), 129–133.

- [133] Morgan, A. J., L. H. San Jose, W. D. Jamieson, J. M. Wymant, B. Song, P. Stephens, D. A. Barrow, and O. K. Castell (2016). Simple and versatile 3d printed microfluidics using fused filament fabrication. *PloS one* 11(4), e0152023.
- [134] Mukhopadhyay, S. (2011). *Nanoscale Multifunctional Materials: Science & Applications*. John Wiley & Sons.
- [135] Multi3D. Accessed august 20 2017. <https://www.multi3dllc.com/product/electrifi-3d-printing-filament/>.
- [136] Nakanishi, Y., S. Ohta, T. Shirai, Y. Asano, T. Kozuki, Y. Kakehashi, H. Mizoguchi, T. Kurotobi, Y. Motegi, K. Sasabuchi, et al. (2013). Design approach of biologically-inspired musculoskeletal humanoids. *International Journal of Advanced Robotic Systems* 10(4), 216.
- [137] Nakazawa, G., A. V. Finn, M. Vorpahl, E. Ladich, R. Kutys, I. Balazs, F. D. Kolodgie, and R. Virmani (2009). Incidence and predictors of drug-eluting stent fracture in human coronary artery: a pathologic analysis. *Journal of the American College of Cardiology* 54(21), 1924–1931.
- [138] Nicholson, J. C. (2015). *Nanoenhanced additive manufacturing: Additive introduction onto halloysite nanotubes and into 3D printing filament for tailored material characteristics*. Ph. D. thesis, Louisiana Tech University.
- [139] Nishio, S., H. Ishiguro, and N. Hagita (2007). Geminoid: Teleoperated android of an existing person. In *Humanoid robots: new developments*. InTech.
- [140] Novakova-Marcincinova, L. and I. Kuric (2012). Basic and advanced materials for fused deposition modeling rapid prototyping technology. *Manuf. and Ind. Eng* 11(1), 24–27.
- [141] Oh, J.-H., D. Hanson, W.-S. Kim, Y. Han, J.-Y. Kim, and I.-W. Park (2006). Design of android type humanoid robot albert hubo. In *Intelligent Robots and Systems, 2006 IEEE/RSJ International Conference on*, pp. 1428–1433. IEEE.
- [142] Oliveira, J. E., L. H. C. Mattoso, E. S. Medeiros, and V. Zucolotto (2012). Poly (lactic acid)/carbon nanotube fibers as novel platforms for glucose biosensors. *Biosensors* 2(1), 70–82.
- [143] Orejola, W. C. and C. A. Orejola (2015, November 24). Autonomous artificial heart. US Patent 9,192,702.
- [144] Osada, J., S. Ohnaka, and M. Sato (2006). The scenario and design process of childcare robot, papero. In *Proceedings of the 2006 ACM SIGCHI international conference on Advances in computer entertainment technology*, pp. 80. ACM.

- [145] Otsuka, K. and C. M. Wayman (1999). *Shape memory materials*. Cambridge university press.
- [146] Paik, J. K., E. Hawkes, and R. J. Wood (2010). A novel low-profile shape memory alloy torsional actuator. *Smart Materials and Structures* 19(12), 125014.
- [147] Paik, J. K. and R. J. Wood (2012). A bidirectional shape memory alloy folding actuator. *Smart Materials and Structures* 21(6), 065013.
- [148] Park, B. K., D. Kim, S. Jeong, J. Moon, and J. S. Kim (2007). Direct writing of copper conductive patterns by ink-jet printing. *Thin Solid Films* 515(19), 7706–7711.
- [149] Pelletier, B., S. Spiliopoulos, T. Finocchiaro, F. Graef, K. Kuipers, M. Laumen, D. Guersoy, U. Steinseifer, R. Koerfer, and G. Tenderich (2014). System overview of the fully implantable destination therapy—reinheart-total artificial heart. *European Journal of Cardio-Thoracic Surgery* 47(1), 80–86.
- [150] Pennington, D., K. Kanter, L. McBride, G. Kaiser, H. Barner, L. Miller, K. Naunheim, A. Fiore, and V. Willman (1988). Seven years’ experience with the pierce-donachy ventricular assist device. *The Journal of thoracic and cardiovascular surgery* 96(6), 901–911.
- [151] Pfeifer, R., F. Iida, and M. Lungarella (2014). Cognition from the bottom up: on biological inspiration, body morphology, and soft materials. *Trends in cognitive sciences* 18(8), 404–413.
- [152] Pierce, M. D. and S. A. Mascaro (2013). A biologically inspired wet shape memory alloy actuated robotic pump. *IEEE/ASME Transactions on Mechatronics* 18(2), 536–546.
- [153] Potnuru, A. (2013). *Low noise, interactive robotic system for psychiatric rehabilitation of children*. The University of Texas at Dallas.
- [154] Potnuru, A. (2017). Simulation and experimental study of niti double helix stents for human coronary arteries. In *ASME 2017 International Mechanical Engineering Congress and Exposition*, pp. V003T04A028–V003T04A028. American Society of Mechanical Engineers.
- [155] Potnuru, A., M. Jafarzadeh, and Y. Tadesse (2016). 3d printed dancing humanoid robot “buddy” for homecare. In *Automation Science and Engineering (CASE), 2016 IEEE International Conference on*, pp. 733–738. IEEE.
- [156] Potnuru, A. and Y. Tadesse (2014). Synthesis and characterization of hybrid actuator based on polypyrrole and sma. In *ASME 2014 International Mechanical Engineering Congress and Exposition*, pp. V003T03A003–V003T03A003. American Society of Mechanical Engineers.

- [157] Potnuru, A. and Y. Tadesse (2015). Artificial heart for humanoid robot using coiled sma actuators. In *Bioinspiration, Biomimetics, and Bioreplication 2015*, Volume 9429, pp. 94290R. International Society for Optics and Photonics.
- [158] Potnuru, A. and Y. Tadesse (2017). Characterization of coiled sma actuators for humanoid robot. In *Active and Passive Smart Structures and Integrated Systems 2017*, Volume 10164, pp. 101640W. International Society for Optics and Photonics.
- [159] Potnuru, A. and Y. Tadesse (2018a). Effect of spring geometry and characterization of coiled shape memory alloy (csma) actuators for soft robots. (submitted-under revision). *Journal of Intelligent Material Systems and Structures*.
- [160] Potnuru, A. and Y. Tadesse (2018b). Investigation of polylactide and carbon nanocomposite filament for 3d printing. *Progress in Additive Manufacturing*, 1–19.
- [161] Potnuru, A., L. Wu, and Y. Tadesse (2014). Artificial heart for humanoid robot. In *Electroactive Polymer Actuators and Devices (EAPAD) 2014*, Volume 9056, pp. 90562F. International Society for Optics and Photonics.
- [162] Poulsen, P. R., J. Carl, J. Nielsen, M. S. Nielsen, J. B. Thomsen, H. K. Jensen, B. Kjær-gaard, P. R. Zepernick, E. Worm, W. Fledelius, et al. (2012). Megavoltage image-based dynamic multileaf collimator tracking of a niti stent in porcine lungs on a linear accelerator. *International Journal of Radiation Oncology• Biology• Physics* 82(2), e321–e327.
- [163] Ranatunga, I., M. Beltran, N. A. Torres, N. Bugnariu, R. M. Patterson, C. Garver, and D. O. Popa (2013). Human-robot upper body gesture imitation analysis for autism spectrum disorders. In *International Conference on Social Robotics*, pp. 218–228. Springer.
- [164] Rehnmark, F., R. O. Ambrose, B. Kennedy, M. Diftler, J. Mehling, L. Bridgwater, N. Radford, S. M. Goza, and C. Culbert (2005). Innovative robot archetypes for in-space construction and maintenance. In *AIP Conference Proceedings*, Volume 746, pp. 1070–1077. AIP.
- [165] Rengier, F., A. Mehndiratta, H. Von Tengg-Kobligk, C. M. Zechmann, R. Unterhinninghofen, H.-U. Kauczor, and F. L. Giesel (2010). 3d printing based on imaging data: review of medical applications. *International journal of computer assisted radiology and surgery* 5(4), 335–341.
- [166] Ricks, D. J. and M. B. Colton (2010). Trends and considerations in robot-assisted autism therapy. In *Robotics and Automation (ICRA), 2010 IEEE International Conference on*, pp. 4354–4359. IEEE.
- [167] Rivlin, R. (1948). Large elastic deformations of isotropic materials iv. further developments of the general theory. *Phil. Trans. R. Soc. Lond. A* 241(835), 379–397.

- [168] Roche, E., A. Menz, P. Hiremath, N. Vasilyev, D. Mooney, and C. Walsh. Design of an anatomically accurate, multi-material, patient-specific cardiac simulator with sensing and controls. *Google Scholar*.
- [169] Roche, E. T., M. A. Horvath, I. Wamala, A. Alazmani, S.-E. Song, W. Whyte, Z. Machaidze, C. J. Payne, J. C. Weaver, G. Fishbein, et al. (2017). Soft robotic sleeve supports heart function. *Science translational medicine* 9(373), eaaf3925.
- [170] Rosochowski, A. and A. Matuszak (2000). Rapid tooling: the state of the art. *Journal of materials processing technology* 106(1-3), 191–198.
- [171] Saharan, L., A. Sharma, M. J. de Andrade, R. H. Baughman, and Y. Tadesse (2017). Design of a 3d printed lightweight orthotic device based on twisted and coiled polymer muscle: igrab hand orthosis. In *Active and Passive Smart Structures and Integrated Systems 2017*, Volume 10164, pp. 1016428. International Society for Optics and Photonics.
- [172] Saharan, L. and Y. Tadesse (2016). Robotic hand with locking mechanism using tcp muscles for applications in prosthetic hand and humanoids. In *Bioinspiration, Biomimetics, and Bioreplication 2016*, Volume 9797, pp. 97970V. International Society for Optics and Photonics.
- [173] Sakagami, Y., R. Watanabe, C. Aoyama, S. Matsunaga, N. Higaki, and K. Fujimura (2002). The intelligent asimo: System overview and integration. In *Intelligent Robots and Systems, 2002. IEEE/RSJ International Conference on*, Volume 3, pp. 2478–2483. IEEE.
- [174] Sangiorgi, G., G. Melzi, P. Agostoni, C. Cola, F. Clementi, P. Romitelli, R. Virmani, and A. Colombo (2007). Engineering aspects of stents design and their translation into clinical practice. *Annali dell'Istituto superiore di sanita* 43(1), 89–100.
- [175] Santhanam, R., Y. Krishna, and M. Sivakumar (2013). Behaviour of niti sma helical springs under different temperatures and deflections. *ISRN Materials Science* 2013.
- [176] Sathyanarayana, S. and C. Hübner (2013). Thermoplastic nanocomposites with carbon nanotubes. In *Structural Nanocomposites*, pp. 19–60. Springer.
- [177] Sa'ude, N., M. Ibrahim, and M. H. I. Ibrahim (2013). Mechanical properties of highly filled iron-abs composites in injection molding for fdm wire filament. In *Materials Science Forum*, Volume 773, pp. 448–453. Trans Tech Publications, Switzerland.
- [178] Sawyer, P., M. Page, L. Baseliust, C. McCool, E. Lester, B. Stanczewski, S. Srinivasan, and N. Ramasamy (1976). Further study of nitinol wire as contractile artificial muscle for an artificial heart. *Cardiovascular diseases* 3(1), 65.

- [179] Scassellati, B. (2007). How social robots will help us to diagnose, treat, and understand autism. In *Robotics research*, pp. 552–563. Springer.
- [180] Schumacher, C. M., M. Loepfe, R. Fuhrer, R. N. Grass, and W. J. Stark (2014). 3d printed lost-wax casted soft silicone monoblocks enable heart-inspired pumping by internal combustion. *RSC Advances* 4(31), 16039–16042.
- [181] Schwarz, M., J. Pastrana, P. Allgeuer, M. Schreiber, S. Schueller, M. Missura, and S. Behnke (2013). Humanoid teensize open platform nimbro-op. In *Robot Soccer World Cup*, pp. 568–575. Springer.
- [182] Serruys, P. W., F. Unger, J. E. Sousa, A. Jatene, H. J. Bonnier, J. P. Schönberger, N. Buller, R. Bonser, M. J. van den Brand, L. A. van Herwerden, et al. (2001). Comparison of coronary-artery bypass surgery and stenting for the treatment of multivessel disease. *New England Journal of Medicine* 344(15), 1117–1124.
- [183] Shamsuddin, S., H. Yussof, L. I. Ismail, S. Mohamed, F. A. Hanapiah, and N. I. Zahari (2012). Humanoid robot nao interacting with autistic children of moderately impaired intelligence to augment communication skills. *Procedia Engineering* 41, 1533–1538.
- [184] Shearn, D., E. Bergman, K. Hill, A. Abel, and L. Hinds (1990). Facial coloration and temperature responses in blushing. *Psychophysiology* 27(6), 687–693.
- [185] Shergold, O. A., N. A. Fleck, and D. Radford (2006). The uniaxial stress versus strain response of pig skin and silicone rubber at low and high strain rates. *International Journal of Impact Engineering* 32(9), 1384–1402.
- [186] Shimada, M., T. Minato, S. Itakura, and H. Ishiguro (2006). Evaluation of android using unconscious recognition. In *Humanoid Robots, 2006 6th IEEE-RAS International Conference on*, pp. 157–162. IEEE.
- [187] Shiraishi, Y., T. Yambe, Y. Saijo, F. Sato, A. Tanaka, M. Yoshizawa, T. Sugai, R. Sakata, Y. Luo, Y. Park, et al. (2008). Sensorless control for a sophisticated artificial myocardial contraction by using shape memory alloy fibre. In *Engineering in Medicine and Biology Society, 2008. EMBS 2008. 30th Annual International Conference of the IEEE*, pp. 711–714. IEEE.
- [188] Sigwart, U., J. Puel, V. Mirkovitch, F. Joffre, and L. Kappenberg (1987). Intravascular stents to prevent occlusion and re-stenosis after transluminal angioplasty. *New England Journal of Medicine* 316(12), 701–706.
- [189] Sobkowicz, M. J., J. R. Dorgan, K. W. Gneshin, A. M. Herring, and J. T. McKinnon (2009). Supramolecular bionanocomposites: grafting of biobased polylactide to carbon nanoparticle surfaces. *Australian journal of chemistry* 62(8), 865–870.

- [190] Song, S.-H., J.-Y. Lee, H. Rodrigue, I.-S. Choi, Y. J. Kang, and S.-H. Ahn (2016). 35 hz shape memory alloy actuator with bending-twisting mode. *Scientific reports* 6, 21118.
- [191] Sousa, V. C. d., C. De Marqui Junior, and M. H. Elahinia (2018). Effect of constitutive model parameters on the aeroelastic behavior of an airfoil with shape memory alloy springs. *Journal of Vibration and Control* 24(6), 1065–1085.
- [192] Spinella, I. and E. Dragoni (2010). Analysis and design of hollow helical springs for shape memory actuators. *Journal of Intelligent Material Systems and Structures* 21(2), 185–199.
- [193] Srivastava, S. et al. (2012). Effect of aggregation on thermal conductivity and viscosity of nanofluids. *Applied Nanoscience* 2(3), 325–331.
- [194] Stebner, A., S. Padula III, R. Noebe, B. Lerch, and D. Quinn (2009). Development, characterization, and design considerations of ni19. 5ti50. 5 pd25pt5 high-temperature shape memory alloy helical actuators. *Journal of Intelligent Material Systems and Structures* 20(17), 2107–2126.
- [195] Sugiyama, Y., A. Shiotsu, M. Yamanaka, and S. Hirai (2005). Circular/spherical robots for crawling and jumping. In *Robotics and Automation, 2005. ICRA 2005. Proceedings of the 2005 IEEE International Conference on*, pp. 3595–3600. IEEE.
- [196] Suzuki, Y., K. Daitoku, M. Minakawa, K. Fukui, and I. Fukuda (2008). Dynamic cardiomyoplasty using artificial muscle. *Journal of Artificial Organs* 11(3), 160–162.
- [197] Tadesse, Y. (2012). Actuation technologies suitable for humanoid robots. In *ASME 2012 International Mechanical Engineering Congress and Exposition*, pp. 1–10. American Society of Mechanical Engineers.
- [198] Tadesse, Y. (2013a). Actuation technologies for humanoid robots with facial expressions (hrwfe). *Transaction on Control and Mechanical Systems* 2(7).
- [199] Tadesse, Y. (2013b). Electroactive polymer and shape memory alloy actuators in biomimetics and humanoids. In *Electroactive Polymer Actuators and Devices (EAPAD) 2013*, Volume 8687, pp. 868709. International Society for Optics and Photonics.
- [200] Tadesse, Y., J. Brennan, C. Smith, T. E. Long, and S. Priya (2010). Synthesis and characterization of polypyrrole composite actuator for jellyfish unmanned undersea vehicle. In *Electroactive Polymer Actuators and Devices (EAPAD) 2010*, Volume 7642, pp. 764222. International Society for Optics and Photonics.
- [201] Tadesse, Y., R. W. Grange, and S. Priya (2009). Synthesis and cyclic force characterization of helical polypyrrole actuators for artificial facial muscles. *Smart Materials and Structures* 18(8), 085008.

- [202] Tadesse, Y., D. Hong, and S. Priya (2011). Twelve degree of freedom baby humanoid head using shape memory alloy actuators. *Journal of Mechanisms and Robotics* 3(1), 011008.
- [203] Tadesse, Y., S. Priya, H. Stephanou, D. Popa, and D. Hanson (2006). Piezoelectric actuation and sensing for facial robotics. *Ferroelectrics* 345(1), 13–25.
- [204] Tadesse, Y., K. Subbarao, and S. Priya (2010). Realizing a humanoid neck with serial chain four-bar mechanism. *Journal of Intelligent Material Systems and Structures* 21(12), 1169–1191.
- [205] Tadesse, Y., N. Thayer, and S. Priya (2010). Tailoring the response time of shape memory alloy wires through active cooling and pre-stress. *Journal of Intelligent Material Systems and Structures* 21(1), 19–40.
- [206] Tadesse, Y., L. Wu, and L. K. Saharan (2016). Musculoskeletal system for bio-inspired robotic systems. *mechanical engineering* 138(3), S11.
- [207] Takatani, S., M. Shiono, T. Sasaki, I. Sakuma, J. Glueck, M. Sekela, G. Noon, Y. Nose, and M. DeBakey (1991). A unique, efficient, implantable, electromechanical, total artificial heart. *ASAIO transactions* 37, M238–M240.
- [208] Tanaka, F., B. Fortenberry, K. Aisaka, and J. R. Movellan (2005). Developing dance interaction between qrio and toddlers in a classroom environment: Plans for the first steps. In *Robot and Human Interactive Communication, 2005. ROMAN 2005. IEEE International Workshop on*, pp. 223–228. IEEE.
- [209] Tanaka, F. and H. Suzuki (2004). Dance interaction with qrio: a case study for non-boring interaction by using an entrainment ensemble model. In *Robot and Human Interactive Communication, 2004. ROMAN 2004. 13th IEEE International Workshop on*, pp. 419–424. IEEE.
- [210] Tanaka, K. (1986). A thermomechanical sketch of shape memory effect: one-dimensional tensile behavior. *Res. Mechanica* 18, 251–263.
- [211] Taniguchi, H. (2013). Flexible artificial muscle actuator using coiled shape memory alloy wires. *APCBEE procedia* 7, 54–59.
- [212] Thuc, H. L. U. and P. Van Tuan (2014). An effective video based system for human fall detection. *Int. J. Advanced Research in Computer Engineering & Technology* 3(8), 2820–2826.
- [213] TOKI, C. Bio metal, toki corporation.

- [214] Trepanier, C., M. Tabrizian, L. Yahia, L. Bilodeau, and D. L. Piron (1998). Effect of modification of oxide layer on niti stent corrosion resistance. *Journal of biomedical materials research* 43(4), 433–440.
- [215] Trovato, G., T. Kishi, N. Endo, K. Hashimoto, and A. Takanishi (2012). Development of facial expressions generator for emotion expressive humanoid robot. In *Humanoid Robots (Humanoids), 2012 12th IEEE-RAS International Conference on*, pp. 303–308. IEEE.
- [216] Tsagarakis, N. G., G. Metta, G. Sandini, D. Vernon, R. Beira, F. Becchi, L. Righetti, J. Santos-Victor, A. J. Ijspeert, M. C. Carrozza, et al. (2007). icub: the design and realization of an open humanoid platform for cognitive and neuroscience research. *Advanced Robotics* 21(10), 1151–1175.
- [217] Tsai, M.-J. and C.-T. Wu (2014). Study of mandible reconstruction using a fibula flap with application of additive manufacturing technology. *Biomedical engineering online* 13(1), 57.
- [218] Tsiakatouras, G., E. Tsellou, and C. Stergiou (2014). Comparative study on nanotubes reinforced with carbon filaments for the 3d printing of mechanical parts. *World Transactions on Engineering and Technology Education* 12(3), 392–396.
- [219] Umeda, H., T. Gochi, M. Iwase, H. Izawa, T. Shimizu, R. Ishiki, H. Inagaki, J. Toyama, M. Yokota, and T. Murohara (2009). Frequency, predictors and outcome of stent fracture after sirolimus-eluting stent implantation. *International journal of cardiology* 133(3), 321–326.
- [220] van de Ven, A. A., A.-m. A. Sponselee, and B. A. Schouten (2010). Robo md: a home care robot for monitoring and detection of critical situations. In *Proceedings of the 28th Annual European Conference on Cognitive Ergonomics*, pp. 375–376. ACM.
- [221] Van Osch, T. H., J. Perelaer, A. W. de Laat, and U. S. Schubert (2008). Inkjet printing of narrow conductive tracks on untreated polymeric substrates. *Advanced Materials* 20(2), 343–345.
- [222] Vincent Hughes IT, Kambiz Chizari, D. T. (2016). 3d printable conductive nanocomposites of pla and multi-walled carbon nanotubes. *Material Matters* 11(2).
- [223] Walters, P., D. Huson, C. Parraman, and M. Stanić (2009). 3d printing in colour: Technical evaluation and creative applications. In *Impact 6 International Printmaking Conference*.
- [224] Walters, P., A. Lewis, A. Stinchcombe, R. Stephenson, and I. Ieropoulos (2013). Artificial heartbeat: design and fabrication of a biologically inspired pump. *Bioinspiration & biomimetics* 8(4), 046012.

- [225] Wang, X., B. Verlinden, and J. Van Humbeeck (2015). Effect of post-deformation annealing on the r-phase transformation temperatures in niti shape memory alloys. *Intermetallics* 62, 43–49.
- [226] Wang, Z., Y. Liu, and X. Jiang (2008). The research of the humanoid robot with facial expressions for emotional interaction. In *Intelligent Networks and Intelligent Systems, 2008. ICINIS'08. First International Conference on*, pp. 416–420. IEEE.
- [227] Wei, X., D. Li, W. Jiang, Z. Gu, X. Wang, Z. Zhang, and Z. Sun (2015). 3d printable graphene composite. *Scientific reports* 5, 11181.
- [228] Weiguo, W., M. Qingmei, and W. Yu (2004). Development of the humanoid head portrait robot system with flexible face and expression. In *Robotics and Biomimetics, 2004. ROBIO 2004. IEEE International Conference on*, pp. 757–762. IEEE.
- [229] Weydahl, E. S. and J. E. Moore (2001). Dynamic curvature strongly affects wall shear rates in a coronary artery bifurcation model. *Journal of biomechanics* 34(9), 1189–1196.
- [230] Wilkin, J. K. (1988). Why is flushing limited to a mostly facial cutaneous distribution? *Journal of the American Academy of Dermatology* 19(2), 309–313.
- [231] Wu, L., I. Chauhan, and Y. Tadesse (2018). A novel soft actuator for the musculoskeletal system. *Advanced Materials Technologies*.
- [232] Wu, L., M. Larkin, A. Potnuru, and Y. Tadesse (2016). Hbs-1: A modular child-size 3d printed humanoid. *Robotics* 5(1), 1.
- [233] Wu, L. and Y. Tadesse (2016). Musculoskeletal system for bio-inspired robotic systems based on ball and socket joints. In *ASME 2016 International Mechanical Engineering Congress and Exposition*, pp. V04AT05A020–V04AT05A020. American Society of Mechanical Engineers.
- [234] Wu, W., M. Qi, X.-P. Liu, D.-Z. Yang, and W.-Q. Wang (2007). Delivery and release of nitinol stent in carotid artery and their interactions: a finite element analysis. *Journal of Biomechanics* 40(13), 3034–3040.
- [235] Xu, J., J. Yang, N. Huang, C. Uhl, Y. Zhou, and Y. Liu (2016). Mechanical response of cardiovascular stents under vascular dynamic bending. *Biomedical engineering online* 15(1), 21.
- [236] Yamada, T. and T. Watanabe (2004). Effects of facial color on virtual facial image synthesis for dynamic facial color and expression under laughing emotion. In *Robot and Human Interactive Communication, 2004. ROMAN 2004. 13th IEEE International Workshop on*, pp. 341–346. IEEE.

- [237] Yamasaki, F., T. Matsui, T. Miyashita, and H. Kitano (2000). Pino the humanoid: A basic architecture. In *Robot Soccer World Cup*, pp. 269–278. Springer.
- [238] Yan, S., X. Liu, F. Xu, and J. Wang (2007). A gripper actuated by a pair of differential sma springs. *Journal of intelligent material systems and structures* 18(5), 459–466.
- [239] Yates, S. J. and A. L. Kalamkarov (2013). Experimental study of helical shape memory alloy actuators: effects of design and operating parameters on thermal transients and stroke. *Metals* 3(1), 123–149.
- [240] Yeo, J., S. Hong, D. Lee, N. Hotz, M.-T. Lee, C. P. Grigoropoulos, and S. H. Ko (2012). Next generation non-vacuum, maskless, low temperature nanoparticle ink laser digital direct metal patterning for a large area flexible electronics. *PLoS One* 7(8), e42315.
- [241] Zhang, B., T. Masuzawa, E. Tatsumi, Y. Taenaka, C. Uyama, H. Takano, and M. Takamiya (1999). Three-dimensional thoracic modeling for an anatomical compatibility study of the implantable total artificial heart. *Artificial organs* 23(3), 229–234.
- [242] Zhang, D., B. Chi, B. Li, Z. Gao, Y. Du, J. Guo, and J. Wei (2016). Fabrication of highly conductive graphene flexible circuits by 3d printing. *Synthetic Metals* 217, 79–86.

BIOGRAPHICAL SKETCH

Akshay Potnuru received his BE degree in Mechanical Engineering from GITAM University, India in 2010, and his Master of Science degree with thesis at The University of Texas at Dallas, Richardson. Currently, he is working towards his PhD at The University of Texas at Dallas in the Department of Mechanical Engineering. His research interests are in humanoid robotics which helps in the recovery of psychologically rehabilitated patients, emerging applications of smart and conductive materials, smart actuators like coiled shape memory alloys and polypyrrole, energy harvesting from human body using pyroelectric materials, modeling, 3D printing nano materials like conductive nano-carbon PLA composites and stents. He has published three journal papers and six conference papers. He has worked as a teaching assistant (TA) for computer aided design (CAD) courses and labs for more than 150 students at The University of Texas at Dallas for 6 years. He was awarded the “Outstanding Teaching Assistant Award in 2012”.

CURRICULUM VITAE

Akshay Potnuru

July 11, 2018

Contact Information:

Department of Mechanical Engineering
The University of Texas at Dallas
800 W. Campbell Rd.
Richardson, TX 75080-3021, U.S.A.

Voice: (469) 307-9315
Email: axp112630@utdallas.edu

Educational History:

Btech, Mechanical Engineering, Gandhi Institute of Technology & Management (GITAM) University, 2010

MS, Mechanical Engineering, The University of Texas at Dallas, 2013

PhD, Mechanical Engineering, The University of Texas at Dallas, 2018

Coiled shape memory alloy actuators (CSMA) and conductive filament for the realization of 3D printed robots

PhD Dissertation

Mechanical Engineering, The University of Texas at Dallas

Advisors: Dr. Yonas Tadesse, D. Qian, M. Minary, W. Taylor, W. Park, and O. Rios

Low noise, interactive robotic system for psychiatric rehabilitation of children

Masters Thesis

Mechanical Engineering, The University of Texas at Dallas

Advisor: Dr. Yonas Tadesse, D. Qian, and W. Park

Employment History:

Teaching Assistant, The University of Texas at Dallas, January 2012 – May 2017

Research Assistant, The University of Texas at Dallas, May 2012 – August 2012

Professional Recognitions and Honors:

School Awards

- Awarded “Jonsson School Graduate Scholarship”

Professional Awards

- Awarded “Outstanding Teaching Assistant Award”

Professional Memberships:

American Society of Mechanical Engineers (ASME)

Institute of Electrical and Electronics Engineers (IEEE)
International society for optics and photonics (SPIE Proceedings)

Publications:

Journals:

1. Potnuru, A. and Tadesse, Y., 2014. Characterization of pyroelectric materials for energy harvesting from human body. *Integrated Ferroelectrics*, 150(1), pp.23-50.
2. Wu, L., Larkin, M., Potnuru, A. and Tadesse, Y., 2016. Hbs-1: A modular child-size 3d printed humanoid. *Robotics*, 5(1), p.1.
3. Potnuru, A. and Tadesse, Y., 2018. Investigation of Polylactide and Carbon Nanocomposite Filament for 3D printing. *Progress in Additive Manufacturing*, DOI: 10.1007/s40964-018-0057-z
4. Potnuru, A. and Tadesse, Y., 2018. Effect of spring geometry and characterization of coiled shape memory alloy (CSMA) actuators for soft robots. *Journal of Intelligent Material Systems and Structures*, (Submitted-Under Revision)
5. Potnuru, A. and Tadesse, Y., 2018. Interactive study of human with Humanoid “Buddy” for teaching and rehabilitation of autistic children with soft pump artificial heart actuated by CSMA . (In Preparation)
6. Potnuru, A. and Tadesse, Y., 2018. A novel double helix stent for human coronary artery. (In Preparation)

Conferences:

1. Potnuru, A., Wu, L. and Tadesse, Y., 2014, March. Artificial heart for humanoid robot. In *Electroactive Polymer Actuators and Devices (EAPAD) 2014* (Vol. 9056, p. 90562F). International Society for Optics and Photonics.
2. Potnuru, A. and Tadesse, Y., 2014, November. Synthesis and Characterization of Hybrid Actuator Based on Polypyrrole and SMA. In *ASME 2014 International Mechanical Engineering Congress and Exposition* (pp. V003T03A003-V003T03A003). American Society of Mechanical Engineers.
3. Potnuru, A. and Tadesse, Y., 2015, March. Artificial heart for humanoid robot using coiled SMA actuators. In *Bioinspiration, Biomimetics, and Bioreplication 2015* (Vol. 9429, p. 94290R). International Society for Optics and Photonics.

4. Potnuru, A., Jafarzadeh, M. and Tadesse, Y., 2016, August. 3D printed dancing humanoid robot “Buddy” for homecare. In Automation Science and Engineering (CASE), 2016 IEEE International Conference on (pp. 733-738). IEEE.
5. Potnuru, A. and Tadesse, Y., 2017, April. Characterization of coiled SMA actuators for humanoid robot. In Active and Passive Smart Structures and Integrated Systems 2017 (Vol. 10164, p. 101640W). International Society for Optics and Photonics.
6. Potnuru, A., 2017, November. Simulation and Experimental Study of NiTi Double Helix Stents for Human Coronary Arteries. In ASME 2017 International Mechanical Engineering Congress and Exposition (pp. V003T04A028-V003T04A028). American Society of Mechanical Engineers.